Integration of CO2 air capture and solid oxide electrolysis for methane production

Ebbehøj, Søren Lyng; Mogensen, Mogens Bjerg; Jensen, Søren Højgaard; Riisager, Anders

Publication date:
2015

Document Version
Publisher's PDF, also known as Version of record

Technical University of Denmark

Integration of CO_2 air capture and solid oxide electrolysis for methane production

Søren Lyng Ebbehøj
Department of Energy Conversion and Storage

Ph.D. Thesis, February 2015

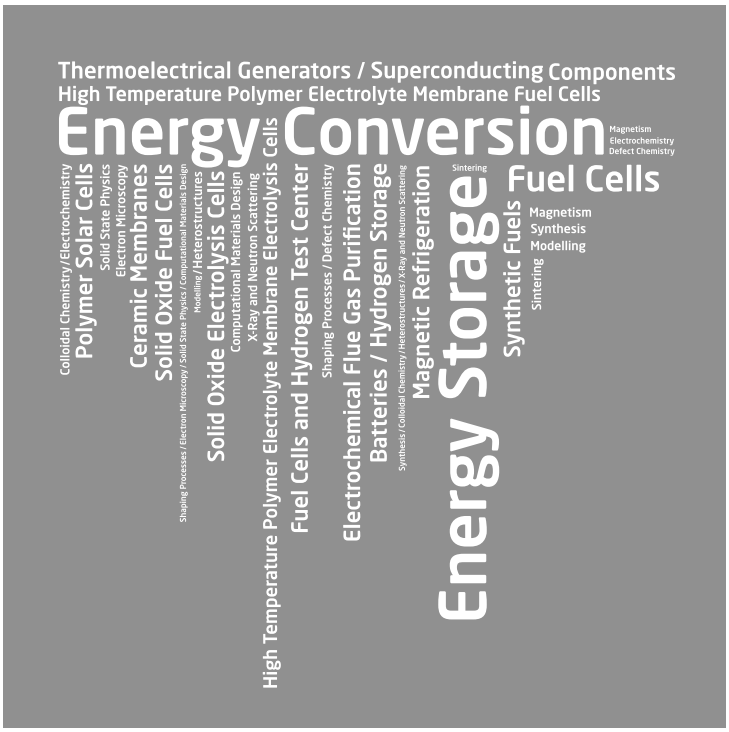

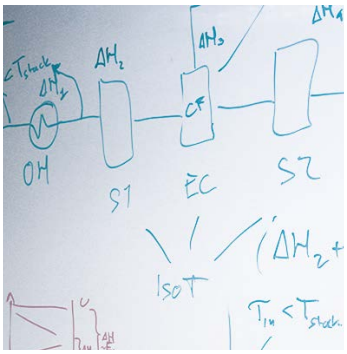

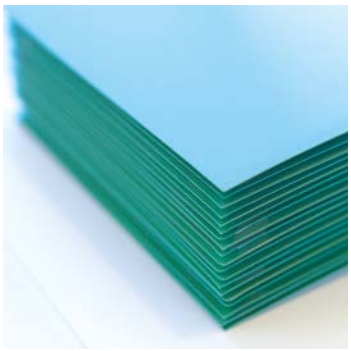

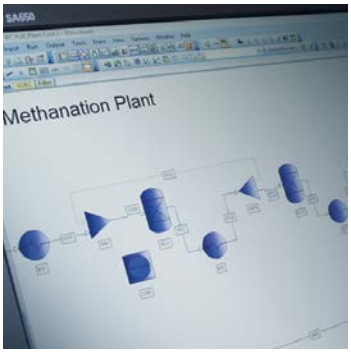

DTU Energy
Department of Energy Conversion and Storage

Integration of CO_2 air capture and solid oxide electrolysis for methane production

Author

MSc. Søren Lyng Ebbehøj
Department of Energy Conversion and Storage
Technical University of Denmark
E-mail: slebb@dtu.dk / ebbehoj@gmail.com

Supervisors

Professor Mogens Bjerg Mogensen
Department of Energy Conversion and Storage
Technical University of Denmark
E-mail: momo@dtu.dk

Dr. Søren Højgaard Jensen
Department of Energy Conversion and Storage
Technical University of Denmark
E-mail: shjj@dtu.dk

Dr. Anders Riisager
Department of Chemistry
Technical University of Denmark
E-mail: ar@kemi.dtu.dk

Publisher

Department of Energy Conversion and Storage
Technical University of Denmark
Risø Campus
Frederiksborgvej 399
DK-4000 Roskilde
Denmark
www.energy.dtu.dk
Tel: +45 46 77 58 00
Email: info@energy.dtu.dk

Submitted on February 28th, 2015

ISBN 978-87-92986-32-0

This thesis is written in partial fulfillment of the requirements for the degree Doctor of Philosophy (PhD) at the Department of Energy Conversion and Storage, Technical University of Denmark.

The work described herein was financed by the EUROSTARS E! 6691 – CAPFUEL project via the Danish Agency for Science, Technology and Innovation, contract no. 0604-00577B – EUROS (11-108005).

For those who never made it back

Abstract

This work studied the production of substitute natural gas (SNG) from CO_2 captured from the atmosphere followed by co-electrolysis with H_2O in solid oxide electrolyzer cells (SOEC) and downstream catalytic methane production.

Over the coming 20 years, Denmark is on a track to remove fossil fuels from all sectors of the energy system except for transportation. In the recently published Energikoncept 2035 [1], the Danish grid operator, Energinet.dk lays out a scenario based on 72 % wind power and 21 % biomass and waste in the electricity grid mix. In this scenario, biogas and electrolysis gasses are projected to be used for production of process heat, peak-load power generation and on the longer term to replace hydrocarbons in the most energy intensive parts of the transportation sector; especially aviation. As a prerequisite for the scenario, no biomass can be imported to enhance the supply of combustible resources. In such an energy system, technologies for production of CO_2 neutral hydrocarbons for easy storage and use in the existing infrastructure; especially in the natural gas grid; may be of great value. The studied technology fulfills those demands.

The main goal of the work was to design a plant and develop a thermodynamic model of the plant operation, enabling analyses related to selection of operating parameters; analysis and optimization of internal heat recovery and integration between the main technological sub-systems. Finally to identify the main areas of technological development through economic analyses.

The work included experimental work on an example of a system for capture of CO_2: the humidity swing (HS) system, qualitatively evaluating the H_2O uptake and CO_2 desorption characteristics of the sorbent material, especially in relation to the supply of H_2O to the sorbent. It was found that H_2O supplied in the gas phase resulted in slow uptakes and desorption rates of CO_2 whereas supplying liquid water to the sorbent resulted in fast desorption in the first hours, after which the rate dropped sharply.

A method was developed and used to characterize the impurities present in CO_2 stream from the HS system in addition to the temperature vacuum swing (TVS) system under development by Climeworks Ltd. The method relied on adsorption of impurities on a filter consisting of nickel-yttria-stabilised-zirconia (Ni/YSZ), similar to the material used in the fuel electrodes of SOECs followed by elemental analysis by glow discharge mass spectrometry. The method had a sub-ppm detection limit. Across the tested systems, a range of elements known to be detrimental to solid oxide cell (SOC) operation were detected in the range from tens of ppb to 20 ppm.

The SNG plant was modelled using the process integration software package PRO/II alongside the design process, and a series of minor studies using PRO/II and thermodynamic analysis software FactSage® aided the design process. This included studying a long range of questions

such as alternative strategies for CO_2 compression; the structure of the methanation plant; and the risk of carbon formation in both SOEC and methanation reactors, etc.

The model was based on a thermodynamic 0-dimensioal model of the electrolyzer sub-system, developed to technological specifications from the thermodynamic SOEC model published by Sun et al. [2] This model was used for a study of operating parameters, and two design cases were identified for the full plant based on these results. The two cases both operated at 80 atm, and had SOEC operating temperatures of 850 °C and 600 °C. The area specific resistance (ASR) of the SOECs were extrapolated to high pressure and low temperatures based on data for standard DTU Energy Ni-YSZ based cells, and the pressure dependency of the individual cell processes.

With the full plant model finished, the potential for internal recovery of surplus heat was analyzed, and a network of heat exchangers synthesized in order to minimize the requirements for external heating and cooling services. Based on the process flow sheets and the heat exchanger network, the dimensions and costs of the equipment of the plant were calculated and additional cost components such as installation of equipment, land use, labor costs, operation and maintenance, etc. were estimated according to standard methods.

The plant had a yearly production capacity of 575,000 Nm^3 of SNG with a methane content above 98.5 % which resulted in a Wobbe index of 49 MJ/Nm^3 which is sufficient for injection into the natural gas grid. The SOEC stack power was around 700 kW, and the plant operated at an energy efficiency of 65 % (HHV) and 58 % (LHV).

An economic analysis based on guidelines from the Danish energy agency and standard methods was conducted accounting for interest rates, taxes, depreciation etc. at a minimum acceptable rate of return set to the minimum of 4 %.

The economic analysis resulted in SNG production prices of 1.88 €/Nm^3 and 2.94 €/Nm^3 based on an electricity price of 18.6 €/MJ, a price of process heat at 120 °C of 11.9 €/MJ and a price of cell area of 0.23 €/cm^2.

The main cost drivers were identified as the capital costs of the SOEC and air capture systems and the heat exchanger network. For operating costs, the electricity price had a significant impact, whereas the dependency of the SNG price on the heat price was minor.

The technical issues where discussed in separate chapters interspersed by chapters documenting the modelling and design process. Finally, a comprehensive discussion at the end treats the technical issues of the plant in the light of the economic analysis.

Resume (popular Danish abstract)

Frem mod 2035 udfaser Danmark gradvist fossile brændsler. Udfasningen omfatter alle dele af energisystemet med undtagelse af transportsektoren, der dog på længere sigt også skal omstilles.

I sådan en massiv omstilling, er der brug for biogas og syntetisk naturgas til at dække el-produktion i timer med svag vind og højt forbrug, samt procesvarme til industrien. På længere sigt bliver der også brug for biobaserede eller syntetiske brændstoffer til flytransport og andre energitunge dele af transportsektoren.

Projektet bag denne afhandling udviklede og studerede produktion af syntetisk naturgas fra kuldioxid, CO_2, opsamlet fra atmosfæren. CO_2'en omdannedes sammen med vand til syntesegas – en blanding af brint og kulmonooxid. Denne omdannelse skete i keramiske elektrolyseceller ved højt tryk. Afslutningsvis omdannedes den producerede syntesegas til syntetisk naturgas gennem katalytisk metanering.

Målet var, at designe anlægget og sideløbende udvikle en computermodel til at simulere produktionen ved varierende tryk, temperatur, omsætningsgrad og resulterende gassammensætning, samt til brug for optimering af designet. Derudover var det at regne på økonomien i anlæggets drift og identificere indsatsområder for videre forskning og udvikling.

Det simulerede anlæg er i stand til at producere 575.000 kubikmeter syntetisk naturgas om året, med indhold af metan på over 98,5 % og et energiindhold, så højt at gassen kan indføres direkte i naturgasnettet. Energieffektiviteten af anlægget var mindst 58 % baseret på den nedre brændværdi af gassen.

En simpel livscyklusanalyse viste, at den syntetiske naturgas er tæt på at være CO_2-neutral, forudsat, den produceres ud fra strøm, der også er CO_2 neutralt. Dette burde være tilfældet fra år 2035. En grundig økonomisk analyse af opbygning og drift af anlægget viste derudover, at produktionsprisen for den syntetiske naturgas bliver omkring 14 kr. per kubikmeter med energipriser (el og varme), der er forudsagt for år 2035 af Energinet.dk. Til sammenligning er prisen for opgraderet biogas ca. 6 kr. per kubikmeter. Analysen viste også at med overskuelige forbedringer af de involverede teknologier, kan produktionsprisen nedsættes til omkring 9 kr. per kubikmeter

Resultaterne af den tekniske modellering af anlægget blev afslutningsvist brugt til at identificere de overordnede omkostningsfaktorer. De vigtigste var kapitalinvesteringerne i anlægget til CO_2-opsamling, elektrolyseanlægget og elprisen.

Afhandlingen viser, at anlægget er teknisk gennemførligt med eksisterende teknologi, men at det er relevant at arbejde med forskning og udvikling i de centrale teknologier for at nedbringe produktionsomkostningerne til eller under niveauet for opgraderet biogas.

Foreword

At the dawn of the 21st century, the threat of the largest, and potentially most devastating ecological disaster yet to face mankind seemed to finally materialize on the horizon of the minds of the leaders and populations of the world.

Slowly but steadily, vast resources are directed at all parts of the multi-dimensional environment, climate science, sustainable energy and resource management field, an effort which takes place in all sectors: From scientific research, engineering over social sciences and the arts to public management. On all levels from local communities over cities to large scale international organizations, not only in the environmental protection agencies and NGOs, but also in political and economic fora. Also the corporate world is turning its attention towards sustainability and alternative energy guided by the ensnaring prospects of green growth and public demand for corporate social and environmental responsibility.

This vast effort, especially in the fields of climate sciences and renewable energy engineering, produces new insight in the current state of the challenges facing local and international societies at a breathtaking rate. Each week see the publication and media reporting of new disheartening reports on the state of the global climate system and the painfully slow pace at which progress is made on the political scene. Here politicians are more concerned with the short-term trouble shooting of the consequences of the financial crisis than the long-term solutions needed to solve the much more ominous threats of the ecological, political, strategic and ultimately economic disastrous consequences of a significantly warmer world at the end of this century.

But amidst all the gloom and despair, we are making immense technological and regulatory progress as more and more companies, universities and research institutions join the dash towards developing the technologies and frameworks of the future energy systems.

To be an engineer in such times, is to be one amongst untold thousandths in the public and private sectors working together to solve some of the largest problems ever to face mankind. It is an emotional exercise of balance: On the one hand, the utter disillusion with the disappointing inability of our political systems to handle grave problems responsibly and in time. On the other, an experience of great excitement and optimism at the vast attention and resources directed at the cause, in addition to the great technological advances seen these years and promised for the immediate future.

Ultimately, the engineering profession is one of great responsibility and great reward. No matter which way we choose to proceed, advanced engineering applications must be at the very core of the solution to the problems. This is an effort and responsibility, of which I am proud and excited to be a minuscule part, and one to which I hope, in all humility, that this work may contribute.

Acknowledgements

Completing a work like this one is impossible without the help, support and engagement from a great number of people. Only my name is printed on the cover, but I wish to use this space to mention theirs. This project would never have happened without every single one of them.

I wish to thank my supervisors for their untiring engagement in the project: Mogens Bjerg Mogensen for being my main collaborator, for his immense knowledge in these fields and others and his willingness to teach. Also his undying patience in times of trouble is gratefully appreciated. Søren Højgaard Jensen is thanked for his immense expertise in the field of solid oxide cells and his cheerful attitude towards this project. I thank Anders Riisager for the support and interest in the project even though it moved I directions far from his field.

This financing by the EUROSTARS E! 6691 – CAPFUEL project via the Danish Agency for Science, Technology and Innovation, contract no. 0604-00577B – EUROS (11-108005) is gratefully acknowledged.

Amongst my colleagues at the Department for Energy Conversion and Storage, especially Sune Dalgaard Ebbesen has my warmest thanks for his endless patience and readiness to help out on details and basic concepts of solid oxide electrolyzers. I would also like to thank the following: Karin Vels Hansen for her help on impurities, and solid state characterization; Peter Holtappels for his faith in the project and support in times of crisis; Anders Petersen for excellent work on the impurity collection setup and for punctual work meeting unreasonably tight deadlines; Anne Hauch for always having time for a question; Carsten Brorson Prag for interesting discussions, and proofreading; Christopher Graves for his help on modelling; Jón Steinar Garðarsson Mýrdal for help with proof-reading; Rasmus Rode Mosbæk, Jean-Claude Njodzefon, Federica Vico and Kristian Bastholm Knudsen for being cheerful and valued colleagues. Pernille Hedemark, Lene Thorsted, Lene Danielsen, Annette Bruckloher, Lene Christensen, Anita Voss, Heidi Adler Berggren, Niels Michael Petersen and John Agertoft for their support and positivism. Also, I thank Tânia Ramos, my former MSc supervisor and now great colleague and friend.

I extend a special thanks to Rafiqul Gani from the Department of Chemical Engineering for teaching me the basics of process design and for helping out with the software. I also thank Ralph Cos from Simsci Invensys for his untiring software related trouble shooting.

At Climeworks, my special thanks go to Jan Wurzbacher for his interest and collaboration, and to Nic Piatkowski and Anca Timofte for inviting me into their labs and for the help.

At the Lenfest Centre for Sustainable Energy, my warmest and most heartfelt thanks goes to Klaus Lackner for his deep insight and for great discussions, scientific and otherwise, and to Allen Wright for the support and invaluable help in the lab. Also I thank Peggy Lackner for opening her home for me during my visit in New York.

Finally, I would like to thank my friends for understanding, patience with my endless ramblings and for helping out wherever they could. I thank my family, Niels Ebbehøj and Karen Lyng for their unquestioning belief in me and for helping with practicalities and proofreading. Especially, I would like to thank my brother Anders Lyng Ebbehøj for being the amazing friend and support that he is.

To each and every single one of you, and everyone else, not mentioned:

Thank you.

Table of contents

Abbreviations

AC	Air capture	OPEX	Operating expenditure
AC1	Air capture heating duty (100 °C)	PFD	Process flow diagram
AC2	Air capture cooling duty (20 °C)	pp	Percentage points
AC3	Air capture cooling duty (40 °C)	ppb	Parts per billion
ASR	Area specific resistanse	ppm	Parts per million
BC	Base case	ReSOC	Reversible solid oxide cell
BET	Brunnauer emmet teller	ROI	Return on investment
BioNG	Bio natural gas	RU	Reactant utilization
CAPEX	Capital expenditure	Rx	Reactor
CEPCI	Chemical engineering plant cost index	SEM	Scanning electron microscopy
CF	Conversion factor	SHIFT	Water gas shift and methanation reactions
CGO	Gadolinium doped cerium oxide	SMSA	Specific metallic surface area
DAT	Dual approach temperature	SNG	Substitute natural gas
DCFROI	Discounted cash flow return on investment	SOC	Solid oxide cell
DME	Dimethyl ether	SOEC	Solid oxide electrolyzer cell
DTU	Technical University of Denmark	SOFC	Solid oxide fuel cell
ECHEM	Electrochemical reactions	SSA	Specific surface area
EMAT	Exchanger minimum approach temperature	Syngas	Synthesis
FM	Feed module	TPB	Tripple phase boundary
GDMS	Glow discharge mass spectrometry	TREMP	Topsøe recycle energy-efficient methanation process
GHSV	Gas hourly space velocity	TVS	Temperature Vacuum Swing
HEN	Heat exchanger network	U1	Hot utility stream (120 °C)
HENS	Heat exchanger network synthesis	U2	Hot utility stream (300 °C)
HHV	Higher heating value	U3	Cold utility stream (10 °C)
HRAT	Heat recovery approach temperature	V	Vapor phase
HS	Humidity swing	WGS	Water gas shift
Hx	Heat exchanger	YSZ	Yttria-stabilized zirconia
IRGA	Infra red gas analyser		
L	Liquid phase		
LCIA	Life cycle impact assesment		
LHV	Lower heating value		
LSM	Lanthanum strontium manganite		
MARR	Minimum acceptable rate of return		
MCR	Haldor Topsøe A/S methanation catalyst		
MFC	Mass flow controller		
MNU	Minimum number of units		
NG	Natural gas		
Ni/YSZ	Nickel/yttria stabilized zirconia		
OCV	Opoen circuit voltage		

Symbols

E^{tn}	Thermoneutral potential
I	Total current
I_A	Current density
P	Total pressure
$p(CO_2)_1$	Partial pressure of CO_2 at air capture inlet
$p(CO_2)_2$	Partial pressure of CO_2 at air capture outlet
P_{cell}	Cell power
P_{stack}	Stack power
R_I	Resistance of ionic conduction in electrodes
R_{II}	electrochemical resistance of fuel electrode
R_{III}	Electrochemical resistance of oxygen electrode
R_{IV}	Gas diffusion resistance
R_S	Series resistance
R_V	Gas conversion resistance
T	Temperature
T_{filter}	Filter operating temperature
T_{stack}	SOEC stack temperature
$T\Delta S$	Absolute temperature times entropy
U_{cell}	Cell voltage
$x(i)$	Mole fraction of component *i*
ΔG	Gibbs free energy difference
ΔG_{mixing}	Free energy of mixing of ideal gasses
ΔH	Enthalpy difference
$\Delta H_{ELECTROCHEM}$	Enthalpy change of ELECTROCHEM unit operation
ΔH_{OHMIC_HEAT}	Enthalpy change of OHMIC_HEAT unit operation
ΔH_{SHIFT1}	Enthalpy change of SHIFT1 unit operation
$\Delta_{HSHIFT2}$	Enthalpy change of SHIFT2 unit operation
ΔS	Entropy difference
ΔT	Approach temperature
$\Delta T_{logmean}$	Logarithmic mean temperature difference
Θ_{max}	Saturation of air capture sorbant

Part I - Introduction

Chapter 1 Introduction

The Danish society in on the track to one of its largest transitions since the industrial revolution. A track on which we are among the world leaders and one which will take us through a transition from a fossil fuel based economy towards a society built on sustainable energy and resource management. In a small step on that track Energinet.dk recently published an analysis of the long term initiatives which must be taken in order to reach the targets set forth by the Danish Energy Agency and the Danish Parliament [1]. The analyses have the form of a scenario based on several earlier scenarios published by Energinet.dk [3, 4] and the Danish Energy Agency [5].

In the given scenario for the energy system in 2035, large parts of the energy system will be electrified, based on 72 % wind power and 21 % biomass and waste incineration in the electric grid. The target is to displace all fossil fuels from all sectors in the energy system, except for transportation before 2035, and to gradually transition the transport sector toward 2050. Also large parts of the heating services needed will be provided by electricity, and the district heating grids are expected to play a central role in short term energy storage and integration. Assuming biomass cannot be imported in this scenario, Energinet.dk expects biogas and electrolysis derived gasses to play key roles in peak-load electricity production, generation of industrial process heat and approaching 2050, to replace fossil fuels in the most energy intensive parts of the transportation sector. The natural gas grid is expected to play a key role, akin to the district heating grid for heating services. Therefore, the study and development of technologies capable of displacing fossil fuels such as natural gas, preferably in the existing infrastructure is relevant with 20 year to reach a sustainable CO_2 free energy system.

1.1 Synthetic fuels via electrolysis

Solid oxide electrolyzer cells (SOEC) are versatile electrochemical energy conversion devices operating at high temperatures (600 °C – 1000 °C) and converts oxidized species such as H_2O and CO_2 to H_2 and CO, under consumption of electrical and thermal energy. Operating on a mixture of H_2O and CO_2, the process is called co-electrolysis and the product is synthesis gas (syngas) which is a precursor for a wide range of processes in the petrochemical industry, also processes for production of synthetic fuels (synfuels).

Over the past decade, the addition of technology for collecting CO_2 directly from the atmosphere has been found to be viable, and the synergies between direc air capture of CO_2 (air capture) and synfuel production via electrolysis has attracted more attention. The main advantages of using CO_2 air capture is, that it provides a carbon source, not dependent on biomass resources, and that the energy content of produced synthetic fuel is many times higher than for hydrogen. once an electrolyzer cell has been installed, it is beneficial to spend as much energy as possible on as few gas molecules as possible, as this increases the amount of energy which can be stored per storage volume and, possibly, per gas conditioning unit. Thus, electrolyzing CO_2 rather than, say, CO should be preferred and reducing it all the way to hydrocarbons is imagined to be beneficial. Finally, collecting CO_2 from the atmosphere, assuming 100 % conversion to fuel, allows for the production of carbon neutral hydrocarbon fuels, not relying on biomass. The general concept of such a plant is shown in Figure 1-1.

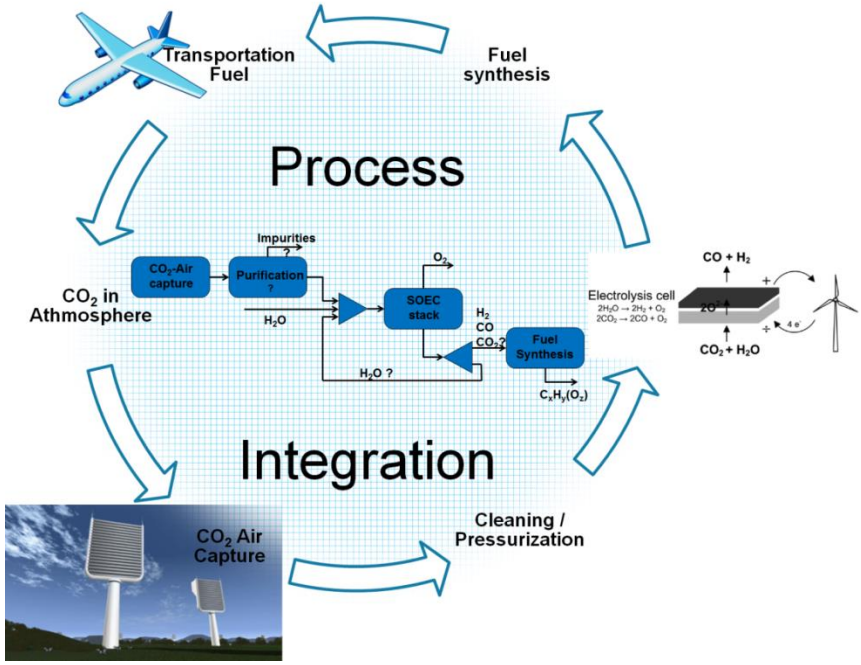

Figure 1-1. General concept of the technology developed in the project. CO_2 is captured from the atmosphere after which it is cleaned of impurities and pressurized along with steam. It is then converted to syngas in solid oxide electrolyzer cells. Downstream, the syngas is converted in a catalytic process into some hydrocarbon fuel, here exemplified with jet fuel, which is subsequently combusted by an end user. During combustion, the same amount of CO_2 is emitted as was collected in the first place, and with the atmosphere as a reservoir, the cycle is closed.

In this work, catalytic methanation was chosen for the synfuel production, due to the simplicity and the synergy with pressurized co-electrolysis. The end product is thus substitute natural gas, rather than jet fuel as depicted in the figure, but the general principles remain the same.

The project had as the main goal to develop and model a plant integrating these three overall steps, and use the model for analyzing modes of operation, operating parameters, sustainability and economy of operation, etc. This is described in detail in the following section.

1.2 Aim and structure of the work

This thesis treats the design, modelling and analysis of a plant producing substitute natural gas from CO_2 captured from the atmosphere via solid oxide co-electrolysis followed by catalytic methanation. The thesis has the form of a monograph and includes a chapter which has been submitted for publication in the *Journal of Power Sources* (Chapter 3 on analysis of impurities in CO_2 streams).

The thesis follows the design and modelling process and is divided into five parts:

Part I contains the introduction stating the scope and relevance of the work.

Part II contains a series of basic theoretical concepts important for the remaining text.

Part III contains experimental work and discussions on two different systems for capture of CO_2 from the atmosphere and the performed experimental study on the risks of poisoning of solid oxide electrolyzer cells associated with impurities in CO_2 gas streams.

Part IV contains the main body of the work on plant design, integration of the three main sub-systems (air capture, electrolysis and methanation), and the development of the thermodynamic model of the full plant. This part is made up by design and modelling chapters interspersed by chapters on results and preliminary discussions. The design and modelling chapters contain a series of minor studies, aiding the design choices along the way.

Part V contains the economic assumptions, prerequisites and analysis, in addition to the overall discussions on the plant. Finally, the conclusions and outlook are presented.

1.3 Outline

Part II – Theoretical concepts

Chapter 2 present theoretical concepts for the main parts of the plant: The capture of CO_2 from the atmosphere is discussed regarding the main challenges for commercialization; solid oxide electrolysis is treated with special focus on the thermodynamics of co-electrolysis; and methanation technology is treated focusing on the technological implementation. Finally, the basic concepts of heat integration studies are presented for readers unfamiliar with the topic.

Part III – CO_2 air capture and impurities

Chapter 3 contains a few experiments on one of the CO_2 capture technologies studied. After this, the input data of the chosen air capture system are presented, and the modelling strategy for the air capture plant is presented.

Chapter 4 contains the experimental work on impurities in CO_2 streams in relation to solid oxide electrolysis. A method for detecting sub-ppb concentrations of impurities in CO_2 streams was developed and the studies of a series of air capture systems are presented and discussed. This chapter has been submitted as a full paper for *Journal of Power Sources.*

Part IV – System design and modelling

Chapter 5 presents the employed modelling strategy and contains a description of the development of the syngas plant model. This includes the air capture system in addition to the developed SOEC model. The strategy for energy balances is presented, and alternative strategies for compression of CO_2 are studied, and a heat integration analysis is performed.

Chapter 6 includes results from thermodynamic parameter studies using the syngas plant model developed in Chapter 5. The results are discussed in relation to the integration with methanation technology.

Chapter 7 present the design choices related to the methanation sub-plant and the integration with the syngas plant. The design choices are documented by calculations and modelling, and the chapter concludes with defining two design cases of the full plant model to be analyzed in the remainder of the work.

Chapter 8 contains the heat integration study of the full plant in both design cases, followed by the synthesis of the heat exchanger network allowing for internal recovery of process heat.

Chapter 9 is the final process integration chapter. The heat exchanger network is implemented, and pressure drops and equipment for re-pressurization is added to the model. Finally, sizing and costing calculations for all equipment in the plant are presented.

Chapter 10 contains the results of operating the full plant model for both design cases. The results are treated in the framework of mass balance, heat balance and overall energy balance.

Part V – Analysis

Chapter 11 contains the information needed for the economic analysis of the plant. The chapter is split into economic prerequisites, price assumptions for products, heat and electricity, and finally the methodology of the economic analysis is presented.

Chapter 12 presents the economic analysis of the plant by calculating the production costs of the substitute natural gas product for a given profitability measure. The main cost drivers are identified and the sensitivity to a series of technological assumptions is analyzed.

Chapter 13 holds the overall discussion on the work with a special focus on the techno economic aspects of the integration and operation of the modelled plant.

Chapter 14 contains a short summary of the main findings and questions, states the overall conclusions and thought on the outlook and future work for the process is presented.

Appendices

The appendices contain input for PRO/II and HEXTRAN simulations, in addition to removable reference sheets including product flow diagrams and lists of unit operations of the plant. The reader is encouraged to cut out the reference sheets for easy access while reading.

Part II – Theoretical concepts

Chapter 2 Theory and basic concepts

In this chapter, the background theory and basic concepts of the three main technological steps in the designed plant are presented. These include capture of CO_2 from the atmosphere (section 2.1), solid oxide electrolyzer cells (SOEC), reactions and thermodynamics (section 2.2) and methanation reactions and technology (section 2.3). Finally the basic concepts of heat integration studies, composite curves and heat exchanger networks are presented (section 2.4).

The texts are meant to give the reader a basic understanding of the key concepts, required for the considerations and discussions in the remainder of this thesis, and thus, the sections vary in style and scope.

2.1 Capture of CO_2 from the atmosphere

Direct capture of CO_2 from the atmosphere (*CO_2 air capture* or simply *air capture*) has been discussed extensively over the last 15 years. Originally, the concept of removing CO_2 from gasses by absorption was developed for production of CO_2 [6], and since for scrubbing the atmospheres of space craft and submarines [7]. Since then, the field has developed into scrubbing flue gasses from power plants and CO_2 intensive industries. Such technologies have been thoroughly reviewed elsewhere [8, 9]. The newest branch is direct air capture, introduced by Lackner et al. in 1999 [10].

A common trait for these technologies is that they rely on absorption of the CO_2 on some form of solid sorbent or liquid, after which an amount of energy is supplied and the sorption equilibrium shifts to a higher equilibrium partial pressure of CO_2 and the CO_2 is released [10]. The CO_2 may then be sequestered underground or otherwise[11]. Alternatively the CO_2 may be recycled and utilized for production of fuels or chemicals which is the case in the present work.

2.1.1 Thermodynamics of air capture

CO_2 removal from flue gasses has mixed reputations due to the large amounts of energy needed for regeneration of the sorbents in each cycle. This, in part, is caused by the requirement to drive the partial pressure of CO_2 ($p(CO_2)$) to very low concentrations, as is described below. The range of partial pressures of flue gas purification is typically round 5-15 % for inlet and 0.1 – 1 % outlet partial pressures [11].

In the case of air capture applications, the inlet $p(CO_2)$ is often lower by a factor of 100 compared to that of flue gas cleaning, which has caused some to doubt the thermodynamic and especially the economic viability of the concept [12]. The thermodynamic efficiency of such systems depends strongly on the relative difference between inlet and output partial pressures. While this has to be large in flue gas capture, direct air capture can work with very small differences, approaching the reversible limit. Even so, direct air capture still needs more energy than for flue gas capture, since the theoretical free energy of mixing depends on the absolute partial pressure at the outlet (see below). The outlet concentrations of air capture devices will always be lower than that of flue-gas cleaning systems, as even the inlet concentration (typically ~400 ppm) is lower than the outlet concentration of flue gas systems. The increase in energy is only a few times higher, however, as the thermodynamic efficiency is higher, and because the required energy increases logarithmically [9]. Depending on the conditions, this results in theoretical free energy consumptions of air capture larger by a factor of app. 1.5 -2.5 compared to flue gas purification [9, 13].

Such operation requires that the partial pressure is only lowered by a small fraction, which is possible as the goal is to produce CO_2, not to scrub the atmosphere. Thus, the air is only skimmed for the top few percent of the available CO_2. Adopting such a strategy however, limits the options on pre-treatment of the gas such as cooling, as exceedingly large quantities of air would have to be treated. This favors passive absorption devices, and requires operation of the absorption part of the cycle at ambient conditions.

Mixing of gasses is a spontaneous process, so ΔG_{mixing} is negative. Thus the theoretical free energy needed for separating CO_2 from an atmosphere of absolute temperature T, pressure P and CO_2 partial pressure $p(CO_2)_1$, in the reversible limit is given by the free energy of mixing.

$$\Delta G_{unmixing} = -\Delta G_{mixing} = -RTln\left(\frac{p(CO_2)_2}{P}\right) \qquad \text{Equation 2-1}$$

Here, R is the gas constant and $p(CO_2)_2$ is the resulting partial pressure of CO_2 after the separation process. In the reversible limit $p(CO_2)_2 = p(CO_2)_1$. Such operation represents an extreme case of skimming where the operation does not lower the partial pressure of CO_2 in the passing gas stream, but can still load the sorbent. Equation 2-1 then serves as the minimum theoretical free energy required for separation. Calculating ΔG_{mixing} from Equation 2-1 for ambient conditions where $p(CO_2)_1 = p(CO_2)_2$ = 400 ppm, yields ΔG_{mixing} = 19 kJ/mol. In real applications, the outlet pressure will be lower than the inlet partial pressure, and a significantly more complicated expression replaces Equation 2-1. Lackner [14] concluded that for complete removal of the CO_2, the accompanying increase ΔG_{mixing} is approximately $R{\cdot}T$. Then $\Delta G_{mixing} \approx$ 21.5 kJ/mol. This is the equivalent of 0.49 GJ/ton. If the CO_2 is to be used for fuel production, the energy content of the fuel can be used as a comparison. The free energy of mixing is equal to around 2.5 % of the standard enthalpy of combustion for methane for example (~891 kJ/mol).

With the above numbers settled, the goal of developing viable air capture technologies is in essence a question of finding the right sorbent and the right strategy for releasing the CO_2 from that sorbent. A wide range of technologies has been investigated, which have been reviewed by others [9, 15, 16].

Physisorption on solid sorbents such as activated carbon or zeolites is not sufficiently selective for CO_2 at ambient conditions [9], and is generally not binding the CO_2 tightly enough at atmospheric partial pressures. This means that chemisorption strategies are needed, with a relatively strong selective binding of CO_2. Moving to tighter binding of CO_2 increases the needed energy input for reclaiming the CO_2. Using the well-known example of sodium hydroxide solutions, an order of magnitude for the energy input can be calculated:

Solutions of NaOH take up CO_2 rapidly even at atmospheric partial pressure, through formation of sodium carbonate:

$$2NaOH_{(aq)} + CO_{2(g)} \rightarrow Na_2CO_{3(aq)} + H_2O_{(l)} \qquad \textbf{Reaction 2-1}$$

ΔH = -109.4 kJ/mol

In order to reclaim the CO_2 so-called “causticization” is used, applying calcium hydroxide and regenerating the sodium hydroxide:

$$Na_2CO_{3(aq)} + Ca(OH)_{2(aq)} \rightarrow 2NaOH_{(aq)} + CaCO_{3(s)}$$ **Reaction 2-2**

ΔH = -5.3 kJ/mol

The calcium carbonate is then separated from the solution, and the filter cake is calcined, releasing the CO_2:

$$CaCO_{3(s)} \rightarrow CaO_{(s)} + CO_{2(g)}$$ **Reaction 2-3**

ΔH = 179.2 kJ/mol

Finally, the calcium oxide may be regenerated to calcium hydroxide by hydration:

$$CaO_{(s)} + H_2O_{(l)} \rightarrow Ca(OH)_{2(aq)}$$ **Reaction 2-4**

ΔH = - 64.5 kJ/mol

Of the above reactions, only Reaction 2-3 is endothermic. The heat developed by the other reactions is not easily recovered, as they take place at low temperatures however. Comparing ΔH of the calcination step (ΔH = 179.2 kJ/mol) to the free energy of mixing (ΔG_{mixing} ≈ 21.5 kJ/mol) and the heat of combustion of methane (ΔH ≈ 891 kJ/mol) shows how the heat of desorption shows that the calcination enthalpy takes up 20 % of the enthalpy of combustion. This example shows how the energy required for desorption may entirely change the picture of what was laid out by the basic thermodynamic considerations shown above.

Some authors report that drying the $CaCO_3$ filter cake uses an amount of energy comparable to ΔH of the calcination reaction, adding further to the energy consumption [17, 18]. Zeman showed that this amount can be lowered significantly by different calcination technologies [19]. Even so, he ended up at a total energy consumption of a plant based on this technology of 328 kJ/mol due to other losses.

The above example serves to illustrate two issues inherent to air capture technologies based on thermal cycles: The need for chemical bonding of CO_2 to the sorbent greatly increases the theoretical amount of energy needed to reclaim the absorbed CO_2 from the sorbent. This illustrates the importance of carefully selecting and fine-tuning the sorbent chemistry to balance the heat of absorption against the need for selective CO_2 absorption at low partial pressures. Secondly, the chosen chemistry should include few steps, and preferably not include phase separations or intermediate steps. The reason is that extra unit operations will introduce energetic or even mass losses and add to the complexity of the air capture system in terms of operation and capital investment.

A further complication of air capture technologies is that most systems are not able to produce pure CO_2 streams at ambient conditions. Zeman tested calcination by burning natural gas in oxygen in order to produce a pure CO_2 stream combining the CO_2 produced by burning and the CO_2 from the calcination itself [19]. Such strategies need to be employed in order to avoid secondary separation steps, which my impose prohibitively large costs [17, 18].

In this work, two air capture strategies were treated, which showcase some of the above points.

2.1.2 Temperature vacuum swing

The first strategy is based on amine functionalized solid sorbents [20, 21], binding CO_2 through the formation of bicarbonates at humid, ambient conditions [20, 22]. The process, which is under development by Climeworks Ltd. employs a so-called temperature vacuum swing (TVS) for the desorption of CO_2. This means that prior to the desorption phase, the pressure in the sorbent container is lowered to 25 – 250 mbar, and heating of the sorbent provides the heat of desorption. The advantage of combining temperature and vacuum swings is that the lowered pressure allows for desorption temperatures below 100 °C, reducing the degradation of amines at higher temperatures [23]. With this system, thermal energy demands between 272 kJ/mol and 687 kJ/mol was reported [22]. The reason for the large spread is that depending on the relative humidity during absorption, H_2O is co-absorbed in different H_2O:CO_2 ratios [22]. The H_2O desorbs along with the CO_2, adding to the heat of desorption.

The Climeworks system have a series of advantages even though the thermal energy need is larger than that of the NaOH based system discussed above. First of all the system is quite simple, requiring only a vacuum chamber, a means of supplying the heat and a vacuum pump. No phase separations from liquids or liquid or solid handling are required. Furthermore, the needed energy may be supplied as low grade heat, which is cheap compared to high temperature calcination for example. Further the sorbent is kept immobile in the vacuum chamber during the entire process, and needs no transport processes. Even though an amount of energy is paid for the co-adsorbed H_2O, it turns out, the H_2O fraction desorbs from the sorbent at lower temperatures compared to the CO_2 fraction [24]. This means that no further phase separation steps are needed, and CO_2 streams of ~98 % have been reported by this fairly simple system [20].

2.1.3 Humidity swing

The second system is significantly different from the TVS system discussed above.

The humidity swing (HS) relies on anion exchange resins incorporating functionalized quaternary ammonium ions with hydroxide counter-ions [25]. Upon exposure to CO_2 at dry ambient conditions, the hydroxide ions are exchanged for bicarbonate ions, taking up above 99 % of the ammonium sites. Increasing the relative humidity of the gas phase over the resin, is thought to change the hydration of the ammonium ions, causing half of the bicarbonate ions to desorb as CO_2 leaving the carbonate form [25, 26]. Thus, the practical capacity of the sorbent is half the amount of ammonium ions as the carbonates are not accessible by the humidity swing. The desorption process takes place at ambient conditions. Regenerating the resin is done in a second step by drying it, which will cause CO_2 to adsorb and form bicarbonate. The energetics of the process have been discussed, but it turns out the energy needed for regeneration is strictly provided by the air during the evaporation of H_2O [26].

Thus, unlike the two systems described above (TVS and the NaOH system), the sorbent in the HS system is regenerated in the absorption part of the cycle rather than the desorption step.

This system has not been as extensively studied in the published literature, and thus, a few questions remain to be dealt with in order to create a technical implementation. The main questions all relate to management of water, as this is a key feature of the system.

The first question relates to the supply of water to the resin. The theoretical amount of water taken up by the dry resin was calculated from CO_2 uptake data to around 5 moles per mole of CO_2 [26]. The authors mention that in real systems, the water uptake would be larger, and preliminary results have shown H_2O:CO_2 ratios as high as 25 [27]. This means that supplying water in the form of steam probably becomes prohibitively energy intensive. Instead, liquid water might be used, which could slightly reduce the amount of CO_2 to be reclaimed, because of dissolution.

The second question relates to the loss of water in the drying phase. Assuming no liquid water is present in the sorbent material, 25 moles of water are lost for each mole of CO_2 produced. This requires ready access to a cheap, clean water supply. With access to water under a desert or at the sea, desalination at less than 10 kJ/mol is expected to introduce only minor extra costs [26]. Comparing this to the desorption energy needed in the thermal swings described above this might not be a show-stopper for the technology.

The last main question related to separation of the CO_2. The equilibrium partial pressure of CO_2 over the humid resin is on the order of 5 % - 8 % depending on the saturation of the resin. This might be increased by pumping as in the TVS system, but this would cause desorption of parts of the co-absorbed H_2O as well which is not preferable for many applications. The alternative is to let the CO_2 desorb into a carrier gas, which would then require further separation steps [28].

In the next chapter, one of these questions is gaged superficially.

2.2 Solid oxide electrolyzer cells: reactions and thermodynamics

Solid Oxide Electrolyzer Cells (SOEC) are electrochemical devices used for reduction H_2O and CO_2 to H_2 and CO. Several types of electrolyzer cells exist with various active materials, chemistries and consequently different operating parameters. This work focuses exclusively on solid oxide electrolyzers. As the name indicates, the cells are constructed from ceramic materials, which make them well suited for operation at elevated temperatures.

Being electrochemical devices, each cell consists of two electrodes, one for oxidation and one for reduction. These are separated by an electrolyte. In the case of solid oxide cells, the electrolyte consists of a ceramic material, and the electrolodes are entirely ceramic or have ceramic components. The cells treated in this work are based on a zirconium oxide electrolyte stabilized with 8 mole % yttrium oxide (yttria stabilized zirconia, YSZ). The inclusion of yttrium oxide stabilizes the cubic crystal structure of the ceramic and induces an oxygen deficiency in the lattice. This allows the material to conduct oxygen ions (O^{2-}) at elevated temperatures, such as 600 °C - 1000°C. The electrolyte is gas-tight and electronically insulating in order to seal off the two half-cells.

The electrodes of the cells in this work consist of porous composite materials allowing the access of gasses to reactive sites close to the electrolyte surface. Figure 2-1 shows a schematic representation of part of a cross-section of an SOEC. The layer thicknesses are not to scale.

The cathode, in this work referred to as the fuel electrode is responsible for the reduction of H_2O and CO_2. It consists of a ceramic-metallic (cermet) composite of YSZ, providing ionic conduction and mechanic support, and a nickel phase providing electronic conductivity and acting as a catalyst. The composite electrode material is called Ni/YSZ. The active sites for the reduction of H_2O and CO_2 are the tripple phase boundary lines (TPB) between the gas (porous) phase, the ionic conductor (YSZ) and the electric conductor (Ni). A fine distribution of the particles of the two solid phases is preferred in order to produce long TPB lines to enhance the activity of the electrode.

The anode, in this work referred to as the oxygen electrode, is responsible for the formation of O_2 from the O^{2-}ions arriving across the electrolyte. The electrode structure consists of a purely ceramic composite of YSZ for ionic conductivity and lanthanum doped strontium manganite (LSM) which is a ceramic electronic conductor. Here too, the active sites are the TPBs between the two solid materials and the gas-phase.

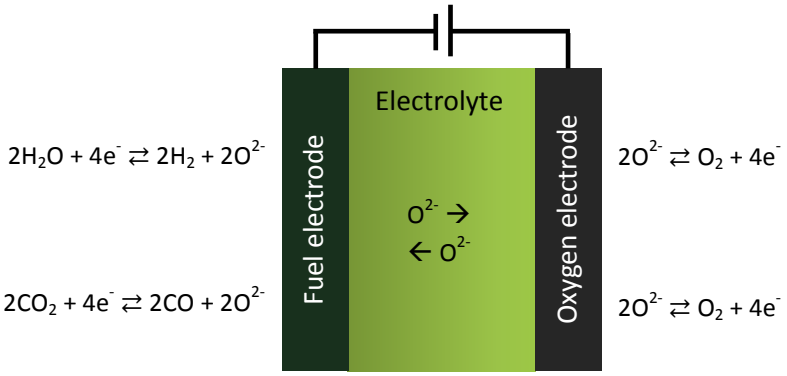

Figure 2-1. Working principle of a Solid Oxide Electrolyzer Cell (SOEC).

Each part of the cell (fuel electrode, electrolyte and oxygen electrode) consists of very thin layers in a laminated structure. While ionic conduction is only needed close to the electrolyte, an electronically conducting path needs to be open from the active sites close to the electrolyte and to the cell surfaces for contacting purposes. In order to keep the electronic and ionic resistances across the cell as low as possible, the layers are kept thin, i.e. on the order of 10 µm. As ceramic materials are brittle, the thin cells need mechanical support. This comes in the form of an approximately 300 µm thick Ni/YSZ support structure on the fuel electrode side. As long as the individual Ni-particles are in contact, the electronic conductivity of the Ni-phase is high so that thick layers do not increase the resistance. The support layer consist of YSZ like the active electrode layer, but has larger particle sizes and a more open structure to allow for unhindered gas transport.

2.2.1 Reactions in solid oxide fuel cells

As mentioned above, an SOEC is an electrochemical device. When a flow of reactant gasses is supplied to the fuel electrode and a potential is applied across the cell, a current will result from transport of oxygen ions created in the fuel electrode reaction with electrons supplied by an external circuit. Here exemplified for H_2O:

$$2H_2O + 4e^- \rightleftarrows H_2 + 2O^{2-}$$ **Reaction 2-5**

The oxygen ions are transported across the electrolyte and combine at the active sites of the oxygen electrode:

$$2O^{2-} \rightleftarrows O_2 + 4e^-$$ **Reaction 2-6**

Here the created electrons are collected by the contacts and travels through the external circuit.

Similar reactions take place for CO_2 as shown in Figure 2-1, and the resulting electrolysis reactions are:

$$2H_2O \rightleftarrows 2H_2 + O_2 \quad \text{Reaction 2-7}$$

$$2CO_2 \rightleftarrows 2CO + O_2 \quad \text{Reaction 2-8}$$

In addition to the electrolysis reactions, the large amount of Ni present in the fuel electrode and support layer is an excellent catalyst for a range of other reactions at the elevated operating temperatures of the SOEC. Of these, the water gas shift (WGS) reaction (Reaction 2-9), the methanation (Reaction 2-10) reaction and various solid carbon forming reactions such as the Boudouard reaction (Reaction 2-11) contribute significantly to the composition of the effluent gas stream from the SOEC [29-32].

$$CO_2 + H_2 \rightleftarrows CO + H_2O \quad \text{Reaction 2-9}$$

$$CO + 3H_2O \rightleftarrows CH_4 + H_2 \quad \text{Reaction 2-10}$$

$$2CO(g) \rightarrow CO_2(g) + C(s) \quad \text{Reaction 2-11}$$

2.2.2 Thermodynamics of SOEC operation

In electrolyzer cells the electrolysis reactions assumes a special position, in that they are driven by the externally controlled electrical signal. The methanation, WGS and Boudouard reactions are equilibrium reactions, which change only as a function of the operating conditions and gas composition. Ideally, the amount of energy needed for the electrolysis reactions to take place is defined by the Gibbs free energy change, and the needed voltage is the reversible voltage:

$$E_{rev} = \frac{-\Delta G}{zF} \quad \text{Equation 2-2}$$

Here, ΔG is the Gibbs free energy of reaction, z is the amount of electrons in the reaction equation and F is Faradays constant. However, all systems have losses, here expressed as overpotentials. In general terms the overpotential (η_{cell}) of the cell may be written as the contributions from the processes in the different parts of the cell:

$$\eta_{cell} = \eta_{anode} + \eta_{electrolyte} + \eta_{cathode}$$ Equation 2-3

Here, η_{anode} related to the electrochemical processes in the anode, $\eta_{electrolyte}$ relates to the ionic conduction in the electrolyte, and $\eta_{cathode}$ related to the electrochemical processes in the cathode. The over voltages can be explained as the voltages providing the extra energy needed to overcome the non-idealities of the cells.

The reversible voltage (Equation 2-2), also called the open cirquit voltage (OCV), is the voltage when no current is drawn. In order to draw a current, the operating voltage (U_{cell}) of the cell is:

$$U_{cell} = E_{rev} + \eta_{cell}$$ Equation 2-4

The energy supplied by the over voltages eventually dissipates as heat in the cells, and thus, the combined over voltages relate to the entropy of the reactions:

$$\eta_{cell} = \frac{-T\Delta S}{zF} - \frac{-\Delta Q}{zF}$$ Equation 2-5

Here, T is the absolute temperature, ΔS is the entropy and ΔQ is the remaining energy which may be supplied as heating of the cell. As the electrolyzer has an internal resistance, the heating needed may be supplied as Joule heating (resistive heating) directly in the cell by applying a larger voltage. This can then be written as the overvoltage related to the heating need, η_Q and Equation 2-5 converts into:

$$\eta_{cell} + \eta_Q = \frac{-T\Delta S}{zF}$$ Equation 2-6

This means that the cell can be operated at a voltage where all energy is supplied by the current passing through the cell. This voltage is called the thermoneutral voltage, E_{tn}, and accounts for the entire enthalpy change of the electrolysis reaction:

$$E_{tn} = \frac{-\Delta H}{zF} = \frac{-\Delta G}{zF} + \frac{-T\Delta S}{zF} = E_{rev} + \eta_{cell} + \eta_Q$$ Equation 2-7

This also means that if further heating ($Q_{heating}$) is to take place in the cell, in order to provide part of the preheating of the feed gasses, an extra over potential, $\eta_{heating}$, may be applied, and $U_{cell} > E_{tn}$:

$$U_{cell} = \frac{-\Delta G}{zF} + \frac{-T\Delta S}{zF} + \frac{Q_{heating}}{zF} = E_{rev} + \eta_{cell} + \eta_Q + \eta_{heating}$$ Equation 2-8

The enthalpy change, Gibbs free energy change and temperature times entropy change of the reactions (Equation 2-7) vary with pressure and temperature. For the temperature dependence at 1 atm, the resulting curves are shown in Figure 2-2 for the electrolysis of H_2O (a) and CO_2 (b).

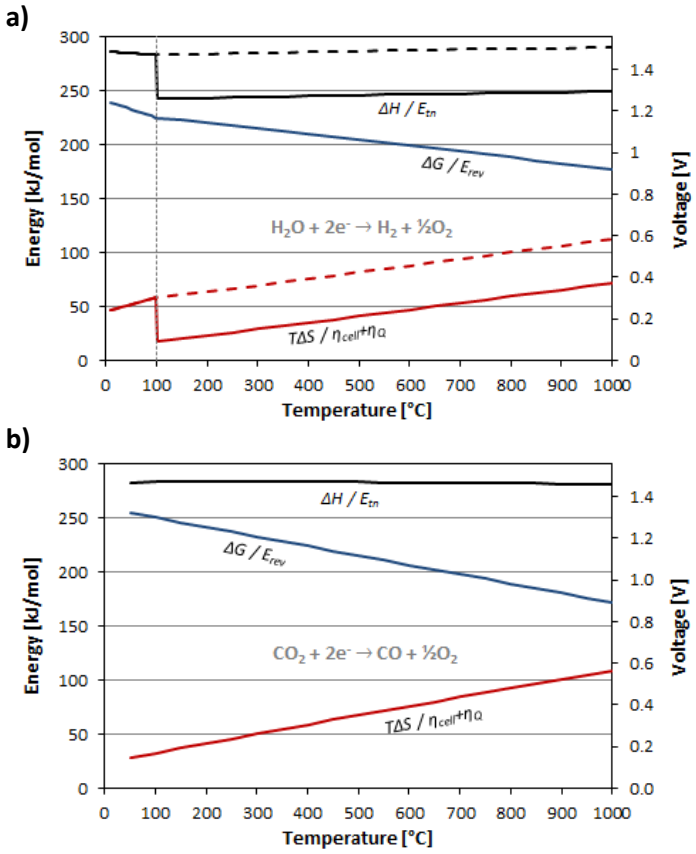

Figure 2-2. Enthalpy (ΔH*)*, Gibbs free energy (*ΔG*) and temperature times entropy (*TΔS*) changes of the H_2O (a) and CO_2 (b) electrolysis reactions as a function of temperature at 1 atm. The corresponding thermoneutral (E_{tn}), reversible (E_{rev}) and cell and thermal over voltages ($\eta_{cell}+\eta_\Omega$) voltages are shown. For H_2O electrolysis, *ΔH* and TΔS values are shown including the enthalpy/entropy of evaporation (dashed lines).

In Figure 2-2 a, the evaporation of water at 100 °C is seen as a drop in enthalpy and entropy changes. If steam is used as a reactant, this is a reasonable representation. If liquid water is the reactant, this needs to be evaporated, and the enthalpy and entropy changes are larger. This is shown by the dashed lines. Evaporation of water typically takes place in a pre-heating step, and steam is led into the cell at the operating temperature. Thus, the full lines show the needed voltages of the cell.

At the typical operating temperatures of SOECs of around 750 °C to 850 °C, the Gibbs free energy changes (reversible voltages) of the two reactions are almost identical. This means that these two reactions are especially well suited for co-electrolysis at these temperatures.

2.2.3 Polarization curves

When a voltage is applied to a cell, a current will flow. Plotting the voltage versus the current density (current divided by the geometric cell area), yields a current-voltage curve, or simply I-V curve. Three examples of such curves are shown in Equation 2-4 for three different gas compositions representing electrolysis of CO_2, steam and co-electrolysis at 850 °C [33].

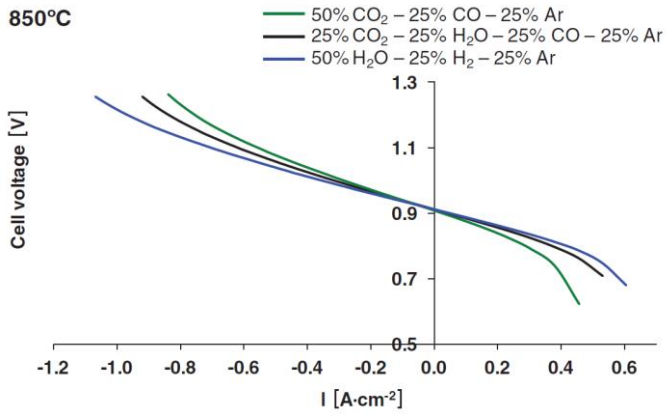

Figure 2-3. I-V curve for a YSZ-based solid oxide cell in both fuel cell and electrolysis mode for three different gas compositions at 850 °C. Reprinted with permission from [33], Copyright (2012), The Electrochemical Society.

The figure covers both positive and negative current densities. This refers to fuel cell and electrolysis operation respectively of the same cell. The IV curves are continuous at zero current density which means they are reversible, and any cell may be operated freely in either electrolysis or fuel cell mode. The curves cross the voltage axis at almost the same point. This is the OCV or reversible voltage, where no current is drawn, and confirms what was mentioned above, that E_{rev} is practically identical for the two electrolysis reactions at these temperatures.

The curves are linear around the voltage axis, and the slopes of the curves are the area specific resistance (ASR), which is straight forwardly found from Ohms law:

$$\eta_{cell} + \eta_Q = R_{cell}(P,T) \cdot I_{cell} = R_{cell}(P,T) \cdot A \cdot \frac{I_{cell}}{A} = ASR(P,T) \cdot I_A \qquad \text{Equation 2-9}$$

Here, $R_{cell}(P,T,)$ is the cell resistance at a given set of operating conditions, I_{cell} is the current drawn, and A is the cell area and I_A is the current density. Remembering that the voltage at no current (intersection with the voltage axis) represents the OCV (E_{rev}), Equation 2-9 can be re-written:

$$U_{cell} = OCV + ASR(P,T) \cdot I_A \qquad \text{Equation 2-10}$$

Outside the region of linearity, the I-V curves begin to curve towards larger absolute voltages (up or down depending on the sign of the current). This is caused by increased ASR stemming

from gas transport and conversion related resistances in the fuel electrode and support structure.

2.2.4 Pressurized operation of the SOEC

As mentioned above, the magnitude of the ASR depends on the operating conditions, such as the temperature, pressure, conversion of reactants to products etc. This is important to take into account when the operating point of the SOEC is selected, and will be treated further in Chapter 5 on the development of the SOEC model.

Further, the chemical equilibria of the WGS, methanation and Boudouard reactions depend strongly on the operating conditions in addition to the gas composition. The Boudouard reaction will be treated in Chapter 6.

The WGS reaction (Reaction 2-9) ties the two electrolysis reactions together, involving both reactants and products of Reaction 2-7 and Reaction 2-8. The reaction is endothermic with a reaction enthalpy change of $\Delta H = 41$ kJ/mol for the conversion of CO_2 and H_2 into CO and H_2O. This means it will have a larger influence on the gas composition of the SOEC at elevated temperatures. Ebbesen et al. showed that the composition of the outlet stream from an SOEC was in accordance with the WGS equilibrium at the given conditions. It should be noted, that the WGS reaction is not sensitive to the pressure of the system. Therefore, it is not nessecary to take into account when deciding on the operating pressure of the cell.

The methanation reaction (Reaction 2-10) also takes place on the Ni-catalyst. The reaction is highly exothermic with $\Delta H = -206$ kJ/mol, and due to the stoichiometry of the reaction, where 4 molecules react to form 2, it is also highly sensitive to the operating pressure.

This means, that at low temperature and/or high pressure, the methanation reaction may have a very large impact on the composition of the effluent stream from the electrolyzer. It should be noted here, that the generation of heat by the methanation reaction can cover significant amounts of the η_Q needed for the cell operation, resulting in a lowered thermo-neutral voltage of the cell. Thus, the optimal operating voltage becomes a complicated function of the operating conditions, and the needed composition of the product. This is further discussed in Chapter 5 on the development of the SOEC model, and the results and discussion in Chapter 6.

2.3 Methanation reactions and technology

Methanation of synthesis gas to methane is catalyzed by cheap, supported nickel catalysts and usually take place above 200 °C. The WGS reaction (Reaction 2-9 and repeated in Reaction 2-12) proceeds on the Ni-catalyst as well, as in the fuel electrode of SOEC. The reactions of the CO and CO_2 fractions of the syngas with H_2 follow the reaction schemes Reaction 2-13 and Reaction 2-14 respectively. The latter is a combination of CO methanation (Reaction 2-13) and the WGS reaction (Reaction 2-12):

$$CO_2 + H_2 \rightleftarrows CO + H_2O \qquad \Delta H^o = 41.2 \text{ kJ/mol} \qquad \text{Reaction 2-12}$$

$$CO + 3H_2 \rightleftarrows CH_4 + H_2O \qquad \Delta H^o = -206 \text{ kJ/mol} \qquad \text{Reaction 2-13}$$

$$CO_2 + 4H_2 \rightleftarrows CH_4 + 2H_2O \qquad \Delta H^o = -165 \text{ kJ/mol} \qquad \text{Reaction 2-14}$$

Other reactions such as the Boudouard reaction (Reaction 2-11) may take place on the Ni-catalyst as well, but the above mentioned are the dominant ones. The risk of forming solid carbon in the reactors due to the Boudouard and other reactions is treated later in this thesis (Chapter 5).

2.3.1 Feed module

Production of methane is highly sensitive to the composition of the synthesis gas used. For pure synthesis gas, the methanation reaction requires a mixture of 3 moles of H_2 for every mole of CO. This ration is a direct consequence of the stoichiometry of the reaction equation. In the case of synthesis gas from an SOEC, however, unreacted H_2O and CO_2 will also be present in the gas depending on the reactant utilization and operating conditions [33]. Unreacted water shifts the methanation reactions (Reaction 2-13 and Reaction 2-14) to the left (away from methane), and it should be removed from the syngas. This is easily done through condensation. CO_2, on the other hand, reacts with H_2 to form CH_4 through Reaction 2-14 with a stoichiometric H_2 to CO_2 ratio of 4.

It is valuable to have a single number, called the feed module (FM), describing the optimal stoichiometric feed gas composition for methanation. The feed module is a property of a syngas mixture, describing the composition of gasses relevant for production of methane or other synthetic fuels such as methanol or DME, and optimal operation of the fuel synthesis step requires that the FM has a certain value. The FM is derived from the stoichiometry of the two reactions:

For the methanation of CO, the stoichiometric H_2/CO ratio is 3 (Reaction 2-13):

$$\frac{x(H_2)}{x(CO)} = 3 \Leftrightarrow x(H_2) = 3 \cdot x(CO)$$ Equation 2-11

And for the methanation of CO_2, the H_2:CO_2 ratio is 4 (Reaction 2-14):

$$\frac{x(H_2)}{x(CO_2)} = 4 \Leftrightarrow x(H_2) = 4 \cdot x(CO_2)$$ Equation 2-12

For the mix between the reactions, the right amount of hydrogen needs to be present to exactly balance the two reactions:

$$x(H_2) = 3 \cdot x(CO) + 4 \cdot x(CO_2)$$

$$\Leftrightarrow x(H_2) - x(CO_2) = 3 \cdot x(CO) + 3 \cdot x(CO_2)$$

$$\Leftrightarrow \frac{x(H_2) - x(CO_2)}{x(CO) + x(CO_2)} = 3 = FM$$ Equation 2-13

This fraction is the feed module. Explained in words, a part of the H_2 is used to convert CO_2 to CO with the stoichiometry 1:1 through the WGS reaction (Reaction 2-12), and the amount of H_2 available for methanation of CO is $x(H_2) - x(CO_2)$ as written in the numerator in Equation 2-13. The amount of CO thus created is added to the original amount of CO and the resulting amount of CO available for reaction with H_2 is $x(CO) + x(CO_2)$ which is the denominator in Equation 2-13. Now that all CO_2 is converted to CO under consumption of H_2, the fraction between them needs to be 3 as per the methanation reaction.

Changes in operating temperature shift the equilibrium of the WGS reaction, as was discussed above. The derivation of the FM is based on the stoichiometry of the methanation reactions including the WGS reaction (Reaction 2-13, Reaction 2-14 and Reaction 2-12). This means that changes in the WGS equilibrium does not change the FM of the syngas. Other reactions such as the electrolysis reactions or the Boudouard reaction (see section 2.2) might change the FM of a mixture. If the FM is not exactly equal to 3, it will also change with the extent of the methanation reaction, as the relative amounts change when the reactants are being consumed in a strict stoichiometric ratio of 3.

2.3.2 Methanation plant technology

The methanation reactions are highly exothermic and consequently, large temperature increases are seen within methanation reactors. This imposes severe demands on the durability of the catalysts, or requires cooling of the reactor itself during operation. The MCR supported Ni-catalyst for methanation produced by Haldor Topsøe A/S operate in the temperature range from 220 °C to 700 °C. Above 700 °C, the Ni-particles of the MCR catalyst

tend to sinter, leading to fast degradation of the catalyst. [34]. On the other hand, most methanation catalysts are not sufficiently active below ~300 °C, although the MCR catalysts may be operated as low as 220 °C. Further, high temperatures shift the reaction towards the products, so that cooling is needed in order to drive the reactions towards 100 % CH_4. For these reasons, most methanation plants are designed with a series of reactors (usually 3-4) with intercooling steps in order to protect the catalyst and reactors themselves [35]. This is called a methanation train.

The development of heat, is dependent on the initial gas composition, more specifically the mole fraction of methane $x(CH_4)$. The higher, the methane content (at constant inlet temperature and pressure), the lower the maximum heat development, as less CH_4 is produced in the reaction.

In the first reactor of a methanation train, $x(CH_4)$ is usually low, and thus the risk of temperature rises above 700 °C inside this reactor is greater. In traditional methanation setups, this is handled by increasing $x(CH_4)$ in the reactor inlet stream by recycling a fraction of the effluent stream to the inlet. This increases the mole fraction of CH_4 in the inlet stream which lowers the conversion and thus the heat generation. The resulting lowered temperature increase comes at a trade-off: The increased methane content lowers the methane production and thus utilization of the reactor and catalyst. Also, the recycle increases the flowrate significantly, requiring a large extra volume of the reactor and downstream heat exchanger (cooler) in addition to a recycle compressor. Further, a methanation train, usually consisting of three or four reactors, has a condenser for water recovery before the last reactor.

The above principles are illustrated conceptually for the Haldor Topsøe A/S TREMP® (Topsøe Recycle Energy-efficient Methanation Process) process in Figure 2-4, which is reproduced from Jensen et al.[35]. The TREMP® process utilizes Topsøe's proprietary MCR catalysts, which were mentioned above.

In Figure 2-4 a) a generic layout of a TREMP methanation plant with 4 methanation reactors and a condenser placed after reactor 3 is illustrated. Note the recycle after the first reaction step, keeping the outlet temperature of the reactor below 700 °C. In b), a schematic representation of the temperature profile throughout the plant is illustrated as a function of the mole fraction of CH_4. The red lines represent temperature increases in the reactors and decreases in the intercoolers. The first red line on the left (①) representes the temperature rise in the first reactor if no recycle loop was present ($x(CH_4)^{inlet} \approx 0$). Recycling a fraction of the effluent stream from the first reactor effectively increases $x(CH_4)^{inlet}$ which limits the CH_4 production in the reactor and consecquently the outlet temperature (②). In the following reactors, the CH_4 production is limited in spite of the intercooling steps, as the inlet CH_4 concentrations are higher. The shift from the blue to the black curve in reaction step 4 is caused by the removal of H_2O from the gas stream which shifts the equilibrium towards a higher CH_4 concentration.

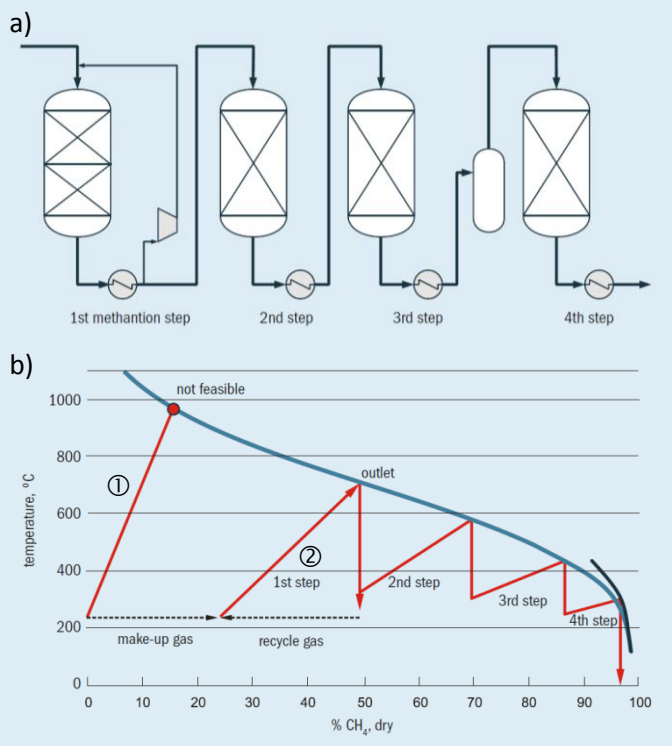

Figure 2-4. Conceptual layout of a methanation plant (a). In the schematic, four methanation reactors with intercooling are shown. Note the recycle loop including the compressor after the first intercooler (see text), and the condenser before the last reactor. b) *x(CH$_4$)* vs. T profile with and without recycle loop. The red arrows represent temperature increases in the reactors and decreases in the intercoolers. ①: Temperature rise in first reactor in the absence of a recycle loop. ②: Temperature rise in the first reactor in the presence of a recycle loop. Reproduced from [35]

The TREMP process is optimized to produce waste heat at high temperature and pressure and to use the generated steam for on-site power generation. As an alternative, the large amount of heat which is shed in the intercoolers might be recovered and used in other parts of the plant. The study of such integration of heating and cooling demands of a plant is called heat integration studies. The basic concepts are described in section 2.4 of this chapter, and is the focus of Chapter 8 of this thesis.

2.4 Heat integration studies

In this section, the basic concepts of heat exchangers are presented along with two methods used in the heat integration studies in this work. This is meant as a basic introduction for engineers and scientist not familiar with these concepts. For more detailed developments of the theory, equations and methods of heat transfer and heat exchanger equipment, I refer to the literature [36-39].

2.4.1 Hot and cold streams

Most industrial processes have streams (solid, liquid, gaseous or mixed) which need to have energy in the form of heat added to them or removed. Such streams are classified as *hot streams*, in the case of streams needing to have heat removed, or *cold streams*, which need to have heat added. This naming convention is independent of the actual temperature of the individual stream. Most times, a hot stream is one that is cooled down or condenses as it sheds heat and cold streams heat up, melt or evaporate as heat is supplied. For this reason, hot and cold streams are also referred to as heat sources and heat sinks respectively.

Utilities is the collective term for all external energy sources or sinks such as electricity, district heating, excess process heat from other industrial processes, cooling water etc. In this connection, “external” means that these energy sources or sinks do not originate in the process in question, but come from outside of the system boundaries.

In order to save energy and money in industrial processes, it is preferable to spend excess heat from hot streams to supply heat to cold streams. Reversely, it is preferable to use the cooling capacity of a cold stream to extract heat from hot streams. The alternative would be to use utilities in all cases, which would severely hamper the energy efficiency and most often the economic profitability of the plant.

Using heat available from hot streams in the plant to fulfill the demands of cold streams is called *internal heat recovery* or *process-process heat recovery*. This requires careful matches of the heating and cooling demands in order to maximize the amount of heat which is recovered in the system. The study of systems with the goal of attaining high internal heat recovery and minimize the use of utilities is called *heat integration studies*.

Heat exchangers are used in order to transfer heat from one stream to another without mixing the two. Such equipment can be quite expensive, and consequently, in addition to maximizing the internal heat recovery and minimizing the use of utilities, heat integration studies will often have an economic component, in order to find the balance of these two goals with the need to minimize the amount of capital invested in equipment.

2.4.2 Heat exchangers and heat curves

As mentioned above, a heat exchanger is a piece of equipment used for exchanging heat between two streams. Heat exchangers are passive devices allowing the heat in the hot stream to transfer to the cold stream with the temperature difference between them as the driving force.

Heat exchangers have a hot and a cold *side* which refers to the parts of the exchangers, incorporating the hot and the cold stream respectively. Each stream has a *source state* and a *target state*, consisting of inlet temperature and phase and outlet temperature and phase, respectively. Figure 2-5 illustrates a schematic representation of a shell and tube heat exchanger with counter flow configuration (the streams enter at opposite ends of the exchanger) (a), and the corresponding conceptual *heat curves* of the interacting streams. The heat curves represent each stream with a source (inlet) temperature and a target (outlet) temperature. The vertical distance between the inlet and outlet temperatures of a stream represents the temperature difference of the heating or cooling, and the horizontal distance is the heat which is shed or absorbed by the stream. The position of a stream on the x-axis (heat flow) is arbitrary, as only the difference in thermal energy between the inlet and outlet needs to be considered.

In the figure, the streams do not change phase during the exchange. Phase changes are identified in this type of diagrams as horizontal line segments as the stream temperature does not change while heat is being supplied or removed during the phase transition.

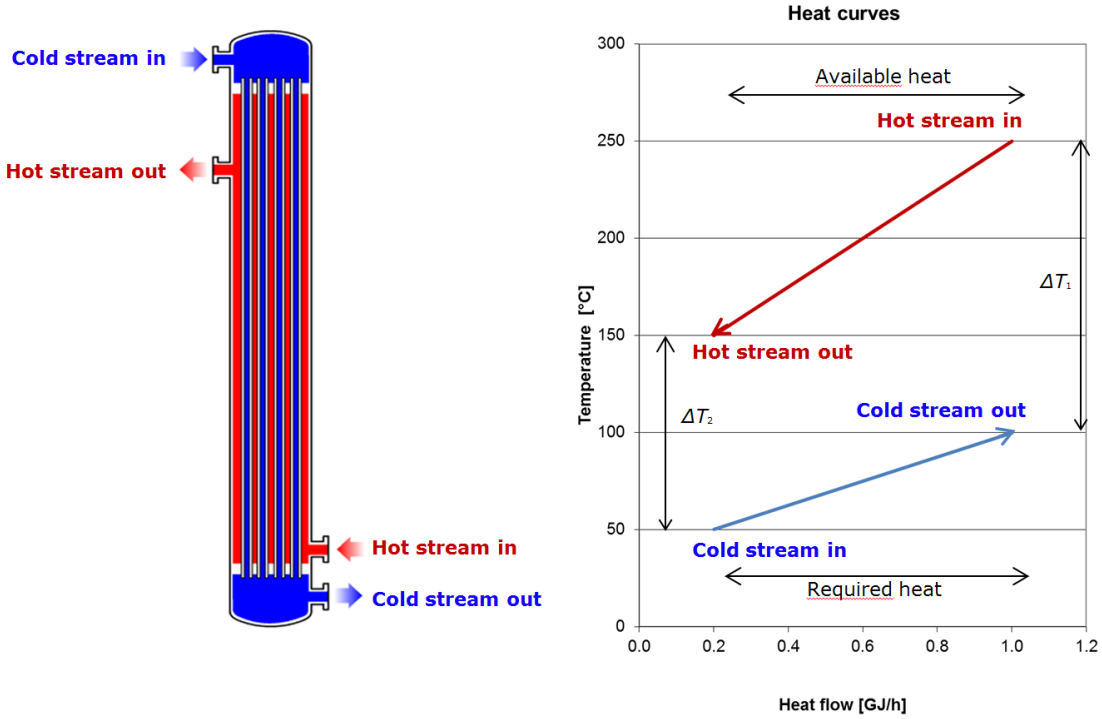

Figure 2-5. a) Schematic representation of a shell and tube heat exchanger where a cold stream is led through the tubes absorbing heat from the hot stream in the shell. Reproduced from [40]. b) Conceptual heat curves for the hot and cold streams interacting in the heat exchanger. The source and target temperatures are given by the ends of the curves.

As mentioned above, the driving force for the exchange of heat in a heat exchanger is the temperature difference. As seen in Figure 2-5 b, the temperature difference changes over the length of the exchanger, and often, the logarithmic mean temperature difference is used instead:

$$\Delta T_{\log\ mean} = \frac{\Delta T_1 - \Delta T_2}{ln(\Delta T_1/\Delta T_2)}$$ Reaction 2-15

Here, ΔT_1 and ΔT_2 are the temperature differences between the two streams at each end of the heat exchanger, with ΔT_1 being the larger difference. The minimum temperature difference in a heat exchanger is often called the *approach temperature*, and the symbol ΔT is used in place of the more complicated relations. The simplified, generalized governing equation for the amount of heat which can be exchanged is given as Equation 2-14.

$$Q = U \cdot A \cdot \Delta T_{\log mean}$$ Equation 2-14

In the equation, Q is the amount of exchanged heat. U is the overall *heat transfer coefficient* which depends on the heat transfer coefficients of the two streams in relation to the heat exchanger, the material and geometry of the wall separating the streams and the physical configuration of the heat exchanger. A is the area of interface between the streams. Calculating the exact heat transfer coefficient, U, and the temperature difference is cumbersome except for simple cases, and specialized software is often used. The software used in this work is described at the end of this chapter.

It is important to note from Equation 2-14 that if the temperature difference in the exchanger is low and everything else is equal, less heat may be exchanged. This is often compensated for by increasing the area of interaction between the streams, A. This, in turn, increases the cost of the exchanger, as it becomes larger, and A with the units of m^2 is used as a simplified sizing parameter for the determination of the cost of individual heat exchangers.

2.4.3 Composite curves

An entire plant will often contain far more than one hot stream which needs to be cooled and far more than one cold stream which needs to be heated, and a way of visualizing these streams is needed. This is done by aggregating the heat curves of all hot streams in the plant into one curve: the hot *composite curve* and the heat curves of all cold streams into the cold composite curve. These are plotted in the same type of diagram . The process is illustrated in Figure 2-6 for two hot streams and two cold streams.

The aggregation of hot streams into the hot composite curve is done by first organizing all the hot streams after increasing outlet temperature and plotting them in a temperature vs. heat flow diagram so that the stream with the lowest temperature is placed at lowest heat flow.

The rest are added at higher heat flow so that there are no vertical overlaps and no gaps between them on the heat flow scale. The same is done for the cold streams. This situation is depicted in Figure 2-6 a).

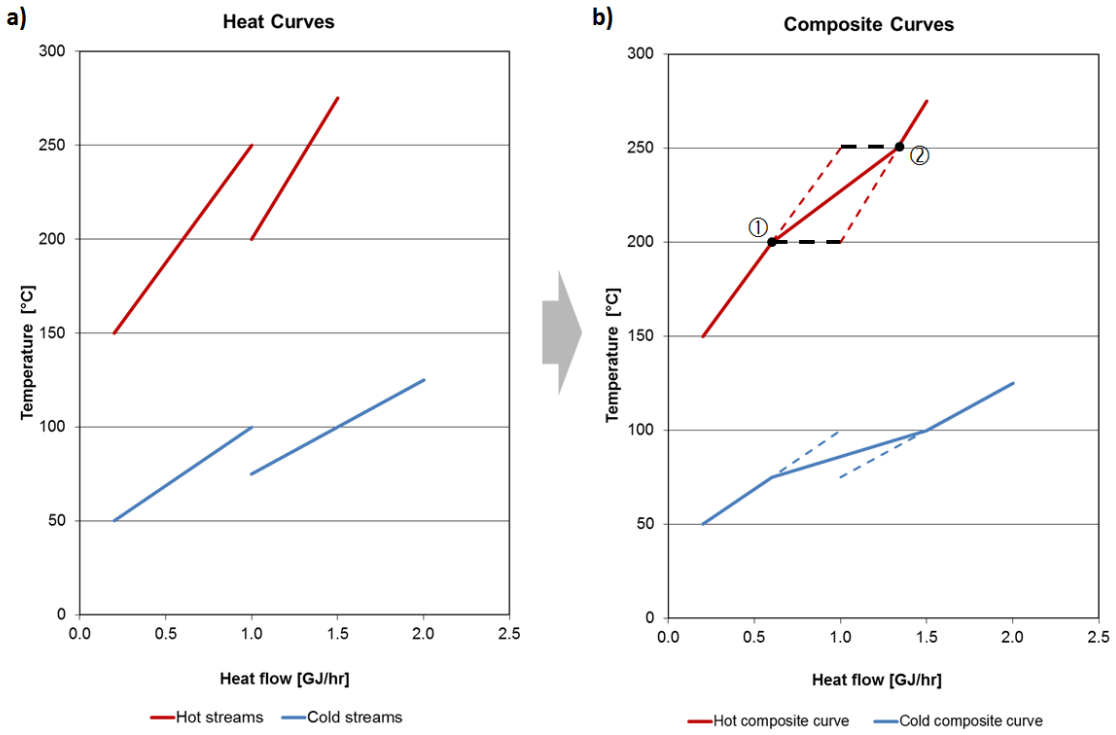

Figure 2-6. Aggregation of the hot and cold stream heat curves (a) into the hot composite curve and the cold composite curve (b).

The next step is to consider the temperature intervals in which the hot streams overlap, and those in which the cold streams overlap. In the example in the figure, the hot streams overlap between 200 °C and 250 °C and the cold streams overlap between 75 °C and 100 °C. This is shown in Figure 2-6 b) for the hot streams. The curves are now aggregated by connecting the two curves in the interval of overlap. At the colder end of the temperature interval, the heat flow value of the stream with the lowest temperature (the stream on the left) is used (point 1), and at the higher end of the interval, the stream with the higher temperature is used (point 2). The two points are then connected.

The described way of aggregating the curves is the equivalent of adding the incremental heat flow at each temperature, and cumulating the heat flows over all temperatures for each curve. The two composite curves now represent all the heat that is available or required in the plant for each temperature interval.

2.4.4 Composite curve analysis

The composite curves turn out to be a powerful tool for visualizing the heat flows and potential for heat integration in a plant. The hot composite curve shows how much heat is

available at which temperature, and the cold composite curve shows how much heat is needed at which temperatures. This means, that comparing the two composite curves of a plant will give theoretical numbers for the amounts of heat which is recoverable internally in the process. In any region where the curves overlap vertically, with the hot curve having higher temperatures than the cold curve, heat may be transferred from the hot streams to the cold streams in one or more heat exchangers. If at any point, the hot curve has lower temperatures than the cold curve, no heat may be transferred. Any such part of the curves, or any part of either curve, not overlapping with the other, represents heating or cooling duties which need to be supplied by external utilities. The latter of these situations is illustrated in Figure 2-7 a) for the composite curves generated above. In the figure, the composite curves have the low temperature end at zero heat flow, which is how they are conventionally drawn.

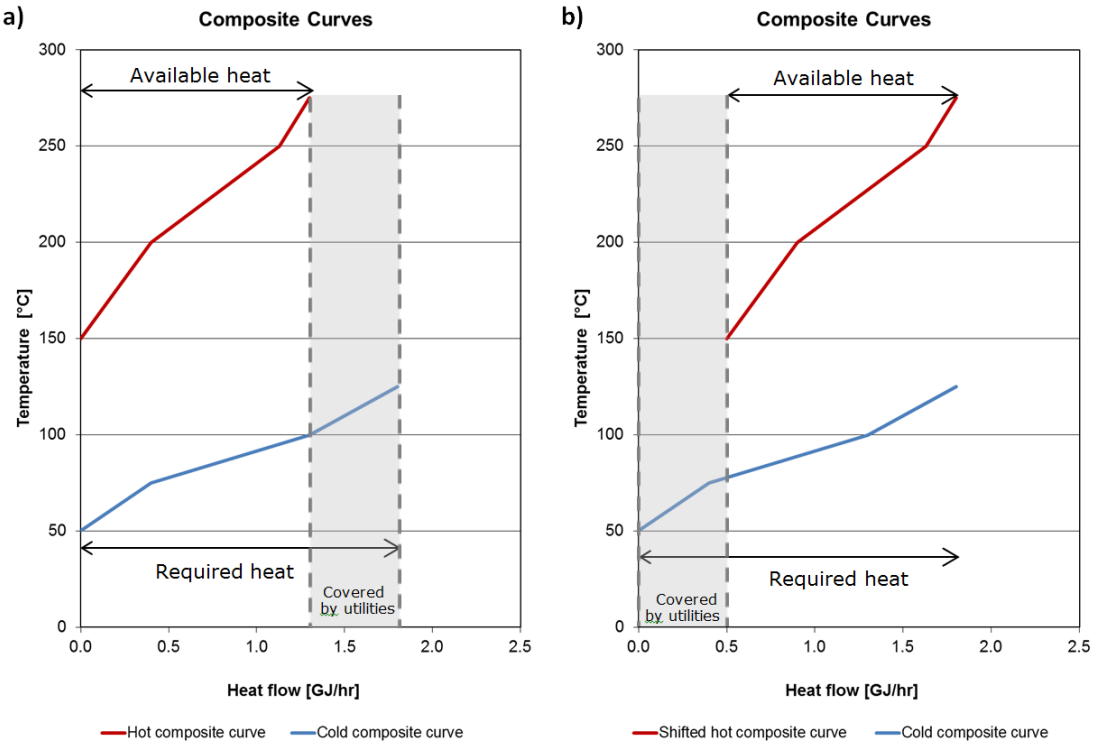

Figure 2-7. Comparison of the composite curves from Figure 2-6. The vertical overlap represents the maximum amount of heat which can be recovered in the process by transfer from the hot streams to the cold streams. The width of the shaded area represents the minimum amount of heat which needs to be supplied by external utilities. a) Both curves beginning at zero heat flow. Utility heating needs to be supplied at high temperatures b) The hot curve has been shifted to match heat recovery at high temperatures, and utility heating is then needed at low temperatures.

In Figure 2-7 a), the cold curve which represents all the heating demands in the plant, covers a larger amount of heat than the hot curve. This means, that even though the hot curve is significantly warmer, it does not possess sufficient energy to cover all the demands for heating in the plant. The excess demand for heating (the width of the shaded area) has to be supplied by external heating utilities. In this case, the hot utility has to be supplied at a temperature

above 125 °C as this is the target temperature of the part of the cold curve which needs to be heated.

It was mentioned earlier, that the curves may be shifted along the x-axis, as only the range of heat flows spanned by each curve is important. In Figure 2-7 b), this is utilized and the hot composite curve has been shifted to higher values of the heat flow. This has been done so that the high temperature parts of the curves overlap, and that the maximum temperature ends of the curves are placed at the same value for heat flow. In this situation, the amount of recoverable heat is the same, and the minimum amount of hot utilities needed is the same. But the utilities may be supplied at significantly lower temperatures. This may be seen from the maximum temperature in the interval is around 78 °C. The operation of shifting curves along the heat flow axis is purely graphical and does not represent any physical processes in the plant.

2.4.5 Heat integration

In real plants, the composite curves are often much closer on the temperature scale than the ones shown in the example above, and they may have cross-over points. This means that the approach temperature of the individual heat exchangers may become limiting in order to avoid exceedingly large areas of the units. In such circumstances, the amount of heat which may be recoverable in the system may be limited due to restrictions on the horizontal positioning of the curves. The minimum temperature difference, one will allow in a heat integration problem is called the heat recovery approach temperature (HRAT). In most real systems, the amount of recoverable heat is a direct, however complicated, function of the value of HRAT. HRAT is really a temperature difference between the two closest points on the curves. It is usually given in Kelvin, and has values between 5 and 35 K in real systems depending on the stream compositions, economics of the plant etc. This point of closest approach on the temperature scale of the two curves is called the pinch point, and this type of analysis is often called pinch analysis.

The analysis of composite curves gives the theoretical amounts of recoverable heat as well as minimum hot and cold utility requirements, but the technical implementation of these concepts is often more complicated. With many streams in the plant, several choices for both hot and cold utilities and complicated geometries of the composite curves, the actual amount of recoverable heat is lower, and the utility consumption higher than the theoretical amounts.

In order to determine the technically and economically feasible amount of heat which may be recovered, the so-called heat exchanger network synthesis (HENS) problem needs to be solved. There are several approaches to this, and many are computer based or assisted. In this work, the dual approach temperature (DAT) method is used [41]. This method recognizes, that while relatively large values of HRAT may be required, the temperature differences of individual heat exchangers, especially those with streams of high heat transfer coefficients, may be allowed to be lower. This introduces the exchanger minimum approach temperature

(EMAT) which is the minimum allowable temperature difference in any heat exchanger in the network.

In this work, the HENS problem is solved using the heat transfer simulation software HEXTRAN [42]. HEXTRAN takes as input, a list of all the heating and cooling duties in the plant including the compositions of the streams involved and their source and target states. In addition to this, two utility services (one hot and one cold) are supplied. With a set of HRAT and EMAT values, the program generates a series of networks, often between 20 and 60 candidates, calculates the annualized cost of each network, and returns the one with the lowest cost. The generation of each network is done by matching hot and cold streams for exchange of heat in a series of temperature intervals defined by the inlet and outlet temperatures of all streams. In the case where this produces matches of the same streams in adjacent intervals, these are combined. This gives a series of heat exchange services, and any remaining heating or cooling duties are matched to the utilities.

The cost of the networks is calculated from a set of utility prices, economic constraints and a generalized costing equation for heat exchangers. For the calculations in this work, the basic costing model for heat exchangers from the economic analysis software [43-45] was used:

$$cost = fS + C \qquad \text{Reaction 2-16}$$

Here, *S* is the sizing parameter (area) of the heat exchanger, *f* is the linear cost factor and C is the basic constant exchanger cost. For exchangers operating at 80 atm produced from 316 Stainless steel, these values are: *f*=155,12 \$/m^2 and *C*=3956,1 \$ or *f* = 119.3 €/m3 and *C* = 3043.2 € [43-45].

The annualized cost of the network is calculated by HEXTRAN with the following equation:

$$C_a = C_o + C_c \cdot crf \qquad \text{Reaction 2-17}$$

Here $crf = \frac{i\cdot(1+i)^{\eta}}{(1+i)^{\eta}-1}$ Is the capital recovery factor (crf). C_a is the annualized cost of running the network, C_o is the operating cost (the annual costs of the utilities), and C_c is the capital costs of the network. *i* and *η* are the internal rate of return and plant lifetime respectively. The interest rate is used in place of the internal rate of return, as this is the minimum value of *i* if the project is to be economically viable. This is discussed further in Chapter 10, outlining the economic methods and assumptions.

Once a satisfying heat exchange network has been synthesized in this way, the heat exchanged internally in the process and the needed utility streams is returned, and the cost of the utilities along with the needed heat exchangers may be calculated.

2.4.6 Summary on heat integration.

To summarize, the main goal of heat integration studies is to analyze the potential for energy savings through utilizing the thermal energy available in the hot streams in the plant to heat the cold streams.

The composite curves of a plant represent all the heat available in the hot streams as well as the heat needed by all the cold streams. The composite curves are represented in temperature vs. heat flow diagrams, and the curves may be shifted freely along the heat flow axis, restricted only by the heat recovery approach temperature (HRAT) which specifies the maximum amount of recoverable heat for a given set of composite curves.

The analysis of composite curves gives the theoretical maximum amount of the heat which may be recuperated internally in the system, in addition to the theoretical minimum demands for external heating and cooling services, in the form of hot and cold utilities.

Solving the HENS problem for a full plant has the added benefit of yielding technically and economically relevant results, in addition to providing the basis for calculating the sizes and costs of the required heat exchangers.

This concludes the introduction to composite curves and heat integration. Composite curve analysis is used several times in this work, whereas the heat integration study is performed for the full plant developed over the chapters of this thesis.

Part III – CO_2 capture and impurities

Chapter 3 CO_2 air capture – experiments and modelling

Various strategies for direct air capture of CO_2 were mentioned in the Theory chapter. The main concern in relation of commercialization of these systems, namely the energy consumption, was discussed. While the energy consumption of most known systems is high, it does not appear to be a given feature of the concept. The thermodynamic minimum energy requirement is significantly lower, and it is less than 5 % of the total energy content of corresponding amounts of methane for example. The two technologies considered in this work exemplify different takes on these issues in that they represent a thermal swing in the case of the temperature vacuum swing (TVS) technology and the alternative humidity swing (HS) technology.

In the following sections, the two technologies considered for this work are treated. For the humidity swing system, a few experiments are reported in relation to the supply of water to the sorbent. For the temperature vacuum swing technology, the input data and modeling strategy adopted in this work is explained.

3.1 Experimental work on the humidity swing system

The HS system uses an anion exchange resin incorporating quaternary ammonium ions with carbonate/bicarbonate counter-ions. The resin has the form of 10-100 µm particles supported in a porous polypropylene backbone. The composite is referred to as the sorbent material or simply sorbent in the following.

The main issues relating to the HS technology seems to relate to the supply of H_2O to the resin, and the kinetics of CO_2 release from the sorbent.

A bench scale test reactor was constructed for the impurity sampling experiments described in Chapter 4 and a series of experiments were run in order to superficially gage the H_2O supply and desorption characteristic of the anion exchange resin. The experiments were conducted using two different strategies for supplying water to the sorbent material. Due to time constraints, the setup, flowrates and reactor geometry was not optimized beyond what was needed to provide the amounts of CO_2 necessary for the impurity collection experiments.

3.1.1 Experimental

A setup was custom built to produce a continuous flow of CO_2 totaling approximately 4.5 l at varying concentrations. Central to the setup was two parallel polycarbonate tube reactors, each filled with 15 cartridges containing rolled, corrugated strips of sorbent material with a thickness of around 1 mm. Each cartridge contained 8-16 g of material (average = 11.7 g) as measured at a dew point of 16.1 °C, at ambient conditions. Thus, the two reactors each contained 177 g of sorbent material on average, and a total void space of 1.947 l. Figure 3-1 (a) shows pictures of one dry (left) and one wet (right) cartridge as well as the packing of the cartridges in the polycarbonate reactors (b).

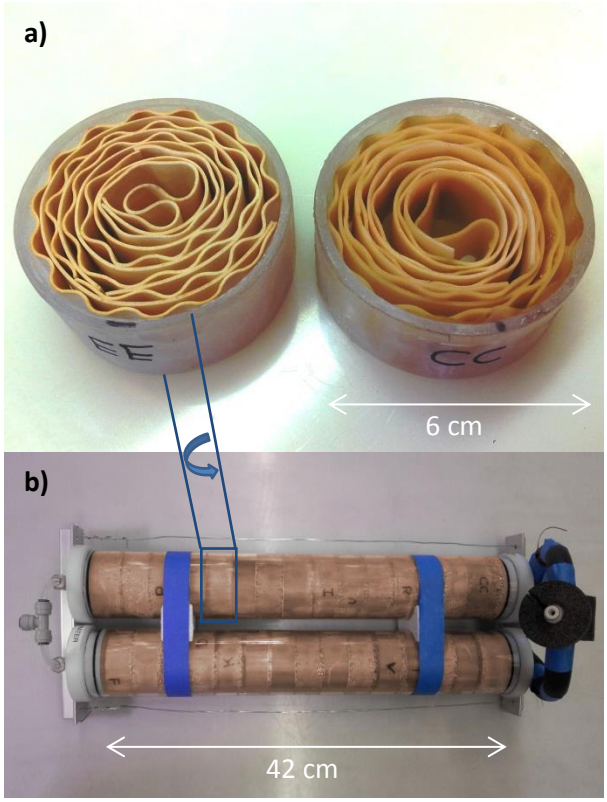

Figure 3-1. a) Resin containing sorbent material in cartridges, dry (left) and wet (right). b) 15 cartridges packed in each parallel polycarbonate reactor tube. The inlet make-up gas inlet is through the insulated tubing on the right.

The partial pressure of CO_2 over the resin in the humid desorption state is on the order of 5 % in a carrier gas or 5 kPa in vacuum. Thus, the setup used for the impurity collection experiments needed a make-up gas to continuously flush the CO_2 away from the resin in order for more to desorb. Also, in some experiments, the carrier gas was used to continuously supply H_2O in the vapor phase to the resin. For the make-up gas, 1 % H_2 in N_2 (0.99985 ± 0.02 %, Tech Air, USA) was used.

Figure 3-2 shows a schematic representation of the bench scale test reactor setup.

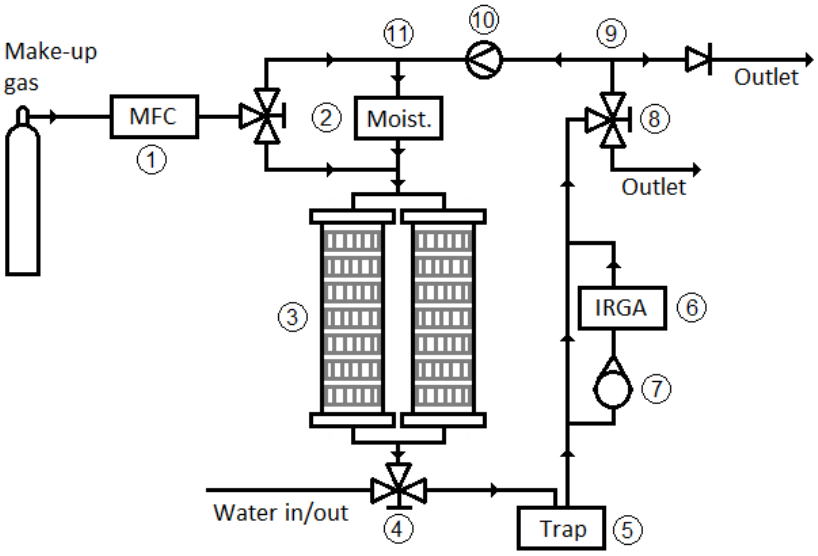

Figure 3-2.Schematic representation of the bench scale test reactor setup for desorption experiments. ① Mass flow controller, regulating the make-up gas flow. ② Moisturizer for supply of vapor phase H_2O. ③ desorption reactor tubes with sorbent material cartridges. ④ Three-way valve controlling liquid water inlet/outlet. ⑤ Water trap. ⑥ Infrared gas analyzer (IRGA) for CO_2 logging. ⑦ Ball flow meter. ⑧ Three-way valve for purging. ⑨ T-junction separating outlet and recycle streams. ⑩ Recycle circulation pump. ⑪ T-junction connecting recycle stream and make-up gas stream before the moisturizer.

The flow rate of the make-up gas was controlled by a mass-flow controller at 0.3 l/min ①. The gas was led through a temperature controlled bubbler flask ② operated at 25 °C, prior to being fed into the two parallel reactors containing the sorbent material in stacked cartridges ③. Emerging from the reactors, the gas streams were recombined, and passed a three-way valve ④ allowing introduction and removal of liquid water to the reactors, and then led through a water trap ⑤. The CO_2 content in the stream was continuously logged by an infrared gas analyzer (IRGA) connected to a computer ⑥. This was placed in a bypass loop and protected against pressure spikes in the main stream by a ball flow meter operated at 0.8 l/min ⑦. After this, a three-way valve allowed for purging the system ⑧ and a T-junction ⑨ separated the exhaust gas stream from a recycle loop. The recycle loop was driven by a pump ⑩ operated at ~10 l/min, and the recycle was mixed with the make-up gas in a T-junction ⑪ before it entered the moisturizer. The recycle loop ensured good mixing and a high flow through the reactors. The high reactor flow was designed to enhance the speed at which H_2O in the gas phase could be brought into the reactors from the bubbler flask and to ensure, limitations from macroscopic gas transport processes in the setup were minimized. The make-up gas flowrate was controlled by the mass flow controller, and simple mass balance required the same flowrate in the outlet stream, even though the flowrate in the recycle loop is significantly larger.

The gas phase volume of the system was 3.67 liters. The resin made up 60 % by mass of the sorbent material including the polypropylene backbone. The CO_2 capacity of the resin was estimated by Wang et al. [25] from the ion charge density. 21.3 Nl/kg (normal liters/kg) corresponding to 12.8 Nl/kg of sorbent material (including the backbone) was obtained. They also measured the capacity of the resin experimentally and arrived at 18.4 Nl/kg corresponding

to 11.0 Nl/kg of sorbent material. The total capacity of the system was then app. 3.9 or 4.5 l of CO_2 for one cycle or between 0.16 and 0.18 moles.

5 drops of 10% HCl in water was added to the bubbler flask before each experiment in order to ensure that CO_2 dissolving in the water, would not form bicarbonates or other compounds with other species potentially present in the deionized water. The resulting capacity for CO_2 absorption in the bubbler flask containing 0.700 l of de-ionized water was then calculated by Henrys law at 25 °C to 0.35 ml - 1.04 ml for CO_2 partial pressures of 1 % - 3 % respectively. With the above total capacity of 3.9-4.5 l per desorption cycle, this amount is negligible.

Before each experiment, the cartridges were dried and allowed to equilibrate in the lab air for at least five hours. After installation, in the reactors, the setup was flushed in make-up gas for 20 minutes in order to remove all lab air from the system.

Two types of tests were conducted. In the first type, all water needed for desorption was provided by saturation of the make-up gas stream in the bubbler flask. In the second type, deionized water with added HCl was led directly into the reactors from the inlet port at the bottom (see Figure 3-2 ④) while they were open to the lab air at the top. Filling the reactors this way took app. 2 min. When the reactors were full, the inlet tube was connected, and the make-up gas flow set to 1.0 Nl/min, pushing the air back out in app. 2 min. when the reactors were empty, the three-way valve at the bottom was switched to close the water inlet, the make-up gas flow was set to 0.3 Nl/min and the pump and data logging were started. In total, 6 experiments were conducted. Two with vapor-phase H_2O, two with liquid H_2O and two with vapor-phase H_2O and reduced numbers of cartridges in the reactors. The experiments are summarized in Table 3-1, were the resin saturation and total amount of adsorbed CO_2 was calculated from the equilibration conditions (temperature and dew point) as per Wang et al. [46].

Table 3-1. Summary of the performed experiments. The "H_2O phase" marks whether the H_2O needed for desorption was supplied in the vapor phase (V) through the moisturizer or in the liquid phase (L) through the water inlet. The degree of saturations, θ, and CO_2 capacities were calculated from the temperature and relative humidity during the equilibration before the experiments.

Experiment	H2O phase	# of cartridges	θ [%]	Capacity [l]
1	V	30	0.84	3.8
2	V	30	0.82	3.7
3	L	30	0.90	4.1
4	L	30	0.88	4.0
5	V	2	0.80	0.24
6	V	10	0.62	0.93

3.1.2 Results and discussion

In the first two experiments, H_2O was supplied to the reactors by the make-up gas and recycle gas flowing through the bubbler flask. Once the make-up gas flow, recycle pump and the IRGA logging the CO_2 concentrations were started, the CO_2 concentration began to rise slowly. The

results are shown in Figure 3-3. The cumulated amount of desorbed CO_2 over time was calculated from the CO_2 concentration curve and the make-up gas flow which set the rate of removal of the CO_2.

The figure shows that over the first 6 h, the concentration rises steadily. After this, the curve starts to flatten, and around 10 h a maximum is reached. After this, a long slow decline is observed over the following approximately 60 h, while slowly leveling out. The cumulated desorbed amount of CO_2 follows this behavior, accelerating during the first 6-10 h after which the curve starts leveling out over the remaining ~60 h of the experiment. The second experiment was cut short after 40 h, but follows the same trends.

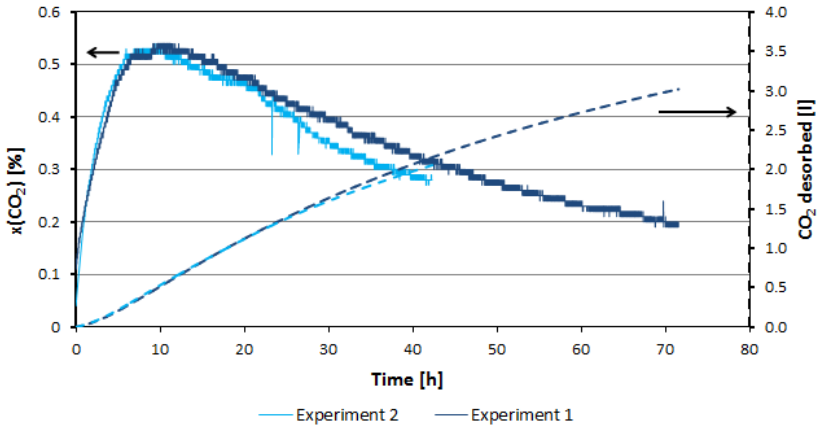

Figure 3-3. Desorption curves of experiments 1 and 2 run with vapor-phase H_2O. Solid lines show logged vapor phase CO_2 concentrations (left y-axis). Dashed lines show cumulated desorbed CO_2 calculated from the make-up gas flowrates and CO_2 concentration (right y-axis). Saturations calculated from the adsorption conditions were ~84 % (dark blue) and 82 % (light blue) corresponding to 3.7 and 3.8 l of CO_2 respectively.

During the first part of the desorption process, the sorbent is still close to saturation, and the desorption rate is comparatively high. It should be noted, however, that only around 3 l of CO_2 is removed from the setup during the entire 70 h of experiment 1. Under other conditions [25, 46] the desorption rates of these materials seem to be significantly higher. During the desorption process, vapor-phase water is supplied to the reactor at a relatively slow rate. Assuming that 25 moles of H_2O is adsorbed for every mole of CO_2 released [27], the time to supply the needed amount of H_2O was calculated to app. 5 hours. This calculation rests on the assumption that the gas is fully saturated in water when leaving the moisturizer and that all H_2O is adsorbed from the gas stream during one pass through the reactors. It is tempting to assume that the supply of H_2O is simply too slow, and that this is the reason for the slow observed desorption rate in the beginning of the experiment. This could be caused by slow adsorption of H_2O on the resin, as the assumption that the inlet gas is saturated is probably sound.

In a second set of experiments (3 and 4), H_2O was supplied and removed via the inlet/outlet port at the bottom of the reactors. Once the water had drained out, the setup was sealed, and

the data logging started. The cumulated desorbed CO_2 was calculated as described above, and the results are shown in Figure 3-4, where the insert shows the time range between 0 and 2 h.

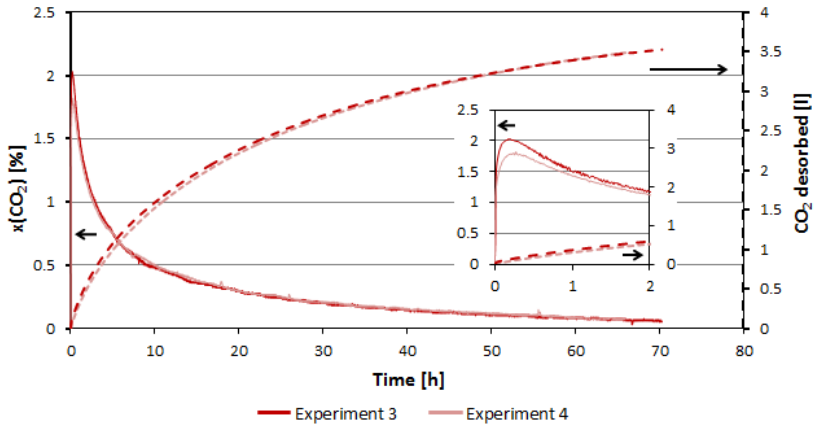

Figure 3-4. Desorption curves of experiments 3 and 4 run with liquid H_2O. Solid lines show logged vapor phase CO_2 concentrations (left y-axis). Dashed lines show cumulated desorbed CO_2 calculated from the make-up gas flowrates and CO_2 concentration (right y-axis). The insert have the same axes and show the time interval from 0 to 2 h. Saturations calculated from the adsorption conditions were ~88 % (pink) and ~90 % (red) corresponding to 3.9 and 4.1 l of CO_2 respectively.

Two things are immediately observed from the figure: First, the increase in $x(CO_2)$ in the first part of the experiment is significantly steeper than was observed in Figure 3-3, with $x(CO_2)$ reaching the maximum after only 10 min. Secondly, the maximum concentration is 2 % and 1.75 % in the two experiments, compared to just over 0.5 % in experiments 1 and 2. After the maximum has been reached, $x(CO_2)$ drops sharply over a few hours after which, the slow decay of $x(CO_2)$ is similar to what was observed for the first experiments.

In experiments 1 and 2 (Figure 3-3), the adsorbed volume of CO_2 was calculated from the sorbent mass and adsorption equilibration conditions to be 3.7 and 3.8 liters for the two experiments. For the second set (Figure 3-4) the volumes were 3.9 and 4.2 liters. Thus all of the four experiments were terminated before all CO_2 had been released. In the first experiments, the time it took to desorb 3.0 liters of CO_2 was ~70 h, whereas for the second set, the time was ~40 h and ~41 h depending on the saturation. It is interesting to note, that with similar saturations in all experiments, even when the peak CO_2 concentration was 5 times higher in the liquid H_2O experiments, the time to desorb 3 liters in the liquid H_2O experiments was still almost 60 % of those of the vapor-phase H_2O experiments.

Insufficient work has been done to fully characterize the HS system with regards to the kinetics of H_2O uptake and CO_2 release. From the curves presented above, a few hypotheses can be constructed, however:

The first parts of the desorption curves, are thought to be dominated by the rate at which water can be supplied to the sorbent material: As water is led into the reactor with the combined make-up gas and recycle stream, the sorbent material in the cartridges take up H_2O

and starts to give off CO_2. If the water supply did not limit the process, the rate at which the concentration rises would be governed entirely by the desorption rate and the rate at which CO_2 is removed from the system by the gas flow. The fact that this is not the case, and that there is a marked difference between the supply of H_2O in the vapor phase and as a liquid suggests, the water supply is the limiting step in this part of the curve.

As $p(CO_2)$ in the gas stream increases, the driving force decreases, and the desorption gradually slows down. With no CO_2 being removed from the system, this is seen as an asymptotic approach to the equilibrium partial pressure over more than 100 h in this setup (not shown). As CO_2 is continuously removed from the system at the concentration of the gas stream, the rate of removal becomes greater than the rate of desorption at some point, resulting in a maximum of the concentration curve. After this point, the long period of decreasing concentration is governed by the rate of CO_2 removal which depend on the decreasing rate of desorption, gradually emptying the resin.

There might be a third component participating in governing the rate in the first part of the desorption process: As H_2O enters the reactors in the vapor phase, it is absorbed on the resin of the first cartridges which start giving off CO_2. This increases the concentration in the gas stream to levels above those at which the sorbent was equilibrated. This was on the order of 400-500 ppm (0.04 – 0.05 %). Further down the reactor, where the sorbent has not yet been wetted by the slow input of water, large amounts of the CO_2 would then absorb on the dry sorbent. In order to start desorbing CO_2 from the downstream cartridges, which are now saturated in CO_2 at the conditions of the reactors, the first cartridges need to be saturated in water before the front moves further along the reactor to reach the following cartridges.

This hypothesis was tested by two extra experiments (5 and 6) with varying reactor loadings of 1 and 5 cartridges in each reactor (compared to 15 in each in experiments 1 through 4). The H_2O was supplied in the vapor phase via the moisturizer, and the results are shown in Figure 3-5.

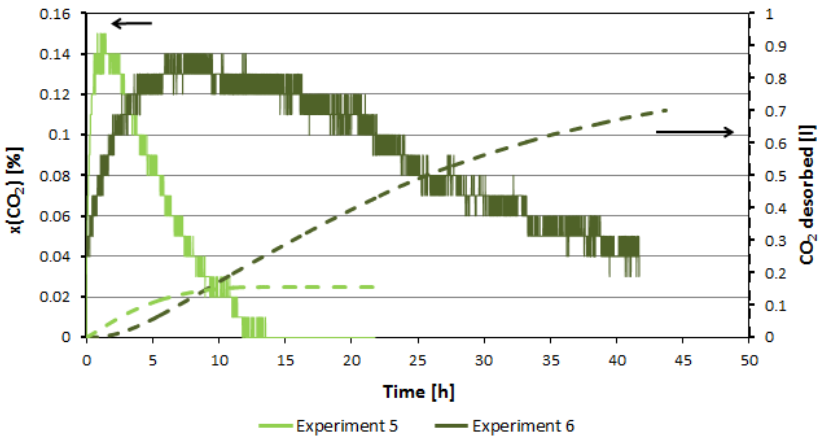

Figure 3-5. Desorption curves of experiments 5 and 6 run with vapor-phase H_2O. One experiment was run with one cartridge in each reactor (5) and one with ten cartridges in each reactor (6). Solid lines show logged vapor

phase CO_2 concentrations (left y-axis). Dashed lines show cumulated desorbed CO_2 calculated from the make-up gas flowrates, CO_2 concentration and time (right y-axis). .

From experiment 6 with 10 cartridges, it is seen that the x(CO_2) maximum has shifted to around t = 8 h from around 10 h for experiments 1 and 2 with 30 cartridges (Figure 3-3). In experiment 5 with only one cartridge in each tube, the maximum concentration is similar to experiment 6, but the rate of increase leading up to the maximum is significantly steeper. The maximum occurs around t = 2 h in this case.

These results seem to support the hypothesis that CO_2 adsorbs on sorbent material in downstream cartridges in the beginning of the regular experiments with filled reactors. In the experiments with fewer cartridges, all of the sorbent is wetted significantly faster (especially in the case of only two cartridge), and no re-adsorption of CO_2 occurs.

This further strengthens the theory that the limiting step in the first parts of the vapor-phase H_2O experiments is the rate at which H_2O is supplied to or absorbed by the sorbent. Also this hypothesis underscores the importance of carefully balancing the reactor geometry to the H_2O supply in a technological implementation.

3.1.3 Development

The humidity swing system has promising features, in that it allows for the supply of energy for the desorption step at ambient conditions, through the use of water as opposed to other systems, needing large amounts of heat at higher temperatures.

These experiments show, that the imagined supply of H_2O in the gas phase at ambient conditions seems dubious as the rate at which the water adsorbs onto the resin is slow, causing desorption cycles to last for days even in small batches.

On the other hand, the bench scale setup used in these experiments was not in any way optimized, and further studies are needed in order to confirm these experiments and especially to find a satisfying explanation for the sluggish H_2O uptake. For example, it is not clear whether the slow rate is related to diffusion issues in the porous structure of the polypropylene backbone, surface reactions on the resin beads themselves, or reactions inside the resin beads. Another explanation could be related to local heat development as the H_2O is adsorbed, increasing the temperature of the sorbent and gas stream to close to the dew point of the gas. This would slow down the uptake of H_2O.

The fact that liquid water increases the initial desorption rate significantly seems to favor the first two explanations (transport or surface reactions) but the fact that the time to desorb 3 liters only decreases by 40 % by changing from the vapor phase to liquid H_2O seems to suggest, that the long-term desorption rate is still slow. An explanation for this behavior might be that the equilibrium CO_2 partial pressure over the resin and also the rate of desorption is dependent on the saturation of the resin, as was seen by Wang et al. [25, 46]. Studying this, however was not possible in the setup in question as it requires detailed knowledge of the

saturation of the resin over time, as well as careful accounting for the H_2O balance of the system.

In addition to this, the material in question has been only superficially studied, and in-depth analyses of the chemistry and kinetics of the adsorption/desorption reactions on the resin itself, and possible rate limitations stemming from gas transport phenomena in the porous support material should be investigated.

Once the kinetics of the system are firmly laid out, and a solution to the potential problem with supplying water has been solved, the next step would be to investigate and decide on strategies for pressurization of the produced CO_2 from a few percent in a carrier gas or a vacuum to atmospheric pressures and beyond.

While desorption under vacuum may not be well suited for this due to the large amounts of H_2O present in the system and adsorbed on the resin, further separation steps with other sorbents, hydrophobic membranes or even cryogenic means might present viable routes, provided materials can be found with the right thermodynamic properties.

Due to the development state of the HS system, it was assumed to introduce too many uncertainties and unknown factors into the further system modeling. For this reason, the temperature vacuum swing technology was chosen instead. This technology is described in the next section.

3.2 Temperature vacuum swing technology

The chosen technology for this study was the temperature vacuum swing (TVS) developed by Climeworks Ltd. [20]. The working principles were described in the theory chapter (2.1.2).

To summarize, the technology relies on tethered amines binding CO_2 primarily through ammonium carbamate formation. The sorbent material is packed in a vacuum chamber, where ambient air is blown through during the adsorption cycle.

Once the sorbent reaches saturation, the chamber is sealed, and a vacuum pump reduces the pressure inside. Once the system reaches the operating pressure, the sorbent is heated to around 80 °C where desorption of CO_2 takes place. At slightly lower temperatures, co-adsorbed H_2O desorbs and is removed by the vacuum pump. The H_2O:CO_2 adsorption stoichiometry is between 2.5:1 and 3:1. In the current implementation, the produced water vapor is vented to the atmosphere. The desorbing H_2O replaces leftover air in the vacuum chamber, so that the CO_2 stream produced by further heating carries only traces of N_2 and O_2. The remaining H_2O is removed through condensation, and the resulting stream is saturated in H_2O at app. 20 °C.

As the desorption cycle is finished, the chamber is cooled to around 40 °C and the pressure is equalized by ambient air. Finally, the chamber ports are opened, and the system is ready for another cycle.

3.2.1 Figures for modeling and confidentiality

The detailed operating conditions, system layout, economics etc. are proprietary information, and cannot be disclosed in this work. In order to model the operation of the plant however, a number of key figures were supplied by Climeworks Ltd. These allowed for a black-box treatment of the system in connection with the overall plant modelled in this work.

Climeworks have finished a pilot plant setup, capable of producing app. 50 tons of CO_2 per year. Their next development step is a plant consisting of 12-14 similar units in parallel operation, with a yearly CO_2 capacity of 1000 tons. This is still a relatively small plant, especially compared to the corresponding fuel synthesis plant. Due to the constraints of confidentiality and the need for good numbers, however, the 1000 ton/year plant was chosen to set the capacity of the entire plant modelled in this work. This means that the dimensions of the SOEC and methanation sub-systems were chosen to fit the production capacity of the air capture plant.

The data received from Climeworks are presented in Table 3-2.

Table 3-2. Operating and economic parameters of Climeworks' air capture plant. The plant has a CO_2 capacity of 1000 tons/y. The heating and cooling duties (AC1 – AC3) are assumed to be exchanged with reservoirs with approach temperatures of 5 K.

Modelling details for 1000 ton of CO2 per year air capture plant				
Mass balance				
	Total	**Adsorption**	**Desorption**	**Cooling**
Cycle time:	4.5 h	2.5 h	1.5 h	0.5 h
	Temperature [°C]	**Pressure [atm]**	**Dew point [°C]**	**Flowrate [kmol/h]**
CO_2 stream:	20	1	20	2.881
	CO_2	**H_2O**	**N_2**	**O_2**
Composition				
[kmol/h]	2.827	0.034	0.015	0.005
[mole %]:	98.1	1.2	0.5	0.2
Energy balance				
	[kWh/ton CO_2]	**[MJ/h]**	**Explanation**	
AC1 (100°C):	1660	743	Desorption cycle heating	
AC2 (20°C):	760	340	Vacuum pump cooling	
AC3 (40°C):	130	58	Chamber and sorbent cooling	
Electricity:	230	103	Vacuum pump, fans, misc.	
Economics				
Capital cost of working plant:			360,000 - 720,000	€
Capital cost of sorbent (lifetime):			125,000 - 250,000	€

As a matter of interest, the production price of CO_2 from the above mentioned plant was calculated, assuming only the capital costs mentioned in the table are needed and that the operating costs can be directly calculated from the energy consumption and the assumed

utility prices of heating (11.9 €/GJ), cooling (0.1 €/GJ) and electricity (18.6 €/GJ) (see 0, section 11.1.5) for further details on the economic assumptions in this work). The resulting production prices with a plant lifetime of 20 years and a discounted return on investment of 4 % after depreciation was 83 – 121 €/ton of CO_2. This price is high but not prohibitively so. Cutting the costs for energy in half reduced the price range to 61 – 99 €/ton, showing how integration of the heating and cooling needs of the operation with available and needed process heat from elsewhere is highly relevant.

3.2.2 Modelling and continuous operation

Solid oxide electrolyzer cells (SOEC) as well as catalytic methanation are continuous processes and consequently, the plant needs to operate in a continuous mode. The air capture technology is a batch process, however, and needs to be run in a way which results in a continuous stream of CO_2 for the rest of the plant.

The standard air capture plant consists of 12-14 parallel batch-operated units. Each unit consists of a vacuum chamber containing the sorbent in addition to balance of plant components around it. Climeworks expect to integrate heating, cooling, electricity and vacuum services between the single units, meaning fewer, larger units running in a continuous fashion will service all the 12-14 batch-operated vacuum chambers. The operation of each chamber is shifted in time compared to the previous; ensuring continuous gas production with a constant pCO_2. This is illustrated conceptually in Figure 3-6. Each unit has a CO_2 capacity of app. 40 kg of CO_2 per cycle, lasting 4.5 h. In total, the plant has a yearly CO_2 production capacity of 1000 tons.[47]

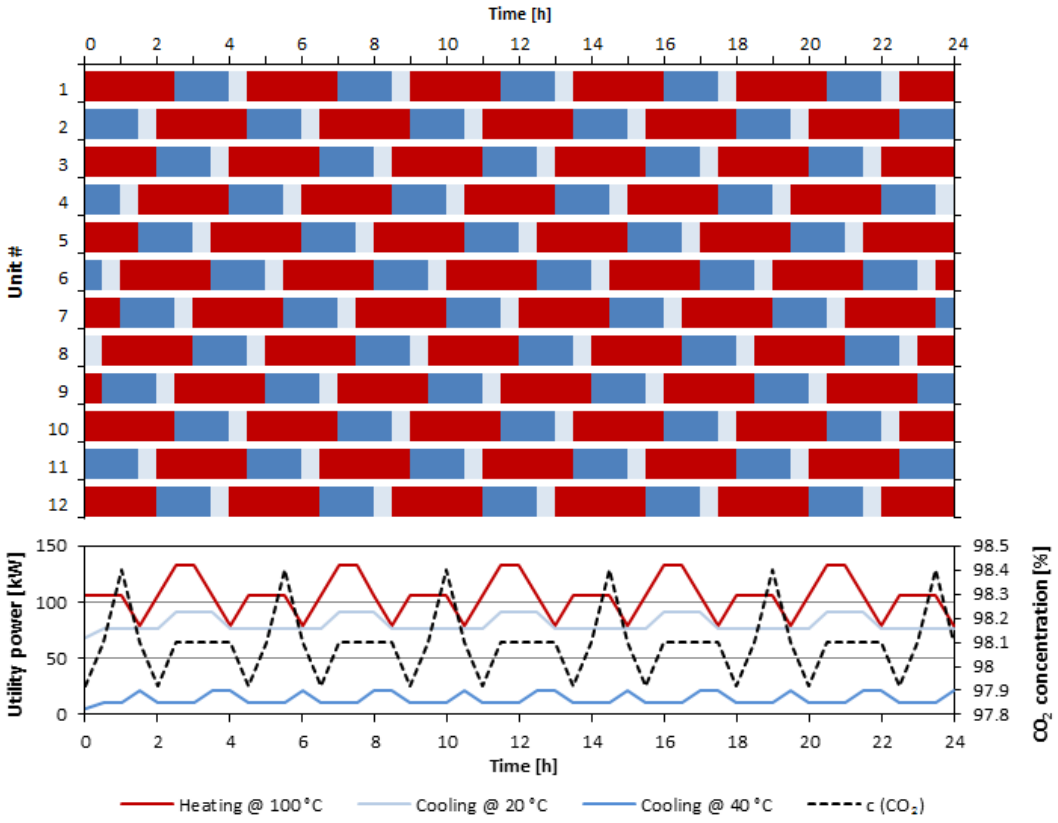

Figure 3-6. Conceptual illustration of the operation, utility consumption and roughly estimated CO_2 output concentration for 12 air capture units shifted in time by 0.5 h each. The cycle is divided into the adsorption phase of 2.5 h (■), The desorption phase of 1.5 h (■) and the cooling phase of 0.5 h (■). A maximum CO_2 concentration during desorption is assumed to be 99% for 1 h with 98% in the 0.25 h before and after.

The air capture plant is thus assumed to produce a continuous CO_2 stream at ambient conditions (T = 293.15 K, P = 1 atm) at a flow rate of 2.88 kmol/h or 70 Nm^3/h. The composition of the stream is 98.1 % : 0.19 % : 0.50 % : 1.2 % (CO_2 : O_2 : N_2 : H_2O) as the stream is saturated in water.

The utility consumptions are divided between heating at 105 °C (743 MJ/h), for heating the sorbent in the desorption part of the cycle (■); cooling at 40 °C (58 MJ/h) in the cooling part of the cycle (■) and cooling of the vacuum pump at 20 °C (340 MJ/h) during the cooling and desorption (■) parts of the cycle. These duties comprise both latent and sensible heat, and the values are determined from current operational experience. A detailed modelling is thus not practical. For this reason, and for the sake of making the process continuous, it is assumed for integration purposes that the heating and cooling duties are supplied by heat reservoirs at constant temperature, with which the rest of the plant may exchange heat.

In addition to the produced CO_2, the sorbent captures large amounts of water as well[22]. This was measured to around 2.5-3 moles of H_2O for each mole of CO_2 depending on the relative

humidity. In the plant model, the water is released as a by-product, but the possibilities of utilizing this water is examined later.

In the plant simulation, the air capture plant is represented simply as an inlet stream of the above mentioned composition and the presented heating and cooling duties are included in the heat integration study in Chapter 8.

Chapter 4 Analysis and cleaning of CO_2 for solid oxide electrolysis

4.1 Abstract

A new method for characterizing the impurity content of CO_2 streams captured from the atmosphere is presented in this paper. The method relies on selective chemisorption of impurities detrimental to the operation of solid oxide electrolyzer cells (SOEC) on a solid material that consists of a porous Ni-YSZ composite very similar to the support material used in fuel electrode supported solid oxide cells. This enables collection of most impurities detrimental to SOEC operation, as the filters are identical, and allows for sub ppm detection of a long list of elements without the deployment of specific sorbents for each potential chemical species. Differences in operating conditions between the sampling filter and SOEC operation are discussed with regards to the detection capabilities of the system.

Two sources of air captured CO_2 were tested in various development stages, namely a carbonate-bicarbonate humidity swing system, and a diamine based temperature-vacuum swing system, confirming the development stage of the diamine based temperature vacuum swing system, and also showing the development of gas phase impurities after 11 months of operation. The levels of all detected impurities were below 25 ppm, and the need for further reduction of the impurity level in the feed gas for SOEC applications is discussed.

4.2 Introduction

Solid oxide electrolyzer cells (SOECs) are known to be sensitive to a range of impurities in the cathode feed gas in concentrations that in some cases are as low as 5 ppb [48]. Therefore, production of synthetic fuels via co-electrolysis of H_2O and CO_2 captured from the atmosphere (CO_2 air capture) or from point sources requires a high level of control of the types and levels of impurities present in the gas. In general, significant amounts of work has been conducted on the effects of impurities in the feed gas streams for solid oxide fuel cells (SOFC), and the

impurity contents of a range of technologically relevant feed gasses such as gasified coal, biogas and hydrogen have been studied [49-51]. For electrolysis applications however, only limited amounts of works have been published and very few studies on electrolysis feed gasses have been conducted to our knowledge [48, 52].

Measuring unknown species in the gas phase by conventional measures such as gas chromatography is challenging due to the extremely low concentrations [52]. Other strategies such as adsorption of the impurities on specific columns followed by analysis require knowledge about the chemical species in order to select the correct sorbents for collection. This knowledge, however, is practically non-existing as the knowledge of which species are detrimental SOEC operation is incomplete.

In this work, we developed a strategy for analysis of such low levels of unknown impurities in CO_2 streams captured from the atmosphere. In this method, crushed SOEC cathode material consisting of a nickel/yttria-stabilized zirconia (Ni-YSZ) cermet, operated at SOEC operating temperatures of 750°C, was used as a sorbent. This technique is already in use at DTU Energy as a gas filtering system [53-55] that protects the cathodes of SOECs from impurities in the feed gasses during cell tests. Following collection of impurities, the filters were analyzed by glow discharge mass spectrometry (GDMS) yielding the elemental composition of the samples.

The assumption behind this strategy is that any chemical species that would poison the cathode of the electrolyzer cell by adsorption, absorption, chemisorption or deposition, would be caught by the same mechanisms in the filter, as the materials and temperature are the same. This is inspired by how the fuel electrode support of Ni-YSZ based solid oxide cells (SOCs) tend to act as a filter for impurities [52, 56]. The operating conditions of the filter differ from that of an SOC under current draw, introducing a difference in operating conditions, however. This is discussed further in this paper.

In this study, the CO_2-streams from two different air capture technologies where analyzed: the carbonate-bicarbonate humidity swing system (HS) [14, 25], and the diamine based temperature-vacuum swing system (TVS) [20, 21].

4.3 Experimental

The setup used for sampling impurities had to be connected directly to the CO_2 air capture setups, because transporting captured CO_2 in bags or bottles introduces the risk of adsorption on or desorption from the gas container. Due to the differences between the available setups of the HS and TVS techniques which are at different development stages, slightly different impurity collection setups were used for the two experiments.

4.3.1 Basic setup for impurity collection

The filters used for collecting impurities consisted of ceramic tubes with an inner diameter of 4 mm, packed loosely with approximately 0.5 g of electrode support material. This consisted of a cermet of 40 vol% Ni (of solids) and ZrO_2 stabilized by 3 mole% Y_2O_3 (Ni-YSZ) with a porosity of

app. 30 %. The particle sizes of both Ni and YSZ were app. 1 µm [57]. The cermet was ground to app. 0.5 mm particles. The filter material was kept in place by plugs of Ni felt of around 0.2 g.

During operation of the filter, the Ni-content needs to be in the reduced, metallic state like in SOCs. In order to lower the equilibrium redox potential of the CO_2 stream to below that of the Ni/NiO equilibrium potential, small amounts of H_2 were added to the gas stream prior to introduction to the filter. The thermodynamically required amounts were calculated using the software package FactSage® [58], based on the expected concentrations of CO_2 in the gas stream. The H_2 was provided as a mixture with N_2 in different concentrations for each experiment. To avoid any impurities from the protection gas, this gas was cleaned before mixing with the collected CO_2. This protection gas was cleaned in a filter equivalent to the one used for sampling impurities before it was mixed with the CO_2 and the combined stream was fed to the sampling filter.

4.3.2 Temperature-vacuum swing setup

Three versions of the TVS system were sampled. Each setup was connected to the collection setup via a T-junction.

A schematic of the setup is shown in Figure 4-1. The protection gas (1) consisted of 5 % H_2 in N_2 (5.0 ± 0.1 %, Messer Gasses, Switzerland). It was regulated to 0.10 l min^{-1} by a flow controller (FC) (2), and led through a Ni-YSZ filter of 5.0 g, operated at 750 °C to remove any impurities in the gas (3). After cleaning, the protection gas was mixed with the CO_2 stream, flowing from the air capture device at 0.4 l min^{-1} in a T-junction (4). After combining the streams, the gas was led through the sampling filter (5), operated at 750 °C before it was vented to the atmosphere (6). The nominal composition of the gas stream through the sampling filter was 1%/19%/80% (H_2/N_2/CO_2) at a rate of 0.5 l min^{-1}.

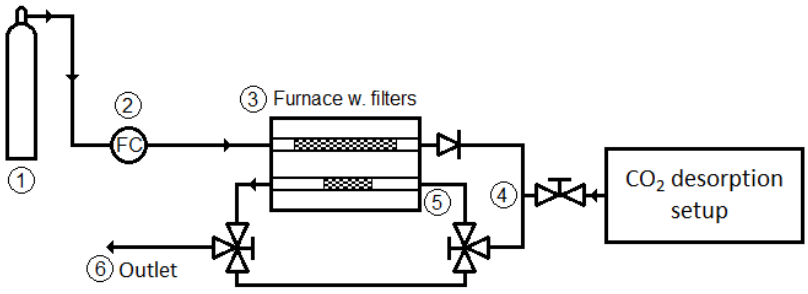

Figure 4-1. Schematic representation of the setup for collection of impurities from the CO_2 enriched stream from the TVS setup. 1) Protection gas. 2) Flow controller (FC). 3) Filter cleaning the protection gas. 4) T-junction for mixing the CO_2 stream and the protection gas. 5) Sampling filter in furnace. 6) Exhaust of sampling stream.

4.3.3 Humidity swing setup

In the humidity swing (HS) setup, a simple bench scale absorption/desorption reactor was used to provide the CO_2 enriched stream. In this setup, a make-up gas was needed to sweep the

reactor to collect the desorbed CO_2. The protection gas mentioned above was used for this purpose as well. It consisted of 1 % H_2 in N_2 (0.99985 ± 0.02 %, Tech Air, USA).

A schematic of the setup is shown in Figure 4-2. The protection gas (1) flow was regulated to 0.30 l min^{-1} by a mass flow controller (MFC) (Aalborg Instruments, GFC 17) (2), and led through a Ni-YSZ filter of app. 5.0 g, operated at 750 °C to remove any impurities in the gas (3). After cleaning, the protection gas was passed through a moisturizing bubbler flask filled with 0.70 l deionized water with 5 drops of 10% HCl (aq) added to minimize the dissolution of CO_2. (4). This saturated the gas stream in water at room temperature, before it was led into the absorption/desorption reactor where corrugated polypropylene sheets containing the active resin beads were stacked (5). At the outlet of the reactor, the stream passed through a water trap (6) and passed an infra-red gas analyzer (IRGA) (Digital Control Systems, CO_2 Concentration Sensor Model 400), logging the CO_2 concentration at 1 s intervals (7). A pump operated at 10 ± 0.5 l min^{-1} (9) recycled most of the stream into the reactor via the moisturizer, in order to increase the CO_2 concentration in the gas stream. A T-junction (9) allowed for 0.30 l min^{-1} (governed by the FC (2)) to be led to the sampling filter (10) operated at 750 °C before the outlet stream was vented to the atmosphere (11). The experiment was run at room temperature (app. 23 °C) and near ambient pressure. The nominal composition of the gas stream through the sampling filter was between 1%/99%/0% and 1%/94%/5% (H_2/N_2/CO_2) at a rate of 0.3 l min^{-1}.

After the test, the total volume of CO_2 which passed through the sampling filter was calculated from the flowrate and the CO_2 concentration profile. For the two HS experiments conducted, the CO_2 volumes were 12.4 and 11.2 liters respectively.

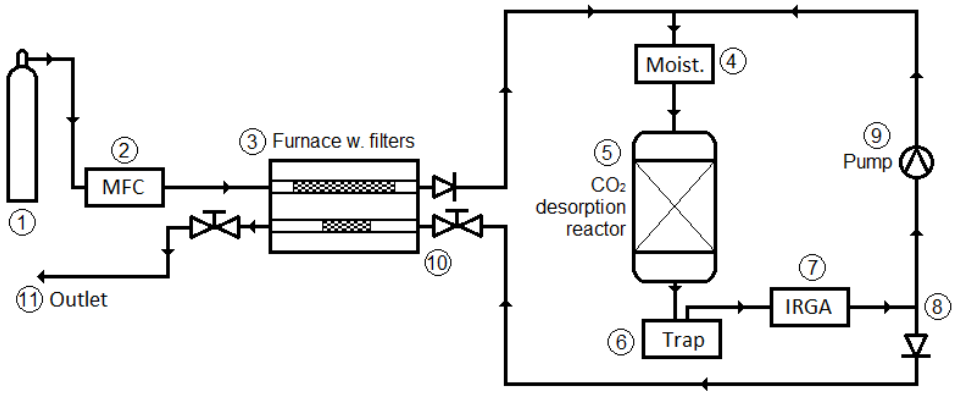

Figure 4-2. Schematic representation of the setup for collection of impurities from the CO_2 enriched stream from the HS setup. 1) Protection gas. 2) Mass flow controller. 3) Filter cleaning the protection gas. 4) Moisturizer. 5) CO_2 absorption/desorption reactor. 6) Water trap. 7) IRGA. 8) T-junction splitting recycle stream from the sampling stream. 9) Pump running the recycle stream. 10) sampling filter in furnace. 11) Exhaust of sampling stream.

4.3.4 Impurity sampling experiments

Four CO_2 sources were analyzed and each source was sampled twice for the sake of reproducibility. Each test contained two samples: the Ni-YSZ filter material and the Ni felt plugs.

For the HS setup, two tests were conducted and termed HS. For the TVS systems, an early version of the lab scale prototype, capable of producing 1 ton of CO_2 per year was sampled twice (TVS-1). A second development step of the prototype was initially sampled only once (TVS-2a) and following ten months of continuous operation it was sampled twice in order to test the impact of long-term operation on the impurity content in the gas stream (TVS-2b). Finally, a pilot plant producing ~55 tons of CO_2 per year was sampled twice (TVS-3). Also, the filters used for cleaning the make-up gas for the two tests on the HS system, and for the TVS-1 and TVS-2a experiments were also sampled. These are named HS* and TVS* respectively.

In addition to the filters saturated with impurities from air capture CO_2, a sample was extracted from a filter material used for cleaning the CO/CO_2 inlet gas for a CO_2 electrolysis cell test similar to the one described by Ebbesen and Mogensen [48]. The cell was a fuel electrode supported, DTU Energy (Risoe) cell with a Ni/YSZ fuel electrode and support and lanthanum-strontium-manganite (LSM)/YSZ oxygen electrode. The inlet gas, from which the impurities were filtered, was a 50%/50% mixture of CO and CO_2 with no H_2 present and was known to be severely contaminated by unknown impurities detrimental to SOEC operation. The cell started to degrade rapidly after only 75 l of CO had passed through the cell, and the test was cancelled. This showed how quickly the Ni-YSZ filter of 15 g was saturated at the high impurity content. This sample is termed SOEC-gas in this work. Table 4-1 summarizes the 12 sets of samples.

Table 4-1. Summary of the performed tests for various CO_2 sources

Test	Setup	CO_2 capacity	Gas composition ($H_2/N_2/CO_2$)	# of Ni-YSZ samples
HS	Bench scale reactor		1%/99%/0% - 1%/94%/5%	2
TVS-1	Early lab scale pre-pilot	1 ton y^{-1}	1%/19%/80%	2
TVS-2a	Final lab scale pre-pilot	1 ton y^{-1}	1%/19%/80%	1
TVS-2b	Final lab scale pre-pilot after 10 months	1 ton y^{-1}	1%/19%/80%	2
TVS-3	Pilot scale prototype	55 tons y^{-1}	1%/19%/80%	2
HS*	Protection gas filter	N/A	5%/95%/0%	1
TVS*	Protection gas filter	N/A	5%/95%/0%	1
SOEC-gas	CO/CO_2 inlet gas for SOEC cell test	N/A	CO/CO2: 50%/50%	1

4.3.5 Filter characterization and elemental analysis

Following each impurity sampling experiment, the samples were removed from the ceramic tubes, and scanning electron microscopy (SEM) micrographs were obtained with the backscatter detector of a Hitachi TM-3000 Tabletop Microscope. This was followed by elemental analysis by glow discharge mass spectrometry (GDMS), performed at Evans Analytical Group SAS, France. The GDMS analyses were conducted for the following elements: B, Na, Mg, Al, Si, P, S, Cl, K, Ti, V, Cr, Mn, Co, Cu, Zn, As, Se, and Br. The analysis yields the elemental content in each sample in ppm by mass with a relative uncertainty of ±20 % for the confidence interval of 99.7% (± 3·σ). From these measurements, the molar content per gram of sample was calculated and the same values for the reference samples were subtracted, yielding the addition or removal of impurities during the test. Adding the Ni-felt and Ni-YSZ samples from each experiment, the filter masses and molar gas flows are used to calculate the molar content of each element in the gas streams in molar ppm. Finally, the two experiments from each CO_2-source were averaged, yielding the values presented in Table 4-3. In the case of the SOEC-gas, the amount of sulfur adsorbed on the Ni-YSZ support layer of the cell, estimated by Ebbesen et al.[48], was included in the calculations. The absolute uncertainties were calculated according to the usual procedures, based on the relative uncertainties of the original measurements and the averaging of the two runs of each experiment.

BET measurements where conducted in a Quantachrome Autosorb-1 Analyzer using N_2 and Kr as adsorption gases.

4.4 Results

The specific surface area (SSA) of a sample of the filter material as analyzed by BET N_2 adsorption is shown in Table 4-2 along with the BET SSA for the Ni-felt measured by Kr-adsorption and a geometric value estimated from SEM images. Also presented is the H_2 adsorption capacity measured by Ebbesen and Mogensen [48] for the Ni-YSZ supporting material of an SOC, which is the same material, used for the filter. The specific metallic surface area (SMSA) was not measured for the Ni-felt but a geometric estimation of the surface area was performed. The individual threads of the felt have a figure-eight like cross-section and the surface was approximated by two cylinders with radii as measured for the Ni-threads in an SEM micrograph.

Table 4-2. BET and CO-adsorption characterization of Ni-YSZ and Ni-felt filter samples.

Sample	BET SSA [$m^2\ g^{-1}$]	H_2 capacity [$\mu mol\ g^{-1}$]	SMSA [$m^2\ g^{-1}$]	Estimated area [$m^2\ g^{-1}$]
Filter Material	0.708	3.32[a]	0.13[a]	-
Ni-felt	0.009	-	-	0.02

[a]: H_2 capacity measured by Ebbesen and Mogensen [48]

For the Ni felt, there is a discrepancy close to a factor of two between the estimated and measured surface areas. As BET is known to be imprecise at areas lower than 0.1 $m^2\ g^{-1}$

however, no precise measure of the area can be given. The geometric estimate of the area (0.02 m^2 g^{-1}) is probably an overestimation, as it does not take into account Ni surfaces blocked by contact with other Ni-threads or the ceramic tube. The estimated area of the Ni-felt constitute 10 % of the Ni-YSZ SMSA, assuming sample sizes of 0.2 g and 0.5 g, whereas the measured Ni-felt area only constitute 4.5 %. Thus both Ni-felt and Ni-YSZ samples are characterized by GDMS.

4.4.1 Characterization by SEM

Great care was taken during the experiment to keep the sampling filters at reducing conditions, as accidental oxidation of the Ni parts of the samples might significantly impact the results of the elemental analysis. In Figure 4-3, a backscatter SEM micrograph of a filter sample (c) is compared to those of as-sintered NiO-YSZ (a), and as-reduced Ni-YSZ (b) reference samples. In the images, the NiO phase of the as-sintered reference sample appears in dark grey compared to the light grey of the YSZ phase, due to the difference in average electron density of the phases, resulting in a low yield of backscattered electrons for the NiO phase. The Ni and YSZ phases have similar average electron densities and, consequently, backscatter coefficients, and thus both appear light grey compared to that of NiO.

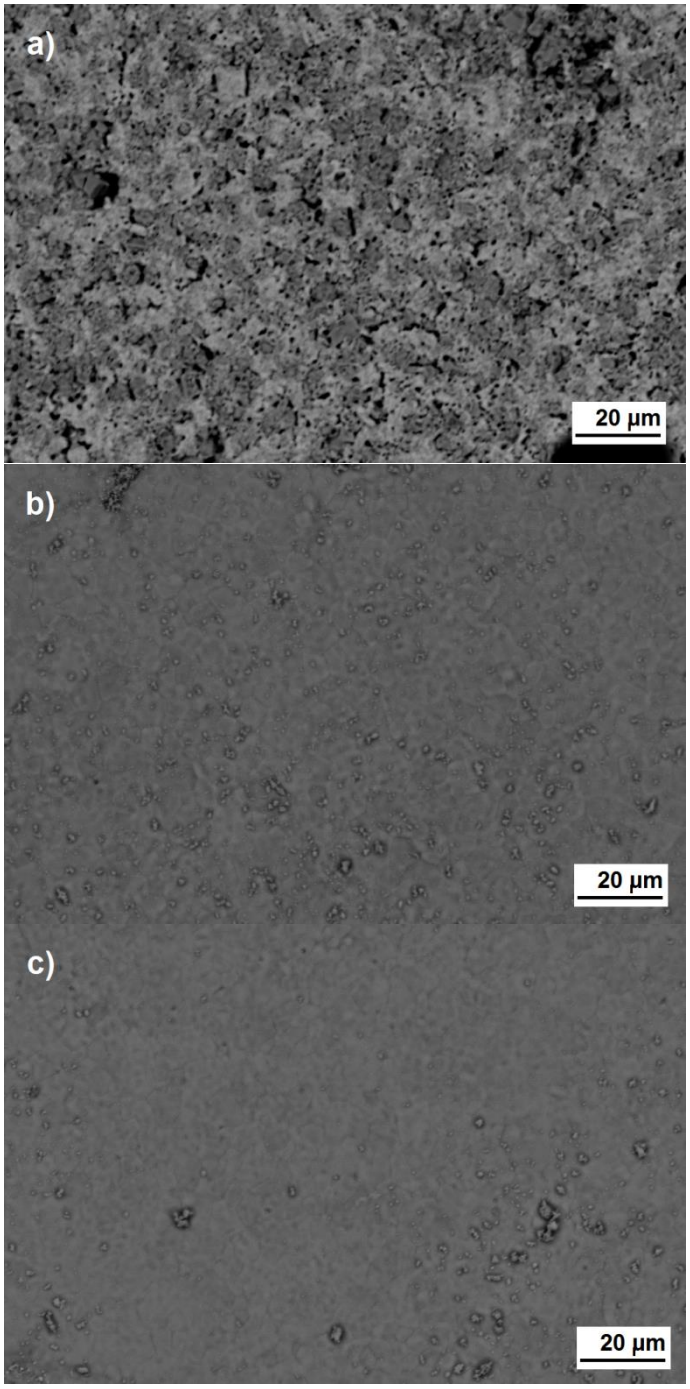

Figure 4-3. SEM images obtained with a backscattered electron detector, providing phase contrast between NiO (dark grey) and YSZ and Ni (both light grey). a) as-sintered NiO/YSZ reference, b) as-reduced Ni-YSZ reference, c) sample from the impurity collection experiments

In the NiO-YSZ sample (a) the NiO is clearly discernible from the YSZ due to the phase contrast, whereas the phases are case completely indiscernible in the Ni-YSZ sample (b). In the filter sample (c) the phases are indiscernible as for the Ni-YSZ reference sample (b), showing the Ni is in the reduced state. This was the case for all samples.

4.4.2 Elemental analysis

The molar concentration of each element in the various gas streams was calculated from the content of each element in ppm by mass of sample, assuming ideal gas behavior. The results are shown as ppm by mole in Table 4-3 along with the absolute uncertainties calculated from relative uncertainties of ±20 % on the original measurements.

In the results, negative values are either artefacts from corrections for the reference samples, and explainable by the uncertainties, or they may represent a clean-up of the filter material by the H_2 and H_2O contents of the gas stream. The latter is thought to be the case especially for B and Na as the values are large, and as oxides of these species have been known to be removable from the fuel electrodes of solid oxide cells [59, 60]. The results for Al have very high uncertainties, resulting from a relatively high Al contents in the Ni-YSZ material, and should be regarded with care. Al is not expected to be mobile under the studied conditions, but as some YSZ materials are known to include small amounts of alumina [61], dust or small grains could be imagined to be removed with the gas flow.

For the HS system, and the TVS-1, TVS-2b and TVS-3 experiments, the results reproduce fairly well at least on and order of magnitude level, between the two individual experiments for each carbon dioxide source. In the TVS-2a experiment, however, there is a larger discrepancy between the levels of most elements of the two individual runs. Comparing the results of those samples with the ones from TVS-1 and TVS-2b, one Ni-felt sample from the TVS-2a experiment was identified as having unusually large values. Especially, the measured impurity contents of this sample were larger than the ones measured for TVS-2b after 10 months of continued operation, where impurities had collected in the system. As the corresponding Ni-YSZ sample was close to the other TVS-2a sample, the second set of TVS-2a samples was discarded due to apparent contamination, and thus, only one experiment was counted for TVS-2a. In this case, the presented uncertainties were calculated from the relative uncertainties on the GDMS measurements on the samples and references.

Table 4-3. Results of the GDMS analysis as ppm (mole fraction) of CO_2 (CO in the case of the SOEC feed gas) seen by the sampling filter. References have been subtracted and the presented values are averaged over the two experiments for each setup, except for TVS-2a. Absolute uncertainties are calculated from relative uncertainties of ±20 % on the original measurements.

	Impurity content in CO_2 stream [ppm molar]					
Element	**HS model reactor**	**TVS-1 prototype**	**TVS-2a prototype[a]**	**TVS-2b prototype**	**TVS-3 pre-pilot**	**SOEC feed gas[b]**
B	-6.92 ± 4.3	-5.63 ± 2.5	-8.02 ± 5.3	5.37 ± 5.8	20.68 ± 6.7	1.04 ± 0.5
Na	-13.59 ± 2.5	-2.43 ± 2.1	-10.13 ± 3.3	-8.50 ± 3.4	-4.36 ± 3.6	-4.26 ± 0.8
Mg	5.61 ± 2.9	1.39 ± 2.0	-0.02 ± 3.2	6.56 ± 3.4	5.12 ± 3.4	-0.89 ± 0.2
Al	-8.31 ± 11.0	-5.60 ± 10.5	0.51 ± 12.7	-8.41 ± 7.9	-1.38 ± 8.2	-72.55 ± 59.2
Si	4.07 ± 2.2	23.39 ± 2.6	1.55 ± 2.8	11.64 ± 3.2	9.83 ± 3.1	-2.90 ± 1.2
P	-0.09 ± 0.0	0.01 ± 0.0	-0.05 ± 0.0	0.05 ± 0.0	0.00 ± 0.0	0.06 ± 0.1
S	1.22 ± 0.1	0.14 ± 0.0	-0.15 ± 0.0	0.37 ± 0.1	0.02 ± 0.0	19.77 ± 2.0
Cl	3.41 ± 0.3	4.79 ± 0.5	3.61 ± 0.5	8.44 ± 0.8	12.55 ± 1.0	-0.10 ± 0.1
K	-0.11 ± 0.0	-0.10 ± 0.0	-0.11 ± 0.0	-0.09 ± 0.0	-0.01 ± 0.0	-0.39 ± 0.1
Ti	-0.05 ± 0.0	-0.01 ± 0.0	0.02 ± 0.0	0.02 ± 0.0	0.06 ± 0.0	0.10 ± 0.2
V	0.03 ± 0.0	0.03 ± 0.0	0.05 ± 0.0	0.13 ± 0.0	0.15 ± 0.0	0.04 ± 0.1
Cr	0.00 ± 0.1	0.05 ± 0.0	0.13 ± 0.1	0.31 ± 0.1	0.26 ± 0.1	0.04 ± 0.1
Mn	0.39 ± 0.8	0.41 ± 0.6	0.58 ± 1.0	1.70 ± 1.0	2.08 ± 1.1	0.04 ± 0.0
Co	1.56 ± 2.5	2.53 ± 2.0	3.76 ± 3.3	6.28 ± 3.3	6.32 ± 3.3	0.00 ± 0.0
Cu	-3.89 ± 1.0	-1.32 ± 0.8	-2.64 ± 1.3	2.48 ± 1.5	-0.02 ± 1.4	-0.08 ± 0.0
Zn	-1.91 ± 0.3	-0.22 ± 0.3	-1.29 ± 0.4	-0.65 ± 0.4	-1.47 ± 0.4	0.76 ± 0.1
As	-0.04 ± 0.1	0.09 ± 0.1	-0.07 ± 0.1	0.22 ± 0.1	0.25 ± 0.1	0.00 ± 0.0
Se	-0.01 ± 0.0	0.00 ± 0.0	0.00 ± 0.0	0.02 ± 0.0	0.02 ± 0.0	0.00 ± 0.0
Br	0.00 ± 0.0	0.00 ± 0.0	0.00 ± 0.0	0.00 ± 0.0	0.00 ± 0.0	0.00 ± 0.0

[a]: Only one set of filter samples (Ni-felt and Ni-YSZ) is included. The uncertainties in this case reflect the uncertainties of this set of GDMS measurements.

[b]: Only one Ni/YSZ filter sample is included. No Ni felt. The sulphur amount includes what was adsorbed on the Ni/YSZ electrode support according to [1].

4.5 Discussion

4.5.1 Sulfur chemisorption and surface saturation

Sulfur in the form of H_2S adsorbs dissociatively on Ni at elevated temperatures via the following reaction:

$$H_2S_{(g)} \leftrightarrows S_{(ads)} + H_{2(g/ads)} \qquad \text{Eq. 4-1}$$

Thus, the presence of small amounts of H_2, shifts the adsorption equilibrium (Eq. 4-1) towards H_2S (g), and it is well known that H_2 adsorbs competitively on Ni, and thus can be used to regenerate deactivated SOCs and Ni-based catalysts [62]. This means that the presence of H_2, even in the small amounts added to keep the Ni phase reduced in this study, may cause an underestimation of the amount of impurities in the CO_2 stream. Also, the adsorption is known to depend on temperature, so that more sulfur adsorbs at lower temperatures. This is the reason for the chosen operating temperature of the filter, as we envision co-electrolysis of CO_2 and H_2O to take place at 850 °C, leaving a large margin to the operating temperature of the filter at 750 °C.

Alstrup et al. proposed a Tempkin-like isotherm describing the chemisorption and surface coverage of H_2S on Ni/$MgAl_2O_4$ catalysts [63]. With values stated by Hansen [64], the expression is:

$$\theta = 1.45 - 9.53 \cdot 10^{-5} \cdot T + 4.17 \cdot 10^{-5} \cdot T \cdot \ln\left(\frac{p(H_2S_{(g)})}{p(H_{2(g)})}\right) \qquad \text{Eq. 4-2}$$

This is valid for H_2S/H_2 ratios between 10^{-6} and 10^{-3}. At significantly lower values, no reaction will occur while, at significantly higher values, bulk sulfides are formed as well. With the H_2 content in all experiments set to 1% and assuming the sulfur is present as H_2S only, the CO_2 streams tested in this work fall within this range except for the SOEC-gas.

The theoretical maximum saturations of exposed Ni surfaces, θ_{max} of the Ni-YSZ filters were calculated from Eq. 4-2 with the measured sulfur concentrations for each experiment. The results are shown in Table 4-4 along with the actual coverages calculated from the measured SMSA of the filter material and GDMS results, using the 3.32 µmoles of Ni surface atoms per g measured by Ebbesen et al. [48]and a S/Ni adsorption stoichiometry of 1/2. In the case of the SOEC inlet gas stream, no H_2 was present, in which case, the S is known to form bulk sulfides [64], and Eq. 2 is not valid.

Table 4-4. Theoretical maximum saturation (θ_{max}) of Ni surfaces exposed to the testing conditions, calculated from equation 2 compared with the actual calculated degree of saturation (θ_{max}) of the filter material Ni surfaces. TVS-2a and TVS-3 could not be calculated due to negative H_2S concentrations. θ_{max} could not be calculated for the SOEC gas as bulk sulfides are formed, and for HS* and TVS* as the total volumes of protection gas were not measured.

Experiment		θ_{max}	$\theta_{measured}$
HS	1. run	0.71	0.81
	2. run	0.72	0.71
TVS-1	1. run	0.87	0.19
	2. run	0.85	0.17
TVS-2a	1. run	N/A	N/A
TVS-2b	1. run	0.83	0.04
	2. run	0.93	0.62
TVS-3	1. run	N/A	N/A
	2. run	0.83	0.07
SOEC feed gas		N/A	2.44
HS* protection gas		N/A	0.16
TVS* protection gas		N/A	0.02

The results from the table clearly show that the filter Ni surfaces of the TVS experiments are far from saturation. S is known to adsorb rapidly and tightly on Ni surfaces, often leading to non-uniform coverages through a reactor bed or fuel cell with increased coverage at the inlet [65]. Thus, when the filters are far from saturation, as in the TVS experiments, it is safe to assumed, that all sulfur is collected in the filters during the these experiments.

In the case of the HS experiments, the filters are saturated, and possibly oversaturated in the case of the 1st run. Thus, the above assumption that all S in the gas stream is removed may not hold. Oversaturation could be explained by reorganization of the Ni surface at high coverage [65], or by uncertainties in the measurements as the H_2S/H_2 ratio is in the low end of the surface adsorption range, and several orders of magnitude from the range of bulk sulfide formation. This means that the sulfur content in the HS gas is likely underestimated by the method. This, however, may not apply to other impurities present in the gas stream. It is important to point out that the low θ_{max} stems from the high dilution of the CO_2 in the protection gas in the HS experiment. Thus, oversaturation would not be a problem at higher CO_2 (and by implication, higher S) content or simply by using larger filters.

The HS* and TVS* samples were used to filter the protection gasses before the addition of the CO_2 streams. The small $\theta_{measured}$ for these samples indicate that very little sulfur was present in the protection gasses used. Consequently, it is a good assumption that all impurities in these gasses have been collected by the first filter before the CO_2 streams were added, and thus have not contributed to the measurements of the HS and TVS experiments.

In the case of the SOEC feed gas experiment, the measured oversaturation of the filter material is in accordance with the expected bulk sulfide formation. At the point of the

observed degradation of the SOEC, the sulfur uptake of the filter must have decreased sufficiently to allow unreacted sulfurous compounds to reach the cell and adsorb on the Ni surfaces in the absence of H_2. This suggests that the measured gas stream sulfur content is an underestimation in this case and only a fraction of the sulfur in the gas stream was collected in the filter.

Hansen correlated the calculated sulfur coverage for a range of H_2S concentrations in the feed gas with the measured performance degradation of a series of SOFC tests [64]. This showed that the sulfur poisoning of SOCs is dependent on the equilibrium coverage which depends on the H_2S/H_2 ratio of the feed as well as temperature, and that for low values of the ratio, only parts of the Ni surface will be covered, even over long term exposure. This was also observed by Ebbesen et al. [66], subjecting the fuel electrode of an SOEC to atmospheres of varying H_2S/H_2 ratios between $3 \cdot 10^{-4}$ and $2 \cdot 10^{-5}$, corresponding to θ_{max} of 98 % to 86 %. Only minor decreases in cell voltage were observed in the entire range and especially for coverages in the low end of that range. Furthermore, the activity for CH_4 reforming, also taking place on the Ni catalyst was only slightly affected in the lower end of the range whereas it was almost completely suppressed for coverages approaching 100%. This shows that different types of sites must exist on the Ni surface: some active for reforming, and some other for reduction of steam. Also, as S poisoning is an equilibrium phenomenon, the performance loss from sulfur impurities in low concentrations may be balanced by H_2 in the feed gas. Thus, when little or no hydrogen is present, as in the case for CO_2-electrolysis [48], sulfur collects on the filter or fuel electrode throughout the test, ultimately forming bulk Ni-sulfides. On the other hand, the presence of H_2 in the gas may limit the degradation from adsorbed S and prevent the irreversible formation of Ni sulfides.

4.5.2 Impurity levels

The elemental analysis shows that a broad selection of trace elements is present in the CO_2 stream from both the HS and TVS systems.

In general, the effects of a large number of compounds on the stability and operation of SOFCs have been studied extensively whereas only few reviews have been published [67, 68]. On the other hand, significantly less information is available on the effects of contaminants on SOEC operation [67]. At the same time, there is evidence, that operation of SOCs in electrolysis mode is more vulnerable towards impurities than in fuel cell mode [52]. This is assumed to be caused by the opposite directions of the H_2O gradients in the fuel electrode. Many glass-forming oxides react with H_2O at high temperatures, forming volatile species at high $p(H_2O)$ outside the cell, but tend to deposit as $p(H_2O)$ drops closer to the triple phase boundary (TPB) causing the volatile species to deposit, typically as oxides [69]. In SOFC mode, on the other hand, H_2O is produced at the TPB and is capable of removing impurities from the cell during operation.

Out of the detected impurities, the following are known to be detrimental to the operation of SOCs in either fuel cell mode or electrolysis mode.

S [70], Cl [71] usually from H_2S or HCl in the electrolysis gasses and also Zn vapor [72] and Se [73], are known to chemisorb reversibly on the electrode surfaces, primarily the Ni phase. The adsorbed species react with the Ni surface atoms to form monolayers blocking the adsorption sites and catalytically active TPB sites and lowers the activity of the electrode, depending on the presence of H_2 as described above. Such degradation modes take place even for very low concentrations of impurities, most commonly known for S as discussed above. We expect Zn to be present mainly as ZnO in these systems, and even though the vapor pressure of Zn over ZnO is relatively high at elevated temperatures [72], Zn is highly soluble in Ni and is thus not expected to be problematic in low concentrations [72].

Ca, Na, Mg and other alkali and alkaline earth metals along with Al, V, Mn and Si have been observed in glassy phases formed at the TPB, metal-ceramic interfaces and grain boundaries of the electrode cermet structure [61, 69]. The glassy phases impede charge transfer reactions and block access to the TPB sites from the gas phase, which is known to seriously impede the operation of SOCs [74].

Compounds of P, As [72] and B [59] are known to react aggressively with exposed ZrO_2 (in the case of P) and Ni (P, AS and B) parts of the electrode of SOFCs, disrupting electrical conductivity and mechanical integrity of the cells. Especially P forms phosphates or pyrophosphates such as $Ni_3(PO_4)_2$ and ZrP_2O_7 [75], which damages the electrode irreversibly, even in small concentrations.

Finally, carbon from hydrocarbons, CO and CO_2 in the electrolysis gasses may deposit given the right thermodynamic conditions [31], disrupting gas flows in the porous phase or in case of severe deposition, damage the mechanical integrity of the electrode [76].

All of the above mentioned elements are found in one or more of the analyzed gasses, mostly in low quantities, underlining the relevance of analyzes such as the one presented in this work.

4.5.3 Impurities from the various CO_2 sources.

The TVS system was analyzed in three different technological development stages. TVS-1 and TVS-2 are two versions of the same setup where changes were made in order to limit contamination from auxiliary materials contained in the TVS-2 setup compared to TVS-1. Comparing the values for TVS-1 and TVS-2a in Table 4-3 show that these modifications have had some impact on the measured trace elements as well. This is especially the case for Si, which was assumed to be present in silicone based rubber seals and oils [24] and definitely in the silane tethered amines of the sorbent materials themselves [20, 21], but also the amounts of Mg, S and P, although the latter two are close to the detection limit of the technique. On the other hand, a slight increase in the Al-content is observed as opposed to the apparent removal in all other experiments, which might arise from a different selection of machine parts in the upgraded system.

Comparing the TVS-2a and TVS-2b figures in Table 4-3, there is an increase in the content of most elements: most importantly B, Mg, Si and Cl, and secondarily P, S, Cr, Mn, Co and Cu.

These species could stem from captured pollutants accumulating in the system over the intervening 10 months of operation or from wear and tear of the system (most probable in the case of Mn, Co, Cu and Cr). Interestingly, Al has dropped again, which suggests this may have been introduced by the changes from the TVS-1 to TVS-2 versions, and subsequently removed from the pre-pilot setup over time during operation. Again, it should be pointed out, however, that conclusions based on the alumina measurements are dubious due to the large uncertainties on the measurements.

Finally, comparing the TVS-3 pre-pilot and TVS-2a prototype, highly similar levels of impurities are observed. The pre-pilot has not seen the same optimizations as for TVS-1 to TVS-2a, which means some of these levels could possibly be lowered. The comparison of TVS-2a and TVS-2b suggests, however, that parts of this improvement could deteriorate over time during system operation. This should be investigated further, in order to attribute the increase in impurities over time to accumulating impurities or to wear and tear, as this would indicate the best way of retaining the lower level of the TVS-2 system.

In the case of S, the development effort on the TVS system have clearly succeeded in bringing down the S content in the CO_2 streams by a factor of ten to around 0.02 ppm. This is below the threshold for sulfur poisoning of Ni/YSZ SOFC fuel electrodes at 750 °C of 0.05 ppm found by Matsuzaki and Yasuda [62]. This is an important result as S is one of the most detrimental impurities present in these gasses, along with P, which is also absent from the TVS-3 gas. If gasses such as these are intended to be used in low-temperature applications in order to increase the electrical efficiency of the SOEC, especially in reversible SOC applications for energy storage, as proposed by various authors [77], the poisoning threshold can be expected to be even lower however [65]. On the other hand, CO_2 captured from the atmosphere is usually imagined for synthetic fuel production. In such applications, high current density operation at high temperatures is usually preferred [29], and the enhanced S poisoning at low temperatures is not expected to be a problem.

The HS system is difficult to compare to the TVS systems, as it is in a very early development stage, and also because the sampling filters where saturated at least in S. Furthermore, it should be mentioned, that the sorbent material used for the HS experiments have been used for various adsorption/desorption experiments at ambient conditions i.e. have been exposed to air for an extended period of time. Thus they can be expected to be contaminated with sulfurous compounds from the air at the beginning of the experiment. The gas from the HS system seems to have fewer impurities present while those present are found in amounts comparable to those of the TVS-1 system. A marked difference is the lower levels of Si which is explained by the silane tethered amines in the TVS sorbent materials [20, 21]. This might hint at a difference in adsorption characteristics of the two systems, resulting in different impurities being captured from the atmosphere, though the specific mechanism for this is hard to speculate about as the chemical species carrying the impurity elements are not known. More likely, the explanation could be that the HS setup is simpler and thus incorporates less components and impurity sources.

The analyzed SOEC feed gas was used in a cell test at DTU Energy similar to those published elsewhere [48]. The CO gas used in the specific test was known to be unusually contaminated and the test was terminated as the cells started degrading rapidly. In addition to a small amount of B, the gas is almost exclusively contaminated with sulfur, supporting the suspicion that this is what has poisoned other DTU Energy cells as well [48].

4.5.4 Carbon in the CO_2

Extensive carbon formation was observed on the Ni-felt samples of some experiments in this study, seen as black discoloration of the felt plugs. GDMS cannot detect carbon however, and thus no quantification of carbon formation was obtained. Carbon deposition is the well-known result of the Boudouard and other coking reactions:

$$2CO \rightleftarrows CO_2 + C$$

In the presence of high steam concentrations the water gas shift equilibrium dominates over the coking reactions, and as such coking only takes place at high C content in the C-O-H composition, which is usually seen for high hydrocarbon, CO or CO_2 concentration or in the absence of steam [30, 31]. Under real co-electrolysis conditions tailored for downstream production of synthetic fuels, large amounts of H_2O are present. Thus, even though significant amounts of carbonaceous species are present in the feed gas, these are not expected to lead to carbon deposition, except for operation at high current densities/reactant utilization [76].

At the elevated temperatures of SOC or filter operation, hydrocarbons are reformed on the Ni catalyst of the fuel electrode or filter, and form syngas. This means, that any S, P, metals and other substituents present in the gas are released. In case of S: in the form of H_2S [78]. This mechanism is expected to be one of the impurity sources in this study: At the operating temperatures of the filter, any hydrocarbon is expected to decompose, and any resulting impurities are expected to adsorb on the filter. It is assumed, that those contaminants are caught by the filter and accounted for in the analysis, even though the hydrocarbon content was not analyzed in this study, as it is not expected to pose problems in real SOEC systems for synfuel production.

4.5.5 Potential problems with the method stemming from differences between the filter and SOEC operating conditions

Considering the assumption that any impurities harming SOECs during operation will adsorb in the filter, the different conditions should be taken into account. There are three main differences between the operating conditions of the filter and the fuel electrode:

1. No current is drawn in the filter, as opposed to the SOEC during operation. This means that the TPB sites are not electrochemically active in the filter. This could influence the formation of impurity phases in the TPB and possibly Ni-YSZ interfaces [68, 79].
2. Many impurities are known to mobilize under high H_2O partial pressures and to follow the steam gradients towards the TPB. When SOCs are operated in fuel cell mode, this can help remove intrinsic impurities from the electrodes, as the steam gradients transport

impurities from the TPB into the bulk gas phase. Under SOEC conditions, the steam gradients point directly at the vulnerable TPB sites. No steam gradients are present in the filter, and with only a few percent H_2O from ambient saturation of the feed gasses, the conditions in the entire filter are much closer to those of the local H_2O starved atmospheres close to the TPB sites of SOECs operated at high absolute current density [76]. We expect this to cause impurities in the gas stream to immobilize on the surfaces and interfaces of the entire filter as explained for Si above.

The above differences allude to a potential problem with this method i.e. that even though the materials are the same, the different atmospheric compositions and operating parameters changes the thermodynamic conditions between the performed collection experiments and operation of real SOECs. This could result in some elements not being detected in the filters under the conditions used in the analysis, while they would still react in the SOEC under operating conditions. On the other hand, the filters used in this work are used routinely to clean the feed gasses for the fuel electrodes of SOECs tested by our group, enabling virtually degradation free long-term operation [53]. This suggest that most impurities present in the gas streams are in fact removed by the filters, although all impurities present in the CO_2 streams analyzed in this work are not necessarily present in the feed gasses used in our laboratories, as seen from the characterization of the SOEC-gas. In the case of the low p(H_2O) of the CO_2 streams analyzed compared to SOEC operation, the difference is expected to ensure that more impurities are collected in the filter compared to SOEC operation. This might cause an overestimation of which harmful impurities and their amounts are present in the CO_2 stream as some may be carried through the SOEC electrode if operated at low conversion.

4.5.6 Feeding captured CO_2 into electrolyzer cells.

The results presented above were obtained from non-optimized test bench, pre-pilot and pilot assemblies. This means that little specific effort has been directed towards minimizing the amount of impurities found in the resulting gas streams, especially for the HS setup. The development from TVS-1 to TVS-2 clearly shows that such development is possible and may contribute to lowering the impurity content in the CO_2 stream significantly. This study shows that feeding the CO_2 from such systems into electrolyzers may still require further treatment of the gasses in order to achieve very low levels of impurities needed for extended electrolysis operation. This has been shown to be achievable with relatively cheap and straight forward methods such as the Ni-YSZ filters also used in this work.

Equation 3 is used for calculating the mass of filter material needed for cleaning a specified gas volume (*V*) with a given S content, *c(S)*.

$$m_{filter}^{needed} = \frac{c(S) \cdot {V_{molar}}^{-1} \cdot V \cdot 10^3 l\, m^{-3}}{n_{SS} \cdot \theta_{max} \cdot 0.5} \qquad \text{Eq. 4-3}$$

Here $c(S)$ is the concentration of S in the gas stream [ppm molar], V_{molar} is the molar volume [Nl mol^{-1}] (24.465 Nl mol^{-1}), V is the volume of gas fed through the filter in normal cubic meters

at 20 °C [m^3], n_{SS} is the amount of Ni surface sites per gram of filter material [µmol g^{-1}], θ_{max} is the maximum saturation of the surface adsorption sites at the given temperature and p(H_2) according to equation 2 , and 0.5 refers to the S/Ni adsorption stoichiometry.

With the values for n_{ss} and *c(S)* from Table 2 and Table 3 respectively, and assuming 1 % H_2 is added to the CO_2, ~31 g of filter material is needed for cleaning 1 Nm^3 of CO_2 from the HS system. A small SOEC plant of app. 700 kW corresponds to app. 1000 ton of CO_2 per year, which would require ~17 ton of Ni-YSZ. For the TVS-1 system this number is reduced to ~2.2 ton per 1000 tons of CO_2 and only 0.29 ton for the TVS-3 system. These numbers demonstrates the importance of working to minimize the amount of impurities in the CO_2 stream, as has been successfully achieved for the TVS-system. In addition to that effort, we envision several strategies for bringing down the requirements for filter material:

1. The current filter material is designed as electrode support in SOCs. This means that the Ni content and particle sizes are determined by balancing the need for percolating electrical paths with the structural stability of the YSZ backbone. In the active fuel electrode layers of state of the art SOCs from DTU Energy, the SMSA is on the order of 0.25 m^2 g^{-1} [80], corresponding to a doubled S capacity compared to the filter material. Percolation is not needed in the case of filters and so, smaller more dispersed Ni-particles with significantly larger surface areas could be used, in order to increase the capacity even further.
2. Cheaper filters should be employed to bring down the impurity levels as far as possible upstream of the Ni-YSZ filter, for cheaper removal of some impurities at higher concentrations. This could be done with general purpose filters such as activated carbon [51], or by specifically targeting the most abundant impurities coming from the specific CO_2 source. This is usually assumed to be highly relevant for biogas which has large contents of S and P containing compounds for example. This, however, would require further studies of the chemical composition of the specific CO_2 stream compared to the elemental analysis developed in this work.
3. Regeneration strategies for the Ni-YSZ filters should be investigated and developed. As illustrated by equation 2, it is known that sulfur and other impurities may be removed from Ni catalysts at high temperatures under a flow of H_2, for example. This and other strategies are currently under further investigation.

4.6 Conclusion

In this paper, we presented a new method for collecting and analyzing impurities in CO_2 streams, combining adsorption on well-known Ni-YSZ filter materials developed as supporting layers in SOCs with elemental analysis by glow discharge mass spectrometry (GDMS). Two different technologies for capture of CO_2 from the atmosphere were analyzed in various development stages and the efforts to minimize the impurity content of the temperature vacuum swing (TVS) system were confirmed.

The method had a sub-ppm detection limit and validation of the method showed that it is a good assumption that all impurities prone to adsorb on the filters are collected. Some

impurities which are detrimental to SOEC operation may not adsorb on the filters, but the application of the filters in cell tests showed that with the given gas composition, most or all detrimental impurities were indeed collected by the filters.

The method for characterization of impurities pointed out the important realization that CO_2 sources for solid oxide electrolysis applications in the future energy system needs to be carefully considered in order to handle the inherent vulnerability of SOECs to impurities in the gas stream.

In the case of the tested CO_2 sources, the impurity content was low in all cases. Further development to limit the concentrations of some impurities may still be needed, and filtering may prove to be the cheaper, more practical way of solving this problem. Further development is needed for the filters in order to raise the capacity and possibly develop cheap, efficient regeneration strategies.

Part IV – System design and modelling

Chapter 5 Development of the syngas plant model

In this chapter the core model in the plant is developed. With the values of operating parameters stated below, this is referred to as the *base case syngas plant model*, *the syngas plant model* or simply, the *base case* (BC).

The model used in this work was developed alongside the development of the process itself. The hierarchical decomposition strategy for process synthesis as formalized by Douglas[81] and presented by Biegler et al. [82] was followed, ensuring the design decisions were made in the right order. The main points in this process are mentioned in the following.

The inputs for the process are CO_2 and H_2O and the outputs are the synthesis gas product and the co-products H_2O and O_2. This is sketched in the input/output diagram in Figure 5-1 a). All input streams are assumed to enter the plant at ambient conditions (P = 1 atm and T = 20 °C). All output streams are kept at the operating pressure (P = 50 atm) and cooled to 20 °C in case of the O_2-stream. The syngas stream is not cooled before it leaves the plant.

The feed streams of CO_2 and H_2O need pre-treatment such as pressurization, pre-heating and purification before they are led to the electrolyzer stack where the chemical and electrochemical conversions take place. The effluent stream from the electrolyzer contains unreacted CO_2 and H_2O in addition to H_2, CO and CH_4, and the H_2O needs to be recovered in a separation step before the syngas led to the downstream fuel synthesis plant.

A recycle stream is included to keep the feed stream to the electrolyzer reducing by adding a small amount of the SOEC effluent stream, and another recycle takes the unreacted H_2O from the separation step back to the SOEC. This is shown schematically in the functions diagram in Figure 5-1 b).

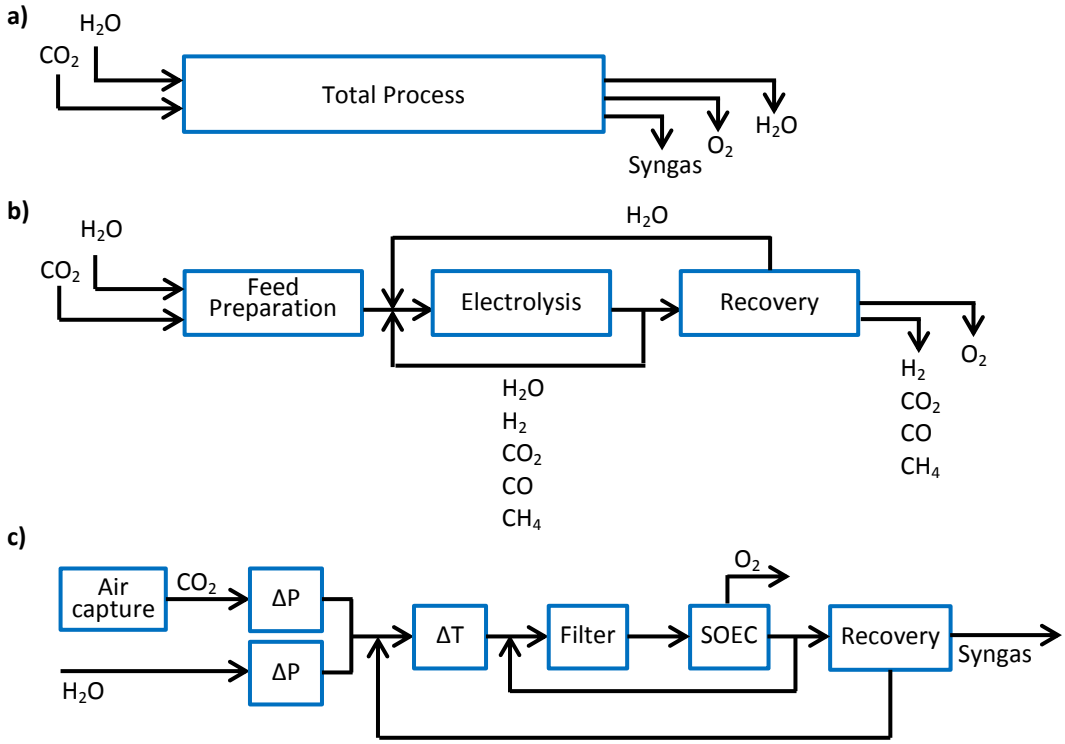

Figure 5-1. Conceptual stages of the syngas plant flow sheet synthesis process. a) Input/output diagram showing the input streams and output streams of the system. b) Functions diagram specifying the main steps conceptually. c) Detailed functions diagram showing the individual function needed in the plant.

A more detailed version of the functions diagram is shown in Figure 5-1 c), where the different functions have been specified. Turning the detailed functions diagram into a detailed process flow diagram (PFD) is done, simply by substituting each functional block in the functions diagram with the appropriate unit operation. This is treated in detail later in this chapter.

5.1 Plant modelling software

In this work, the software suite PRO/II [83] is used to model and simulate the plant. PRO/II is a process simulation program enabling process integration and operational analysis. It is based on a comprehensive chemical component library and thermodynamic property prediction methods. The software incorporates a range of standard unit operations of the petrochemical, chemical and solid processing industries. The program allows for simulating steady state chemical processes based on thermodynamic analysis, and conduction of mass and energy balances of such processes. In this work, PRO/II was used for building the model of the plant as it was designed. All unit operations in the process are supplied with operating conditions and constraints and are connected by a range of streams. The utility of the program then is to set up the mathematical equations and to perform the mass balance of all unit operations and streams, calculate the properties of the individual streams and calculate the energy balance.

PRO/II uses various methods for estimating the physical properties of the mixed streams based on their compositions and conditions. Many such methods exist, developed for different applications and areas of utilization. I this work, the Peng-Robinson equation of state

model[84] for thermodynamic property estimation is chosen, as this is regularly used for vapor-liquid equilibrium calculations including polar compounds in petrochemical and gas processing industries. The choice is based on Peters et al.[85]

Alongside PRO/II, FactSage 6.2[58], which is an integrated database computing software package based on extensive thermodynamic libraries, is used in this work to compute ternary composition diagrams; for ad-hoc calculations; and to validate certain results obtained in PRO/II.

There has been no reason to doubt the results of either program. However, since they are used to supplement each other in this work, and since thermodynamic calculations can be highly sensitive to minor differences in basic thermodynamic parameters, the two programs were compared. This was done by simulating the water-gas shift and methanation reactions (See the section 2.3) in both programs.

In PRO/II the reactions were run in a Gibbs reactor unit operation, minimizing the Gibbs free energy of the system and in FactSage®, the equilibrium module was used, which works in the same way. This was done for varying temperatures (T ∈ {600 °C, 750 °C, 850 °C} and P ∈ {1 atm, 10 atm, 50 atm, 100 atm}) for a given inlet composition. The resulting mole fractions *x(i)* are shown for all five components (*i* = H_2O, H_2, CO_2, CO, CH_4) in Figure 5-2 along with the difference ($x(i)^{PRO/II}$ - $x(i)^{FactSage}$) in percentage points (pp).

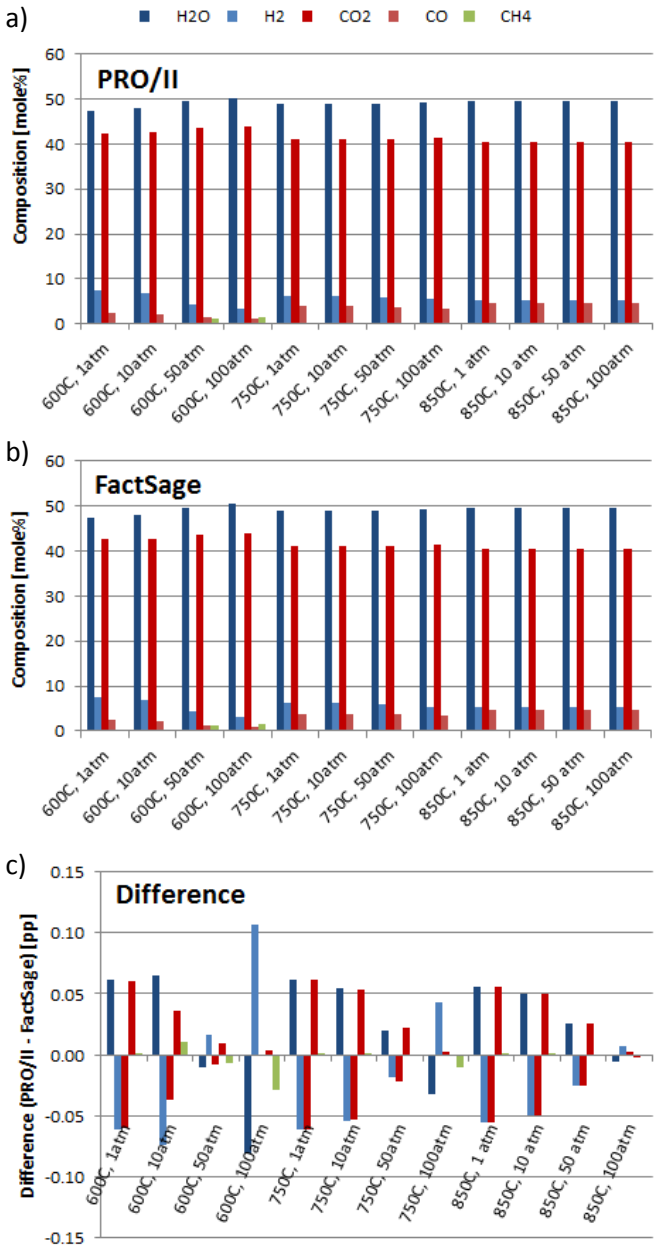

Figure 5-2. Comparison of PRO/II (a) and FactSage® (b) simulations of a Gibbs reactor running the WGS and methanation reactions with identical inlet compositions (0.45/0.10/0.45 for $X_{H_2O}/X_{H_2}/X_{CO_2}$) c) Difference between the two simulations in pp.

The figure shows that the differences between the compositions obtained from the two programs are below 1 pp, which means, the two programs are in good agreement. In any case, this small discrepancy is well within the uncertainties of any input figures for the model and as such the results of the two programs are treated as identical.

In PRO/II, a series of convergence criteria are used for the mass and energy balances, as well as the control loops in the model (control loops are discussed later in this chapter). These often

have tolerances on the order of 0.1 % - 0.01 % relating to the control values. This means that minor errors are introduced to the calculations by the model.

5.2 Main functions of the base case process

The base case (BC) of the design project is based on the Climeworks Ltd. plant, producing ~1000 tons of CO_2 per year, as discussed in the Chapter 3. This figure defines the capacity of the entire plant. Thus, the general strategy of the model is to define the mass balance of all the unit operations in the model based on those 1000 tons/y. The energy balance is then computed by the software based on the enthalpy changes (duties) stemming from changes in chemical composition (chemical reactions), temperature and pressure of each individual unit operation. In the following, the main parts of the functions (Figure 5-1 b) are treated separately. The aim is to describe how the main contributions to the model, such as pressurization of inlet streams; the filtering of the SOEC feed stream; the SOEC model itself; and the separation of water through condensation, are set up and operated. The pressure drops of all units in the model have been left out until the sizing calculations can be performed in Chapter 9 on process integration.

The air capture system was already described in Chapter 3 on air capture. In short, it is not modelled, but it is represented in the model by an inlet stream with a certain composition, temperature, pressure and flow rate. In addition to this, three heating and cooling duties are included in the heat integration studies presented later.

5.3 Filter model

Some initial thoughts on the filtering of impurities from the SOEC feed stream are presented in an earlier chapter (Chapter 4). In the base case model of the plant, the filter is assumed to be operated as a plug-flow packed bed reactor similar to those used for cleaning the inlet gasses of SOEC test rigs at DTU Energy [54, 55] and for impurity sampling in this work, in extensively scaled-up versions.

The filter needs to operate in a reducing atmosphere in order to keep the Ni part of the filtering material (Ni/8YSZ) in the reduced (metallic) state, which is a challenge, considering the otherwise oxidizing feed stream consisting mostly of CO_2 and H_2O. The solution was to recycle a small part of the SOEC effluent stream with its high content of CO and H_2 in order to avoid bringing in H_2 from outside of the process. The required amounts of H_2 and CO were calculated in FactSage in order to ensure that the Ni-filter would stay reduced.

In FactSage, a gas stream corresponding to the filter inlet stream composition of the base case design with a 1:3 CO_2:H_2O stoichiometry was simulated. The system contained the gas stream in addition to a large amount of metallic Ni and small amounts of H_2 and CO in a ratio corresponding to the SOEC effluent composition. Varying the amounts of the reduced species relative to the oxidized species, the system was allowed to equilibrate at 50 atm at 750 °C, corresponding to the operating temperature of the filter (T_{filter}), and 850 °C corresponding to the SOEC operation temperature (T_{stack}). For each temperature, a set mole fraction of H_2 in the filter inlet stream was tested while the amount of solid Ni and NiO was observed. At 0.1 % H_2,

small amounts of NiO was formed at both 750 and 850 °C whereas for 0.5 % H_2, only metallic Ni was seen in the solid phase.

From these considerations, $x(H_2)$ = 1 % in the filter inlet would be sufficient to keep the filter and SOEC reduced. Running the electrolyzer cells with very low H_2 concentrations at the inlet however, may cause a sharp spike in the Nernst voltage at the inlet of the individual cells, creating higher current densities in that part. This causes thermal gradients as the voltage diminishes as more H_2 and CO is produced across the cell. Thus it might be advantageous to operate the system with a higher $x(H_2+CO)$. As the model does not take thermal gradients into account, it was decided to operate the system with $x(H_2+CO)$ = 10 %, which turned out to require app. 3 % of the SOEC effluent stream.

As mentioned previously, the filter needs to be operated at significantly lower temperatures than the SOEC stack, in order to effectively collect the impurities from the gas stream. In the BC this means, the filter is operated at 750 °C.

The filter is modelled by an adiabatic Gibbs reactor in PRO/II. The Gibbs reactor unit operation is an equilibrium reactor capable of handling several specified equilibrium reactions simultaneously, minimizing the overall Gibbs free energy of the system in order to calculate the equilibrium composition. The WGS and methanation reactions take place on the Ni-catalyst of the filter, like in the SOEC cathode, as described in the theory chapter (section 2.3). Also, the combustion of H_2 and CO with the small amount of O_2 present in the stream originating from the air capture plant is allowed to take place at the elevated temperatures of the filter.

5.4 SOEC model

Since PRO/II does not include a model for SOECs, a model was implemented using a series of reaction steps based on the methodology of Sun *et al.[2]* in the same way as Salvati *et al.[86]* The model is a 0-dimensional steady state thermodynamic model of the chemical and electrochemical conversion in the stack, ignoring distributions of flow, current and heat inside the stack. The model takes into account the different reactions taking place at the fuel electrode of the SOECs as described in the theory chapter (section 2.2) of this thesis.

Of the possible reactions taking place at the fuel electrode, it is assumed that only the WGS, methanation and electrolysis reactions contribute significantly to the outlet composition of the fuel electrode, as explained in the SOEC theory chapter (section 2.2) and that these can be separated into a series of reaction stages as shown in Figure 5-3 a). Stage 1 represents the WGS and methanation reactions taking place in the fuel electrode support structure at the inlet of the individual cells. This stage has the inlet gas composition, α, as the input and produces the composition β after the equilibrium is established. Stage II represents the electrochemical reactions taking place at the triple phase boundary (TPB) of the fuel electrode, producing the composition γ governed by a specified conversion. Stage III represents the WGS and methanation reactions taking place in the support structure of the SOEC outlet, resulting in the outlet composition δ after equilibrium. To my knowledge, this model has not been

specifically validated experimentally, but Ebbesen et al. showed that the composition of the exhaust gas from an SOEC was in accordance with the WGS equilibrium.[33]

At this point, carbon forming reactions such as the Boudouard reaction are ignored in the base case, as operating parameters are chosen outside the (T, P, composition) region of thermodynamically stable solid carbon formation, primarily through the high H_2O:CO_2 ratio which suppresses the coking reactions as mentioned in the theory chapter (section 2.2). This was investigated using fact sage, and the results are discussed in Chapter 6 on the Syngas plant results and discussion.

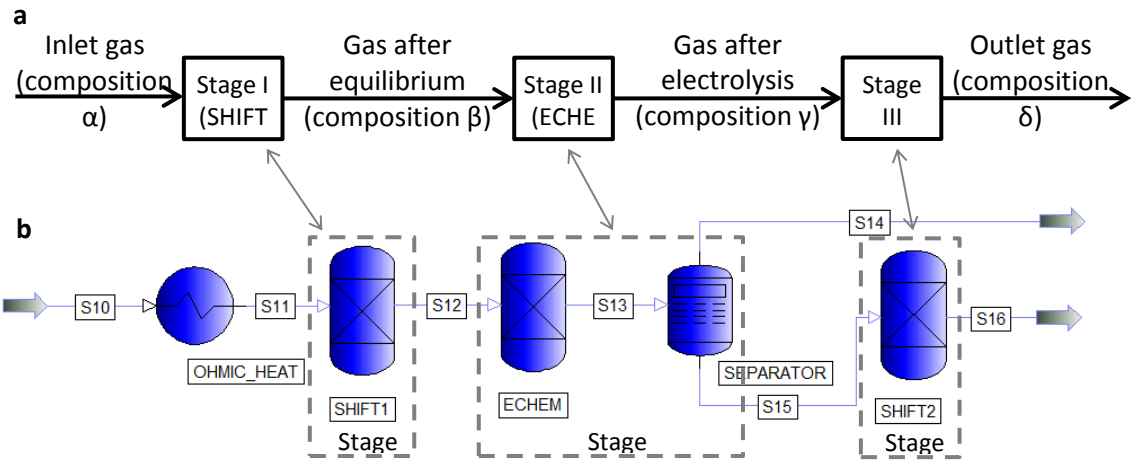

Figure 5-3. Principle behind the 0D thermodynamic SOEC model. a) Modified schematic of the model developed by Sun et al. [2]. Each line represent a gas composition and each box represents chemical reactions. b) PFD showing PRO/II implementation of the model. The lines are process streams with some chemical composition. The icons are unit operations. The arrows show the correspondence of the PRO/II unit operations to the chemical reactions in the model. SHIFT1 and SHIFT2 represent the WGS and methanation equilibrium reactions. ECHEM and the SEPARATOR represent the electrochemical conversion of CO_2 and H_2O in and the separation of O_2. The OHMIC_HEAT unit operation represents the part of the Joule heating in the cell stemming from > E_{tn} operation.

Translating the model into PRO/II is done using a series of unit operations as shown in the PFD in Figure 5-3 b). Each unit in the model calculates the enthalpy change of the reactions. When operated at thermoneutral conditions, the sum of the enthalpies is balanced with the energy supplied by the current needed to perform the electrochemical reduction of H_2O and CO_2 in Stage II. As explained in section 2.2.2 in the theory chapter, the current is accompanied by an series of overpotentials related to the various processes involved in the electrochemical reactions. At the thermoneutral voltage, all heat supplied in this way is consumed in the reactions, and the cell has a net heating output equal to zero. Se the sub-section on energy balance below for further details on this.

In the PFD, the stream, S10, on the far left is the inlet stream to the SOEC stack, which comes with a temperature, pressure, flow rate and chemical composition (α). The outlet streams on the far right, S14 and S16, represent the effluent streams from the oxygen electrode and fuel

electrode (composition δ) respectively. The intermediate streams S12 and S15 have the compositions β and γ respectively. The following unit operations are included in the model:

- **OHMIC_HEAT** is a simple heat exchanger, accounting for any extra Joule heating in the stack if it is operated above the thermoneutral potential E_{tn}. As mentioned above, temperature gradients in the cell are not accounted for in this model, and thus extra Ohmic heating above E_{tn} is treated in one operation at the inlet. The Joule heating which is consumed in the reactions in the stack is accounted for in the individual units. See section 5.4.1on the Energy balance below for details. It is important to note, that this unit operation does not represent a physical heat exchanger in the plant. It is merely used to represent heating in the stack if operated above the thermoneutral voltage.

  Simple heat exchangers are supplied with an outlet temperature and calculate the heating or cooling duty in order to bring the inlet stream temperature to the required outlet stream temperature.

- **SHIFT1** is an isothermal Gibbs reactor modelling the WGS and methanation reactions taking place on the Ni catalyst of the fuel electrode support structure and inside the electrode itself.

  The Gibbs reactor unit is an equilibrium reactor capable of running several specified reactions in parallel, minimizing the overall Gibbs free energy to obtain the equilibrium composition. In this reactor the WGS and methanation reactions are allowed to proceed under isothermal conditions at the temperature of the inlet stream, based on the thermodynamic databases of PRO/II. The heating or cooling duty required to balance the enthalpy change of the reactions under the isothermal condition is calculated.

- **ECHEM** is a simple conversion reactor accounting for the electrochemical (electrolysis) reactions of CO_2 and H_2O reduction under isothermal conditions at the temperature of the inlet stream.

  The reactor is supplied with a Conversion Factor (CF) for each reaction and returns the achieved composition (including the O_2 fraction) along with the combined electric and heating duty required to balance the enthalpy change of the reaction under the isothermal condition. A conversion factor is supplied for

- The **SEPARATOR** is a so-called stream calculator. This is a virtual unit which – in this case – does not perform any calculations. It simply splits off the O_2 component, representing the electrolyte and oxygen electrode reactions. The outlet streams are pure O_2 (S14) and the remaining components of composition γ (S15), both with the same temperature and pressure as the inlet stream.

- **SHIFT2** is another isothermal Gibbs reactor modelling the WGS and methanation reactions taking place at the outlet of the stack. It works exactly like SHIFT1 and yields the SOEC effluent stream (S16) with composition δ in addition to the required reactor duty.

It is assumed that the SOEC is equally selective towards the CO_2 and H_2O electrolysis reactions. In reality, this is not the case, as rates of reaction and diffusion are different, and also the thermoneutral potentials of the reactions are different (1.29 V for H_2O and 1.46 V for CO_2 electrolysis). According to Sun *et al.*[2] however, the error introduced is compensated by the subsequent WGS reaction in SHIFT2. Intuitively, this makes sense as all components of the electrolysis reactions take part in the WGS reaction, and thus, the equilibrium composition only depends on the extent of electrolysis (oxygen-removal), that is given by the current, not which species were reduced electrochemically.

5.4.1 Energy balance

As described above, the model is set up to handle the mass balance first with the specified thermal conditions (isothermal operation and inlet temperature). The units SHIFT1, ECHEM and SHIFT2 calculate the enthalpy changes resulting from the reactions. Each unit then requires an energy input or output to balance the enthalpy changes in order to comply with the isothermal operating condition. The energy balance is then performed, treating the SOEC as a single unit, based on the duties of each individual stage. The current is defined by the needed electrochemical conversion, which is specified in the ECHEM unit, and the operating voltage is calculated from the needed enthalpy changes of the four main units of the SOEC model: OHMIC_HEAT, SHIFT1, ECHEM and SHIFT2. The SHIFT 1 and 2 units along with the ECHEM unit account for the enthalpy changes related to the reactions only, and in effect, they will return a combined duty corresponding to the thermoneutral voltage. In case another voltage is needed, for example to supply additional heating of the cell, the OHMIC_HEAT unit is used. Thus, this unit is only involved in > E_{tn} operation or to compensate if < E_{tn} operation is preferred, in which case, it will have a negative heat duty.

This works because the overall operation of the SOEC stack is endothermic, and all energy losses in the cell result in generation of heat, which may be consumed in the reactions as described in the introduction.

With a given area specific resistance (ASR, see below), the needed cell area and by implication, number of cells is determined from the cell resistances calculated from the operating current and voltage.

Along with the conversion, f_i^{conv}, of CO_2 and H_2O in kmol/h, the model calculates the enthalpy changes of each unit operation in the model: ΔH_{OHMIC_HEAT}, $\Delta H_{SHIFIT1}$, $\Delta H_{ELECTROCHEM}$ and ΔH_{SHIFT2} from a given set of flow rate (f^{S10}), stack temperature (T_{stack}), and conversion factor (CF). The needed current, I is calculated as:

$$I = 2F \cdot \sum f_i^{conv} \text{ for } i \in \{H_2O; CO_2\} \qquad \text{Eq. 5.1}$$

Where *F* is the Faraday constant. The stack power, P_{stack}, is calculated as the power needed to balance all reaction enthalpies and the required extra heating if the cell voltage, $U_{cell} \neq E_{tn}$:

$$\sum_{n=1}^{4} \Delta H_n = \Delta H_{OHMIC\_HEAT} + \Delta H_{SHIFT1} + \Delta H_{ELECTROCHEM} + \Delta H_{SHIFT2} = P_{stack} = I \cdot U_{cell} \quad \text{Eq. 5.2}$$

If the temperature of the inlet stream (S10) is equal to the wanted operating temperature, $\Delta H_1 = 0$ and $U_{cell} = E_{tn}$ as all the produced joule heating is consumed in the reactions and the stack is operated at the thermo neutral potential. E_{tn} may be calculated via the following equation, where the consumed Joule heating is accounted for in ΔH_n of the reaction stage unit operations (n = {2;4}):

$$E_{tn} = \sum_{n=2}^{4} \Delta H_n \Big/ 2F = \frac{\Delta H_{SHIFT1} + \Delta H_{ELECTROCHEM} + \Delta H_{SHIFT2}}{2F} \quad \text{Eq. 5.3}$$

In this model however, some of the pre-heating of the reactants is expected to be supplied via Joule heating, ($T_{inlet} < T_{stack} \Rightarrow \Delta H_1 > 0$) and thus $U_{cell} = E_{tn} + U_{heat}$, where U_{heat} is the overvoltage needed to supply that amount of heat. U_{cell} is then calculated as:

$$U_{cell} = \sum_{n=1}^{4} \Delta H_n \Big/ 2F = \frac{\Delta H_{OHMIC\_HEAT} + \Delta H_{SHIFT1} + \Delta H_{ELECTROCHEM} + \Delta H_{SHIFT2}}{2F} \quad \text{Eq. 5.4}$$

As discussed in the Chapter 4 on impurities, the filter protecting the fuel electrode from impurities needs to be operated at a significantly lower temperature than the SOEC to ensure all impurities are collected in the filter. In this modelling, the filter temperature is chosen to be 100 K lower than the SOEC operating temperature so T_{filter} = 750 °C in the base case. This means that the effluent stream from the filter needs to be heated. As will be discussed in further detail later, high grade heat at > T_{stack} = 850 °C cannot be expected to be readily available except from in the outlet stream of the SOEC. This could be imagined to be integrated, but a minimum approach temperature (with the associated heat loss) of at least 10 °C is required for gas-gas heat exchangers, and so some heat has to be supplied as electricity. Also heat exchangers at these high temperatures are costly, and so it is assumed that it makes

economic sense to leave out the heat exchanger between the filter and SOEC stack in favor of the simpler system, and supply the entire heating duty as Joule heating in the cell. This means that $U_{cell} > E_{tn}$ and Eq. 5.4 will be used for calculating the cell voltage in the model.

5.4.2 Area specific resistance

The central sizing parameter of the SOEC unit is the cell area required for the needed conversion of steam and CO_2. The total cell area is related to the current density and cell voltage by the ASR measured in $\Omega \cdot cm^2$. As mentioned in the theory chapter (section 2.2.2), the internal resistance of a cell originate from rate limitations of the various chemical and transport related processes in the cell, and as such, these depend on the operating conditions such as chemical composition, temperature and pressure. In order to allow analyses of the economics of the plant at varying operating conditions (T, P) is was necessary to obtain values for ASR as a function of both temperature and pressure, preferably in the ranges of T = 1 atm – 100 atm and P = 600 °C – 850 °C. In the following two sections this is treated for P and T respectively.

5.4.2.a Pressure dependence of ASR

There are many examples of reported ASR values for varying conditions in the literature. High pressure operation of solid oxide cells, however, is a relatively new phenomenon, pursued only by a small number of groups.[87-92] Also, it has not been possible to find consistent experimental data for operation of full cells above 8 atm. For this reason, the ASR was extrapolated to higher pressures from known resistance values of Ni/YSZ|YSZ|LSM-YSZ cells obtained at 1 atm. This was done by considering the various constituents of ASR, which can usually be separated into the following contributions for this type of cells:

$$ASR = R_S + R_I + R_{II} + R_{III} + R_{IV} + R_V \qquad \text{Eq. 5.5}$$

Here, R_s is the series resistance to ionic conduction in the electrolyte; R_I is the resistance towards ionic conduction in the YSZ parts of the composite oxygen electrode; R_{II} is the TPB-related charge transfer resistance of the fuel electrode; R_{III} is the TPB related resistance of the oxygen electrode reaction; R_{IV} is the gas diffusion resistance and R_V is the gas conversion resistance, both of the fuel electrode. The contributions from ionic conduction depend only on the temperature; not on the pressure and are added to form a constant in the expression: the electrolyte resistance ($R_E = R_S + R_I$). In the case of the gas conversion and diffusion resistances, these were assumed constant with regards to total pressure based on the work of Primdahl *et al.*[93, 94]

For the oxygen electrode, the following expression for the dependence of the electrode resistance, R_{III}, on the pressure was found experimentally by Thomsen *et al.*:[95]

$$R_{III} = k\left(p_{O_2}\right)^{-n} \qquad \text{Eq. 5.6}$$

Since only oxygen is present at the electrode in electrolysis mode, the total pressure is equal to the O_2 partial pressure and equation Eq. 5.6 is equivalent to:

$$R_{III} = k(P)^{-n} \quad \text{Eq. 5.7}$$

For a 50/50 LSM-20/8YSZ composite electrode operated at 850 °C, an *n* value of *n* = 0.26 ± 0.02 was obtained.[95]

For the fuel electrode, a similar dependence of the electrode resistance, R_{II}, on the partial pressures of H_2O H_2, CO_2 and CO is used. In the present work, it was assumed that the electrode reactions of the H_2O/H_2 and CO_2/CO systems behave similar pressure dependencies, and thus the relation simplifies to:

$$R_{II} = c\left(p_{H_2+CO}\right)^{-l} \cdot \left(p_{H_2O+CO_2}\right)^{-m} \quad \text{Eq. 5.8}$$

Mogensen *et al.*[96] suggest that the H_2 (and with the above assumption, also the CO) dependence is negligible compared to that of H_2O (and CO_2) in the relevant range of composition, and so the expression simplifies further:

$$R_{II} = c\left(p_{H_2O+CO_2}\right)^{-m} \quad \text{Eq. 5.9}$$

At the fuel electrode, the partial pressure and total pressure are not the same, and the following relation then governs the dependence on the total pressure:

$$p_{H_2O/CO_2} = P \cdot \left(x(H_2O) + x(CO_2)\right) \quad \text{Eq. 5.10}$$

$$\Leftrightarrow R_{II} = c\left(P \cdot \left(x(H_2O) + x(CO_2)\right)\right)^{-m} \quad \text{Eq. 5.11}$$

Different values of *m* have been reported in the range of -0.5 to 1 [96]. For electrodes developed at DTU Energy however, Høgh [97] found *m* = 0.27 ± 0.09 Ω·cm^2.

Thus, the final expression for the dependence of ASR on the total pressure, at constant temperature and with the above simplifications and assumptions is:

$$ASR = R_E + c\left(P \cdot \left(x(H_2O) + x(CO_2)\right)\right)^{-0.27} + k(P)^{-0.26} + R_{IV} + R_V \quad \text{Eq. 5.12}$$

Where R_E, R_{IV} and R_V are constants.

In the SOEC of the base case in this work, the gas compositions at the fuel electrode are given in Table 5-1 for the inlet, outlet and average composition, not counting the small fraction of N_2 present in the stream. Also, the ratio of oxidized to reduced species in the gas is shown for each composition. ASR contributions are not commonly measured for $(H_2O+CO_2)/(H_2+CO)$-ratios of 3 as is the average ratio in the base case simulation in this work. For the relevant type of cells, the closest values I could find were from Ebbesen *et al.*[33], where the fraction $x(H_2O+CO_2)/x(H_2+CO) = 2$. The composition is shown in the table as well, and the resistances measured at 805 °C are shown in Table 5-2.

Table 5-1. Gas compositions over the fuel electrode in the base case simulations along with those stated in [33]. The ratio of oxidized to reduced species is given for each composition.

Component	Gas composition at fuel electrode [%] BC Inlet	BC Outlet	BC Average	Ebbesen et al.
- H_2O	80.4	40.1	60.3	25
- H_2	1.8	38.5	20.2	0
- CO_2	17.4	5.4	11.4	25
- CO	0.4	5.6	2.9	25
- CH_4	0	10.2	5.1	0
- Ar	0	0	0	25
$\frac{x(H_2O)+x(CO_2)}{x(H_2)+x(CO)}$	~44	~1	~3	2

Table 5-2. Resistance contributions of the various processes of a Ni/8YSZ/8YSZ/LSM/YSZ cell at OCV, operated at 1 atm and 850 °C. From [33]

	Process	Cell part	Resistance [mΩ·cm^2]
Total ASR			201
R_s	Ionic conduction	electrolyte	70
R_I	Ionic conduction	fuel+oxygen	38
R_II	Charge transfer	Fuel electrode	34
R_III	Charge transfer	Oxygen electrode	13
R_IV	Diffusion	Fuel electrode	36
R_V	Conversion	Fuel electrode	80

Based on the starting values shown in Table 5-2, ASR was extrapolated for increasing pressure, using Eq. 5.12. The results are given in Figure 5-4.

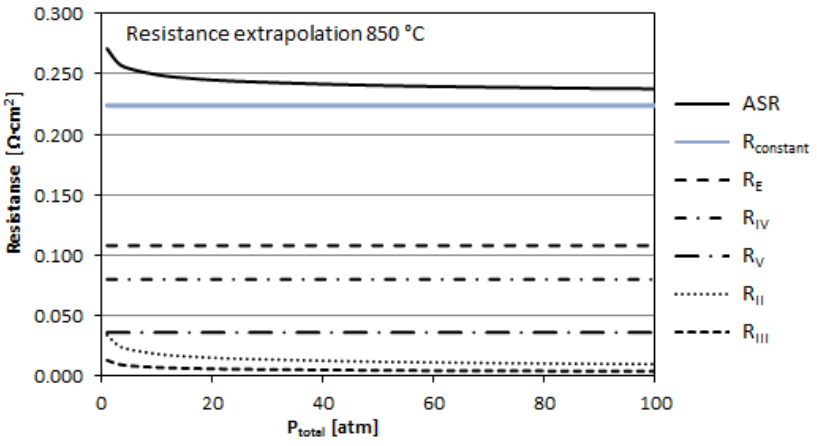

Figure 5-4. Extrapolation with increasing pressure of the resistance contributions and total ASR. The values of Ebbesen *et al.[33]* were used as the starting points for the extrapolations. $R_{constant}$ shows the sum of the constant contributions to ASR.

At the operating temperature and pressure of the base case (T_{stack} = 850 °C P = 80 atm), the ASR of the cell is estimated to be 239 mΩ·cm^2. The resistances treated above were obtained at OCV and so it is assumed that as long as the conversion of reactants do not approach 100 % where the conversion resistance would start increasing, the ASR can assumed to be unaffected by current densities up to reaction utilizations of around 80 % - 90 %.

Clearly this extrapolation relies on a series of assumptions. The constant contributions to the ASR constitute the vast majority of the total value however, meaning only a small room is available for decreasing the ASR with increasing pressure as is seen in the figure. This reduces the uncertainty of the extrapolation with pressure whereas the assumption of independence of current density may be more dubious, depending on the chosen reactant utilization.

5.4.2.b Temperature dependence of ASR

The temperature dependences of the ASR of Ni/YSZ|YSZ|LSM/YSZ cells considered in this work is well known, and ASR values at three different gas compositions were published by Ebbesen et al. for 750 °C 800 °C and 850 °C in electrolysis mode [29]. Based on these values, the Arrhenius plot shown in Figure 5-5 was generated. In the figure, the values are marked Std. cell a, b and c for the following gas compositions: a: 50% H_2O - 50% H_2, b: 50% CO_2 - 50% CO, c: 45% CO_2 - 45 % H_2O - 10% H_2. Simple extrapolation to 600 °C yields prohibitively large ASR values of 1.81 Ω·cm^2, 1.94 Ω·cm^2, and 1.87 Ω·cm^2, for composition a, b, and c respectively.

At DTU Energy, a new Ni/YSZ fuel electrode supported cell with a gadolinium doped cerium oxide (CGO)/lanthanum-strontium-cobaltite (LSC) oxygen electrode. The cells have a CGO barrier layer between the YSZ electrolyte and the oxygen electrode and an LSC current collector layer on the other side of the oxygen electrode [98]. For two cells of this new type with areas of 16 cm^2 and 2 cm^2, ASR values obtained at OCV in 40 % H_2O - 60 % H_2 at temperatures between 650 °C and 750 °C are plotted in the Arrhenius diagram as well. Extrapolation to 600 °C yields ASR values of 0.55 Ω·cm^2, and 0.51 Ω·cm^2 for the larger and smaller cells respectively. The discrepancy of the gas compositions between the tested cells and the expected compositions in the SOEC stack in this work, are assumed not to affect the activation energies.

As these cells have not been tested in gas compositions relevant for co-electrolysis, three assumptions are made:

4. The dependence of ASR on gas composition is small
5. The dependence of ASR on operation mode (fuel cell or electrolysis) is negligible
6. The pressure dependence of this type of cells is similar to the one discussed in the previous section.

With these assumptions, the above mentioned ASR value of the larger cells (0.55 Ω·cm^2) is used as a basis for extrapolation of the pressure dependence. With the same dependence as for the standard cells mentioned above, an ASR values of 0.5 Ω·cm^2 (rounding to the nearest 100 mΩ·cm^2) is obtained.

These cells are still under development, and little is known about their long-term stability. In addition, they have not specifically been tested in electrolysis conditions. Thus, for high temperature applications, ASR values for the standard DTU Energy cells will be used in this work. For the low temperature applications (<700 °C), the extrapolated value (0.5 $\Omega \cdot cm^2$) of the new cell type is used.

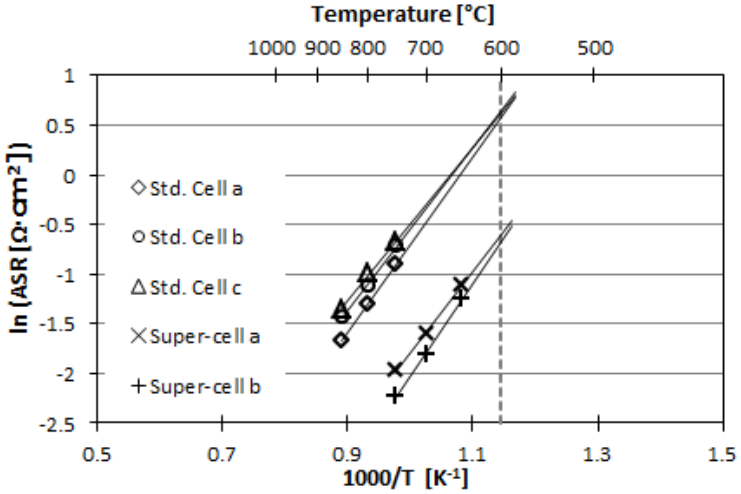

Figure 5-5. Arrhenius plot for ASR values of cells from DTU Energy. Values from [29] (std. cell a, b, and c) and a the new, improved cell type [98]. Extrapolations to 600 °C are shown for both cell types.

5.5 Water recovery

Recovering unreacted H_2O from the SOEC effluent stream is important, as water is an inhibitor of the methanation and other synfuel reactions downstream of the syngas plant. This is done straightforwardly by condensing the steam for gas-liquid separation, lowering the mole fraction of H_2O in the syngas stream ($x(H_2O)^{syngas}$). The size of this figure is governed by the H_2O tolerance of the following fuel synthesis. The operating pressure of the system has a large impact on the needed temperature to condense the water, depending on the wanted recovery. A simple simulation of this relationship was run in PRO/II in which an SOEC effluent stream with the H_2:CO ratio of 2, of the was fed to the condenser at varying total pressures and for 99 %, 97 % and 95% recovery of H_2O corresponding to values of $x(H_2O)^{syngas}$ of 1, 3 and 5 % respectively. The results of the simulation are shown in Figure 5-6.

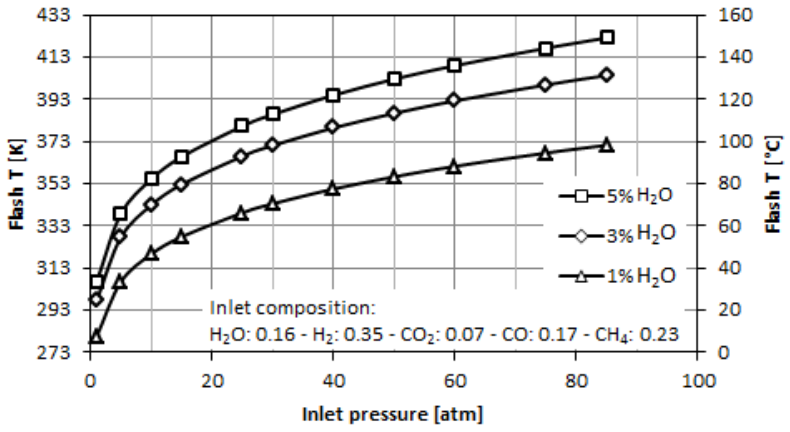

Figure 5-6. Temperature and pressure dependence of flash separation through condensation for varying recovery fractions (1 %, 3 % and 5 %). The inlet composition is given in the figure.

As both effluent streams from the condenser need to be re-heated before they are recycled or led to the downstream fuel synthesis plant, , a high condensation temperature is expected to be most economical, depending on the operating temperature and the tolerance of the following synthesis steps. In the base case, a recovery of 95 % is chosen; resulting in a condensation temperature of around 420 K at 80 atm. The temperature will change for other compositions of the SOEC effluent stream and a control loop is included in the PRO/II model to handle this as is explained later.

5.6 Compression

Pressurized operation of the syngas and fuel synthesis plants is advantageous for a series of reasons such as lower operating voltage of the SOEC caused by increased methane production, lower internal resistances of the SOEC, increased methane production in both the cell and methanation plants etc. as already described in the introduction.

The SOEC feed stream consists mainly of H_2O and CO_2. In the case of water, compression through steam production is simple: A pump feeds the water into an evaporator at the wanted pressure, where the water is heated to evaporate and form steam at the wanted pressure.

In the case of CO_2, this possibility does not readily exist. Compression of gasses is significantly more energy intensive than pressurizing condensed phases however, and consequently the CO_2 phase diagram (see Figure 5-7) was examined for alternative strategies. The figure shows two alternative general routes to producing CO_2 at high pressure (50 atm in this case), via a condensed phase. These two alternative routes are illustrated in the diagram and are termed the *liquid cryogenic* (2) and *solid cryogenic* (3) routes as alternatives to *simple compression* (1)

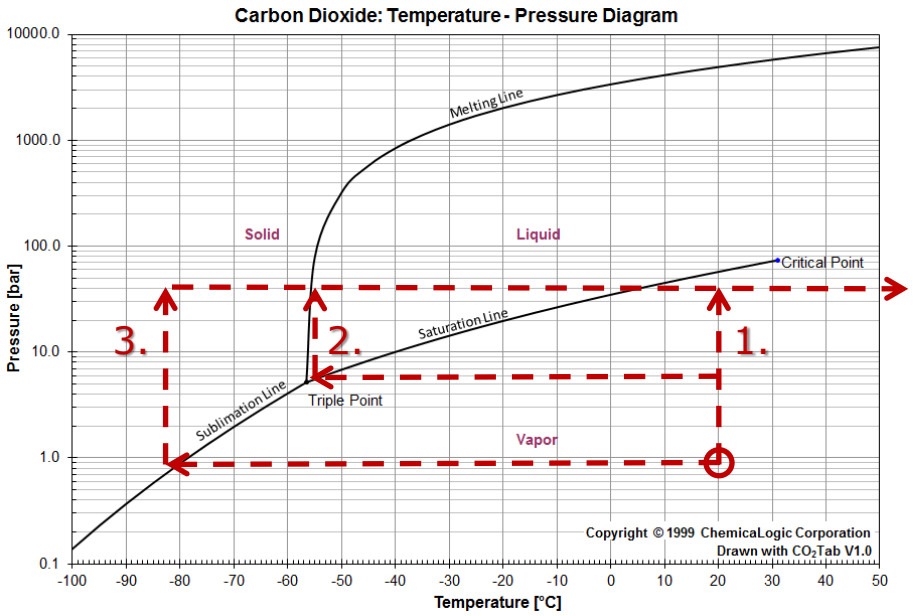

Figure 5-7. Phase diagram of CO_2 showing potential compression routes. The direct compression (1), liquid cryogenic (2) and solid cryogenic (3) routes are shown conceptually in the diagram. The pressure changes are represented as ideal reversible operations, meaning temperature changes are ignored. Reprinted with permission: Copyright © 1995-2013 ChemicaLogic Corporation. All rights reserved.

For the simple compression route (1), a compressor increases the stream pressure from 1 atm to 50 atm. This heats up the stream significantly (not shown in the diagram), and a heat exchanger increases the temperature to 750 °C.

In the *liquid cryogenic* route (2), the CO_2 stream is pressurized through evaporation from the liquid state. In order to do this, the stream must be first compressed to above 5.12 atm (triple point pressure) followed by cooling until the stream has condensed at around - 56.6 °C (216.6 K). After the phase change, the liquid may be easily pressurized in a pump and finally heated and evaporated under pressure to yield steam at the desired temperature and pressure (750 °C, 50 atm in this case). In PRO/II, this is modelled by a compressor followed by a heat exchanger, a pump and finally a second heat exchanger as shown in the PFD in Figure 5-8 a).

In the *solid cryogenic* route (3), the CO_2 stream is cooled cryogenically at ambient pressure until it condenses to the solid state at - 78.5 °C (194.7 K) after which it is heated to 750 °C at 50 atm to produce a gaseous stream. In PRO/II, this is modelled by a two consecutive melter/freezer unit operations, which are heat exchanger modules capable of handling solid streams. The second is set to operate at 50 atm and heat the stream all the way to 750 °C. The PFD is shown in Figure 5-8 b). This strategy has the added advantage of enabling removal of N_2 and O_2 contaminants, still in the vapor phase as the CO_2 condenses.

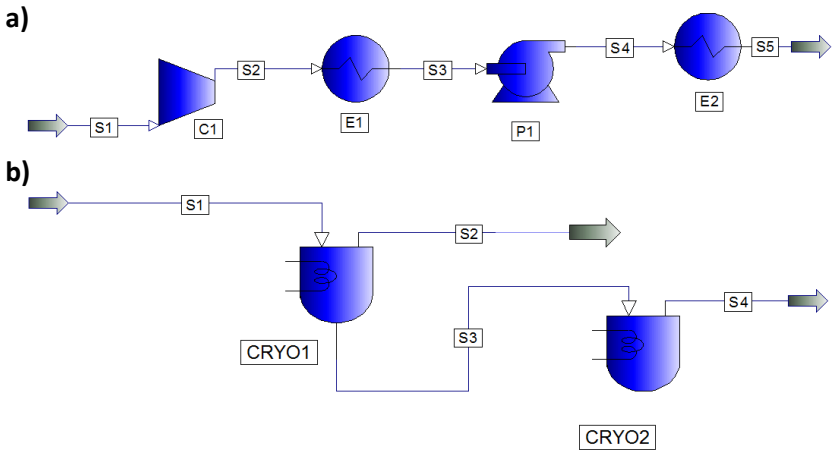

Figure 5-8. PFDs showing the cryogenic compression sub-systems. a) liquid cryogenic compression (route 2) including a compressor (C1), heat exchanger (E1), pump (P1) and another heat exchanger (E2). b) solid cryogenic compression (route 3) with a cryogenic freezer unit (CRYO1) and a melter (CRYO2).

In the case of the liquid cryogenic route, temperature and pressure changes were simulated in PRO/II, using the PFD in Figure 5-8 a) and the energy consumptions of the four unit operations were recorded for varying condensation pressures. This was done to investigate if higher condensation pressures were energetically favorable, as this would require less cooling. The input stream was set to 298 K and 1 atm, the outlet stream was set to 298 K and 50 atm, and the results are shown in

The resulting works of compression and pumping are shown in Figure 5-9 along with the heating/cooling duties and the sums of the work and heat. For the heat, perfect heat exchange was assumed ($\Delta T_{min}=0$) for the sake of simplicity.

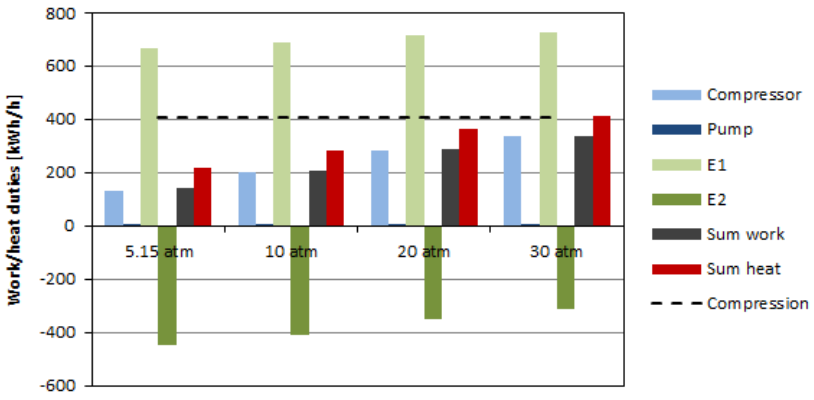

Figure 5-9. works of compression and pumping and heat duties for four calculation cases. The summed work and summed heat (assuming an approach temperature of 0 K) are shown.

The figure shows the cooling duty of the heat exchanger E1 (see Figure 5-8) increasing with the work of compression. This is caused by compression heating up the gas significantly, and thus there is no energy to be saved on the cooling by increasing the pressure. In addition, the figure illustrates how minuscule the pumping work is compared to all other contributions to the total energy consumption. Based on these results, the initial compression is chosen to be as low as possible. The CO_2 stream is compressed to 5.25 atm, just above the triple point, before it is cooled to 220 K.

In order to compare the three compression cases, two variations of the BC syngas plant were modelled using each of the cryogenic routes as design alternatives to the base case. A rigorous comparison requires consideration of the overall system energy balance in each case, especially in order to account for possible recuperation of heating and cooling duties related to the compression. The analysis of heat and electricity in the plant is considered at the end of this chapter in section 5.8 .

5.7 The process flow diagram

With the main unit operations in the process described, the resulting PFD for the BC syngas plant is shown in Figure 5-10. In the following section, the individual unit operations are described systematically.

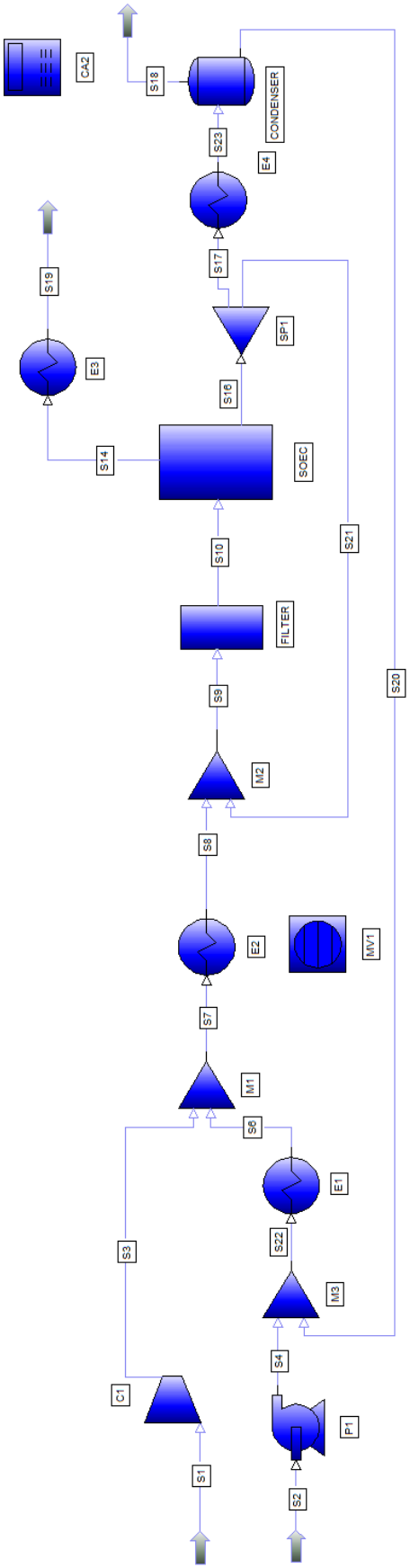

Figure 5-10. PFD of BC syngas plant

- The input stream **S1** is the CO_2 stream coming from the air capture plant.
- The compressor **C1** compresses the stream to the operating pressure of the SOEC, in this case 80 atm. The compressor is running with an adiabatic efficiency of 75 % as per Peters *et al.*[99], and it is assumed that the heat generated can be used to heat up the stream. For 80 atm, the temperature increase is approximately 510 °K.
- The input stream **S2** is the water inlet stream.
- The pump **P1** increases the pressure of the water stream to the operating pressure of 80 atm. The pump is running with an adiabatic efficiency of 80 %.
- In the mixer **M3**, the water recycled from the condenser is mixed with the input stream.
- The heat exchanger **E1** evaporates the water stream by heating it to 296 °C.
- In the mixer, **M1**, the CO_2 and H_2O streams are mixed.
- The heat exchanger **E2** is the pre-heater, increasing the temperature to the needed operating temperature of the filter.
- The mixer, **M2**, mixes the input stream with the SOEC recycle stream, described above.
- The **FILTER** is modeled as an adiabatic Gibbs reactor allowing the WGS and methanation reactions to equilibrate along with burning of H_2 and CO with the small amount of O_2 present in the feed stream from the air capture plant.
- The **SOEC** model is described in section 5.4 above, and results in the O_2 by-product stream (S14) and the SOEC effluent stream (S16).
- The heat exchanger **E3** cools down the O_2 byproduct stream to recover the heat.
- The splitter **SP1** splits off a small amount of the effluent stream to keep the combined mole fraction of H_2 and CO in the SOEC feed stream (S10) equal to 10 %. This constitutes a split fraction of app. 3 %.
- The heat exchanger **E4** represents the cooling duty of the condenser, where the SOEC effluent stream is cooled to 144 °C.
- The **CONDENSER** flash drum separates the liquid water from the vapor phase and feeds it into the water recycle stream (S20) leading back to the mixer M2.
- The product stream, **S18**, contains the syngas product containing H_2O, H_2, CO_2, CO, CH_4 and N_2.

5.7.1 Control loops

The model contains 4 control loops controlling the operation of certain units in the PFD. These are run in the Multi-Variable Controller (MV1). The control loops are explained in the following.

7. **Feed module and water input flow rate.** As discussed in the introduction, the syngas composition needs to be tailored to the chosen downstream fuel synthesis technology. As the CO_2 flow rate is fixed by the production of the air capture plant, the FM (See section 2.3.1) of the syngas composition is adjusted by regulating the water inlet flow rate (S2). This is done in an iterative fashion, ensuring, the FM (calculated by the calculator module, CA1) is as required, controlled to within a relative tolerance of 0.3%. See section 2.3.1 in the theory chapter on the feed module for further information.

8. **Redox potential of the filter inlet stream.** The filter and SOEC both need to be operated in a reducing atmosphere, in order to keep the Ni catalysts of both in the metallic state. A small recycle from the SOEC effluent stream is used for this purpose. Depending on the precise composition of the effluent stream (and thus the recycle stream), the split fraction of the splitter (SP1) is adjusted to keep the combined mole fraction of H_2 and CO above 10 % in the feed stream for the SOEC.

9. **Temperature of filter inlet stream.** The filter is operated at 100 °C below the operating temperature of the SOEC (T_{stack}) as described in section 5.3 and Chapter 4. The SOEC recycle stream (described above) is at the stack temperature, and since its flow rate is varied in control loop 2 described above, control loop 3 is used to vary the heating duty of the pre-heater (E2) in order to operate the filter at the right temperature ($T_{filter} = T_{stack} –$ 100 °C).

10. **Condenser operating temperature.** The amount of water separated from the vapor phase depends on the temperature of the flash drum. A maximum H_2O content in the syngas stream is chosen to 5 % as described in section 5.5 and the control loop ensures that the heat exchanger, E4, cools the inlet stream of the flash unit to the right temperature, achieving this fraction.

This concludes the documentation of the syngas plant model. All parameters can be changed, but the key operating parameters of the setup are shown in Table 5-3 along with their base case values.

Table 5-3. Input parameters for the syngas plant model and their BC values.

Parameter	Base Case value	
T_{stack}	850	°C
P_{stack}	50	Atm
CF	70	%
$x(H_2)^{S9}$	1.0	%
FM	3	
$x(H_2O)^{SYNGAS}$	5.0	%

5.8 Results for energy consumption of the syngas plant

Analyzing the energy consumption and possibilities for heat integration in the base case (BC) syngas plant requires a look at the electricity consumption and the heating and cooling duties.

5.8.1 Electricity consumption

The plant consumes electricity mainly in the SOEC and air capture subsystems, but also pumping and compression requires small amounts of electricity. The electrical energy requirements are listed in Table 5-4 along with the operating parameters of the SOEC stack, resulting from the simulation at T_{stack} = 850 °C, P = 80 atm and CF = 70 %.

Table 5-4. Electrical energy requirements of the BC syngas plant. The size of the plant is

Electric duty	Energy requirement	
Air capture	92.8	MJ/h
H_2O inlet pump	0.79	MJ/h
CO_2 inlet compressor	50.1	MJ/h
SOEC (P_{stack})	2260	MJ/h
- U_{cell}	1.243	V
- I	505	kA
Total energy demand	**2404**	**MJ/h**

The main electricity consumption of the air capture subsystem is the vacuum pump, evacuating the desorption chamber and collecting the CO_2 stream. The table shows how pressurization of the water stream is energetically favorable compared to pressurizing a gas stream as mentioned previously. The clear message of the table, however, is that the SOEC subsystem accounts for the vast majority of the electricity consumption in the BC syngas plant. This should not be surprising as this is where the chemical conversion takes place. It should be noted, that the base case plant do not account for pressure drops in any of the unit operations, which means that these numbers give a slight underestimation of the actual process electricity consumption. This is discussed in the main system integration chapter (Chapter 9) along with the sizing calculations.

5.8.2 Heat duties and integration

In addition to the electrical energy consumption, large amounts of heating and cooling are required in the plant. Each heat exchanger in the PFD (Figure 5-10) in addition to the heating and cooling needs of the air capture plant yields a heating or cooling duty (energy requirement or surplus) at specified temperatures. These are summarized in Table 5-5 for the heat exchangers in addition to cooling of the desorption chamber and vacuum pump and heating during the desorption period of the air capture plant.

Table 5-5. Heating and cooling duties of the BC Syngas plant. L = liquid phase, V = vapor phase.

			Source state		Target state		Duty
Unit	**description**	**Condition**	**T [K]**	**Phase**	**T [K]**	**Phase**	**[MJ/h]**
AC1	Desorption heating	cold	378		378		670
AC2	Cooling of vacuum pump	hot	293		293		307
AC3	Adsorption heating	hot	313		313		52
E1	H_2O evaporation	cold	331	L	538	V	497
E2	SOEC pre-heating	cold	557	V	1021	V	276
E3	O_2 by-product cooling	hot	1123	V	298	V	130
E4	H_2O condensation	hot	1123	V	401	L	454

The table shows, not surprisingly, how all duties involving phase changes (AC1, E1 and E4) dominate the heating and cooling needs of the plant. Comparing with the electricity needs listed in Table 5-4 shows that the SOEC electricity consumption is still the largest energy requirement.

From the duties in Table 5-5, the composite curves of the BC were generated as explained in the theory chapter (section 2.4.3). These are shown in Figure 5-11 along with the similar diagrams for the two alternative compression cases discussed in section 5.6 on Compression above. The figures show characteristic slopes between ~550 K and 1123 K on the hot composite curves and corresponding slopes on the cold composite curves. These represent the pre-heating (cold composite) and after-cooling (hot composite) of the SOEC inlet and effluent streams respectively (E2 and E4 in Table 5-5). The shift in temperature between these two curves (100 K) comes from the internal heating from the filtering temperature to the SOEC operating temperature, which is done inside the SOEC by Joule heating. The almost horizontal stretch on the cold composite curves 550 K represents the latent heat of evaporation of water in the evaporator (E1). In the diagram for the solid cryogenic route, the heat of evaporation is "hidden" in the pre-heating part of the cold composite curve which is what gives this curve a lower slope than for the other two cases. The flat pieces of the cold curve just under 400 K represent the large heating duty of the air capture plant during the desorption cycle (AC1).

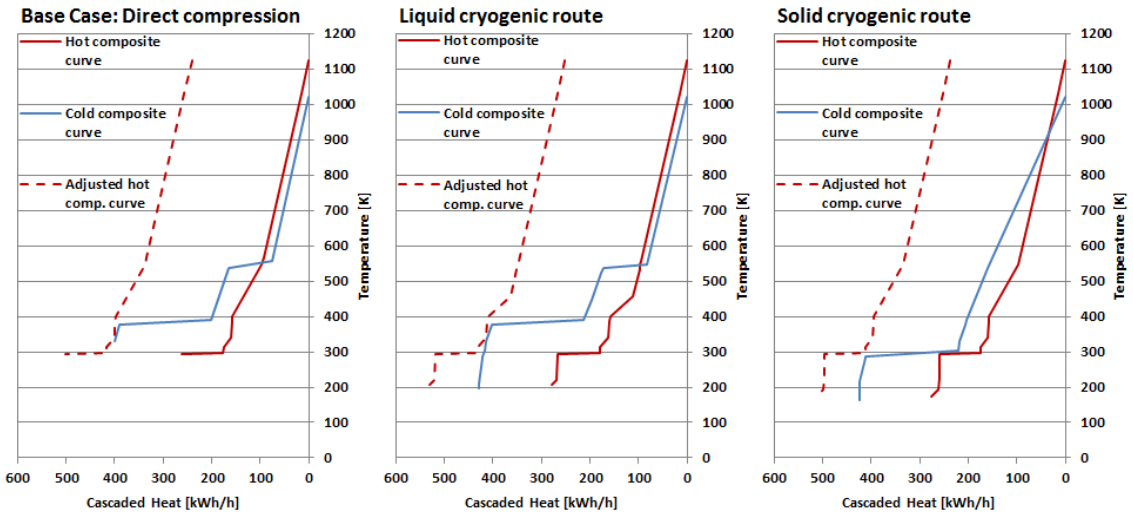

Figure 5-11. Composite curves for the syngas plant with the three different compression strategies. Hot, cold and adjusted composite curves are shown.

The adjusted hot composite curves are shifted to satisfy the requirement for a heat recovery approach temperature (HRAT) of 10 K, and the horizontal (heat flow) overlaps gives the maximum amount of recoverable heat in the three networks. The minimum hot and cold utility requirements are calculated from the parts of the curves, not overlapping. In the BC, the resulting minimum utility requirements amount to 865 and 366 MJ/h for the hot and cold utilities respectively, while 577 MJ/h can theoretically be recovered inside the network. In order to find a more precise estimate of the utility needs, the heat exchanger network

synthesis (HENS) problem needs to be solved. This is done for the full plant in Chapter 8 on heat integration later.

From the composite curves, however, a few points are clear already

1. The heating and cooling needs in the syngas plant do not match, as a significantly larger heating duty is required than excess energy from the required cooling can supply.

2. As fuel synthesis processes such as methane production are highly exothermic this mismatch or at least part of it can be expected to be covered by excess heat from the methanation plant when the whole plant is considered.

3. The high temperature parts of the heat exchange network can be expected to be fully integrated as the temperature difference between the pre-heating and after-cooling is covered by Joule heating in the cell. This means that relatively low grade heat can be utilized for the remaining heating duties.

5.8.3 Comparison of compression cases

This simple analysis based on the composite curves, however, forms a basis of comparing the three compression cases. These hot and cold utility requirements are compared to the needed work for compressors, pumps and the SOEC electricity consumption, for each compression case and the results are shown in Figure 5-12 for the three cases.

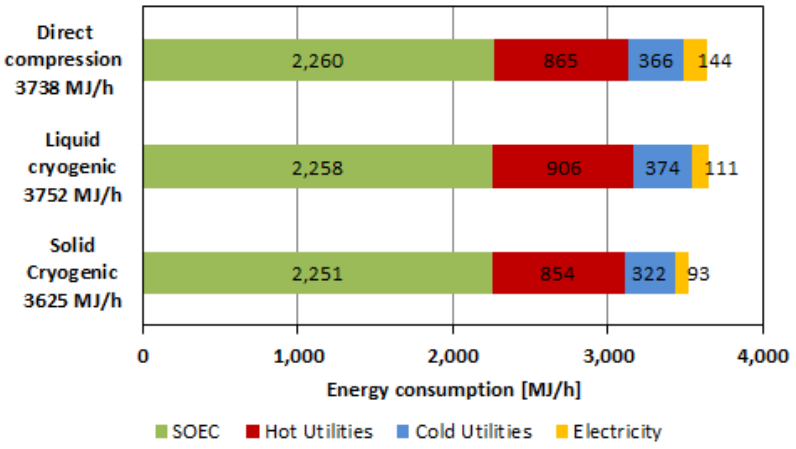

Figure 5-12. Energy requirements for the three compression cases. The SOEC electricity consumption includes the requirement for Joule heating from T_{filter} to T_{stack}. Hot and cold utility needs are calculated as the minimum utility requirements from analysis of composite curves and their overlap at an EMAT of 10 K. Electricity includes pumps and compressors where applicable. Total energy consumption is given for each case on the left.

The figure shows that the vast majority of the energy consumption of the plant is – not surprisingly – the electricity consumed by the SOEC stack. Also, there is a significant heating need (need for hot utilities) primarily driven by the latent heat of water evaporation and the large heating demand of the air capture plant. Also, the electricity consumption of pumps and compressors constitute only small fractions of the total energy and total electricity

consumptions (5.0 and 5.9 % respectively for the direct compression case). In terms of total energy consumption, the solid cryogenic route has the lowest energy requirement and the liquid cryogenic route has the highest. The margins are small however, with only 3 % lower consumption for the solid cryogenic route compared to direct compression, and it should be noted, that auxiliary electricity consumption and further non-idealities in heat integration (apart from the EMAT of 10 K) suggest smaller savings in a real implementation of the system. Based on these considerations, the direct compression strategy is selected in this work, favoring the simpler system and especially the system where most non-idealities are already accounted for in terms of efficiencies in the pumps and compressors.

5.9 Summary

In this chapter, the basic strategy of the modelling in this work was presented, and the thermodynamic steady state model of the syngas plant was developed. Finally the model was used to investigate three strategies for compression of the CO_2 inlet stream.

The modelling strategy of the work is to adjust the mass balance of the entire plant model to fit the air capture plant capacity of 1000 tons of CO_2 per year. Operating parameters for the remaining units in the model have been chosen based literature, basic simulations and assumptions, as presented throughout the chapter.

The SOEC model received special attention, as this is the part of the plant where the majority of the chemical conversion and energy consumption takes place. The model was developed from the thermodynamic model published by Sun et al.[2] The model in this work differs from the Suns model, in that it represents a technological implementation of an electrolyzer stack. Also, the present model treats the SOEC sub-system as any piece of equipment, adjusting the current density and operating voltage according to the chosen operating conditions of temperature, pressure, flowrate and required conversion.

Finally two alternative designs to the direct compression of the CO_2 inlet stream were studied, and the results showed, that with the assumption that all heat from the compression in the base case (BC) can be used to heat up the CO_2 stream, the energy savings are small. Based on that, the BC design was kept.

In the following chapter, the model is used to study the space of operating parameters of the SOEC, and for various syngas compositions.

Chapter 6 Syngas plant results and discussion

The central part of the model developed in this work is based on the work of Sun *et al.*[2] as described in Chapter 5. The model should be seen as a next step, developing the fundamental model of Sun *et al.* to represent a technological implementation by considering the operating parameters in relation to the rest of a surrounding plant more carefully. This chapter includes a documentation of the operation of the developed model in terms of operating parameters in addition to a discussion on the comparison of these results with the model of Sun et al. and how the two models differ. At the end of the chapter, the risk of forming solid carbon, which would block adsorption sites and damage the structure of both the filter and the electrolyzer, is evaluated for various operating parameters of the plant, in order to determine a set of "safe" operating parameters.

Sun et al. uses the term *reactant utilization* (RU) in order to quantify the conversion of reactants to products in the solid oxide electrolyzer cells (SOECs). It is not entirely clear, how the term is defined in the paper, but it seems to be used as the term conversion factor (CF) is used in this work i.e. the fraction of oxidized reactants which are converted in the electrochemical reactions alone. This means that their RU does not equate the experimentally measurable conversion of H_2O and CO_2 from the inlet and outlet streams of an electrolyzer, as this would include conversion due to the water gas shift (WGS) and methanation reactions. Rather, their use of RU is related to the electrochemical conversion as measured/set by the current through the cell. This number can be set in the models used, and for a fixed CF, the experimentally measurable RU (inlet/outlet gas compositions and flowrates) will depend on the operating temperatures due to the dependencies of the methanation and WGS reactions.

Figure 5-1is a repetition of Figure 5-3 from the previous chapter, comparing the layout of the Sun et al. model and the one developed in this work. It is repeated here for easy reference.

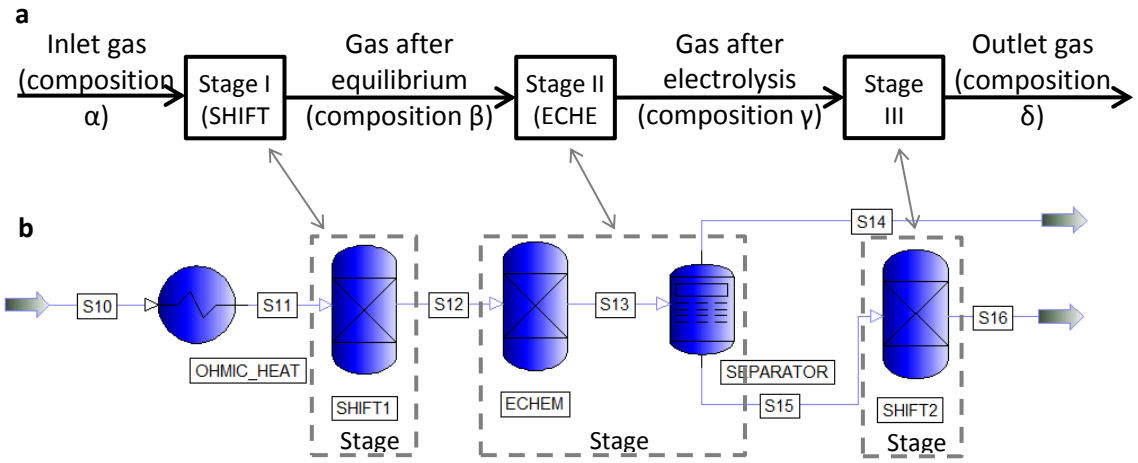

Figure 6-1. Principle behind the 0D thermodynamic SOEC model. a) Modified schematic of the model developed by Sun et al. [2] Each line represent a gas composition and each box represents chemical reactions. b) PFD showing PRO/II implementation of the model. The lines are process streams. The icons are unit operations. The arrows show the correspondence of the PRO/II unit operations to the chemical reactions in the model. SHIFT1 and SHIFT2 represent the WGS and methanation equilibrium reactions. ECHEM and the SEPARATOR represent the electrochemical conversion of CO_2 and H_2O in and the separation of O_2. The OHMIC_HEAT unit operation represents the part of the Joule heating in the cell stemming from > E_{tn} operation.

The PRO/II input file used for the simulations presented in this chapter is included in Appendix A.

6.1 Technological model and fixed feed module

The main difference between the two models is the way they handle the operating conditions and the feed module (FM). In the model by sun et al. the input parameters include operating temperature and pressure, the inlet composition, α (see Figure 6-1) and the conversion factor of Stage II. The Feed module then varies with varying operating conditions. In this work, the model includes control loops constraining the operation of the SOEC according to the pre-set conditions. The two constraints in this case are the control loops keeping the FM) constant in the syngas product and the SOEC recycle loop keeping the Ni-phases of the filter and SOEC reduced. The latter of these loops changes the recycle flowrate according to the H_2 content of the SOEC effluent stream, which depends on the operating conditions. The loop controlling the feed module reacts to changes in operating parameters and recycle rate, by changing the inlet H_2O flowrate to keep the FM of the syngas stream constant. It should be mentioned, that the syngas stream is different from the SOEC effluent stream in that most of the H_2O fraction has been removed in the condenser. The expression for the FM, however, does not include H_2O, and so, this will be the same in the two streams. In this chapter, only the SOEC effluent stream is considered with regards to the compositions resulting from the model. Sun et al. use the symbol "δ" to signify the composition of the effluent stream. This is also used in this chapter.

The fundamental model of Sun *et al*. on the other hand, takes a specific inlet composition and flowrate independent of operating conditions and does not include a recycle loop. This results

in varying flow rates of the outlet stream. This causes the FM to vary with the operating temperature and pressure, which is illustrated in Figure 6-2 a) and b) respectively. The diagrams in the figure reproduce the compositions of SOEC outlet streams from figures 8 and 14 from Sun *et al*. in addition to the combined mole fraction of all carbonaceous species ($x(C_{comb.})$) and the FM, both calculated from Sun et al.s data.

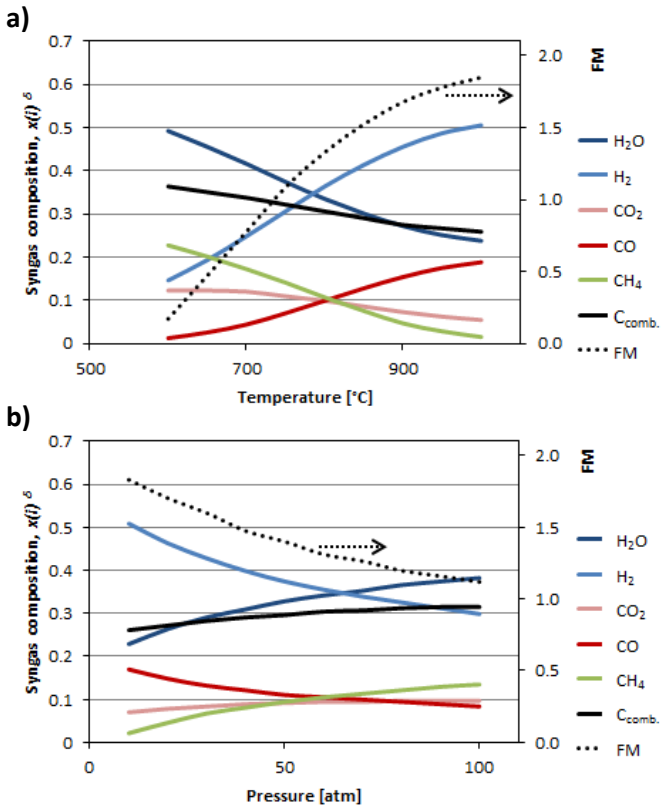

Figure 6-2. Equilibrium composition (δ) from figures 8 and 14 in Ref.[2] vs. temperature (a) and pressure (b) along with the combined mole fraction of all carbonaceous species ($C_{comb.}$, black curve) and the FM (dashed) calculated from the molar compositions.

The figure shows how the FM (dotted lines) increases with increasing temperature (a) and decreases with increasing pressure. The FM is independent of the WGS reaction as this reaction is incorporated in the module, and so the methanation reaction is the only contributor to the observed effect as the inlet composition was kept the same for all simulation conditions. The methanation reaction consumes H_2 three times faster than CO, which means that when the equilibrium is shifted towards methane, the FM drops. This is seen in Figure 6-2 a) as more methane is produced at lower temperatures and Figure 6-2 b) as more methane is produced at higher pressures. $x(C_{comb.})$ increases with $x(CH_4)$ as H_2 is consumed, lowering the total amount of gas in the stream.

6.2 Operating parameters and syngas production

With the base case syngas plant model, a series of parameter case studies were run in order to investigate the influence of the main operating parameters on the synthesis gas composition, under the constraints of the developed model. A small amount of N_2 is present in the gas streams of all simulations, stemming from the air capture plant. This was included in the calculations, and it was below 0.5 % in all cases. Thus, it is not shown in the diagrams.

The dependence of the composition of the SOEC effluent stream (S16, composition δ) on operating temperature (T_{stack}) was studied at FM = 3, corresponding to methane production, CF = 70 % and pressures of 50 atm and 80 atm. The results are shown in Figure 6-3..

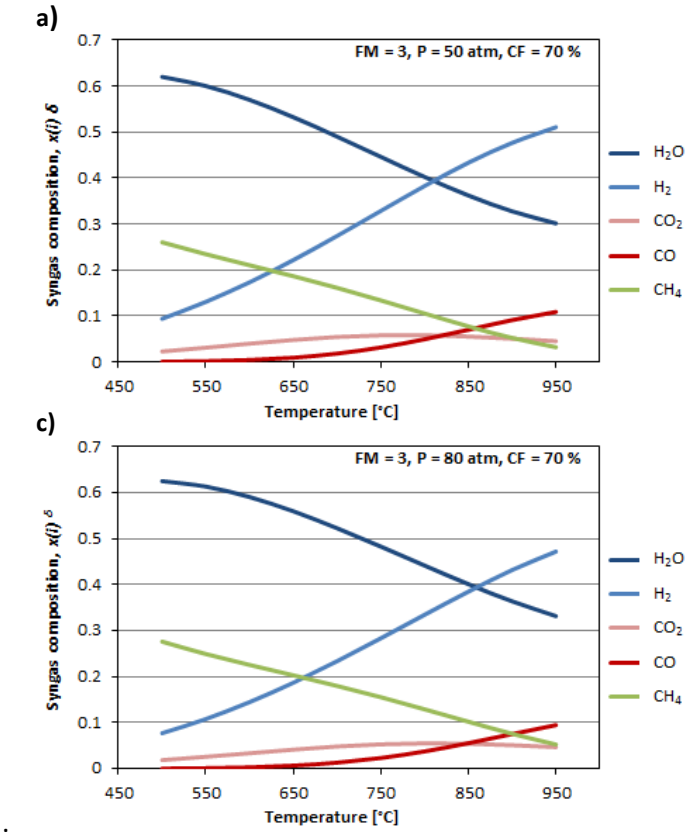

Figure 6-3. Effect of temperature on the composition of SOEC effluent stream (S16, composition δ) in mole fraction (x(i)δ) of each compound. CF = 70 %. a) P = 50 atm. b) P = 80 atm.

In general, the diagrams in the figure show the clear exothermicity of the methanation reaction, as the methane content increases for lower temperatures. At higher temperatures, where the methanation reaction is suppressed, the WGS reaction dominates the equilibrium composition, and $x(CO_2)^{\delta}$ is seen to decrease.

The pressure difference between a) and b) shows how the methanation reaction equilibrium is shifted only slightly towards methane at high pressures. This is further elaborated in Figure

6-4, showing the pressure dependence of the composition, still for FM = 3 and CF = 70 % and at T_{stack} = 850 °C.

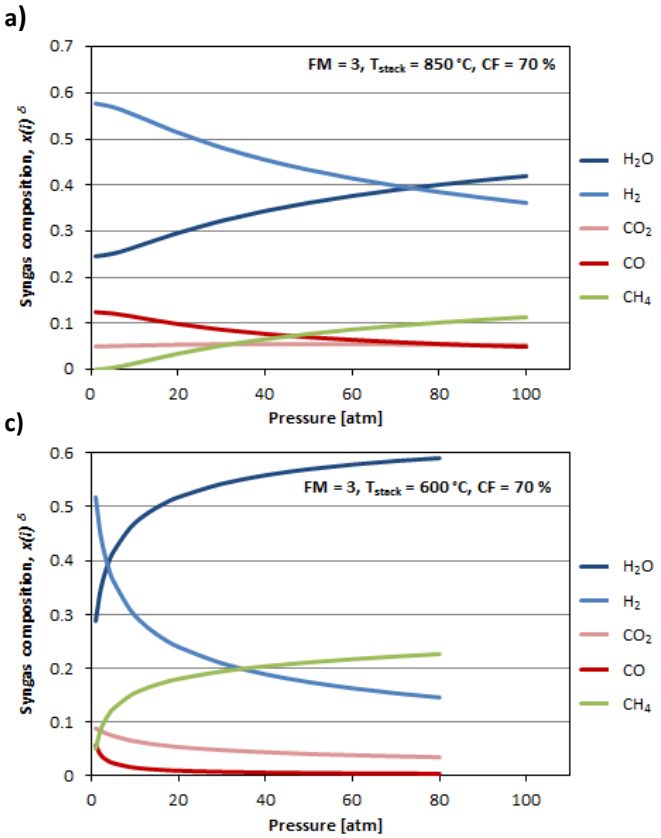

Figure 6-4. Effect of pressure on the composition of SOEC effluent stream (S16, composition δ) in mole fraction ($x(i)^{\delta}$) of each compound. CF = 70 %. a) T_{stack} = 850 °C b) T_{stack} = 600 °C

The diagrams show the pressure dependence of the methanation reaction, as the mole fraction of methane increases with increasing pressure in accordance with Le Chatelier's principle. It should be noted, that while $x(CH_4)$ increases in the entire pressure range from 1 to 100 atm, the effect is largest at low to intermediate pressures (app. 1 ~ 2 atm) after which the curve starts to level off, depending on the temperature. As an example of the slowing trend, $x(CH_4)^{\delta}$ at 850 °C is only 0.150 at 200 atm (not shown) compared to 0.11 at 100 atm. The difference between 850 °C and 600 °C however is dramatic, and especially in the lower pressure range, at 600 °C, $x(CH_4)^{\delta}$ increases sharply after which it starts levelling off, as was observed from the difference between the two diagrams in Figure 6-4.

The expected effects of pressure on the other participants in the reaction are also seen, while the $x(CO_2)^{\delta}$ remains almost constant as the WGS reaction is independent of pressure.

6.2.1 Effect of conversion on composition

A series of simulations were run similar to the ones for temperature and pressure at T_{stack} = 850 °C, for FM = 3 and at pressures of 50 and 80 atm, varying the CF. The results are shown in Figure 6-5.

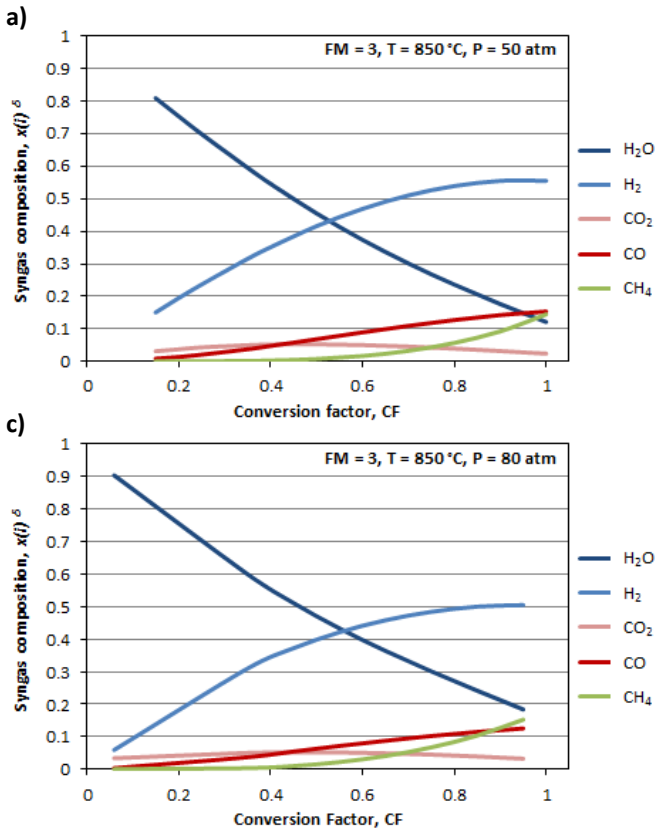

Figure 6-5. Effect of reactant utilization on the composition of SOEC effluent synthesis gas stream (S16) in mole fraction (x(i)δ) of each compound, ignoring N2. TSOEC = 850 °C. a) P = 50 atm. b)P = 80 atm.

The diagrams show how the water content drops as more is converted in the SOEC as expected. The methanation production also increases as more CO and H_2 is made available with higher conversion. At 100 % conversion, the water content is between 10 % and 20 %, depending on the pressure, as it is produced in the methanation reaction at the fuel electrode outlet. Small amounts of CO_2 are also present at 100 % conversion governed by the WGS equilibrium.

More CO is produced with increasing conversion of CO_2 (CF) as expected. For low CF, there is an increasing trend governed by the WGS reaction as H_2 is produced in over-stoichiometric quantities. This drives the WGS reaction towards CO and H_2O. As the methanation reaction starts consuming CO, however, $x(CO)^{\delta}$ goes through an inflection point and the curve flattens as the methane content rises.

In general, the goal of syngas generation for downstream fuel production should be to generate as large amounts of H_2 as possible in the SOEC. This calls for operating the cells at high CF, high pressure and temperature. In some cases, such as for the production of methanol or DME, large quantities of methane in the syngas is detrimental to the fuel synthesis reactions, and a mode of operation should be found to minimize methane production. The easiest way to suppress the methanation reaction is to operate the SOEC at low pressure and high temperature. In this case a high CF should be considered in order to increase the amount of H_2 produced. This may lead to issues with carbon formation as will be discussed below, and with increased conversion resistance due to local fuel starvation, which usually becomes visible around reactant utilizations = 80 % – 90 %.

In the case of methane production, large methane quantities in the syngas is not an issue, and might be favorable as is discussed below.

6.3 Effect of operating parameters on SOEC energy consumption

The study of operating parameters above show that the methanation reaction is highly sensitive to temperature and pressure, and has a large effect on the composition of the SOEC effluent stream, especially at elevated pressures and/or low temperatures. As explained in the introduction, the methanation reaction is highly exothermic, and can contribute significantly to the heat production of the cell, consequently lowering the thermoneutral voltage of the cell at certain operating conditions. This is shown in Figure 6-6 for varying temperature and pressure. The diagrams result from simulations with the BC model at FM = 3 and CF = 70 %. The thermoneutral potentials are calculated as the duties of the units in the SOEC model as described in Chapter 5. The layout of the SOEC model is repeated in Figure 5-3

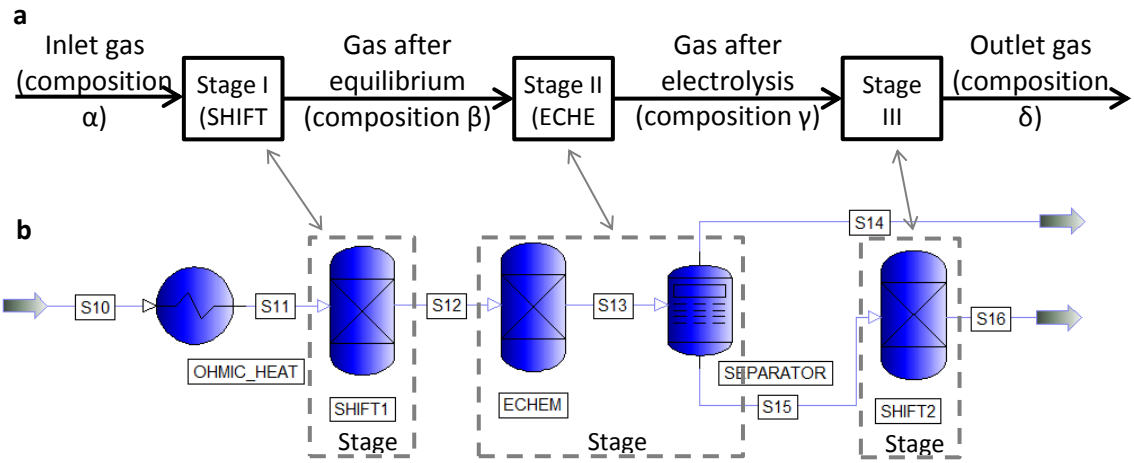

Figure 5-3 at the beginning of this chapter. In summary, the basic thermoneutral potential, E_{tn}, is calculated from the enthalpy changes of the Gibbs reactors, SHIFT1 and SHIFT2 in addition to that of the conversion reactor ECHEM:

$$E_{tn} = \sum^{n} \Delta H_n / 2F = \frac{\Delta H_{SHIFT1} + \Delta H_{ECHEM} + \Delta H_{SHIFT2}}{2F} \qquad \text{Eq. 6.1}$$

Thus, E_{tn} takes the electrochemical conversion, WGS and methanation reactions, along with the joule heating which can be consumed as the $T\Delta S$-contribution to the total reaction enthalpy.

In the terminology of Sun et al. the thermoneutral potential of the electrochemical conversion alone, is given only by the enthalpy change of the ECHEM conversion reactor:

$$E_{tn0} = \sum^{n} \Delta H_n / 2F = \frac{\Delta H_{ECHEM}}{2F} \qquad \text{Eq. 6.2}$$

Figure 6-6 compares the two thermoneutral potentials to the methane production for varying temperatures and pressures. The CF was 70% in all cases, and FM = 3.

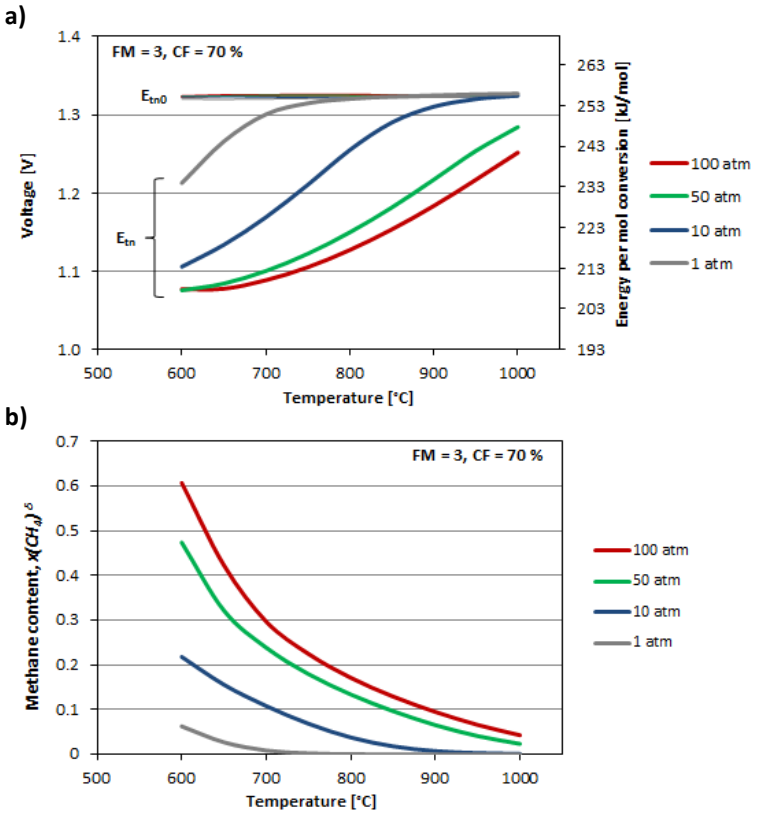

Figure 6-6. Effect of the methanation reaction on the thermoneutral potential of the SOEC in the BC syngas model. FM = 3, CF = 70 %. a) Thermoneutral potential of the co-electrolysis reaction (Etn0) and the thermoneutral potential including WGS and methanation reactions (Etn) as function of temperature and pressure. b) Mole fraction of methane in the SOEC effluent stream as function of temperature and pressure.

A small rising trend of E_{tn0} is observed, but not visible in the figure. Such a trend would not be expected as the electrochemical reactions should be independent of pressure. The ratio of H_2O

to CO_2 in the inlet stream changes slightly in order to keep the FM constant, however, which changes the E_{tn0} slightly. The considerable amount of energy developed by the methanation reaction however, is clearly seen as a significant lowering of E_{tn} at high pressures and/or low temperature. As the thermoneutral voltage decreases, so does the cell power if CF and thus the conversion current is kept constant. This means that less energy has to be supplied to the stack as a larger part is supplied by the methanation reaction directly in the cell.

This effect has led some authors [77, 100] to suggest low temperature operation of SOECs at intermediate to high pressures in order to increase the electrical efficiency of the operation. As mentioned above, this is only relevant in applications where relatively large methane contents are viable with regards to the technological application. In the case of reversible SOC (ReSOC) operation for energy storage applications for example, high methane content is suitable in that it has a higher energy density than syngas. This is possible because the methane is easily converted in fuel cell mode due to the activity towards steam reforming of the fuel electrode Ni catalyst.

In the case of syngas generation for methane production, as is the goal of this project, it is unclear whether high methane content in the syngas is beneficial for the overall process. Generating some of the heat from the methanation directly in the SOEC instead of in a downstream reactor decreases the heat losses from integration. On the other hand, the lower operating temperature of the SOEC increases internal resistances. This will be studied in more detail over the following four chapters.

6.4 Carbon formation in the syngas plant

Sun et al. evaluated the risks of solid carbon formation at varying operating temperature, pressure and *reactant utilization*. They use the term *threshold pressure for carbon formation* under which, no solid carbon is formed. Two main conclusions were drawn:

4. At reactant utilizations (assumed to mean CF) of 60, 70 and 80 %, no solid carbon is formed for CO_2 concentrations below 40 % in the inlet stream (composition α).
5. The *threshold pressure for carbon formation* is around 54 atm at 850 °C for $x(CO_2)^{\alpha}$ = 45 % with $x(H_2)^{\alpha}$ = 10 %.

Typical values of $x(CO_2)^{\alpha}$ in the BC model are around 15 - 20 % for FM = 3 depending on the operating conditions. This means that there is a large margin to the 40 % found by Sun et al. This implies that the *threshold pressure for carbon formation* is significantly higher than the ~54 atm reported. The operating temperature and pressure of the base case where chosen based on the above results of Sun et al. however, and the BC parameters (T_{stack} = 850 °C, P = 50 atm, CF = 70 %) were used to evaluate the risks for solid carbon formation below.

The regions of thermodynamic stability of solid carbon in the space of operating parameters were mapped by looking at the isotherms and isobars of carbon formation in ternary C-O-H composition diagrams calculated in FactSage®.

Figure 6-7 shows the isotherms (a) and isobars (b) of carbon formation at temperatures between 550 °C and 950 °C and pressures between 1 atm and 90 atm respectively. In both diagrams, the compositions of the filter inlet stream, the SOEC effluent stream and the syngas stream after water recovery are shown. These are calculated in PRO/II at the operating parameters of the base case (see above for the parameters).

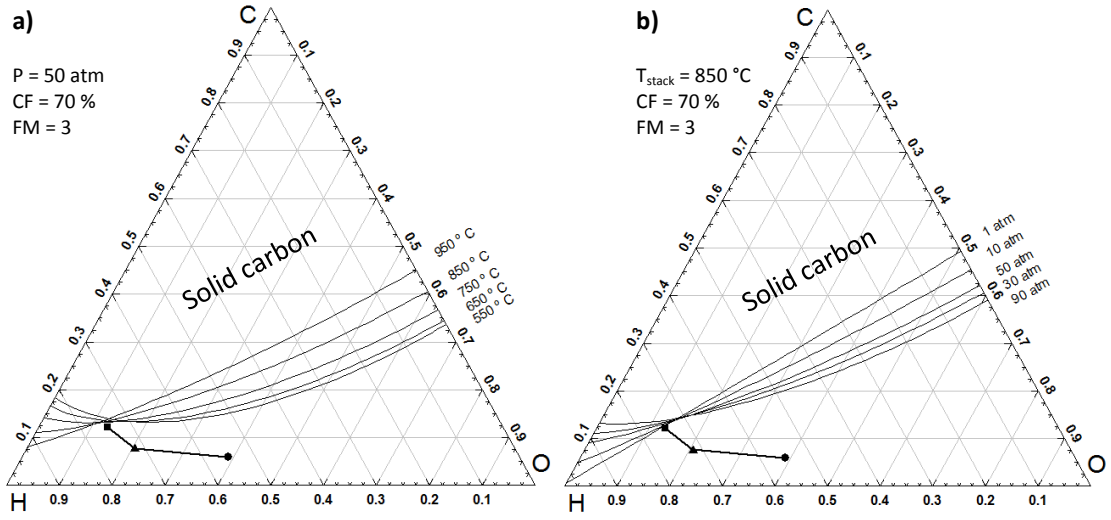

Figure 6-7. C-O-H ternary composition diagram including the compositions of the filter inlet stream (●), the SOEC effluent stream (▲) and syngas stream (■) of the BC operation. a) Isotherms for carbon formation are shown for temperatures between 550 °C and 950 °C at P = 50 atm. b) Isobars for carbon formation at pressures between 1 atm and 90 atm at T = 850 °C.

The composition lines, representing the conversion of the inlet stream (●) via the SOEC effluent stream (▲) to the syngas stream (■), show that the composition in the SOEC (●- ▲) is not close to the region of thermodynamically stable solid carbon. The syngas product is extremely close to the carbon forming regions, but it should be noted that no Ni catalyst is present outside the SOEC and filter in the syngas plant. Also the condensation happens at around 128 °C at 80 atm. At these conditions the Boudouard reaction is extremely slow even in the presence of a Ni catalyst. The compositions only showed minute variations with T and P which is why only one set of points is shown. The reason for this is that only the WGS and methanation reactions depend on T and P, and they do not change the overall ratio between C, O and H.

Only the FM and CF influence the R-O-H ratio, which is illustrated in Figure 6-8. The influence of the target FM is through balancing the flowrate of H_2O compared to the constant flowrate of CO_2. When the H_2O:CO_2 ratio changes, the C-O-H ratio changes as well. The CF defines how much oxygen is removed in the SOEC, and thus directly influences the C-O-H ratio. Figure 6-8 shows the 750 °C and 850 °C isotherms corresponding to the filter and stack temperatures in the BC respectively at 50 atm. Along with these, the compositions at the filter inlet, SOEC effluent and syngas streams are given at feed modules between 1 and 3 (a) and conversion factors between 50 % and 100 % (b). For the CF, the syngas composition (■) is only shown for

CF = 100 %. These positions (filter inlet, SOEC outlet and condenser outlet) are chosen as they represent the three different values of the R-O-H ratio in the model, as the WGS and methanation reactions do not change this ratio.

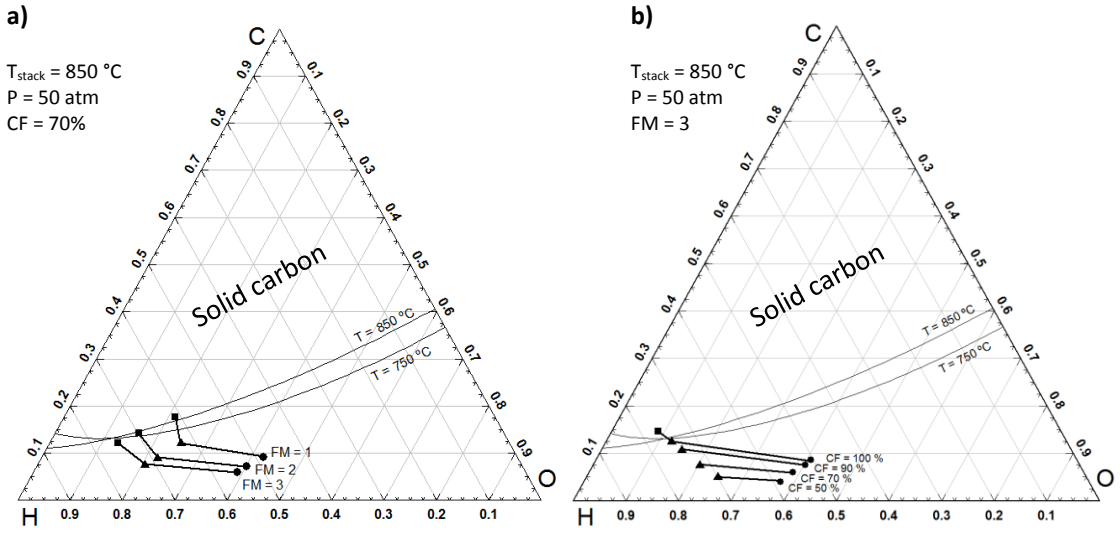

Figure 6-8. C-O-H ternary composition diagram. The isotherms for carbon formation are shown for the filter (750 °C) and stack (850 °C) temperatures. Compositions of the filter inlet stream (●), the SOEC effluent stream (▲) and syngas stream (■) are shown for a) varying FM and b) varying CF.

The diagrams show how the C-O-H ratio depend on the FM and CF. As for the BC values (FM = 3 and CF = 70 %), none of the calculated compositions for the filter inlet and SOEC effluent streams are in the region of solid carbon formation, and the syngas stream cannot form carbon due to the lack of catalyst as explained above. For conversion factors above 90 %, the SOEC outlet stream is approaching the solid carbon region (b).

The conversion resistance in of SOCs is known to be visible in polarization curves around a reactant utilization of 80 % - 90 % (No Reference Selected), which is usually interpreted as localized reactant starvation of the atmosphere close to the active Triple Phase Boundaries (TPB) of the fuel electrode due to a high conversion rate. In the ternary diagrams, this would be seen as a drift of the local composition upwards and to the left, and thus closer to the carbon forming region. For this reason, the cells should be operated with a clear margin towards the region of stable carbon in order to avoid carbon formation. The value of the BC of 70 % is chosen to represent a high conversion but also one staying well in the clear of carbon formation due to local variations in the gas phase composition of the fuel electrode.

6.5 Summary

In this chapter, the simulation results of operating the syngas plant model at varying operating conditions were presented.

With the feed module fixed at FM = 3, the main contribution to the compositional changes was the methanation reaction, which is highly dependent on temperature, due to its exothermicity, and pressure, in accordance with Le Chatelliers principle. The pressure dependence was seen to be larger in the low to intermediate pressure region (1 atm – 20 atm) depending on the temperature.

Tracing the thermoneutral potential of the SOEC at varying temperature and pressure showed strong dependence of the voltage with operating parameters, caused by the extent of the methane production taking place inside the cell. As expected, this is caused by the heat developed by the reaction, contributing to the electrolysis reaction. At constant current, governed by the flowrate and CF, this will lead to a lower cell power and thus lower electrical efficiency. The potential benefits of a low temperature strategy for methanation production remains to be studied in the framework of the full plant developed over the next chapters.

With the FM fixed at 3 and CF well below 100 %, the inlet and outlet compositions of the SOEC were seen to be well outside the region of stable carbon formation. At low conversion, this is assumed to be the case even in the volume close to the triple phase boundaries of the SOEC, and thus, carbon formation is assumed not to be an issue.

In the following chapters, the full plant is designed and models based on the syngas plant model, discussed above.

Chapter 7 Methanation and full plant

In this chapter, the full plant for synthetic fuel production is developed from the synthesis gas plant described in Chapter 5 .

In the following, a series of simulations are presented in order to aid the design decisions made, leading to the final SNG plant, and two design cases of the plant are presented, for use in the rest of the thesis. After this, the possibilities of internal heat recovery are discussed and the heat exchanger network (HEN) is synthesized. Finally, the pressure drops of all units in the plant are estimated and sizing and costing calculations for the units are presented along with the finalized product flow diagram (PFD) of the full plant. These considerations form the basis of the economic analysis of the following chapter.

7.1 Methanation Plant

As mentioned, several different synthetic fuels can be produced from the syngas produced by the syngas plant, depending on the layout of the downstream reactors and syngas composition feed module (FM). In this work, production of methane is chosen in accordance with the need for technologies connecting the Danish electricity and natural gas (NG) grids. In order to feed the produced methane into the grid, the produced substitute natural gas (SNG) needs to be of sufficiently high quality to replace natural gas in the grid. In general, the Danish grid follows the European Association for the Streamlining of Energy Exchange (EASEE) guidelines for natural gas, which requires the Wobbe index to be between 49 MJ/m^3 and 57 MJ/m^3[101]. The Wobbe index is a measure of the energy content in the gas defined as the higher heating value (HHV) divided by the specific gravity of the gas mixture, and depends on the content of CH_4, H_2, H_2O and inerts.

The lower end of the Wobbe index range corresponds to around 99 % methane in SNG mixtrues containing small amounts each of inerts, H_2 and H_2O. This means that optimizing the methane yield is of great importance in order to fulfill the target of feeding the SNG product

directly into the NG grid without addition of higher hydrocarbons, as is common for upgraded biogas.

7.1.1 Feed module and methanation

Conventional strategies of synthesis gas production for fuel synthesis include gasification of coal or biomass for example. The synthesis gasses from these technologies have fixed compositions depending on the hydrocarbon (or carbon) feedstock and the operating conditions. The H_2/CO ratio is below or equal to 1, and in order to increase it, H_2 needs to be added to the syngas before it is fed to the fuel synthesis plant.

Utilizing co-electrolysis for syngas production allows for easy tailoring of the FM of the produced syngas, simply by varying the ratio between the H_2O and CO_2 inlet streams as was discussed in the previous chapters. The advantage of this route is that the extra H_2 is produced in the same setup that produces the syngas, as opposed to an extra system for other technologies.

The feed module was discussed in the introduction of this thesis and the definition is repeated here:

$$FM = \frac{p(H_2) - p(CO_2)}{p(CO) + p(CO_2)} \qquad \text{Equation 7-1}$$

For methane production the ideal value is FM = 3.00. As mentioned, it represents a stoichiometric ratio between the reactants in the methanation reactions, and it turns out, the equilibrium methane content of the produced SNG is highly sensitive to the exact balancing of these reactants, even for very small variations.

In order to study this, the base case (BC) syngas plant model was used to simulate a series of syngas streams with varying FM in the range of 2.90 through 3.10. The syngas streams were then allowed to equilibrate in a methanation reactor modelled as a Gibbs reactor in PRO/II. The reactor model operated the methanation and WGS reactions under adiabatic conditions. The operating pressure was 80 atm and the inlet temperature was 220 °C. The heat development in the reactor was accounted for in the model, but ignored in terms of temperature limits. This particular aspect is discussed in the next section. The resulting mole fractions of CH_4, CO_2 and H_2 are presented in Figure 7-1. All CO was consumed in all cases, and consequently, x(CO) is not shown.

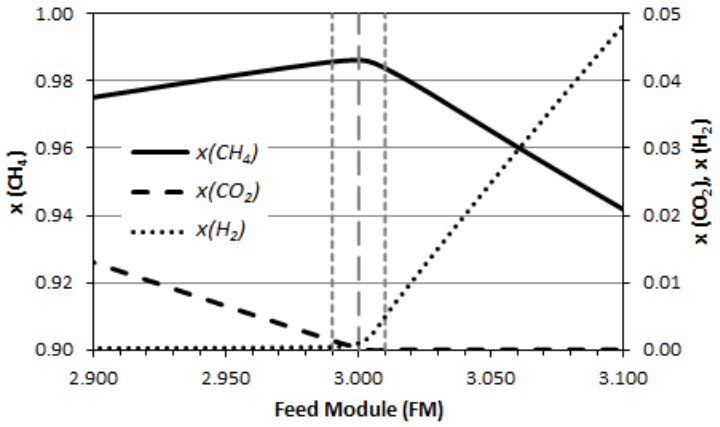

Figure 7-1. SNG composition simulated in an adiabatic Gibbs reactor at 80 atm with an inlet temperature of 220 °C. All CO was consumed and CO and H_2O are not shown.

The figure shows a strong dependence of the SNG composition for very small variations in FM, especially at FM values above 3.000. This emphasizes why careful control with the FM is important in order to achieve compatibility of the produced SNG with the NG. The tight allowance of the FM control loop in the syngas plant (FM = 3.000 ± 0.010) was chosen based on these calculations and this range is shown in the figure.

7.1.2 Need for recycle?

In the section on the methanation reactions and TREMP technology in Chapter 2, the use of a recycle loop after the first reactor in a methanation train for keeping the temperature rise below acceptable limits was discussed. This recycle loop is known to be expensive in terms of capital investment in large scale methanation plants. According to Haldor Topsøe A/S,[102] the price of a $1.4 \cdot 10^9$ Nm^3/y SNG plant is appproximately 1.5 billion €. 10 % of this is the TREMP plant and 20% of this amount is taken up by the recycle compressor. For the expected SNG production capacity of approximately $5.6 \cdot 10^5$ Nm^3/y in this project, these numbers translate roughly into a price for the compressor of 12,000 €, assuming the prices scale linearly with capacity. This calculation of course ignores economy of scale, which would produce a higher price, but serves as an order of magnitude estimate.

In addition to being able to tailor the FM of the syngas, SOEC technology allows for the production of syngas with significant methane content. As the generation of heat in the first methanation reactor depends on the methane content in the feed stream, the possibility of increasing *x(CH4)* of the syngas in order to omit the recycle loop was investigated. The operating temperature and pressure of the BC syngas plant model were varied, resulting in a series of syngas streams with varying compositions at constant FM = 3.00. These streams were allowed to equilibrate in an adiabatic Gibbs reactor with an inlet temperature of 220 °C and operating pressures, P_{METH}, of 50 or 80 atm. The resulting outlet *x(CH4)* and temperatures are shown in Figure 7-2.

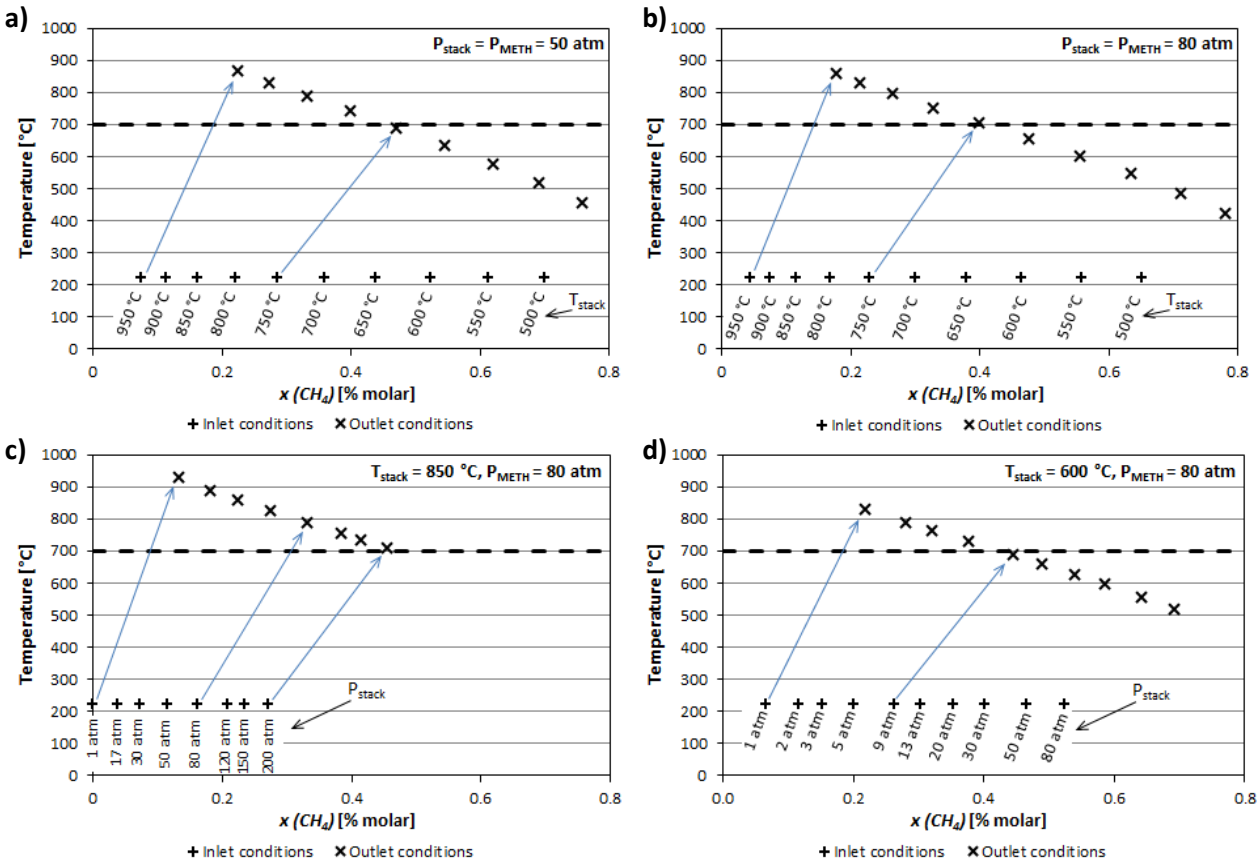

Figure 7-2. Simulated temperature increases of an adiabatic methanation reactor with a feed stream at 220 °C with varying *x(CH₄)*. The correspondence of inlet (+) to outlet (×) compositions are marked for selected pairs. a) and b) show the dependency on T_{stack} for $P_{stack} = P_{METH} = 50$ atm (a) and for $P_{stack} = P_{METH} = 80$ atm (b). c) and d) show the dependency on P_{stack} where $T_{stack} = 850$ °C (c) and $T_{stack} = 600$ °C (d) $P_{METH} = 80$ atm in both cases. The maximum allowable outlet temperature of 700 °C is marked in the diagrams.

In order to maximize the lifetime of the catalyst, the maximum tolerable temperature for the MCR catalysts is chosen for the upper limit of the reactor. This is around 700 °C according to Haldor Topsøe A/S [35], which is marked in the figures. The simulation showed that at $P_{stack} = P_{METH} = 50$ atm (a), the maximum value of T_{stack} resulting in an outlet temperature below 700 °C is $T_{stack} = 750$ °C. This corresponds to a syngas methane content, $x(CH_4) = 28$ % molar and this is the maximum SOEC operating temperature, allowing for the omission of the recycle loop. At 80 atm, the limit is close to 23 % molar, corresponding to a T_{stack} slightly below 750 °C (b). This poses an argument for increasing the pressure of the system from the BC value of 50 atm to 80 atm or even higher.

At the BC temperature of $T_{stack} = 850$ °C, the outlet temperature was above 700 °C in the entire pressure range from 1 atm to 200 atm. The value of *x(CH₄)* increases significantly when T_{stack} is lowered to 600 °C as shown in the previous chapter, and at this T_{stack}, the outlet temperature is below 700 °C for pressures as low as 9 atm. In short, this means that at the BC operating temperature, the recycle loop has to be included. At low operating temperatures, it may be excluded, depending on the selected operating pressure (above 9 atm for $T_{stack} = 600$°C) . A

detailed study of the operating conditions, including the economic consequences of increasing the SOEC area and omitting the recycle compressor is needed to select the optimal operating conditions, which is outside the scope of this work. Two cases are analyzed later in this thesis shedding some light on these differences however.

7.1.3 Operating conditions of full plant design cases

As discussed above, it is advantageous to operate the system at high pressures. On the other hand, pressurization of gasses is expensive in terms of energy and equipment, meaning, the amount of pressure change operations should be kept small. Also, the investigations on CO_2 pressurization in Chapter 5 showed that it is highly advantageous to pressurize the water stream in the evaporation step. The flow rate of H_2O in the SOEC is about 4 times that of the CO_2 stream. This means, it is expected to be advantageous to operate the entire plant at the pressure required for delivery of SNG to the NG grid, as this allows full utilization of the cheap pressurization of H_2O from the liquid state. This assumption negates the added costs of equipment for pressurized operation, such as the SOEC and methanation reactors. On the other hand, both the SOEC and methanation reactors are favorably operated at high pressures even though the advantages of increasing the pressure are higher in a low to intermediate range than in a high pressure range, as was seen in the previous chapter. This is in good accordance with the results of Hansen et al., modelling a co-electrolysis/methanation plant at intermediate pressures (10-20 bar) [103].

The Danish natural gas grid specifications are used to set the delivery pressure of the SNG product and as a consequence of the above considerations, the operating pressure of the entire system. The pressure of the transmission lines in the Danish NG grid is 70 – 80 [101], and consequently, the operating pressure of the plant including the SOEC and methanation subsystems is set to 80 atm.

As mentioned in Chapter 2, high pressure operation of the SOEC subsystem allows for significantly higher electrical efficiencies due to the heat supplied directly in the SOEC by the methanation reactor. This was also confirmed by the results from the syngas plant simulations. It is unclear whether such low temperature operation is advantageous for synthetic fuel production, but this will be tested in this work. Based on the results from the syngas plant, and the above discussion on pressurization, two cases of the full plant are studies in the remainder of this report: Both will be operated at high pressures, but at different temperatures.

Design case 1: *High temperature operation*: In this case, the low ASR of the SOEC when operated at high temperatures is utilized and the operating temperature (T_{stack}) is set to 850 °C, which decreases the needed cell area. The operating pressures of both the SOEC and methanation subsystems are set to 80 atm.

Design case 2: *Low temperature operation*: In this case, the increased electrical efficiency obtained by increased methane production inside the SOEC is utilized in order lower the consumption of electricity in a trade-off for a higher cell area as ASR increases at low temperatures. The operating temperature (T_{stack}) is 600 °C and the pressure is 80 atm for the

SOEC and methanation subsystems. In this case, the Rx 1 recycle loop is omitted from the methanation plant.

7.1.4 Structure of the methanation plant

The amount of reactors in a methanation train is fixed by the syngas compositions, operating conditions and available equipment in the case of revamp projects. The plant designed in this project is a grassroots plant, which means the consequences of different numbers of reactors (Rx) and the placement of the condenser has to be analyzed.

A generic representation of a methanation train is shown in Figure 7-3. Four reactors (Rx 1 through Rx 4) are shown along with the Rx 1 recycle. Between each reactor (Position 1 through 3) an intercooler is placed, and at one of those positions, a condenser may be placed to recover the H_2O content before the stream is reheated and fed into the following reactor.

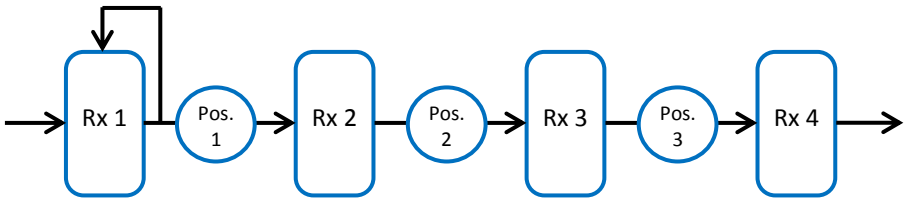

Figure 7-3. Schematic representation of the reactors (Rx) in the methanation train. Between each reactor (positions 1 through 3), an intercooler or the condenser system was placed.

The analysis was conducted by simulating the various layouts of the methanation train in PRO/II. The methanation reactors were represented by adiabatic Gibbs reactors allowing the methanation and WGS reactions to take place. The inlet stream was the syngas stream from the BC syngas plant heated to 220 °C. On each position 1 through 3, either a heat exchanger cooling the gas stream to 220 °C or a condenser in the form of a heat exchanger, a flash unit and a heat exchanger bringing the stream back up to 220 °C was placed. The component molar flowrates of the reactor and condenser outlet streams are shown in Figure 7-4 for each placement of the condenser (Pos. 1-3). The small fraction of N_2 present in the system (~0.013 kmol/h or ~0.4 %) is inert and is not shown in the diagrams. Both the high and low temperature design cases (cases 1 and 2 respectively) were analyzed.

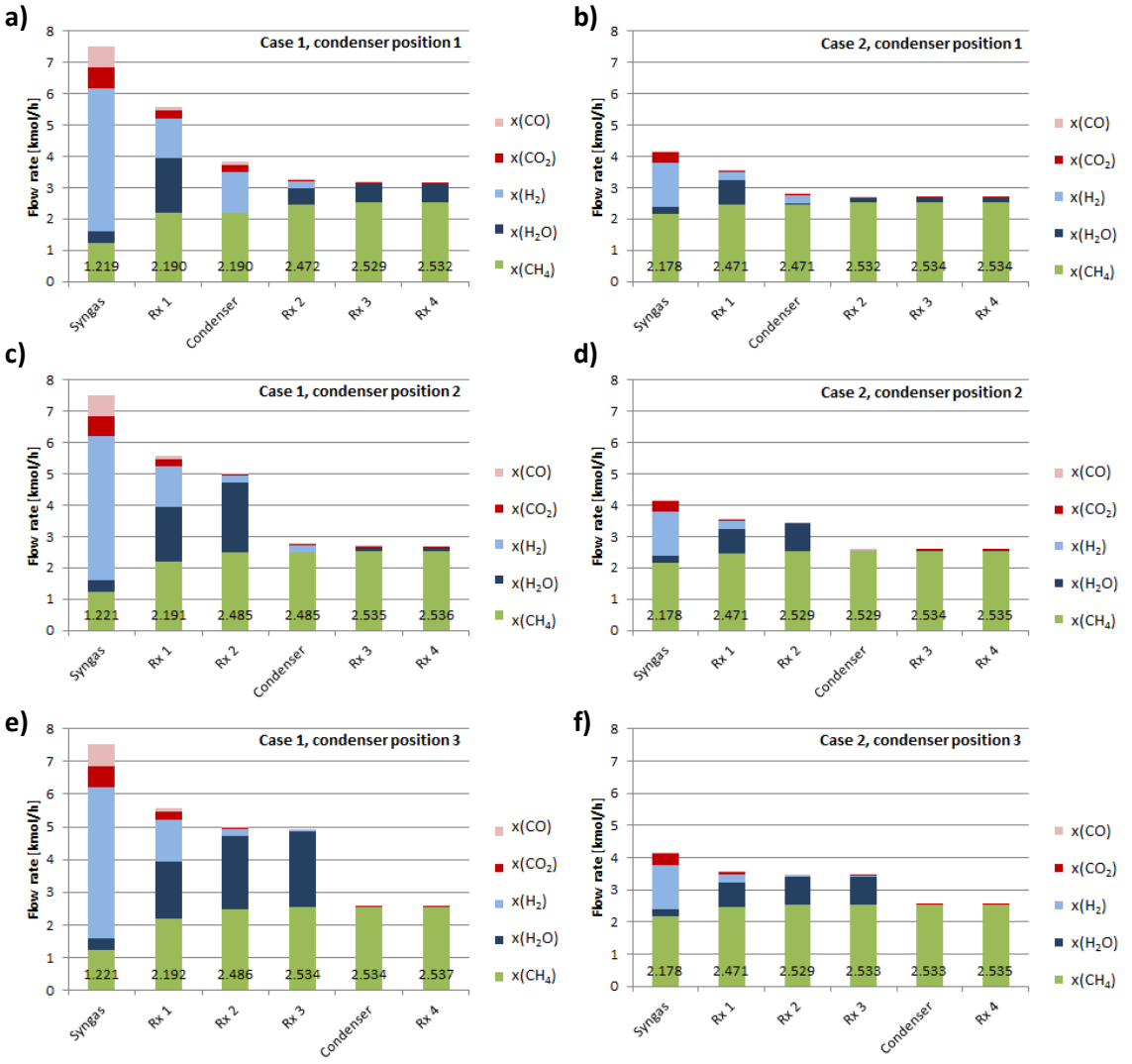

Figure 7-4. Simulated molar flowrates of all stream components at the methanation train inlet, at the outlet of each methanation reactor and at the outlet of the condenser for each of the three positions in each case. For case 1, the flowrate from Rx1 is calculated downstream of the recycle splitter. The flow rates of the methane fraction are given in kmol/h in each diagram. around 0.013 kmol/h of N_2 are present in the streams (~0.4 %). This fraction is not shown in the diagrams.

The figure generally shows how the methane flowrate in the gas streams of both cases, $f(CH_4)$, increase as CO, CO_2 and H_2 is consumed. The SNG compositions and methane flowrates out of Rx 4 are very similar in both cases and for each position of the condenser. In case 1, $f(CH_4)^{Rx\ 4}$ is slightly lower for position one, and larger for position 3. In case 2, the resulting $f(CH_4)^{Rx\ 4}$ is slightly lower for position 1 and the same for positions 2 and 3. Further, the increase in methane content in Rx 4 compared to Rx 3 for the setups with the condenser in position 3 (e and f) is quite small, which makes it tempting to remove a reactor from the PFD. The difference in $f(CH_4)$ in the effluent streams from the condenser and Rx 4 is on the order of 600 Nm^3/y, assuming the plant operates for 8400 hours per year. However, the reactors are quite small, as will be shown later, and with this information, the position 3 layouts with four reactors is chosen for both design cases.

7.1.5 Carbon formation in the methanation reactors

From the results of the syngas plant model simulations, it was concluded that at sufficiently low electrochemical conversion in the SOEC, the gas composition in the SOEC is outside the region of solid carbon formation. This was the case for both high and low temperatures due to the large amount of H_2O in the stream at the given operating conditions. The results also showed that after the removal of H_2O, the composition of the syngas stream was within the region of stable carbon formation.

Below, the regions of thermodynamically stable, solid carbon at the inlet temperature (220 °C) and maximum outlet temperature (700 °C) of the methanation reactors are illustrated in the ternary C-O-H composition diagram. The isotherms are shown for P = 50 atm and P = 80 atm, and the compositions of the syngas stream of both design cases (850 °C and 600 °C) are shown along with the composition of the SNG product stream in both cases.

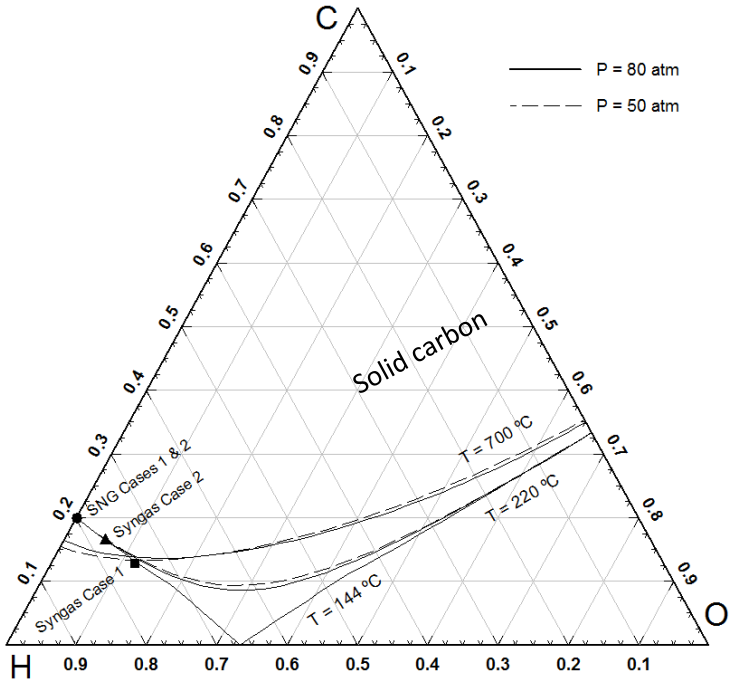

Figure 7-5. C-O-H ternary diagram showing the limits for solid carbon formation at the syngas stream temperature (144 °C), the inlet temperature (220 °C) and maximum outlet temperature (700 °C) of the methanation reactors at P = 50 atm and P = 80 atm. The stream compositions of the syngas in both design cases (P = 80 atm and T_{stack} = 850 °C (■) and 600 °C (▲) respectively) are shown in the diagram along with the composition of the SNG for both cases (●).

From the figure, a series of conclusions may be drawn. Firstly, in this part of the pressure range, lowering the pressure from 80 atm to 50 atm only has a minor impact on the position of the isotherms of carbon formation. Further, at the outlet temperature of the condenser (144 °C), which recovers the H_2O fraction from the syngas stream, the composition is close to the region of thermodynamically stable solid carbon. In this part of the plant, no Ni catalyst is present however, and the rate of carbon formation at these temperatures, even on a Ni catalyst, is so low that this would not pose any problems anyway.

Finally, the syngas composition lies outside the region of carbon formation at the inlet and maximum outlet temperatures of the methanation reactors in case 1. For case 2 where more H_2O has been produced by the methanation reaction in the SOEC and subsequently removed in the condenser, the syngas composition is well within the region at high temperatures as encountered in the first reactor. The SNG compositions of both cases is on the isotherm at the reactor inlet temperatures, which is close to the outlet temperature of Rx 4 (222 °C) This means that from a thermodynamic point of view, there is a risk of carbon formation in RX 1, Rx 2, Rx 3 and, possibly, Rx 4.

An important conclusion from the literature on the formation on various forms of solid carbon on steam reforming and methanation catalysts [104, 105] is that the size of the Ni-catalyst particles has an important effect on carbon formation. For sufficiently small Ni-particles, carbon deposition can be avoided entirely, even at high temperatures. The MCR catalysts, which are assumed to be used in this work, have been operated successfully by Haldor Topsøe A/S, inside the carbon forming region, for several years, and even though this may limit the lifetime of the catalysts, such operation is possible and economically feasible[35].

7.2 Full plant model

With the decision to use 4 reactors in the methanation train of both design cases, and the decision to omit the RX 1 recycle loop in case 2 (low temperature), the PRO/II model was expanded to include the methanation plants as well. The layouts of both design cases 1 (high temperature) and 2 (low temperature) are shown in the PFDs in Figure 7-6 and Figure 7-7.

The PFDs of the models now consist of the syngas plant, including pressurization of the inlet streams, the filter, SOEC and condenser for water recovery, in addition to the methanation train with the four reactors with intercooling and the condenser. Both condensers (one in each sub-plant) send the recovered H_2O back to be mixed with the H_2O inlet stream before it is evaporated. The PFDs of the two design cases differ only in that the recycle loop around the first methanation reactor is not included in case 2.

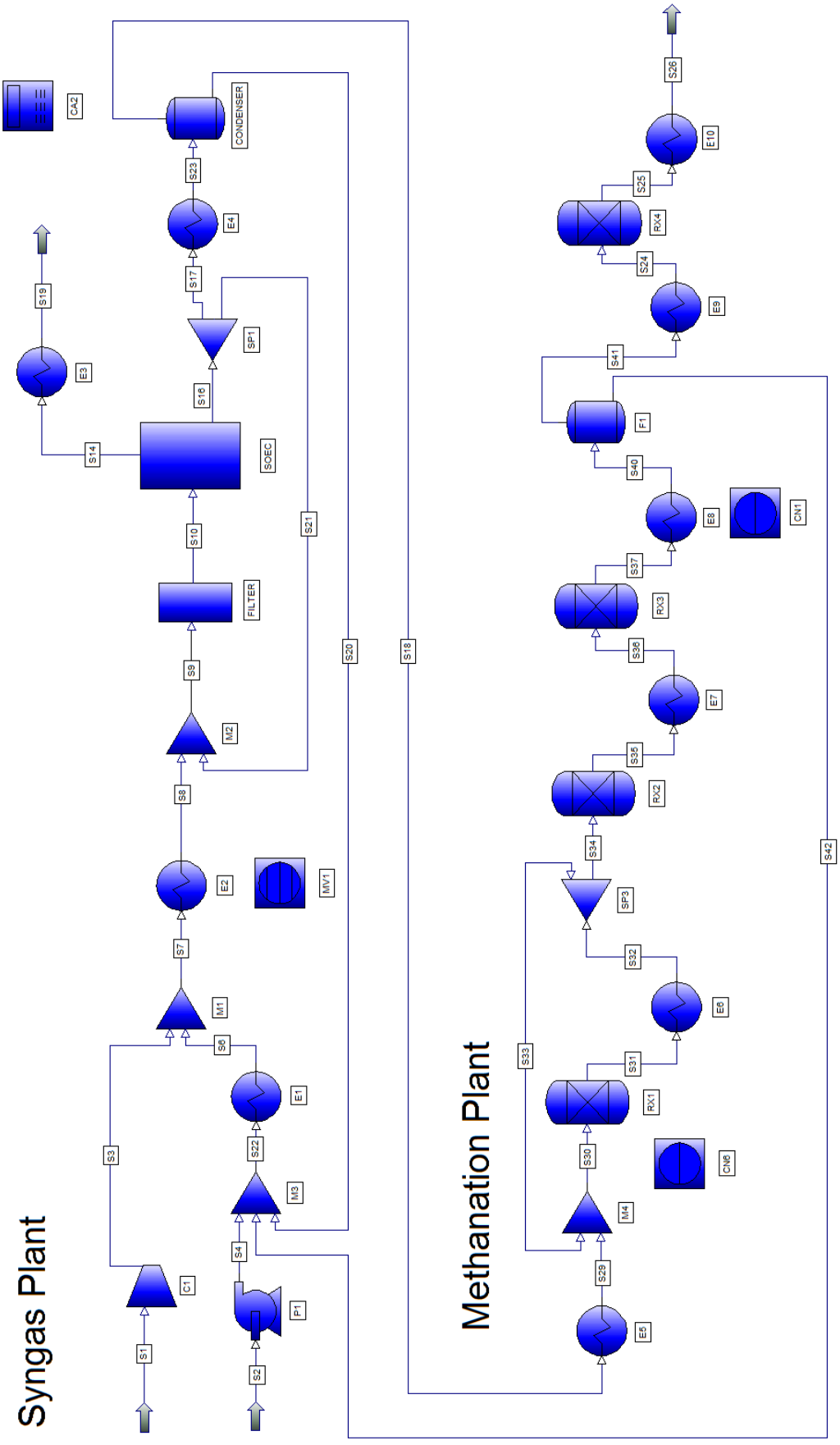

Figure 7-6. PFD showing the full plant high temperature design case 1.

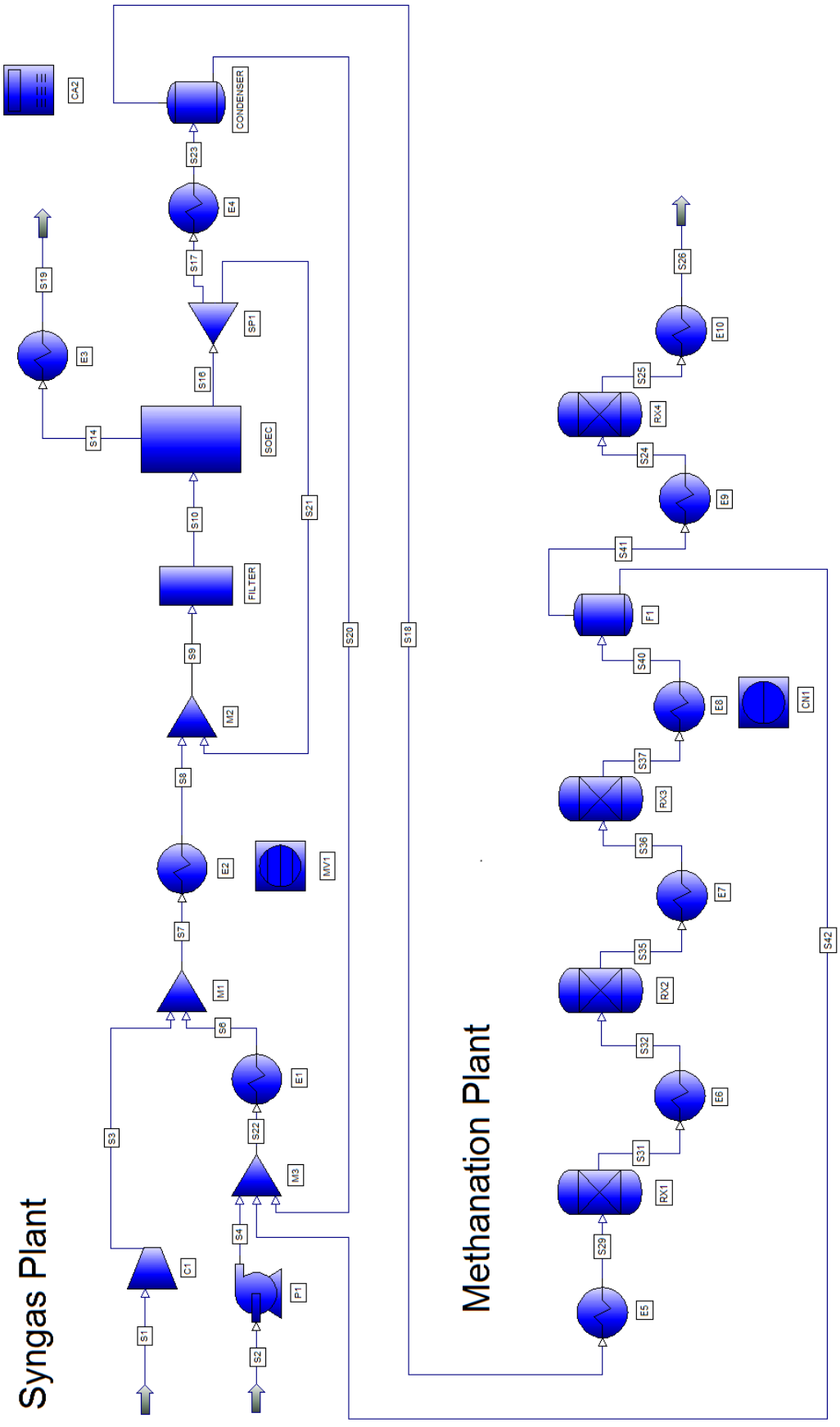

Figure 7-7: PFD showing the full plant low temperature design case 2

The units in the syngas plant are the same as for the base case described in Chapter 5. They are briefly summarized here, and the units of the methanation plant are added:

Syngas Plant

- **S1:** CO_2 inlet stream.
- **C1:** CO_2 inlet compressor ($\eta_{adiabatic}$=75 %).
- **S2:** H_2O inlet stream.
- **P1:** H_2O inlet pump ($\eta_{adiabatic}$=80 %).
- **M3:** Mixes the H_2O inlet and recycle streams.
- **E1:** H_2O evaporator.
- **M1**: Mixes the CO_2 and H_2O streams.
- **E2:** SOEC pre-heater.
- **M2:** Mixes the SOEC input stream with the SOEC recycle stream.
- **FILTER:** Removing impurities and O_2 (adiabatic Gibbs reactor).
- **SOEC:** Models the WGS, methanation and electrochemical conversion in the stack along with Joule heating.
- **E3:** O_2 byproduct heat recovery
- **SP1:** Splits off SOEC recycle stream (app. 3 %) to keep filter and SOEC-cathode reduced.
- **E4:** Condenser cooling.
- **CONDENSER:** Separates the liquid water from the vapor phase (flash unit).
- **S18:** Syngas product stream.

Methanation plant

- **E6** is the methanation preheater, increasing the temperature of the syngas stream (S18) to the required inlet temperature of the first methanation reactor (Rx 1) which is 220 °C.
- **M4** is a mixer adding the Rx 1 recycle stream to the feed stream. This is only included in case 1.
- **Rx1** is the first methanation reactor. It is modelled as an adiabatic Gibbs reactor with the methanation and WGS reactions enabled.
- **E6** is the first intercooler heat exchanger which cools the effluent stream of Rx 1 to 220 °C.
- **SP3** is a splitter, which removes a part of the stream S32 and sends it back to M4 upstream of Rx 1. This is only included in case 1.
- **Rx2** is the second methanation reactor with the same settings as Rx 1.
- **E7** is the second intercooler heat exchanger which cools the effluent stream of Rx 2 to 220 °C.
- **Rx3** is the third methanation reactor with the same settings as Rx 1 and Rx 2.
- **E8** is the condenser, cooling the effluent stream from Rx 3 to 76 °C in order to recover the H_2O fraction.
- **F1** is a flash drum, separating the water from the SNG product. The water is sent back to the mixer M3 where it is added to the pressurized liquid inlet water stream (S4) along with the syngas plant water recycle loop (S20).

- **E9** is a heat exchanger heating the effluent stream from the flash drum to the inlet temperature of Rx 4 which is 220 °C.
- **Rx4** is the fourth and last methanation reactor, converting the remaining syngas to CH_4 and H_2O. It has the same settings as Rx 1, Rx 2 and Rx 3.
- **E10**: Heat exchanger for recovery of heat from the SNG stream.
- The stream **S41** is the product exit stream, leading the SNG product to the NG grid at at 20 °C and 80 atm.

The syngas plant had two control loops which are summarized below in addition to the on contained in the high temperature design case (case 1):

Syngas plant

- **Feed module and water input flow rate:** FM of syngas stream (S18) adjusted by flowrate of water inlet stream (S2).
- **Redox potential of the filter inlet stream:** Adjusted by the split fraction of the SP1 splitter.
- **Temperature of filter inlet stream:** Adjusted to 750 °C by the E2 heat exchanger.
- **Water recovery:** Adjusted by the condenser operating temperature.

Methanation plant

- **Rx 1 temperature control.** This loop controls the split fraction of SP3 in order to keep the outlet temperature of Rx1 below 700 °C. The loop is operated by the controller CN6, with the temperature of S31 as the target parameter and the split fraction for S33 in SP3 as the variable.

Chapter 8 Heat integration study

The methanation process is highly exothermic, as explained in section 2.3 in the theory chapter. One of the advantages of the Topsøe TREMP process is that it utilizes the heat of the reaction to produce superheated steam ready for use in turbines for on-site electricity production [35]. In the case of integration with a syngas plant relying on SOEC technology however, excess heat from the methanation processes is needed for preheating of the SOEC feed streams. From the BC syngas plant (Chapter 5), the needed heating requirement from the syngas plant was calculated to 865 MJ/h in terms of the minimum hot utilities required. The maximum excess heat from the methanation plant was calculated to be on the order of 400 MJ/h, calculated from the enthalpies of reaction for the methanation reactions and the feed composition of the syngas stream in design case 1. Thus, there is a clear mismatch between these figures, and the methanation reactors are not capable of supplying all of the needed thermal energy for the syngas plant. This means that it is important to recover as much heat as possible from the reactors whereas the quality of the heat in relation to electricity production or sale is of minor importance. Because of this, the individual heating and cooling duties of the methanation plant are integrated with the rest of the duties from the full plant during the following heat integration study. An introduction to the basic concepts and methods used in this chapter is found in section 2.4 .

8.1 Heat balance and composite curves

The needed heating and cooling duties of the plants for design cases 1 and 2 were obtained from the heat exchangers in the PRO/II models for the full plant cases, in addition to the three heat duties of the air capture plant (Section 3.2.1). The OHMIC_HEAT heat exchanger of the SOEC model was not included here, as it does not represent a physical heat exchanger unit, but rather electric heating in the stack. This was described in section 5.4 . The hot and cold streams for both cases are summarized in Table 8-1 and Table 8-2, and these tables should then be seen as summarizing the input values of the heat integration study. In the tables, the streams are ordered after the different parts of the full plant which they belong to. The conditions for the source and target states are given along with the heat duties. As mentioned

in the section 3.2.1 in the chapter on air capture, the heating and cooling duties of the air capture sub-system are assumed to be exchanged with a reservoir with approach temperatures of 5 K.

Table 8-1. Input stream data for the heat integration study, concerning the heating and cooling duties for design case 1. The "Stream" column is the inlet stream of the heat exchanger unit operation in question. L and V signifiy Liquid and Vapor phase respectively. The heat duties are obtained from the PRO/II model output.

				Source state		Target state		Heat duty
Sub-plant	**Stream**	**Process**	**Type**	**T [°C]**	**Phase**	**T [°C]**	**Phase**	**MJ/h**
Air Capture	-	AC1	Cold	100.0	L	105.0	L	743.4
Air Capture	-	AC2	Hot	20.0	L	15.0	L	340.4
Air Capture	-	AC3	Hot	40.0	L	35.0	L	58.2
Syngas	S22	E1	Cold	67.0	L	295.9	V	584.0
Syngas	S7	E2	Cold	308.3	V	747.7	V	328.6
Syngas	S14	E3	Hot	850.2	V	20.0	V	158.3
Syngas	S17	E4	Hot	850.0	V	144.1	V-L	544.6
Methanation	S18	E5	Cold	144.1	V	219.9	V	21.7
Methanation	S31	E6	Hot	699.5	V	219.9	V-L	225.4
Methanation	S35	E7	Hot	426.5	V	219.9	V-L	96.5
Methanation	S37	E8	Hot	230.9	V-L	76.2	V-L	101.6
Methanation	S41	E9	Cold	76.2	V	220.0	V	18.8
Methanation	S25	E10	Hot	220.0	V	20.0	V	26.8

Somewhat surprisingly, the largest heating duty in the plant in both cases is the AC1 process, which contains the heat of desorption of CO_2 and H_2O from the sorbent in the air capture sub-plant. With 743 MJ/h, it is larger than the water evaporation and SOEC pre-heating duties (processes E1 and E2) in both cases, but takes place at significantly lower temperatures. The table also shows, that the methanation sub-plant has less than 322 MJ/h available in the hot streams above 220 °C in case 1 and as little as 71 MJ/h above ~220 °C in case 2 where a large portion of the methane production has already taken place in the SOEC stack.

Table 8-2. Input stream data for the heat integration study, concerning the heating and cooling duties for design case 2. The "stream" column is the inlet stream of the heat exchanger unit operation in question. L and V signify Liquid and Vapor phase respectively. The heat duties are obtained from the PRO/II model output.

				Source state		Target state		Heat duty
Sub-plant	**Stream**	**Process**	**Type**	**T [°C]**	**Phase**	**T [°C]**	**Phase**	**MJ/h**
Air Capture	-	AC1	Cold	100.0	L	105.0	L	743.4
Air Capture	-	AC2	Hot	20.0	L	15.0	L	340.4
Air Capture	-	AC3	Hot	40.0	L	35.0	L	58.2
Syngas	S22	E1	Cold	80.1	L	295.9	V	553.7
Syngas	S7	E2	Cold	308.2	V	492.6	V	142.0
Syngas	S14	E3	Hot	600.4	V	20.0	V	108.9
Syngas	S17	E4	Hot	600.0	V	144.1	V-L	432.8
Methanation	S18	E5	Cold	144.1	V	219.9	V	14.1
Methanation	S31	E6	Hot	514.7	V	219.9	V	59.2
Methanation	S35	E7	Hot	283.2	V	219.9	V	11.9
Methanation	S37	E8	Hot	223.9	V	76.2	V-L	63.5
Methanation	S41	E9	Cold	76.2	V	220.0	V	18.7
Methanation	S25	E10	Hot	220.0	V	20.0	V	26.7

With the information for the two design cases from Table 8-1 and Table 8-2, the composite curves for each case were calculated as described in section 2.4.3 of the theory chapter. These are shown in Figure 8-1 for both cases.

The diagrams show the hot (red) and cold (dashed) composite curves for the two cases. The curves start at zero heat per definition. Usually, the amount of heat which may be recovered in the system can be read as the distance on the x-axis where the curves overlap provided that the temperature of the hot curve, $T_{hot} \geq T_{cold} + HRAT$, where T_{cold} is the temperature of the cold curve and HRAT is the heat recovery approach temperature (HRAT). The purple curve represents the cold composite curve shifted along the heat axis (abscissa) so that it is colder by HRAT = 10 K or more in the entire range. The point where HRAT=10 is the pinch point, and heat may only be exchanged at higher temperatures than the pinch point temperature in this case. In this situation (HRAT = 10 K), 1.12 GJ/h may be recovered in case 1 and 0.68 GJ/h in case 2.

This strategy, however, uses all the heat available in the hot streams above the pinch point temperature to heat the low temperature parts of the cold streams, and leaves the high temperature parts (those not overlapped by the hot curve) to be heated with utilities. This approach is impractical as high grade (high temperature) heat is used to supply energy at significantly lower temperatures, and ends up requiring utilities at high temperatures. It is beneficial to use the high temperature heat of the hottest streams in the plant (post-SOEC

cool-down and intercooling after the first methanation reactor) to heat up the SOEC inlet stream (E2) rather than supplying heat for the lower temperature heating duty of the air capture plant (AC1) for example.

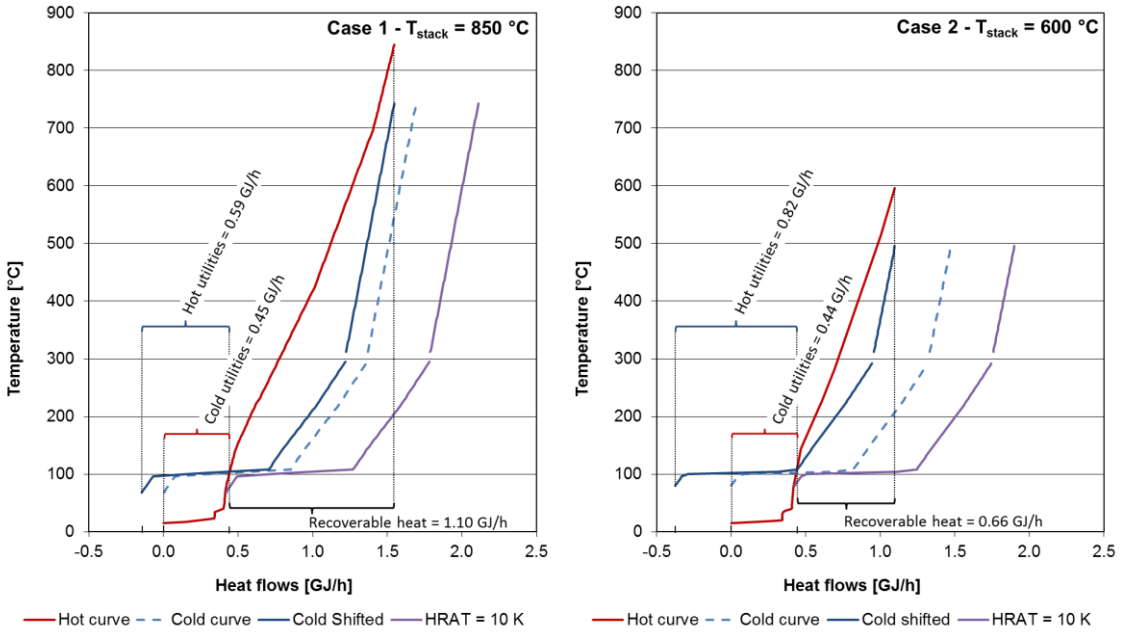

Figure 8-1. Composite curves for the full plant design cases 1 (a) and 2 (b). Hot, cold and adjusted composite curves are shown. See text.

The solid blue curves represent the cold composite curve, shifted to comply with the demand that the available high temperature heat is used to fulfill the high temperature heating duties. This was done by shifting the cold composite curve so that the hot and cold curves have the same maximum values on the heat flow axis. In this case, the cross-over point is the pinch point. Assuming that HRAT = 0 K for simplicity, the maximum recoverable amount of heat may be read as the parts of the curves to the right of this point. The needed hot and cold utilities are then read as the parts of the cold and hot composite curves respectively to the left of the pinch point. These intervals are illustrated in the diagrams. In case 1, a maximum of 1.10 GJ/h may be recovered in the process and the minimum requirements for hot and cold utilities are 0.59 GJ/h and 0.45 GJ/h. In case 2, a maximum of 0.66 GJ/h may be recovered and the minimum utility requirements are 0.82 GJ/h and 0.44 GJ/h (hot and cold respectively). These numbers show how a little less heat may be theoretically recovered, compared to the original placement of the cold composite curve, which was discussed above. This is a consequence of requiring the high temperature heat is preferentially used for high temperature heating requirements.

What is important to note from these considerations is that even though the methanation process supplies large amounts of heat, and even when a maximum amount of heat from the large heating and cooling duties of the syngas (SOEC) plant is recovered, the heating

requirements of the air capture plant are so large, relatively, that significant amounts of heat has to be supplied by utilities. It should be noted here that the last portion of the SOEC preheating from the filter temperature to the operating temperature of the stack is supplied by electric heating in the stack (the OHMIC_HEAT Unit operation, see Chapter 5).

Another important message from the simplified analysis of the diagrams is that the hot utility heating may take place at low to intermediate temperatures with a maximum of around 110 °C. It may not be the most economic choice to supply all heating below this temperature, as will be discussed later, but the possibility is expected to be beneficial for the overall economics of the plant.

8.2 Heat Exchanger Network Synthesis

As described in section 2.4.5 in the theory chapter, the heat transfer simulation program HEXTRAN 9.2[42] is used to solve the heat exchanger network synthesis (HENS) problem, using the dual approach temperature (DAT) method. This method allows for exchanger minimum approach temperatures (EMAT) smaller than the heat recovery approach temperature (HRAT) of the overall network. This means that some heat exchangers are allowed closer approaches than the overall network approach temperature.

In order to synthesize the heat exchanger networks (HEN) of the two cases, HRAT and EMAT need to be established. This is done through simulation in HEXTRAN as will be explained below. For these calculations, a set of utilities are also needed. These are described in the following.

As was explained in the introduction to heat integration studies in Chapter 2, any heat duties which cannot be integrated in the plant needs to be covered by external utilities which are heat sources or heat sinks. The utilities used in this work are explained and prices are calculated in 0 on economic prerequisites, assumptions and methodology on page 177 of this report. A brief summary is given here.

Three utility streams were used for the synthesis calculations. One cold utility at 10 °C (U3) and two hot utilities, one at 120°C (U1) and one at 300 °C (U2). HEXTRAN only accepts two utilities at a time: one hot and one cold. The details and estimated prices of the utilities are summarized in Table 8-3. For the process streams, overall heat transfer coefficients are estimated in HEXTRAN. For the utilities however, the individual heat transfer coefficients of the stream is chosen from tabulated values in Peters et al. [38], based on the phase of the stream in question, assuming tubular surface areas. For heating and cooling of liquid water and for condensing water, the heat transfer coefficient is assumed to be 1000 W/(m^2·K). for steam, 10 W/(m^2·K) is assumed.

Table 8-3. Hot and cold utilities used in the synthesis calculations See section 11.1.5 for details. Each utility stream has a source temperature and a source phase where L and V signify liquid or vapor phase in the source state. The streams are assumed to be water close to atmospheric pressure. Heat transfer coefficients for the individual streams were assigned with 1000 W/(m^2·K) for heating and cooling of liquid water and for condensing steam. Cooling of steam without condensing is assumed to have a heat transfer coefficient of 10 W/(m^2·K).

Utility	Type	Source temperature [°C]	Source phase	Outlet temperature limit [°C]	Heat transfer coefficient [W/(m^2·K)]	Utility cost [€/GJ]
U1	Hot	120	V	10	1000	11.9
U2	Hot	300	V	10	10	17.7
U3	Cold	10	L	300	1000	0.11

For the intermediate temperature hot utility U1, the phase transition (condensation around 100 °C) dominates the available heat, which gives rise to the high heat transfer coefficient. For the high temperature hot utility U2, a significantly larger part of the available heat is sensible heat, and the heat transfer coefficient is estimated to be two orders of magnitude lower. In addition to having a higher heat transfer coefficient, the price of U1 is 49 % lower per GJ compared to U2. This means that heating a cold process stream with the U2 utility will be more expensive both in terms of utility consumption and installed equipment, as the heat exchange area scales with the heat transfer coefficient. The area also scales with the inverse of the approach temperature, which is in favor of the hotter of the two streams, however.

Due to these considerations, it is assumed to be economically beneficial to maximize the use of the intermediate temperature hot utility (U1) compared to U2 both from a capital costs and operating costs point of view. Unfortunately, HEXTRAN only accepts one hot utility stream for these calculations, and thus, the calculations to establish HRAT and EMAT temperatures are performed using the U2 utility, which is then replaced separately with U1 in the relevant heat exchangers once the approach temperatures and HENs are established.

8.2.1 Establishing approach temperatures

The input data for the hot and cold streams from Table 8-1 and Table 8-2 above along with the U2 and U3 utilities were used as a basis for a series of network synthesis calculations for each design case. 25 pairs of HRAT and EMAT values in the ranges of HRAT = {10 °C, 15 °C, 20 °C, 25 °C, 30 °C} and EMAT = {2.5 °C, 5 °C, 10 °C, 15 °C, 20 °C, 25 °C, 30 °C} with the constraint that HRAT $\geq$ EMAT, were used for each design case. The HEXTRAN input files for these calculations are included in Appendix F and G.

Each calculation resulted in the network with the lowest annualized cost (*Ca*) for that particular (HRAT, EMAT) combination. The costs are plotted for both design cases as functions of HRAT and EMAT values in Figure 8-2.

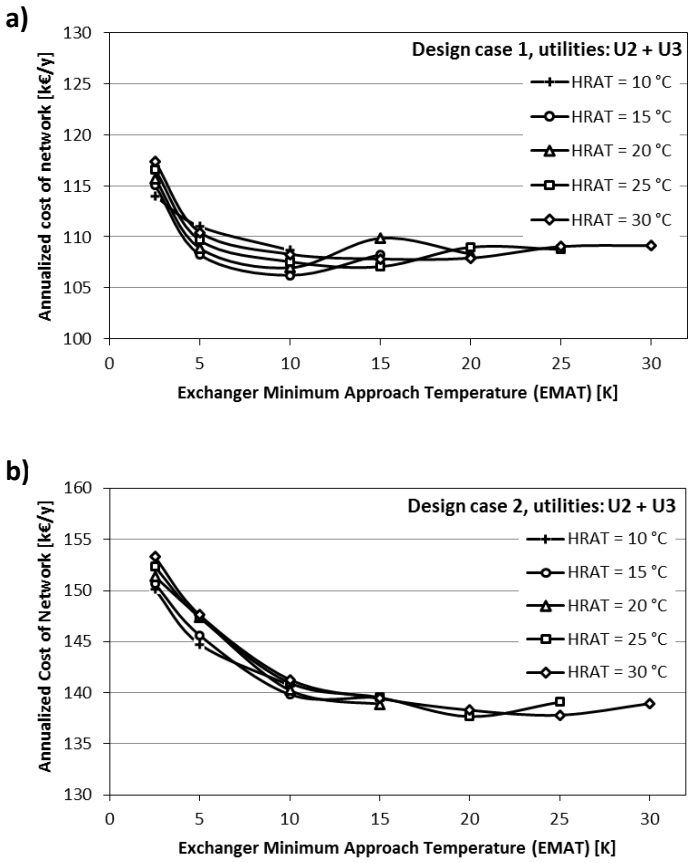

Figure 8-2. Annualized cost of the synthesized heat exchanger networks of design cases 1 (a) and 2 (b) as functions of HRAT and EMAT values, using the U2 and U3 utilities.

From the synthesis calculations, the (HRAT, EMAT)-pair with the lowest annualized cost is a good candidate for the choice of heat exchange network layout. Generally, the possibility to split individual streams between several heat exchangers produces networks of lower cost. In this work, the gains from this were minimal, and they are not considered in favor of the significantly simpler networks with un-split streams.

A closer look at the cooling needs in Table 8-1 and Table 8-2 shows that in order to supply the cooling needed by the AC2 process at 15 °C with the available cold utility U3 at 10 °C, a maximum value of EMAT of 5 K can be accepted for the HEN. This rules out large parts of the approach temperature range, which means, the annualized cost of the network in both cases will be higher, especially for design case 2. The networks with the lowest costs for the two design cases are summarized in Table 8-4.

In all of the networks in the table, the majority of the consumed hot utilities supply heat for the AC1 process (air capture heating). This agrees with the results from the composite curve analysis above. The synthesis calculations also show, that an economic advantage may be gained by supplying a part of the heating needed in process E1 (inlet water evaporation), using the high temperature hot utility U2 in the networks of design case 2. This is the case even though the pinch analysis showed all hot utilities could technically be supplied at lower

temperatures. The numbers in Table 8-4 were calculated in HEXTRAN using the expensive utility U2 for both the AC1 and E1 processes as mentioned above. In the following discussions, however, U2 has been replaced with U1 for the AC1 service, resulting in a lower overall cost of the network and utilities. This is discussed further in a later chapter as part of the economic analysis.

Table 8-4. Summary of the networks with the lowest annualized costs for each design case. These values were calculated using only the high-temperature hot utility, U2. Networks with the lowest costs are emphasized. MNU is the minimum number of units.

Network	HRAT [K]	EMAT [K]	Number of units	Capital costs Total [k€/y]	Capital costs Annualized [k€/y]	Annual utility costs [k€/y]	Annualized network cost [k€/y]
Design case 1 (T_{stack} = 850 °C)			MNU=14				
- 1	**15**	**5**	**16**	**144.1**	**10.6**	**97.6**	**108.2**
- 2	20	5	15	142.8	10.5	98.4	108.9
- 3	25	5	15	143.4	10.6	99.1	109.6
Design case 2 (T_{stack} = 850 °C)			MNU=15				
- 1	**10**	**5**	**19**	**249.5**	**18.4**	**126.4**	**144.8**
- 2	15	5	19	253.8	18.7	127.0	145.6
- 3	20	5	18	270.7	19.9	127.5	147.4

Generally, the theoretical minimum number of units (heat exchangers) can be calculated as:

$$MNU = Number\ of\ hot\ streams + Number\ of\ cold\ streams + Number\ of\ utilities - 1$$

With 8 hot streams, 5 cold streams and two (case 1) or three (case 2) utility services, MNU = 14 and 15 for case 1 and case 2, respectively. The numbers of units presented in the table are higher, and the networks of the full plant could be chosen based on the lowest number of units, as these would result in the least complex plants. The difference in numbers of units between the cheapest plants is small, however, and network 1 is chosen in both design cases, Favoring the networks with the lowest annualized costs. These are emphasized in bold in the figure.

8.2.2 Resulting heat exchanger network layouts

As part of the synthesis calculations, HEXTRAN performs sizing calculations for heat exchangers needed in the network, assuming all heat exchangers are tube and shell heat exchangers with counter flow configuration. Also, overall heat transfer coefficients are calculated for each heat exchanger based on the supplied heat transfer coefficients of the relevant streams, and finally the area of each heat exchanger is calculated.

Table 8-5 and Table 8-6 present the results of the HEXTRAN calculations for the heat exchangers included in the chosen networks for case 1 and 2 respectively. The tables include information on the interacting streams on the hot side (heat source streams) and cold side

(heat sink streams) of each exchanger along with the approach temperature, ΔT, the duty the overall heat transfer coefficient, calculated by HEXTRAN and the area.

In the synthesized networks, each heating or cooling process of the PFD (Table 8-1 and Table 8-2) is replaced by one or more heat exchangers (Hx). Thus, in case 1, for example, the heating of the air capture desorption chamber (process AC1) is split into 4 heat exchangers. In three of the exchangers, hot streams in the plant shed heat as they cool down, and in the last one, the remainder of the needed heating is supplied by the U1 hot utility. This translation of temperature change processes from the flow diagrams (E1, E2, etc.) to heat exchanger equipment (Hx1, Hx2, etc.) is further discussed later.

Based on the tables, the heat exchanger networks are visualized schematically in the HEN diagrams in Figure 8-3 and Figure 8-4 (these are found after the tables). In these diagrams, process streams which are heated up or cooled down are shown as arrows, on the horizontal temperature scale. Hot streams enter the network at high temperatures (right hand side) and exit further to the left at lower temperatures. Cold streams enter at low temperatures and leave at higher temperatures. Each heat exchanger is represented as a connection between exactly two streams: One hot and one cold. These are visualized as two circles and a dashed line connecting the two streams. The circles are placed on the arrows representing the two streams, and mark the inlet temperature of each stream in the exchanger. Thus, all streams (horizontal arrows) begin in a heat exchanger (circle) in the diagram. In the case where a stream passes only one heat exchanger, the termination of the arrow (the arrowhead) represents the outlet temperature of the exchanger. If the stream enters another heat exchanger, the outlet temperature of the first heat exchanger and the inlet temperature of the second exchanger are identical.

Table 8-5. Heat exchanger services resulting from synthesis calculations for design case 1.

	Hot side				Cold side				ΔT_{min}	Duty	U-value	Area
Unit	Stream	T_{in} [K]	T_{out} [K]	P [atm]	Stream	T_{in} [K]	T_{out} [K]	P [atm]	[K]	[GJ/h]	[W/m^2·K]	[m^2]
Hx1	S17	1,123.2	697.3	80	S7	581.5	1020.8	80	102	0.3286	50.00	20.8
Hx2	S31	972.7	631.4	80	S22	506.2	569.1	80	125	0.1604	50.00	4.0
Hx3	S37	504.0	471.1	80	S18	417.2	493.0	80	11	0.0217	50.00	5.4
Hx4	S31	631.4	493.0	80	S1	373.1	373.6	1	120	0.0650	50.00	2.0
Hx5	S14	1,123.3	499.9	80	S22	459.6	506.2	80	40	0.1189	50.00	3.9
Hx6	S35	699.6	493.0	80	S1	373.7	373.8	1	119	0.0096	50.00	0.0
Hx7	S17	697.3	417.3	80	S22	374.9	459.6	80	42	0.2160	50.00	11.6
Hx8	S14	499.9	401.6	80	S41	349.9	493.1	80	7	0.0187	50.00	5.5
Hx9	S25	493.1	383.1	80	S1	373.6	373.7	1	10	0.0147	50.00	1.9
Hx10	S37	471.1	349.3	80	S22	343.6	374.9	80	6	0.0800	50.00	15.0
Hx11	S14	401.6	355.7	80	S22	340.2	343.6	80	16	0.0087	50.00	1.6
Hx12	S1_1	293.1	288.1	1	U3	283.1	288.1	1	5	0.3404	90.91	259.3
Hx13	S1_2	313.1	308.1	1	U3	283.1	308.1	1	5	0.0582	90.91	17.5
Hx14	S14	355.7	293.1	80	U3	283.1	350.7	1	5	0.0119	90.91	6.3
Hx15	S25	383.1	293.1	80	U3	283.1	378.1	1	5	0.0121	90.91	6.4
Hx16	U1	393.1	378.8	1	S1	373.8	378.1	1	5	0.6540	90.91	259.2

Table 8-6. Heat exchanger services resulting from synthesis calculations for design case 2.

	Hot side				Cold side			ΔT_{min}	Duty	U-value	Area
Unit	Stream	T_{in} [K]	T_{out} [K]	P [atm]	Stream	T_{in} [K]	T_{out} [K]	P [atm]	[K]	[GJ/h]	[W/m^2·K]	[m^2]
Hx1	S17	873.1	703.8	80	S7	581.4	765.7	80	107	0.1420	50.00	7.7
Hx2	S31	787.9	717.7	80	S18	417.2	493.0	80	295	0.0141	50.00	0.3
Hx3	S31	717.7	493.0	80	S22	410.1	427.7	80	83	0.0451	50.00	1.6
Hx4	S35	556.3	493.0	80	S22	455.0	459.7	80	38.0	0.0119	50.00	1.1
Hx5	S14	873.5	500.1	80	S22	427.7	455.0	80	72	0.0701	50.00	2.1
Hx6	S17	493.0	417.2	80	S22	385.4	410.1	80	32	0.0636	50.00	7.6
Hx7	S14	500.1	485.2	80	S41	471.7	493.1	80	7	0.0028	50.00	1.9
Hx8	S37	497.1	389.2	80	S22	367.3	385.4	80	22	0.0463	50.00	5.4
Hx9	S14	485.2	364.4	80	S22	358.5	367.3	80	6	0.0227	50.00	3.5
Hx10	S25	493.1	374.0	80	S41	349.3	471.7	80	21	0.0159	50.00	4.5
Hx11	S37	389.2	358.3	80	S22	353.3	358.5	80	5	0.0133	50.00	6.4
Hx12	S17	703.8	493.0	80	S22	459.7	528.5	80	33.3	0.1767	50.00	12.7
Hx13	S1_1	293.1	288.1	1	U3	283.1	288.1	1	5	0.3404	50.00	259.3
Hx14	S1_2	313.1	308.1	1	U3	283.1	308.1	1	5.0	0.0582	90.91	17.5
Hx15	S14	364.4	293.1	80	U3	283.1	359.4	1	5.0	0.0134	90.91	7.1
Hx16	S37	358.3	349.3	80	U3	283.1	353.3	1	5.0	0.0039	90.91	0.5
Hx17	S25	374.0	293.1	80	U3	283.1	369.0	1	5.0	0.0108	90.91	5.7
Hx18	U1	393.1	378.8	1	S1	373.8	378.1	1	5.0	0.7434	90.91	294.6
Hx19	U2	574.1	533.5	1	S22	528.5	569.1	80	5.0	0.1040	9.09	751.6

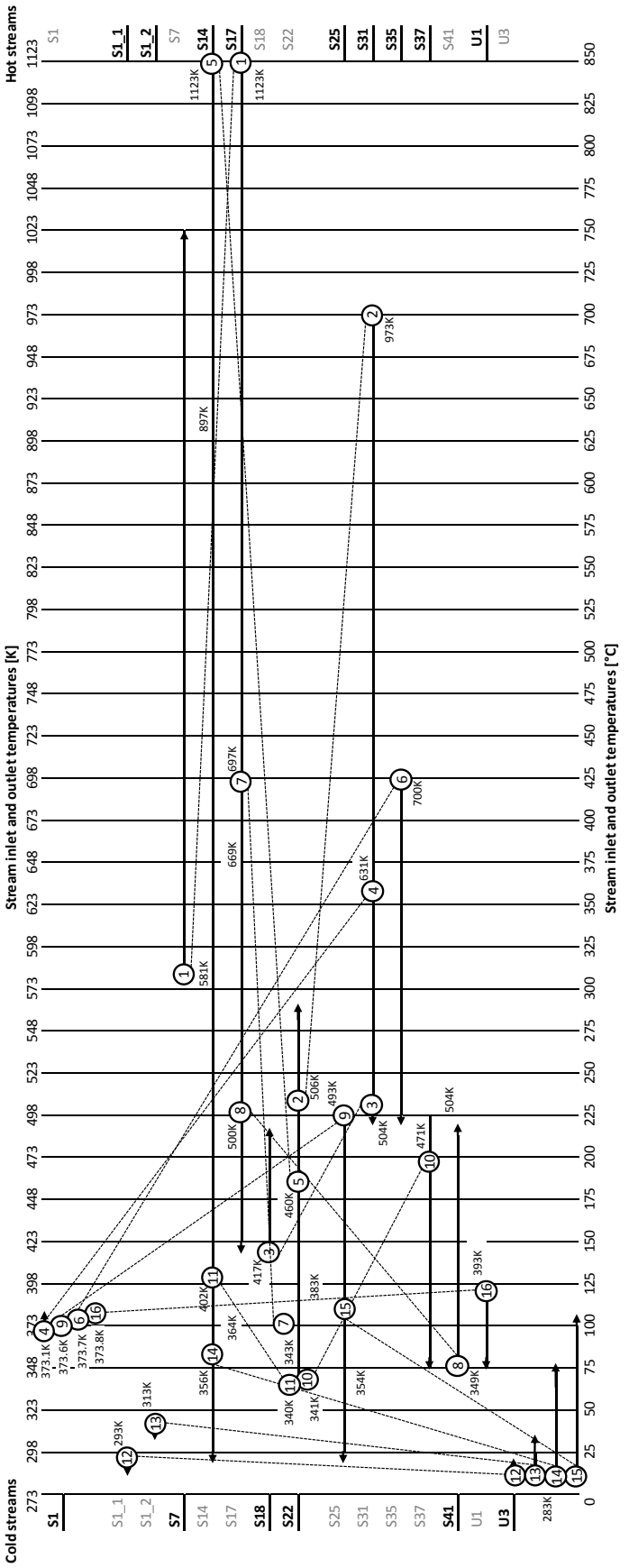

Figure 8-3. HEN diagram for the synthesized network of case 1 with HRAT = 10 K and EMAT = 5 K. The streams are represented as horizontal arrows with the hot streams running from high temperatures (right) to low temperatures (left) and vice versa for the cold streams. Each heat exchanger is represented as two circles connected with a dashed line. The circles mark the inlet temperature of the streams entering the heat exchanger. The outlet temperature is represented by the end of the arrow (stream) or by the following heat exchanger. The numbers of each heat exchanger correspond to those in Table 8-5.

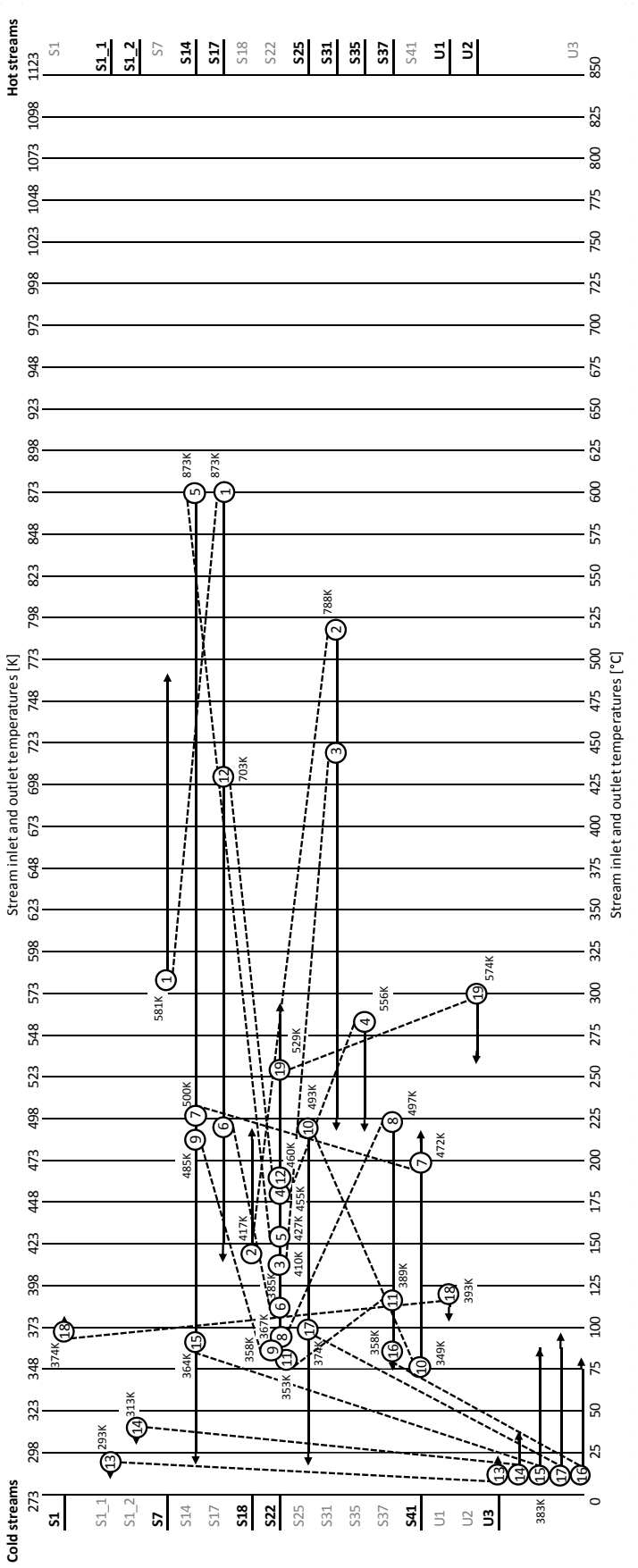

Figure 8-4. HEN diagram for the synthesized network of case 2 with HRAT = 10 K and EMAT = 2.5 K. The streams are represented as horizontal arrows with the hot streams running from high temperatures (right) to low temperatures (left) and vice versa for the cold streams. Each heat exchanger is represented as two circles connected with a dashed line. The circles mark the inlet temperature of the streams entering the heat exchanger. The outlet temperature is represented by the end of the arrow (stream) or by the following heat exchanger. The numbers of each heat exchanger correspond to those in Table 8-6.

8.3 Heat integration summary

In the above considerations on the heat integration of the plant, the following points are important to note:

- The main heating duties in the plant are the heating of the air capture desorption chamber and the water evaporation followed by the SOEC pre-heating. The main cooling duties are the cooling of the SOEC effluent streams (syngas and O_2), the cooling of the air capture plant vacuum pump (AC2 process) and intercooling after the first methanation reactor.
- There is a mismatch between the available and required heat flows of the processes in the plant which means that a significant amount of utilities are needed to fulfill the heating and cooling duties.
- Large parts of the heating and cooling duties can be integrated however, and this can be done in a way, which makes full use of the high temperature heat available to heat high temperature cold streams. This means that only small amounts of the expensive hot utility (U2) needs to be used in case 2 and none in case 1.
- Based on the previous point, if the hot utilities are to be supplied as process heat, the layout of the plant allows for the use of relatively cool process streams of around 110 °C for the majorities of the duties. This means that such integration is significantly easier and more viable, as low temperature process heat would be expected to be more readily available than very high temperature heat.
- The above means that from a heat integration perspective, the lowering of the operating temperature from 850 °C in case 1 to 600 °C in case 2 is not preferable, and the costs of the networks gets larger in the low temperature case. The real comparison between the cases needs the considerations of total energy balance and economy as well, however.
- The number of units in the synthesized networks are larger than the calculated minimum number of units (MNU = 14). Everything else equal, this increases the cost of the network in terms of equipment, and is a consequence of the chosen low HRAT. As the hot utilities are associated with high costs, this is economically viable, however, as the consumption is lowered when more heat is recovered (HRAT is low).
- The HEN diagrams (Figure 8-3 and Figure 8-4), show that the large heating and cooling duties contribute more to the number of heat exchangers in the network, but especially the water evaporation (S22) process interact with a large number of other streams in the network in order to absorb sufficient amounts of heat for the evaporation.
- Finally, it should be noted, that most of the utility streams have very small temperature changes, which is important for deciding the use of the discharge streams.

With this, the heat integration study of the plant in both cases is finished. The next chapter on system integration, sizing and costing calculations is based on the results obtained in this chapter.

Chapter 9 Plant integration, sizing and costing

In this chapter, the final plant integration is described.

The first step was implementing the heat exchanger network in the overall plant design. After this, the pressure drops of all units in the system were calculated and equipment for re-pressurization was added to the flow diagram to balance the pressure drops of the individual units.

In the second step the design of both cases was finalized, and the final Product Flow Diagrams (PFDs) are presented. The PFDs are presented in this chapter and included in the removable reference sheets in Appendix D and E.

In the third step, the sizes of all the individual units in the plant as well as their costs were calculated. The sizing and costing calculations are presented at the end of the chapter along with the assumptions they are based on. Detailed considerations of piping, electrical systems etc. are outside the scope of this work, and they are considered only from an economical point of view in the Chapter 12 on the economic analysis.

9.1 Pressure drops and re-pressurization equipment

In order to finalize the list of units to be sized in the completed system model, the pressure drops of all units in the process flow diagrams (PFDs) (See PFDs at the end of the previous chapter, page 118 and page 119) were estimated and pumps and compressors and pumps were added as appropriate. The following sections explain how the pressure drops were estimated for each type of equipment. The results are shown along with the results of the sizing and costing calculations at the end of the chapter.

9.1.1 Pressure drops of heat exchangers

Incorporating the detailed heat exchanger networks, synthesized in the previous chapter, into the PRO/II model becomes cumbersome from a modelling point of view. Also visualizing the network in the final PFDs becomes highly confusing. Instead, the original temperature change

unit operations were left in the model, and the pressure drops calculated from the heat exchangers in the synthesized networks were summed and entered into the settings of the PFD units.

This means that each temperature change process in the PFD (E1 through E10 in addition to AC1 through AC3) represents between one and seven heat exchangers (Hx 1 through Hx 17 for case 1, and Hx 1 through Hx 20 for case 2). Table 8-5 and Table 8-6 summarize this correspondence of PFD units (E) to actual heat exchangers (Hx).

There is no way of calculating the exact pressure drops for heat exchangers without going into detailed design considerations which is outside the scope of this work. Simple heuristics exist for the pressure drops in tube and shell heat exchangers however, one of which was employed in this work [106]. According to those guidelines, the pressure drops in shell and tube heat exchangers of liquids and gasses with no phase changes can be estimated to 0.340 atm and 0.204 atm respectively and 0.102 atm and 0.068 atm for condensing and boiling streams respectively. In the cases where PFD processes, which include phase transitions, are split into several heat exchangers, it was assumed that the transition takes part in all the Hx units of the given process. In Table 8-5 and Table 8-6, the pressure drop of each temperature change process (E) was calculated as the sum of pressure drops of the individual heat exchangers (Hx), it represents.

Table 9-1. Correspondence of temperature change processes and heat exchangers (Hx 1 through Hx 17) of case 1. The total pressure drops of each process is based on estimated pressure drops of 0.340 atm and 0.204 atm for liquid and vapor streams with no phase changes respectively as well as 0.102 atm and 0.068 atm for condensing and boiling streams respectively are used [106]. See PFD at the end of the previous chapter on page 118.

PFD process	Inlet stream	Source state T [°C]	Source state Phase	Target state T [°C]	Target state Phase	Corresponding Hxs	# of Hxs	ΔP/Hx[a] [atm]	Total ΔP [atm]
AC1[b]	-	100.0	L	105.0	L	Hx4, Hx6, Hx9, Hx16	4	-	-
AC2[b]	-	20.0	L	15.0	L	Hx12	1	-	-
AC3[b]	-	40.0	L	35.0	L	Hx13	1	-	-
E1	S22	67.0	L	295.9	V	Hx2, Hx5, Hx7, Hx10, Hx11	5	0.068	0.340
E2	S7	308.3	V	747.7	V	Hx1	1	0.204	0.204
E3	S14	850.2	V	20.0	V	Hx5, Hx8, Hx11, Hx14	4	0.204	0.817
E4	S17	850.0	V	144.1	V-L	Hx1, Hx7	2	0.102	0.203
E5	S18	144.1	V	219.9	V	Hx3	1	0.204	0.204
E6	S31	699.5	V	219.9	V-L	Hx4	2	0.102	0.203
E7	S35	426.5	V	219.9	V-L	Hx6	1	0.102	0.102
E8	S37	230.9	V-L	76.2	V-L	Hx3, Hx10	2	0.102	0.203
E9	S41	76.2	V	220.0	V	Hx8	1	0.204	0.204
E10	S25	220.0	V	20.0	V	Hx9, Hx15	2	0.204	0.409

[a]: The pressure drop per heat exchanger is assigned according to inlet and outlet phases, assuming, phase changes take place in all Hx of the given process.
[b]: These stream are not part of the PFD as they take place inside the AC plant. They are included here for completeness, but are assumed to be parts of the AC-plant with regards to pressure drops and installed costs.

Table 9-2. Correspondence of temperature change processes and heat exchangers (Hx 1 through Hx 20) of case 2. The total pressure drops of each PFD unit is based on estimated pressure drops of 0.340 atm and 0.204 atm for liquid and vapor streams with no phase changes respectively as well as 0.102 atm and 0.068 atm for condensing and boiling streams respectively are used [106]. See PFD at the end of the previous chapter on page 119.

PFD process	Inlet stream	Source state T [°C]	Source state Phase	Target state T [°C]	Target state Phase	Corresponding Hxs	# of Hxs	ΔP/Hx[a] [atm]	Total ΔP [atm]
AC1[b]	-	100.0	L	105.0	L	Hx18	1	-	-
AC2[b]	-	20.0	L	15.0	L	Hx13	1	-	-
AC3[b]	-	40.0	L	35.0	L	Hx14	1	-	-
E1	S22	80.1	L	295.9	V	Hx3, Hx4, Hx5, Hx6, Hx8, Hx9, Hx11, Hx12, Hx19	9	0.068	0.612
E2	S7	308.2	V	492.6	V	Hx1	1	0.204	0.204
E3	S14	600.4	V	20.0	V	Hx5, Hx7, Hx9, Hx15	4	0.204	0.816
E4	S17	600.0	V	144.1	V-L	Hx1, Hx6, Hx12	3	0.102	0.306
E5	S18	144.1	V	219.9	V	Hx2	1	0.204	0.204
E6	S31	514.7	V	219.9	V	Hx2, Hx3	2	0.204	0.408
E7	S35	283.2	V	219.9	V	Hx4	1	0.204	0.204
E8	S37	223.9	V	76.2	V-L	Hx8, Hx11, Hx16	3	0.102	0.306
E9	S41	76.2	V	220.0	V	Hx7, Hx10	2	0.204	0.408
E10	S25	220.0	V	20.0	V	Hx10, Hx17	2	0.204	0.408

[a]: The pressure drop per heat exchanger is assigned according to inlet and outlet phases, assuming, phase changes take place in all Hx of the given process.
[b]: These stream are not part of the PFD as they take place inside the air capture plant. They are included here for completeness, but are assumed to be parts of the air capture-plant.

In the tables, each heat exchanger shows up twice. This is because each exchanger has a hot and a cold side, each of which are part of different temperature change processes. Below, an example is given considering design case 1 (Table 9-1):

The cold inlet H_2O stream (S22, see the table) is heated and evaporated in process E1. Part of the heating, is supplied in the heat exchanger Hx11. This side of the heat exchanger is the cold side, as the stream is cold at the inlet. As the overall process (E1) includes a phase transition (evaporation), it is assumes that this is also the case in Hx11. The contribution from Hx11 to process E1 is then 0.068 atm, based on the heuristic. On the other side of the heat exchanger (the hot side), the outlet stream of the third methanation reactor (S37) is found (see Table 9-1). S37 is a hot stream and is cooled in the exchanger. During the cool-down, the stream goes through a partial phase transition in process E8 (condensation of the H_2O component). Thus, the heat exchanger Hx11 is also part of this process as seen in Table 9-1. Due to the partial condensation in E8, the pressure drop on the hot side of Hx11 is assumed to be 0.102 atm.

9.1.2 Pressure drop of SOEC stack.

The pressure drop in planar electrode supported SOFC cells and stacks have been modelled and found to be in the region of 5-90 mbar at ambient pressure depending on gas composition, flow channel layout, morphology of the porous system, flow rates, reactant

utilization etc. [107-109]. This is expected to be lower when the overall pressure is increased to 80 atm. For the sake of simplicity however, a value of 0.05 atm was assumed in this work.

9.1.3 Pressure drops of packed bed reactors

The reactors are assumed to be loaded with methanation catalyst such as the Haldor Topsøe A/S TREMP catalysts. These are expected to be come in the form of rings or pentalobes and to contribute to the reactor pressure drop per unit length with 0.1 atm/m [110, 111]. The resulting pressure drops are presented alongside the sizing calculations at the end of this chapter.

9.1.4 Pressure drop of the filter

The filter is treated in the same way as the reactors except that significantly smaller particles are assumed. With cylindrical particles this amounts to 0.3 atm/m. The filter vessel is assumed to have a length of 1 m. thus the total pressure drop of the filter is set to 0.3 atm [110, 111].

9.1.5 Equipment for re-pressurization

With the above considerations, the pressure drops of all units in the PFDs of both cases were estimated. These were in the range of ~0.05 atm to ~0.5 atm with most units around 0.1 atm to 0.2 atm. As these pressure drops are small relative to the operating pressure of the plant, the power consumed by the units for re-pressurization is expected to be small in the overall electricity consumption of the plant. Thus, the placement and operation of the pressure equipment was not studied in detail. The pressure equipment was placed based on the following constraints chosen for both cases:

6. The SOEC needed to operate at 80.0 atm.
7. The syngas should enter the first methanation reactor (Rx1) at 80.0 atm.
8. The SNG product should be delivered at 80.0 atm.
9. The final methanation reactor should operate at > 80.0 atm.
10. All recycle loops need to be re-pressurized before being mixed back into the process.
11. The number of units for re-pressurization (blowers and pumps) should be minimized.

With these constraints, the pressure drops of the individual units were summed working in the up-stream direction from the SOEC, the Rx1 inlet stream and the SNG product stream. This resulted in the placement of two pumps, one on each water recycle stream (P2 and P3). A blower was added on the SOEC recycle stream (B1) and one on the Hx1 recycle stream in design case 1 (B3). In addition to this, a blower was added to the syngas product stream (s18, B2) and to the inlet stream of the last methanation reactor (B4). Finally, the outlet pressures of the CO_2 compressor (C1) and inlet H_2O pump (P1) were increased in order to meet the demands. The details on each piece of pressure equipment can be found in Table 9-6 and Table 9-10 at the end of the section on sizing calculations.

9.2 Finalized process flow diagrams

With the additions of pressure change equipment described in the previous section, the design of the full plant in each case is finalized. The PFDs are presented in Figure 9-1 and Figure 9-2. A summary description of all units in the plant is presented after the figures.

The PFDs of the full plant are also included as reference sheets in Appendix D and E.

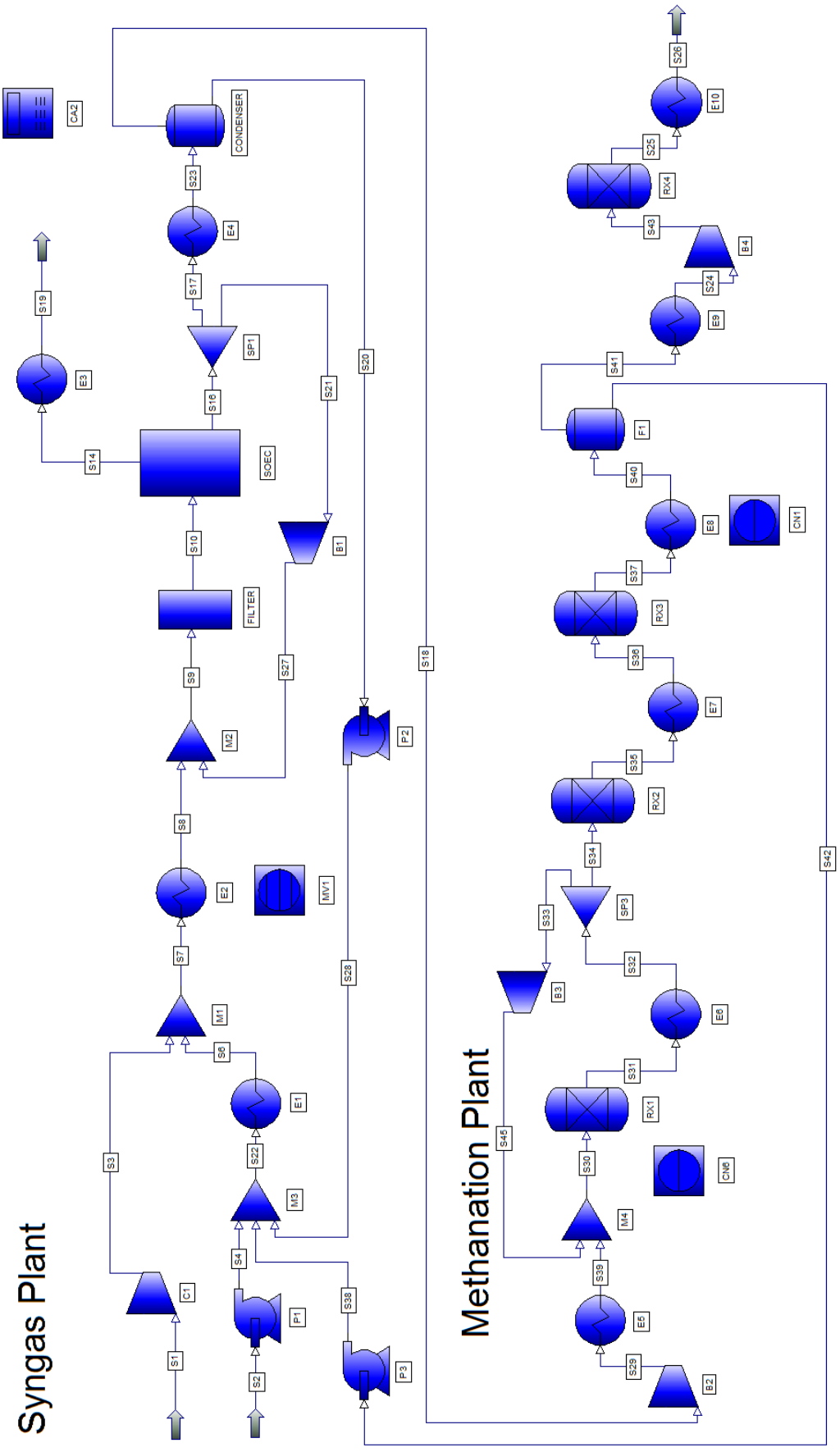

Figure 9-1. PFD showing the finished full plant high temperature design case 1. See the following text for details.

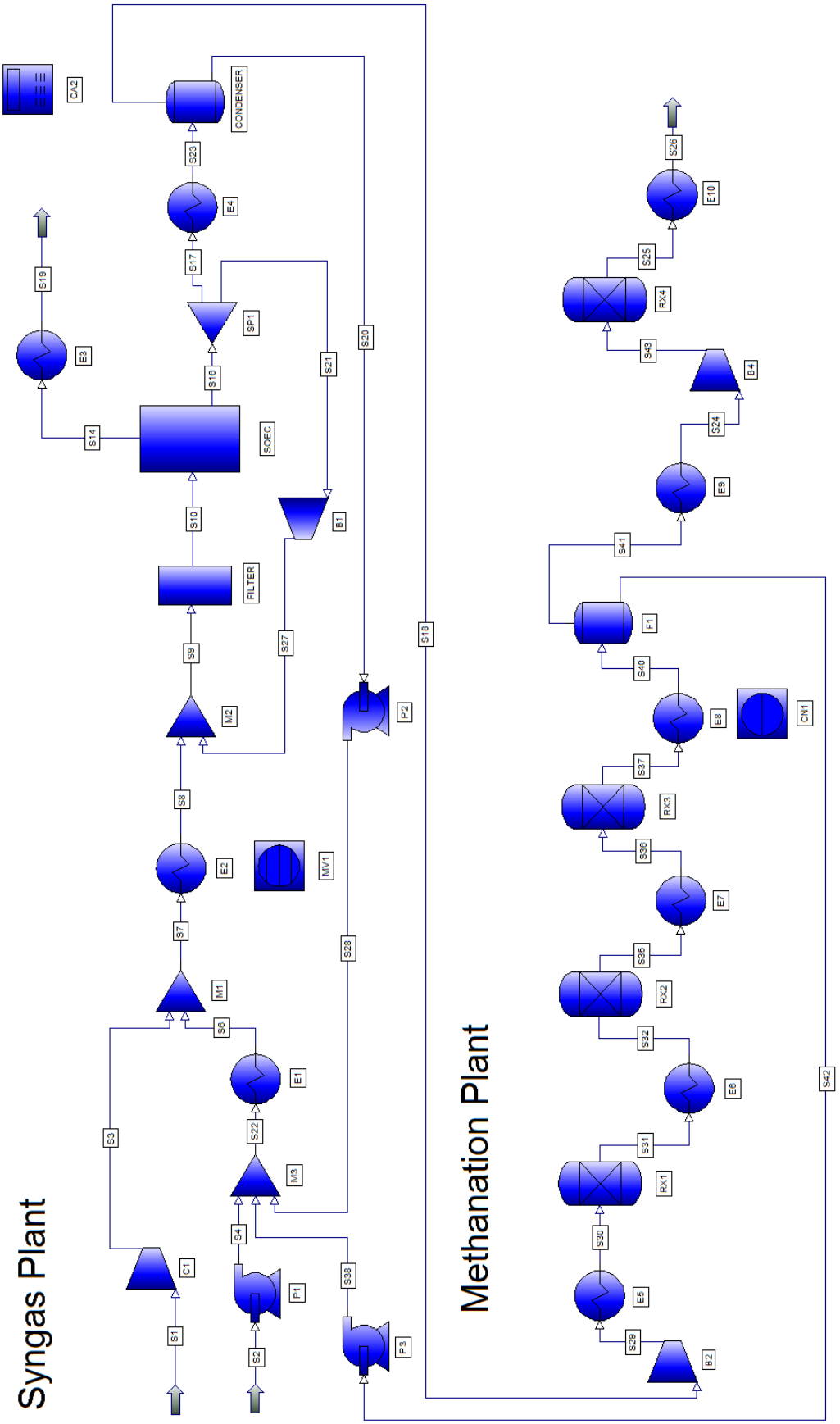

Figure 9-2. PFD showing the finished full plant high temperature design case 2. See the following text for details.

9.2.1 Summary of plant units

Most units of the plant have been described previously, in Chapter 5 and Chapter 7. In the following list, the pressure change equipment is included, and all units are briefly described.

Syngas Plant

- **S1:** CO_2 inlet stream.
- **C1:** CO_2 inlet compressor ($\eta_{adiabatic}$=75 %).
- **S2:** H_2O inlet stream.
- **P1:** H_2O inlet pump ($\eta_{adiabatic}$=80 %).
- **M3: M**ixes the H_2O inlet and recycle streams.
- **E1:** H_2O evaporator.
- **M1**: Mixes the CO_2 and H_2O streams.
- **E2:** SOEC pre-heater.
- **M2:** Mixes the SOEC input stream with the SOEC recycle stream.
- **FILTER:** removing impurities and O_2 (adiabatic Gibbs reactor).
- **SOEC:** Models the WGS, methanation and electrochemical conversion in the stack along with Joule heating.
- **E3:** O_2 byproduct heat recovery.
- **SP1:** Splits off SOEC recycle stream (app. 3 %) to keep filter and SOEC-cathode reduced.
- **B1:** Blower for re-pressurization of the SOEC recycle stream ($\eta_{adiabatic}$=75 %).
- **E4:** Condenser cooling.
- **CONDENSER:** Separates the liquid water from the vapor phase (flash unit).
- **P2:** Pump for re-pressurization of the H_2O recycle ($\eta_{adiabatic}$=80 %).
- **S18:** syngas product stream.

Methanation plant

- **B2:** Blower for re-pressurization of the syngas stream ($\eta_{adiabatic}$=75 %).
- **E6** is the methanation preheater, increasing the temperature of the syngas stream (S18) to the required inlet temperature of the first methanation reactor (Rx 1) which is 220 °C.
- **M4** is a mixer adding the Rx 1 recycle stream to the feed stream. This is only included in case 1.
- **Rx1** is the first methanation reactor. It is modelled as an adiabatic Gibbs reactor with the methanation and WGS reactions enabled.
- **E6** is the first intercooler heat exchanger which cools the effluent stream of Rx 1 to 220 °C.
- **SP3** is a splitter which removes a part of the stream S32 and sends it back to M4 upstream of Rx 1. This is only included in case 1.
- **B3:** Blower for re-pressurization of the Rx1 recycle stream ($\eta_{adiabatic}$=75 %). This is only included in case 1.
- **Rx2** is the second methanation reactor with the same settings as Rx 1.
- **E7** is the second intercooler heat exchanger which cools the effluent stream of Rx 2 to 220 °C.

- **Rx3** is the third methanation reactor with the same settings as Rx 1 and Rx 2.
- **E8** is the condenser, cooling the effluent stream from Rx 3 to 76 °C in order to recover the H_2O fraction.
- **F1** is a flash drum, separating the water from the SNG product. The water is sent back to the mixer M3 where it is added to the pressurized liquid inlet water stream (S4) along with the syngas plant water recycle loop (S20).
- **P3:** Pump for re-pressurization of the H_2O recycle ($\eta_{adiabatic}$=80 %).
- **E9** is a heat exchanger heating the effluent stream from the flash drum to the inlet temperature of Rx 4 which is 220 °C.
- **B3:** Blower for re-pressurization of the inlet stream for Rx4 ($\eta_{adiabatic}$=75 %).
- **Rx4** is the fourth and last methanation reactor, converting the remaining syngas to CH_4 and H_2O. It has the same settings as Rx 1, Rx 2 and Rx 3.
- **E10**: Heat exchanger for recovery of heat from the SNG stream.
- The stream **S41** is the product exit stream, leading the SNG product to the NG grid at 20 °C and 80 atm.

The full plant has five control loops. Four are present in the syngas plant and one in the methanation plant. The latter only exists in design case 1.

Syngas plant

- **Feed module and water input flow rate:** FM of syngas stream (S18) adjusted by flowrate of water inlet stream (S2).
- **Redox potential of the filter inlet stream:** Adjusted by the split fraction of the SP1 splitter.
- **Temperature of filter inlet stream:** Adjusted to 750 °C by the E2 heat exchanger.
- **Water recovery:** Adjusted by the condenser operating temperature.

Methanation plant

- **Rx 1 temperature control.** This loop controls the split fraction of SP3 in order to keep the outlet temperature of Rx1 below 700 °C.

9.3 Equipment sizing and costing calculations

The last part of the design process was to perform sizing calculations of all pieces of equipment in the flow sheets, and to calculate the costs. The goal of the sizing calculations was to identify and compute the relevant sizing parameters, which enter into the costing equations of each type of equipment. Based on these parameters, the delivered cost of each individual unit was calculated.

In the following, the assumptions, sizing and costing equations for the various types of equipment are outlined. Next, sizing and costing equations for the catalyst, sorbent and filter materials are presented, and at the end of this section, the results of the calculations for all equipment, catalyst, sorbent and filter material in the two cases are summarized.

Splitters and mixers were assumed to be parts of the piping system, which is introduced in the economic analysis in Chapter 12, and the phase separations in the flash drums were assumed to take place in the upstream heat exchangers. Thus, these types of units are not included in the following.

9.3.1 Selection of construction materials

The construction materials of the individual units were selected as per Peters et al. [38] based on the need for corrosion resistance towards carbonic acid as well as the temperature of the individual units. Also, the resistance towards hydrogen embrittlement was accounted for [112, 113]. Generally, two types of materials were considered: 304 Stainless Steel (304 SS) and 316 Stainless Steel (316 SS), with SS 304 being the cheapest.

In the few applications, not exposed to H_2, 304 SS was chosen, and for equipment exposed to H_2, 316 SS was chosen. In some cases, a higher grade of steel was chosen if that resulted in a lower price than the lower grade material. This was the case for most of the smallest heat exchangers, which were strictly on or outside the range of good estimates of the costing equation.

9.3.2 Heat exchangers

The standard costing equation of horizontal shell and tube heat exchangers in counter flow configuration is given as Eq. 9-1.

$$cost = (fA + C) \cdot p \qquad \text{Eq. 9-1}$$

Here, A is the area in m^2, the main sizing parameter of the exchanger. f and C are the linear cost factor and the basic cost of the exchanger. Both of these depend on the type of material used in the construction. p is the pressure correction factor, which depends on the maximum pressure of the heat exchanger. In this work, an over-design for high pressures of 50 % was used such that a heat exchanger, operated at 80 atm was designed assuming at least 120 atm [114].

The heat exchangers were sized as part of the network synthesis calculations performed in HEXTRAN using the standard sizing calculation for heat exchangers:

$$Q = AU\Delta T_{\log mean} \qquad \text{Eq. 9-2}$$

Q is the exchanged heat flow, A is the area, U is the overall heat transfer coefficient, which depends on the flows and individual heat transfer coefficients of the interacting streams as well as the design of the exchanger. $\Delta T_{\log mean}$ is the logarithmic mean temperature difference as defined in the section of heat integration studies in Chapter 2 (section 2.4.2)

9.3.3 Reactors

The sizing of reactors was based on the gas hourly space velocity (GHSV) which is the volumetric flow rate per volume of catalyst installed in the reactor [82]:

$$GHSV = \frac{1}{\tau} = \frac{\mu}{V_{cat}} \quad \text{Eq. 9-3}$$

Here τ is the residence time, μ is the volumetric flow rate and V_{cat} is the catalyst volume. The needed reactor volume may be calculated from the catalyst volume as follows:

$$V = \frac{V_{cat}}{1 - \varepsilon} \quad \text{Eq. 9-4}$$

ε is the void fraction of the catalyst, not to be confused with the porosity. Finally, the height *L*, of the cylindrical reactor with radius *r* is found, assuming that $L/2 \cdot r = 4$ [82].

Rostrup-Nielsen et al. [115] from Haldor Topsøe A/S operated a model methanation reactor at a GHSV of 15,000 h^{-1}. This value was also assumed in this work and it was assumed that the catalyst pellets have a void fraction of 70 % based on [116].

The costing procedure of pressure vessels based on Peters et al. [114] is used for the reactors. Here, the reactor costs depend on the total weight, *W*, of the reactor:

$$cost[\$] = p \cdot m \cdot (73 \cdot W^{-0.34}) \quad \text{Eq. 9-5}$$

p is the pressure factor, for which a tabulated value is used [38]. Based on Biegler et al. [82], a 50% pressure over-design was used as a safety margin. *m* is a material correction factor which is set to 3.0 for the selected 316 stainless steel [114]. Assuming a wall thickness of 1 inch, the volume and mass of stainless steel was calculated from the length and diameter of the individual vessel using a steel density of 7,8 ton/m^3 and an added weight of 20 % to account for supports, flanges, bolts, etc. [114].

The vessel containing the filter was sized based on the needed amount of filter material as is discussed in section 9.3.10 below. The void fraction of the filter material was estimated to 50 %. For the height of the reactor, L, and the radius, r, an aspect ratio $L/2 \cdot r$ = 10, providing an elongated bed, ensuring sufficient contacting of all the impurities in the gas stream with the various adsorption sites and surfaces.

9.3.4 Compressors and blowers

The CO_2 inlet compressor was assumed to be a reciprocating compressor, and the re-pressurization equipment for the gas-phase streams was assumed to be blowers. The costs of

both types were estimated based on tabulated values [114]. The sizing parameters are the required work as calculated by the PRO/II model, the outlet (maximum) pressure and the adiabatic efficiency was assumed to be 75 % for both compressors and blowers [114].

9.3.5 Pumps

The pumps were assumed to be reciprocating pumps and their costs were based on tabulated values [114]. The sizing parameters are the required work as calculated by the PRO/II model, the outlet (maximum) pressure and the adiabatic efficiency which was assumed to be 80 % [114].

9.3.6 SOEC stack

The SOEC stack was sized based on the area specific resistance (ASR) connecting the cell voltage U_{cell}, current density I_A, and open circuit voltage (OCV) where the sizing parameter is the required cell area.

The SOEC model described in Chapter 5 gave the operating voltage of the SOEC stack, U_{cell} and the needed total current for the electrochemical conversion I. With the value of OCV calculated from the stream composition leading to the ELECTROCHEM units (See **Error! Reference source not found.** in Chapter 5) and ASR as found by extrapolation in Chapter 5, the needed current density was calculated as:

$$I_A = \frac{OCV - E_{cell}}{ASR} \qquad \text{Eq. 9-6}$$

From the obtained current density, the needed cell area was simply calculated using the required current, I, from the SOEC model results:

$$A = \frac{I}{I_A} \qquad \text{Eq. 9-7}$$

ASR values of 0.24 Ω·cm^2 and 0.5 Ω·cm^2 were used for cases 1 and 2 respectively, as described in Chapter 5. This resulted in needed cell areas of 33.0 m^2 and 166 m^2.

9.3.6.c Cost of electrolyzer cell area

The cost of the SOEC stack is difficult to project. In the yearly projections on Technology Data for Energy Plants from the Danish Energy Authority [117], a price of 590 €/kW in 2011 prices is projected to 2030 for a 5 MW unit. Assuming this unit operates at a power density of 0.5 w/cm^2, this price corresponds to 1.18 €/cm^2. This price, however, is for a whole electrolyzer plant for H_2 production, and thus includes heat management equipment, gas handling equipment, piping, electric systems etc. in addition to the stack assembly and power electronics. For this work, only the stack itself along with casing, insulation, power electronics and machine parts should be included in the price estimates, as the rest are either modelled

(pressure equipment and heat exchangers) or added later as part of the economic analysis (piping, electric systems, etc.).

Various other price estimates were reviewed as presented in Table 9-3. Where no price index years were given, the chemical engineering plant cost index (CEPCI) for the publication year was used to project prices to 2011 prices. Unless otherwise stated in the table, the stack itself along with casing, insulation, power electronics and machine parts were included whereas costs of installation, control systems, piping, gas conditioning, heat management system etc. were excluded.

These estimates, however, are older, and are not projected to 2035. The estimate from the Danish Energy Agency, on the other hand, is made recently, and they concern the same type of cells which are also used for the ASR extrapolations in this work. This estimate also specifically considers an electrolyzer plant and it is projected to 2035. These considerations favor the latter estimate (from the Danish Energy Agency).

Reference [117] considers a full plant. In order to estimate the price of the SOEC stack itself along with casing, insulation, power electronics and machine parts from [117], the references in Table 9-3 were investigated. In the other references, the mentioned components take up a fairly consistent fraction of the total installed price between 71 % and 85 % with an average of 78 %. This percentage was used to correct the cost estimate of reference [117] to obtain an estimated purchased cost of 0.23 €/cm^2 for installed electrolyzer area including the stack, casing, insulation, power electronics and gas manifolds, but excluding compressors, gas conditioning, recycle components, heat exchangers, etc.

Table 9-3. Investment prices of SOFC/SOEC systems from various sources. Except for reference [117], which is the price of a full plant, only the price of stacks, enclosures, isolation, power electronics, fittings and gas manifolds are included. The "Price fraction" entry shows the costs of the included components as a percentage of the total plant costs. The average of this column is used for calculating the Cost of cell area of the plant described in reference [117] Price index year: 2011.

Reference		Publisher	Price per kW €/kW	Power density W/cm 2	Price per area [€/cm2]	Price fraction [%]	Cost of cell area [€/cm2]
[117]	**Full plant**	**Danish Energy Authority**	**590**	**0.5**	**0.295**		**0.23[b]**
[118]	Lower limit	National Renewable Energy Laboratory	246	0.291	0.072	81.8	
[118]	Upper limit	National Renewable Energy Laboratory	313	0.291	0.091	85.2	
[119]	1 atm	National Energy Technology Laboratory	198	0.4	0.079	N/A[a]	
[119]	20 atm	National Energy Technology Laboratory	315	0.5	0.158	N/A[a]	
[120]	1 atm	National Energy Technology Laboratory	377	0.4	0.151	70.8	
[120]	20 atm	National Energy Technology Laboratory	408	0.5	0.204	73.7	
[121]	Lower limit	Topsøe Fuel Cell A/S	702	0.542	0.380	80.0	
[121]	Upper limit	Topsøe Fuel Cell A/S	735	0.483	0.355	76.3	
Average			386		0.172	**78.0**	

[a]: No data were given for the distribution of costs in this reference.
[b]: The value is calculated based on the 78 % of the installed costs spent on SOES stack assembly, power electronics etc., calculated from the remaining references.

The SOEC is calculated as a piece of equipment rather than a catalyst as both the price of the SOEC related equipment and the cells themselves are included in the price.

9.3.7 Air capture plant equipment

The air capture plant, including desorption chambers, pumps, fans, heat exchangers, storage tanks and heat reservoirs were not sized and costed in this work, as the information needed for such calculations is proprietary information of Climeworks Ltd. As described in Chapter 3, Climeworks Ltd. estimated a plant lifetime of 20 years for the 1000 tons of CO_2 per year plant, and an installed price of 360,000 € - 720,000 €.

9.3.8 Air capture sorbent material

The price of the sorbent material over the entire lifetime of the plant was estimated by CLimeworks Ltd. To be 252,000 € - 540,000 €.

9.3.9 Methanation catalyst

The needed amount of methanation catalyst was calculated during the sizing of the reactors. Each loading of the reactors is assumed to have a technical lifetime of 25.000 hours [102], and thus, over the plant lifetime of 20 years, 7 loadings of the catalyst are needed.

The prices of these types of catalysts are not publically available from the main producers such as Haldor Topsøe A/S. Instead, the prices from two online recourses were used: Pingxiang Baisheng Chemical Packing Co., Ltd cites a price of 22 €/kg or 11 k€/m^3 [122] and similar prices were found from Indian import/export data [123]. In lack of a better estimate, this value is used in this study.

9.3.10 Filter material

The price of Ni-YSZ filter material was estimated from prices of the 8 mol% yttria stabilized zirconia [124] and NiO [125] raw materials available online. No bulk prices were found, and a 50 % reduction from the available prices to bulk prices was assumed. Further, it was assumed that the added price of processing the materials into the sintered NiO-YSZ powder ready for installation and in-situ activation (reduction from NiO to Ni) only constitutes a small increment in costs, which is ignored. From the listed prices, a total price for 50 m% Ni-YSZ of 70 €/kg was obtained.

As discussed in Chapter 4, the needed amount of filter material was calculated based on the sulfur content of the plant prototype tested in Chapter 3 (TVS-3) which represents a prototype of one out of 14 parallel units included in the air capture plant in this study. Only the sulfur content is used for the sizing, as insufficient knowledge is available on the capacity of the Ni-YSZ filters for the other impurities present in the gas stream.

The maximum saturation coverages of the Ni-surface of the filters were calculated for each case based on the composition and temperature of the filter inlet stream using Equation 4-2 from Chapter 4. It is interesting to note from the equations, that at high contents of H_2 compared to the S-content, the filter capacity drops as the maximum saturation θ_{max} decreases according to Equation 4-2. Thus, it is recommended to keep the H_2 content in the filter as low as can be allowed without risking oxidation of the Ni-catalyst. This is incorporated in the SOEC recycle control loop (described in section 5.3) which keeps the H_2 content in the inlet stream at 1 %.

In the IMPURITIES CHAPTER, an increase in specific metallic surface area (SMSA) from 0.13 m^2/g to 0.25 m^2/g was tentatively assumed. These values correspond to the filters used in the study ad to active anode material of current state of the art SOCs respectively. Further increasing this value by a factor of 3 is a reasonable, if conservative, assumption:

The total BET surface area of the coarse structure of the filter material used as 0.7 m^2/g, and a strategy of covering the entire surface area in sub-micron Ni-particles by infiltration has been shown to be possible, still leaving triple phase boundary (TPB) sites open for the reactions [126]. Also increasing the surface area of the cermet is possible through production of a more fine-grained microstructure. On the other hand Ni-nanoparticles are vulnerable to sintering especially at high partial pressures of H_2O as is the case in the filter. Based on these considerations, a SMSA of the fully developed filter material was assumed to be 0.7 m^2/g, corresponding to the total BET surface area of the filter used in the study on impurities. If the entire surface is covered in Ni, an amount of Ni surface sites of 17.9 µmol/g is obtained,

without adjusting for the roughness of a layer of Ni-nano particles. For the conditions of the two design cases and a CO_2 capacity of the air capture plant of 1000 ton/y, this corresponds to filter sizes of ~63 kg/y and ~50 kg/y for case 1 and 2 respectively. The difference between the cases results from the increased θ_{max} at the decreased operating temperature of the filter of case 2.

Also mentioned in Chapter 4, are various strategies for regeneration of the filter. With the above numbers, the filter material would amount to ~€ 90,000 over the plant lifetime, and extending the lifetime of the filters beyond one year is preferable.

Regeneration of this type of filters could include changing the gas composition, introducing H_2, O_2, or H_2O for example, or by increasing the temperature or changing the pressure. Such strategies are currently under investigation at DTU Energy, but no firm results can be provided here. For the sake of this analysis, however, it was assumed, that reasonably cheap regeneration strategies can be developed. While increasing the frequency of regeneration cycles decreases the needed size of the individual filter, this frequency becomes important from an economical point of view. Thus, assuming monthly regeneration will yield a significantly lower capital investment of the filters than yearly regeneration. Without knowing the specific strategy, this is not possible to analyze. In this work yearly regeneration of the filters is used as a basis for the calculations. In reality, it would probably be more frequent, which would lower the investment cost. The savings were assumed to be able to cover the costs of regeneration, however, and thus these were ignored. Further, it was assumed that with at least yearly regenerations, the filter material has a lifetime comparable to that of the SOEC stack of five years and thus four loadings of the filter material is needed over the plant lifetime.

9.4 Sizing and costing results

Based on the assumptions and equations in the previous section, the results of the sizing and costing calculations of all units in the plant in both cases are presented in the following tables. These results include all the equipment needed in the plant. Piping, electrical systems etc. are accounted for as part of the economic analysis, as mentioned previously, and splitters, mixers and flash drums are assumed to be parts of the piping system, and of the corresponding heat exchangers in the case of flash drums.

With the values presented below, the modelling and system integration part of the thesis is finished.

The following chapter includes results of operating the model in terms of mass, heat and energy balances. After this, in 0 and Chapter 12, the economics of the plant are presented and discussed. Those calculations are based on the values in the tables below.

9.4.1 Design case 1

Table 9-4. Specifications, sizing parameters, construction materials and cost estimates of the heat exchange equipment in design case 1. All heat exchangers are assumed to be counter flow shell and tube exchangers.

Unit	Hot side T [K]	Maximum P [atm]	Approach T (ΔT) [K]	Heat transfer coefficient [W/m^2·K]	Duty (Q) [GJ/h]	Area (A) [m^2]	Construction material	Cost [€]
Hx1	1123	80	102	50	0.329	20.8	316 SS	9,314
Hx2	973	80	125	50	0.160	4.0	316 SS	5,393
Hx3	504	80	11	50	0.022	5.4	316 SS	5,720
Hx4	631	80	120	50	0.065	2.0	316 SS	4,926
Hx5	1123	80	40	50	0.119	3.9	316 SS	5,370
Hx6	700	80	119	50	0.010	0.0	316 SS	4,466
Hx7	697	80	42	50	0.216	11.6	316 SS	7,167
Hx8	500	80	7	50	0.019	5.5	316 SS	5,743
Hx9	493	80	10	50	0.015	1.9	316 SS	4,903
Hx10	471	80	6	50	0.080	15.0	316 SS	7,960
Hx11	402	80	16	50	0.009	1.6	316 SS	4,833
Hx12	293	1	5	90.9	0.340	259.3	304 SS	50,065
Hx13	313	1	5	90.9	0.058	17.5	304 SS	7,836
Hx14	356	80	5	90.9	0.012	6.3	304 SS	5,880
Hx15	383	80	5	90.9	0.012	6.4	316 SS	5,953
Hx16	393	1	5	90.9	0.654	259.2	304 SS	50,048

Table 9-5. Specifications, sizing parameters, construction materials and cost estimates of the reactors and the filter vessel in design case 1. All units are sized as pressure vessels.

Unit	Maximum T [K]	Maximum P [atm]	Flow rate [m3/h]	Reactor height [m]	ΔP [atm]	Reactor volume [m3]	Total weight [kg]	Construction material	Cost [€]
Rx1	973	80	282	1.08	0.11	0.063	103	316 SS	318
Rx2	699	80	150	0.88	0.09	0.033	68	316 SS	365
Rx3	504	80	134	0.85	0.08	0.030	64	316 SS	374
Rx4	493	80	69	0.68	0.07	0.015	42	316 SS	432
Filter	750	80	396	1.00	0.36	0.011	-	Alumina	1,500

Table 9-6. Specifications, sizing parameters, construction materials and cost estimates of the pressure change equipment in design case 1.

Unit	Maximum T [°C]	Outlet P [atm]	ΔP [atm]	Flow rate [m3/h]	Work [kW]	$\eta_{adiabatic}$ [%]	Construction material	Cost [€]
Compressors (reciprocrating)								
C1	533	80.6	79.6	69.3	18.293	75.00	304 SS	48,569
Blowers (rotary)								
B1	852	80.4	0.4	0.49	0.006	75.00	316 SS	1,187
B2	221	80.0	0.6	4.30	0.062	75.00	316 SS	1,079
B3	220	80.0	79.8	1.56	0.014	75.00	316 SS	1,079
B4	222	80.7	1.5	1.44	0.080	75.00	316 SS	1,079
Pumps (reciprocrating)								
P1	21	81.0	80.0	0.107	0.290	80.00	304 SS	2,914
P2	144	81.0	1.4	0.096	0.004	80.00	304 SS	2,914
P3	20	81.0	1.0	0.041	0.001	80.00	304 SS	2,914

Table 9-7. Specifications, sizing parameters and cost estimates of the remaining equipment in design case 1 of the plant.

Other equipment, catalyst, sorbent and filter material

Unit	Sizing parameters	Lifetime	Quantity	Price/ Quantity	Cost [€]
	Climeworks Ltd. Estimate	**[y]**	**parallel units**		**Average**
Air capture plant (installed)	360,000 € - 719,000 €	20	14	-	540,000
Air capture plant (purchased)	125,000 € - 250,000 €	20	14	-	187,000

	ASR [Ω·cm^2]	Current [kA]	U_{cell} [V]	P_{cell} [kW]	[y]	[cm^2]	[€/cm^2]	
SOEC stack	0.239	607	1.217	738	20	329,626	0.23	76,000

	Climeworks Ltd. Estimate	[y]			
AC sorbent	252,000 € - 540,000 €	20		-	396,000

	Void fraction	V_{cat}/ loading [m^3]	bulk density [kg/l]	[h]	[kg]	[€/kg]	
Methanation catalyst	0.70	0.042	0.9	25,000	267	22	6,100

		Capacity [µmol/g]	Qty/year [kg/y]	[y]	[kg]	[€/kg]	
Filter material		12.7	62.8	5	251	70	17,600

9.4.2 Design case 2

Table 9-8. Specifications, sizing parameters, construction materials and cost estimates of the heat exchange equipment in design case 2. All heat exchangers are assumed to be counter flow shell and tube exchangers.

Heat exchanger equipment (shell and tube heat exchangers)								
Unit	Hot side T [K]	Maximum P [atm]	Approach T (ΔT) [K]	Heat transfer coefficient [W/m^2·K]	Duty (Q) [GJ/h]	Area (A) [m^2]	Construction material	Cost [€]
Hx1	873	80	107	50	0.142	7.7	316 SS	6,257
Hx2	788	80	295	50	0.014	0.3	316 SS	4,529
Hx3	718	80	83	50	0.045	1.6	316 SS	4,833
Hx4	556	80	38	50	0.012	1.1	316 SS	4,716
Hx5	874	80	72	50	0.070	2.1	316 SS	4,950
Hx6	493	80	32	50	0.064	7.6	316 SS	6,233
Hx7	500	80	7	50	0.003	1.9	316 SS	4,903
Hx8	497	80	22	50	0.046	5.4	316 SS	5,720
Hx9	485	80	6	50	0.023	3.5	316 SS	5,276
Hx10	493	80	21	50	0.016	4.5	316 SS	5,510
Hx11	389	80	5	50	0.013	6.4	316 SS	5,953
Hx12	704	80	33	50.0	0.177	12.7	316 SS	7,423
Hx13	293	1	5	50.0	0.340	259.3	304 SS	50,065
Hx14	313	1	5	90.9	0.058	17.5	304 SS	5,981
Hx15	364	80	5	90.9	0.013	7.1	304 SS	4,595
Hx16	358	80	5	90.9	0.004	0.5	316 SS	4,576
Hx17	374	80	5	90.91	0.011	5.7	316 SS	5,790
Hx18	393	1	5	90.91	0.743	294.6	304 SS	56,230
Hx19	574	80	5	9.09	0.104	751.6	304 SS	136,043

Table 9-9. Specifications, sizing parameters, construction materials and cost estimates of the reactors and the filter vessel in design case 2. All units are sized as pressure vessels.

Reactor equipment (pressure vessels)									
Unit	Maximum T [K]	Maximum P [atm]	Flow rate [m3/h]	Reactor height [m]	ΔP [atm]	Reactor volume [m3]	Total weight [kg]	Construction material	Cost [€]
Rx1	788	80	112	0.80	0.08	0.025	57	316 SS	361
Rx2	556	80	96	0.76	0.08	0.021	60	316 SS	353
Rx3	497	80	69	0.68	0.07	0.015	53	316 SS	369
Rx4	493	80	69	0.68	0.07	0.015	42	316 SS	401
Filter	500	80	404	0,64	0.37	0.013	-	Alumina	1,000

Table 9-10. Specifications, sizing parameters, construction materials and cost estimates of the pressure change equipment in design case 2.

Pressure change equipment								
Unit	Maximum T [°C]	Outlet P [atm]	ΔP [atm]	Flow rate [m3/h]	Work [kW]	$\eta_{adiabatic}$ [%]	Construction material	Cost [€]
Compressors (reciprocrating)								
C1	533	80.5	79.5	68.9	18.293	0.75	304 SS	16,190
Blowers (rotary)								
B1	601	80.3	0.4	1.02	0.013	0.75	316 SS	2,159
B2	145	80.2	0.6	2.35	0.041	0.75	316 SS	1,079
B4	223	80.5	2.0	1.44	0.111	0.75	316 SS	1,079
Pumps (reciprocrating)								
P1	20	81.1	80.1	0.104	0.287	0.80	304 SS	2,914
P2	144	81.1	1.5	0.119	0.005	0.80	304 SS	2,914
P3	76	81.1	1.1	0.015	0.000	0.80	304 SS	2,914

Table 9-11. Specifications, sizing parameters and cost estimates of the remaining equipment in design case 2 of the plant.

Other equipment								
Unit	Sizing parameters				Lifetime	Total quantity	Price/ Quantity	Cost [€]
	Climeworks Ltd. Estimate				[y]	parallel units		Average
Air capture plant (installed)	360,000 € - 719,000 €				20	14	-	540,000
Air capture plant (purchased)	125,000 € - 250,000 €				20	14	-	187,000
	ASR [Ω·cm^2]	Current [kA]	U_{cell} [V]	P_{cell} [kW]	[y]	[cm^2]	[€/cm^2]	
SOEC stack	0.5	607	1.110	673	20	1,661,945	0.23	1,529,000
	Climeworks Ltd. Estimate				[y]			
AC sorbent	252,000 € - 540,000 €				20		-	396,000
	Void fraction	V_{cat}/ loading [m^3]	bulk density [kg/l]		[h]	[kg]	[€/kg]	
Methanation catalyst	0.70	0.023	0.9		25,000	145	22	3,300
		Capacity [µmol/g]	Qty/year [kg/y]		[y]	[kg]	[€/kg]	
Filter material		15.9	50.4		5	202	70	14,100

Chapter 10 Process integration results and discussion

In this chapter, the results of running the full plant models (cases 1 and 2) are presented. First, an overview of the flowrates, temperatures, pressures and compositions of selected streams in the plant are presented in tables. Following this, the results are discussed in the framework of mass balance, heat balance and overall energy balance. Finally, a summary is included at the end of the chapter. As such, this chapter should be seen as the conclusion of the modelling work, and to form the basis for the economic analysis of the following chapter. Thus, the economics of the overall plant will not be discussed here.

The PRO/II input files for the full plant model (design cases 1 and 2), used for producing the results presented in this chapter, are included in Appendix B and C.

The reader is advised to keep the PFDs in Appendix D and E close at hand during the reading of this chapter, for easy reference.

10.1 Stream summary of the full plant

Running the two design cases of the full plant model, results in two sets of stream tables over all streams in the plant. The full stream tables are cumbersome and resumes of selected streams in the plant are presented in Table 10-1 and Table 10-2 below. The tables include all inlet and outlet streams of the plant. In addition, the recycle streams are included along with the inlet and outlet streams of the SOEC stack and the syngas stream. Temperatures, pressures, molar flowrates and compositions are given for each stream. A small fraction of N_2 exists in the CO_2 inlet stream, and it is carried throughout the plant into the SNG stream. It was below 0.5 % in most cases however, and has not been included in the table. The reader is referred to the Process Flow Diagrams (PFD) on pages 141 and 142 or the reference sheets included in Appendix D and E while reading the tables.

Table 10-1. Stream summary for selected streams in the full plant model, design case 1. Composition values below 0.5 % are written as "-". The small fraction (< 0.5 %) of N_2, present in most streams of the plant, is not shown.

Stream description		Temperature [°C]	Pressure [atm]	Flowrate [kmol/h]	Composition [mole fraction]					
					H_2O	H_2	CO_2	CO	CH_4	O_2
S1	CO_2 inlet	20	1.0	2.88	0.01	-	0.98	-	-	-
S2	H_2O inlet	20	1.0	5.65	1.00	-	-	-	-	-
S10	SOEC inlet	741	80.0	16.54	0.80	0.02	0.17	-	-	-
S16	SOEC outlet	850	80.0	13.73	0.40	0.39	0.05	0.06	0.10	-
S21	SOEC recycle	850	80.0	0.43	0.40	0.39	0.05	0.06	0.10	-
S19	O_2 outlet	20	79.1	5.66	-	-	-	-	-	1.00
S20	Syngas plant H_2O recycle	144	79.7	4.92	1.00	-	-	-	-	-
S18	Syngas	144	79.7	8.39	0.05	0.61	0.09	0.09	0.16	-
S30	Rx1 inlet	207	80.0	11.71	0.13	0.50	0.07	0.07	0.23	-
S33	Rx1 recycle	220	79.7	3.32	0.31	0.23	0.04	0.02	0.39	-
S42	Methanation H_2O recycle	76	79.2	2.59	1.00	-	-	-	-	-
S26	SNG product	20	80.0	2.85	-	-	-	-	0.99	-

Table 10-2. Stream summary for selected streams in the full plant model, design case 2. Composition values below 0.5 % are written as "-". The small fraction (< 0.5 %) of N_2, present in most streams of the plant, is not shown.

Stream description		Temperature [°C]	Pressure [atm]	Flowrate [kmol/h]	Composition [mole fraction]					
					H_2O	H_2	CO_2	CO	CH_4	O_2
S1	CO_2 inlet	20	1.0	2.88	0.01	-	0.98	-	-	-
S2	H_2O inlet	20	1.0	5.64	1.00	-	-	-	-	-
S10	SOEC inlet	490	80.0	16.87	0.79	0.02	0.17	-	0.01	-
S16	SOEC outlet	600	80.0	11.91	0.59	0.15	0.03	-	0.23	-
S21	SOEC recycle	600	80.0	1.16	0.59	0.15	0.03	-	0.23	-
S19	O_2 outlet	20	79.1	5.66	0.00	-	-	-	-	1.00
S20	Syngas plant H_2O recycle	144	79.6	6.12	1.00	-	-	-	-	-
S18	Syngas	144	79.6	4.63	0.05	0.34	0.08	0.01	0.52	-
S42	Methanation H_2O recycle	76	78.9	0.98	1.00	-	-	-	-	-
S26	SNG product	76	78.9	2.84	-	-	-	-	0.99	-

Comparing the two tables show, that the inlet and outlet streams of the two cases are identical to within the uncertainties of the modelling introduced by the convergence criteria of the control loops. The same is the case for the SOEC inlet stream except for the temperature. The SOEC outlet stream (S16), however, differs in that the CH_4 fraction in case 2 is twice as large as for case 1. This is as expected from the shift of the methanation reaction towards

methane at lower temperatures. After the unreacted water has been removed in the condenser of the syngas plant, the CH_4 fraction in the syngas stream (S18) is 52 % in case 2 compared to only 16 % in case 1. The increase in CH_4 content the Rx1 inlet stream to 23 % in case one is caused by the addition of the recycle stream.

The SOEC recycle stream is seen to be only ~3 % of the SOEC outlet in case 1, whereas it is almost 10 % in case 2. The reason is that the control loop keeps the H_2 content of the SOEC inlet stream at 2 %, which requires a significantly larger recycle fraction, as the H_2 content in the recycle stream is lower in case 2.

It is repeated, that the composition and flowrate of the SNG product stream (S26) is identical in the two cases. Also, the large oxygen stream (S19) should be noted.

10.2 Mass and water balance

The mass balance is performed by the PRO/II model based on the air capture plant capacity of app. 1000 tons of CO_2 per year. As briefly mentioned previously, the air capture plant produces a certain quantity of water for each mole of CO_2. Until this point, this water has not been included in the model, and the model is set up with a water inlet stream instead (S2, see Table 10-1 and Table 10-2). The water balance is treated further below.

Furthermore, the SOEC subsystem produces an O_2 outlet stream, and the final product stream of the plant is the SNG stream. These are the components of the overall mass balance, and the consumption or production rates of these streams are repeated in Table 10-3. Table 10-1 and Table 10-2 above showed that the outlet streams of the plant is identical for the two cases within a slim margin of error which is attributed to minor variations in stream compositions and uncertainties in the calculations stemming from the convergence criteria of the control loops. Thus, table one present only case 1 for simplicity.

In Chapter 3on the air capture system, it was mentioned, that the system captures between 2.3 and 3 moles of H_2O for every mole of CO_2. In Table 10-3, the flowrate of the CO_2 stream is given along with the resulting flowrate of captured H_2O calculated with a H_2/CO_2 ratio of 2.5 (H_2O capture). The following three entries in the table (H_2O inlet, H_2O recycles and H_2O needed) represent the water inlet stream used in the model so far (S2), the two water recycle streams (S20 and S42), and the combined stream where the recycle streams have been mixed with the inlet stream (S22). The flow rate of S22 is set by the control loop adjusting the Feed Module (FM) of the syngas stream, by varying the H_2O inlet stream. Thus, comparing the flowrate of the H_2O inlet stream to that of the H_2O capture shows that even at the low end of the H_2O capture rate, sufficient amounts of H_2O is produced to cover the demands of the plant. If the H_2O inlet stream is replaced with the H_2O capture, the surplus water from the air capture plant is calculated as the difference between these two. This is given in the table as "Net H_2O discharge".

Table 10-3. Mass balance of the full plant model case 1. The internal water recuperation is specified to visualize the flows of water in the system. The "CO_2 capture" and "H_2O capture" rows represent the quantities captured from the atmosphere. The "Water need" is the water flow in the SOEC inlet stream as calculated by the FM recycle loop, and the "Net H_2O discharge" is the excess amount of water (see text).

Mass balance	Design case 1	
	[kmol/h]	[Nm^3/y]
CO_2 capture	2.827	580,889
Water		
- H_2O capture	7.068	1,069
- H_2O inlet (S2)	5.642	854
- H_2O recycles (S20+S42)	7.504	1,136
- H_2O needed (S22)	13.146	1,989
Net H_2O discharge	1.425	216
O_2 production	5.659	1,143,512
SNG production	2.867	579,321

The water balance of the plant shows, that if the H_2O captured from the atmosphere is sufficiently clean, the air capture plant is capable of supplying all the water needed for the SNG production, and still maintain a small production of water of high purity. Wurzbacher et al. [22] state that the H_2/CO_2 ratio from the air capture plant is between 2.5 and 3.0 depending on the temperature, humidity, and pressure of the air. As the minimum value was used, the "Net H_2O discharge" stream may be larger when averaged over a full year.

As the air capture system is operated, the H_2O is removed from the desorption chamber along with the remaining air after the vacuum has been established, but at slightly lower temperatures than the desorption of CO_2. This means that in order to utilize the water, a separation step has to be included. Such separation will leave a small amount of O_2 dissolved in the H_2O stream, however. A small amount of O_2 is already present in the CO_2 stream. This is removed by reaction with H_2 in the filter. Including O_2 in the H_2O inlet stream as well would lead to a amount of O_2 which needs to be removed in the filter, which, in turn, would lead to a slightly larger recycle rate in the SOEC recycle, in order to add sufficient amounts of H_2 to remove this oxygen as well. As a consequence, the energy efficiency of the SOEC sub-plant would decrease, even though the effect would be small. A detailed study of these issues was not conducted, but it is assumed that the impact on efficiency is negligible, and that recovery of the water from the air capture plant can be kept within the price estimate provided by Climeworks Ltd (see Chapter 3).

The remaining water amounts to between 216 and 260 Nm^3/y (for H_2/CO_2 ratios of 2.5 and 3, respectively). This is assumed to be consumed on site. In up-scaled versions of the plant, this might be sold as high purity water, providing another minor revenue stream for the plant.

In addition to the small amount of water produced, a very large amount of O_2 is produced in the plant. As the model is set up, the O_2 is produced at ~79 atm. The purity of the stream is

very close to 100 %, and the stream is assumed to be salable to provide an extra revenue stream for the plant. This is discussed further in Chapter 12 on the economic analysis.

10.2.1 Quality of produced SNG

In the previous section, the amount of produced SNG was given. As mentioned in section 2.3 on methanation technology, strict demands are imposed on the quality of Substitute Natural Gas (SNG) in order for it to be fed directly to the Natural Gas (NG) grid [101]. To briefly summarize, the SNG needs to have a Wobbe index between 49 MJ/Nm^3 and 57MJ/Nm^3, where the minimum values corresponds to a very high content of CH_4 (~99 %). The SNG compositions and thus the energy contents and Wobbe indices were essentially identical with less than 0.5 % variation between the two cases. In Table 10-4, the production rate, composition and fuel gas characteristics are presented for the SNG product of case 1.

Table 10-4. Flowrate, composition and fuel quality of the produced SNG in both design cases, compared to the acceptable range of the Danish NG grid.

SNG quality		**Case 1**
Volumetric rate	**[Nm^3/h]**	68.36
Molar composition	**[%]**	
- H_2O		0.70
- H_2		0.29
- CO_2		0.00
- CO		0.00
- N_2		0.50
- CH_4		98.54
Energy content	**[MJ/Nm^3]**	
- HHV		36.54
- LHV		32.90
Wobbe index	**[MJ/Nm^3]**	
- SNG		49.04
- NG grid standard [101]		49 - 57

The table shows that the produced SNG is exactly on the lower limit of the Wobbe index range. This illustrates the difficulty of producing SNG complying with the grid standards, without the addition of higher hydrocarbons. Apart from drying the gas completely or fine tuning the CO_2/H_2O ratio in order to get rid of the small fraction of leftover H_2, not much can be done to improve the energy content. For comparison a 100 % pure CH_4 stream has a Wobbe index of 53.4 GJ/Nm^3. Even with these measures, retaining this degree of control with the product might be difficult for large scale production, and it may turn out to be more economically viable to ad small amounts of higher hydrocarbons. In this work the obtained SNG quality is considered sufficient, however, and this is not treated further.

10.3 Heat balance

The consumption and production of heating and cooling services, that is the hot and cold utilities, is treated separately from the overall energy balance below.

In Chapter 8 on heat integration, the composite curves (CC) for the heating and cooling demands of the full plant in the two cases were discussed for two values of the heat recovery approach temperature (HRAT). One strategy where HRAT = 10 K and one where HRAT = 0 K requiring the high-temperature heating and cooling duties were preferentially matched. The analysis gave the maximum amounts of heat that it is possible to recover in the system along with the expected needs for hot and cold utilities. In Table 10-5, the values are compared to the values obtained from the heat integration performed in the same chapter.

Table 10-5. Overview of the results of the heat integration of design cases 1 and 2. The predictions from the analysis of the Composite Curves (CC) in Chapter 8 are compared to the process-process recovery and needed utility consumption obtained from the heat integration work.

Cases and analysis method [GJ/h]	Process-process Recovery	Hot utilities	Cold utilities
Case 1			
- CC prediction, HRAT = 10 K	1.12	0.56	0.42
- CC prediction, high T matching, HRAT = 0 K	1.10	0.59	0.45
- Heat integration, HRAT = 10 K	1.04	0.65	0.42
Case 2			
- CC prediction, HRAT = 10 K	0.68	0.80	0.43
- CC prediction, high T matching, HRAT = 0 K	0.66	0.82	0.41
- Heat integration, HRAT = 10 K	0.63	0.85	0.43

The HRAT value of a heat exchange problem is an indicator for the amount of heat which may be recovered internally in the system. This would usually lead to a larger amount of recoverable heat in the HRAT = 0 K scenario than the one where HRAT = 10 K. The opposite dependence, seen in the table, is caused by the constraint of matching the high-temperature duties.

With the relatively low HRAT value of 10 K for in the synthesized networks of both cases, the very close match between the predictions from the composite curves and the attained process-process recovery is expected. It is interesting to note how the consumption of hot utilities in the heat integration is minimized to the theoretical value and the cold utility consumption is larger. This is an effect of HEXTRAN taking into account the relatively large costs associated with hot utility consumption compared to the costs of the cold utility. This is a good illustration of the importance of the economic considerations in heat integration problems.

To conclude, the synthesized networks have heat recoveries and utility consumptions very close to the theoretical values, as seen in the table.

10.3.1 Utility consumption

Certain quantities of each of the two hot utilities (U1 and U2) and of the cold utility (U3) are consumed in the heat exchanger networks of the two plant cases. Table 10-6 summarized the utility consumption in the various heat exchangers for the two cases, and describes the conditions at which the utilities leave the plant.

Table 10-6. Overview of the utility streams used in the plants in both design cases. For those of the cold utilities, which will be sold as district heating, the energy contents are calculated assuming a return temperature of 30 °C.

Utility	Inlet T [K]	Outlet T [K]	Energy consumption [GJ/h]	Energy content [MJ/h]	Use/discharge
			Case 1		
U1:					
- Hx16	119	105	0.654	-	Recycle
U2:					
- None	-	-	-	-	-
U3:					
- Hx12	10	15	0.340	-	Discharge
- Hx13	10	35	0.058	-	Discharge
- Hx14	10	78	0.012	8.37	District heating
- Hx15	10	105	0.012	11.72	District heating
			Case 2		
U1:					
- Hx19	119	106	0.743	-	Recycle
U2:					
- Hx20	301	260	0.104	-	Recycle
U3:					
- Hx14	10	15	0.340	-	Discharge
- Hx15	10	35	0.058	-	Discharge
- Hx16	10	86	0.013	9.88	District heating
- Hx17	10	80	0.004	8.28	District heating
- Hx18	10	96	0.011	2.79	District heating

For each utility stream in the plant, Table 10-6 presents the expected strategy for handling the discharge streams. The temperatures of the hot utilities (U1 and U2) are only lowered by a fraction of the tolerance described in Table 11-3 in the chapter on economic prerequisites, assumptions and method. These streams represent non-specific heat sources at the given temperatures, depending on the availability of high temperature process heat on the specific site of the plant. This will be discussed in depth in 0. In a case where no hot process heat is present and the hot utilities are generated on-site, the streams are sent back to the heat pump and electric boiler for re-heating. In the case where hot process streams are present, further integration is needed in the specific case to account for the rejected hot streams. This is treated in more detail in the chapter on *Part V - Analysis*

Economic prerequisites, assumption and method.

In the case of the cold utility (U3), the outlet streams of some of the heat exchangers (Hx12 and Hx13 in case 1 as well as Hx14 and Hx15 in case 2) are still quite cool, and they are released to the cooling service provider. In the case of the remaining cold utility exit streams, the temperatures have reached those of the district heating network, and the released heat may be sold. This provides an additional (small) revenue stream for the plant. The remaining energy content of these streams is calculated, assuming a return temperature in the district heating system of 30°C [127].

Small amounts of heat are available in the discharged streams and the produced district heating streams. In theory, these could be upgraded using heat pumps, and integrated with other parts of the plant. This requires knowledge of the available hot utilities, which is explicitly not available, and since the amounts of heat rejected in the district heating streams is so small, no attempts at further heat recovery between the discharged utility streams have been conducted. For the hot utilities, however, only the heat which has actually been absorbed from the utility streams are accounted for in the economic analysis, as the decrease in temperature is relatively limited.

10.4 Energy balance

In this section, the overall energy balance of the plant is considered.

The energy balance includes the various energy inputs to the plant, based on the modelled consumptions of heating, cooling and electricity of all units in the plant in addition to the considerations on the use, regeneration and discharge of hot and cold utilities presented in the previous section.

10.4.1 SOEC operation

First, the operating parameters and results for the operation of the SOEC subsystem are presented in Table 10-7. The table compared the conversion factor (CF) of the electrochemical conversion step to the reactant utilization (RU) defined by the difference in flowrates of H_2O and CO_2 between the inlet and outlet streams of the stack. The current is calculated from the flowrates of H_2O and CO_2 and the CF. E_{tn} and U_{cell} are calculated from the enthalpy changes of the unit operations in the model as described section 5.4 . E_{tn} incorporated only the chemical reactions, whereas U_{cell} takes the extra heating (> E_{tn}) in the OHMIC_HEAT step into account as well. The enthalpy changes are defined so that positive values represent energy inputs, and negative values represent heat developed in the cell.

Table 10-7. Operating parameters and results for the SOEC stack in the two design cases. The CF and RU are compared, and the thermoneutral voltage and cell voltage are calculated from the current and enthalpy changes of the four unit operations in the model.

Operating parameters of SOEC stack			
Parameter	**Unit**	**Case 1**	**Case 2**
T_{stack}	[°C]	850	600
CF	[%]	70	70
RU	[%]	61	54
ASR	[Ω·cm^2]	0.239	0.5
Current	[kA]	607	607
$\Delta H_{1\ (OHMIC\_HEAT)}$	[kJ/mol]	7,176	7,241
$\Delta H_{2\ (SHIFT1)}$	[kJ/mol]	54	2,033
$\Delta H_{3\ (ECHEM)}$	[kJ/mol]	255,352	254,854
$\Delta H_{4\ (SHIFT2)}$	[kJ/mol]	-27,768	-49,879
E_{tn}	[V]	1.18	1.07
U_{cell}	[V]	1.22	1.11
P_{cell}	[kW]	738	674
Cell area	[m^2]	33.0	166.2
Current density (I_A)	[A/cm^2]	-1.84	-0.37
Power density	[kW/cm^2]	2.24	0.41

The current is the same in the two cases, as the same amounts of H_2O and CO_2 is converted, as defined by the CF. The overall conversion of reactants between inlet and outlet (RU) is different however, due to the higher methane production at the low operating temperature of case 2. Comparing the enthalpy changes in the two cases in the table shows how a large amount of heat is developed by the methanation reaction in fuel electrode outlet (SHIFT2). The increased methanation activity is seen to decrease both E_{tn} and the cell voltage (U_{cell}). The energy consumption of the OHMIC_HEAT step is similar in the two cases, as the inlet streams are similar, and both need to be heated by 100 °C. It should be noted, that the additional amount of thermal energy provided by the methanation reaction in case 2 compared to case 1 far exceeds the energy spent on heating from the filter temperature to the stack temperature (OHMIC_HEAT).

The cell area is calculated from the area specific resistance (ASR) estimated for the two cases in Chapter 5, and the difference between the two cases is seen to have a significant influence on the area and thus, the current and power densities of the cells.

10.4.2 Full plant energy balance

Based on the energy consumption of the SOEC subsystem and those of the other units in the plant, the energy balance is presented in Table 10-8, along with the energy content of the SNG and the discharged district heating stream.

Table 10-8. Energy balances and energy efficiencies of the full plant for both cases. The emphasized rows are the sums of the below mentioned duties in the case of "SOEC", "Pressure change equipment" and "Hot utilities". The energy efficiency is calculated based on all the electrical and thermal energy (heating and cooling) consumed by the process and the energy content of the SNG stream. The electrical efficiency is calculated based on the electrical inputs and the energy content of the SNG stream.

Energy Balance	Case 1		Case 2	
	[kW]	[MJ/Nm^3]	[kW]	[MJ/Nm^3]
SOEC	**738.3**	**38.8**	**673.6**	**35.4**
- Electrochemical conversion	715.7	37.6	650.8	34.3
- TN Joule heating [a]	22.6	1.2	22.8	1.2
Air Capture electricity	**28.6**	**1.5**	**28.6**	**1.5**
Pressure change equipment	**18.8**	**1.0**	**18.8**	**1.0**
- C1 (CO_2 compression)	18.298	0.961	18.293	0.963
- B1 (SOEC recycle)	0.006	0.0003	0.013	0.001
- B2 (syngas blower)	0.062	0.003	0.041	0.002
- B3 (Rx1 recycle)	0.014	0.0007	-	-
- B4 (Rx4 blower)	0.080	0.004	0.111	0.006
- P1 (H_2O inlet pump)	0.209	0.015	0.287	0.015
- P2 (syngas plant H_2O recycle)	0.004	0.0002	0.005	0.0003
- P3 (methanation H_2O recycle)	0.001	0.0001	0.0001	0.000004
Hot utilities	**181.7**	**9.5**	**235.4**	**12.4**
- U1 (air capture heating)	181.7	8.5	206.5	10.9
- U2 (H_2O evaporation)	-	-	28.9	1.5
Cold utility				
- U3 (Miscellaneous cooling)	**117.4**	**6.2**	**118.5**	**6.2**
Total energy consumption	**1084.7**	**57.0**	**1074.8**	**56.6**
District heating production	**6.7**	**0.4**	**5.8**	**0.3**
Total energy balance	**1079.1**	**56.7**	**1069.0**	**56.3**
SNG energy content				
- HHV	36.5 MJ/Nm^3		36.6 MJ/Nm^3	
- LHV	32.9 MJ/Nm^3		32.9 MJ/Nm^3	
Energy efficiency				
- η (HHV)	64.1 %		64.7 %	
- η (LHV)	57.7 %		58.3 %	
Electrical efficiency				
- $\eta_{electric}$ (HHV)	88.5 %		96.1 %	
- $\eta_{electric}$ (LHV)	79.7 %		86.8 %	

[a]: This row accounts for the Joule heating above the thermoneutral potential (E_{tn}) in the SOEC

The obtained energy efficiencies are relatively high, owing to the high efficiency of the SOEC technology. The main contributions to energy losses come from the heat integration in the form of the hot and cold utility consumptions.

Interestingly, even though the electricity consumption of the SOEC is significantly lower in case 2 compared to case 1, this does not change a lot on the overall system efficiency. When a large part of the conversion of syngas to methane takes place directly in the SOEC stack, as in case 2, the heat is supplied directly in the stack. This lowers the amount of heat available from the methanation plant intercoolers correspondingly. The results are seen as a significantly higher electrical efficiency in case 2 compared to case 1, whereas the overall energy efficiencies are effectively identical. The increased electrical efficiency is the result of a lower cell voltage I case 2, allowed by the decrease of the thermoneutral voltage caused by the increased generation of heat in the cell.

Figure 10-1 shows a graphical representation of the distribution of the energy consumption of the plant. It should be noted, that this is the net consumption, meaning any internally recuperated heat is not shown.

From the diagrams, it is immediately clear that the vast majority of the energy consumptions take place in the electrolyzer. This is not surprising, as this is where the main chemical conversion takes place in form of the electrochemical reduction. The heating above the thermoneutral potential in the stack is seen as well, even though this represents a small part of the electricity consumption of the stack and plant alike. As was already suggested by the discussions in Chapter 5 on the various compression strategies for CO_2, the compression only takes up a small amount of the electricity consumption as well, whereas all other pressure change operations are collected in the “other” fraction. The large heating duty of the air capture plant takes up almost a fifth of the entire plant consumption. The desorption step is where the free energy of separating CO_2 from the atmosphere (ΔG_{mixing}) is provided. ΔG_{mixing} is significantly lower than the consumption of the air capture plant, however, as was discussed in Chapter 2 on air capture theory. The remainder of this energy requirement comes from the binding energy of the CO_2 and the co-desorption of 2.5 – 3 moles of water with every mole of CO_2. Also, as the energy is supplied as heat, the dead weight of the sorbent carrier material and the vacuum chamber itself need to be heated as well.

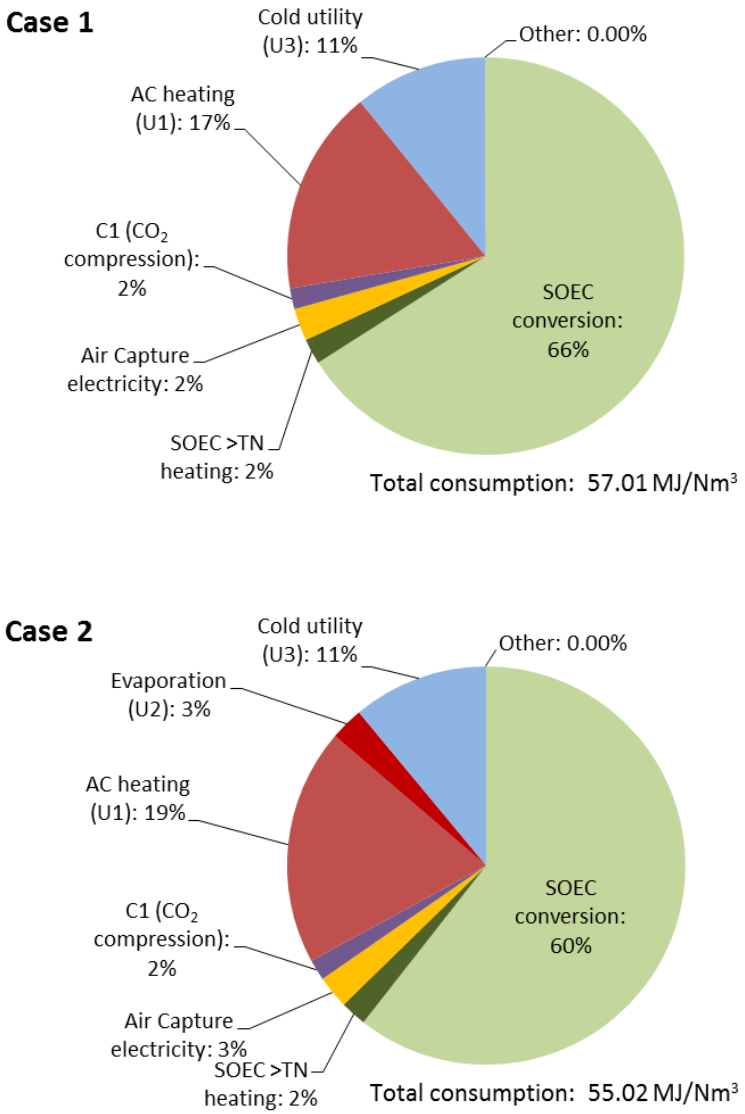

Figure 10-1. Distribution of the energy consumption on the various parts of the plant for both design cases. Internally recovered heat is not shown.

The heating duty and electricity consumption of the air capture plant, combined with the vast majority of the cold utility consumption, takes up more than a quarter of the entire energy requirements of the plant. In case 2, the water evaporation shows up, covered by the high temperature hot utility, and it will add to the operating costs of the plant due to the high estimated price of the high-temperature utility however.

10.5 Summary

The modelling efforts have resulted in a steady state, thermodynamic model, capable of simulating the full plant in the high and low temperature design cases (1 and 2 respectively).

No input streams are needed in the model, as only the air flowing through the adsorption chamber of the air capture plant provides can be assumed to supply the needed water. Thus,

the SNG production rate is governed exclusively by the capacity of the air capture sub-system. Even though small variations in the composition of the SNG are observed depending on the operating parameters of the two cases, the production rates are essentially identical.

The produced SNG has methane contents of 98.5 %, resulting in high energy content for SNG (HHV: 36.5 MJ/Nm^3; LHV: 32.9 MJ/Nm^3). In spite of this, the Wobbe index of the SNG (49.0 MJ/Nm^3) is on the lower end of the acceptable range for inclusion into the NG grid, but it is assumed, that with optimization of the operation of the plant, the quality should be sufficient to avoid addition of higher hydrocarbons.

In addition to the SNG product, by-product streams of pressurized O_2 and water, both of high purity in addition to a small stream of district heating is produced. The water stream is assumed to be consumed on site, and the others are assumed to be marketable, and will be included in the economic analysis.

The lowered temperature in case two compared to case one resulted in a lowered cell voltage of the electrolyzer cells of 1.11 V compared to 1.22 V in case 1. This translated into a 9 % decrease in cell power, at identical cell currents. The difference is caused by the increased methanation activity, providing heating directly in the cell.

The energy consumptions of the plant are concentrated in the air capture plant (29 % and 32 % in case 1 and 2) and the electrolyzer stack (68 % and 62 %). Other energy intense processes, such as H_2O evaporation and methanation train intercooling are almost fully integrated in the internal heat exchanger network.

Only a small drop in energy consumption from case 1 to case 2 is seen, and consequently, the overall energy efficiencies of the two cases are very similar. The electrical efficiency, however, is highly dependent on temperature, which is interesting to note in connection to the discussions on availability of hot process streams. From an energy point of view, low temperature operation seems beneficial if process heat (even at intermediate temperatures) is available. This needs to be discussed in the light of investment and operating expenditures, which is the topic of the next chapter.

Part V - Analysis

Chapter 11 Economic prerequisites, assumption and method

In this chapter, the prerequisites, assumptions and method of the economic analysis are presented.

The second section is related to the estimation of prices of utilities such as electricity, heating and cooling services along with an overview of the revenue streams of the plant.

The first section includes the basic economic prerequisites related to the chosen techno-economic scenario are presented. The values for exchange rates, price index years, inflation, lifetime, depreciation, taxes, salvage and scrap values are based on the scenario and standard conditions employed in socioeconomic studies in the energy sector in Denmark.

Finally, the methodology of estimating the costs of plant construction, commissioning and operation is presented briefly, and the chosen profitability measure is introduced.

11.1 Projection of utility prices and revenue streams

In this section, the prices of utilities (electricity, heating and cooling) are projected. The calculations and assumptions are based on underlying data from the Energikoncept 2035 [1] scenario and on discussions with Energinet.dk [128].

11.1.1 Price of electricity

For the electricity prices a dataset was acquired from Energinet.dk taken from their projections of electricity prices as presented in the report Energikoncept 2035 (Energy Concept 2035) [1, 129]. The data set is a projection based on the assumptions and scenario presented in the report, presenting the electricity price for the CO_2-neutral grid mix projected for Denmark in 2035, calculated on an hourly basis throughout the year.

The price data are plotted versus time for one year in Figure 11-1 a. In order to get a working value for this study which does not consider time variations, a simple average was calculated

to 18.7 €/GJ corresponding to 67.2 €/MWh (red line in the figure). This is presented in Table 11-3 at the end of this section.

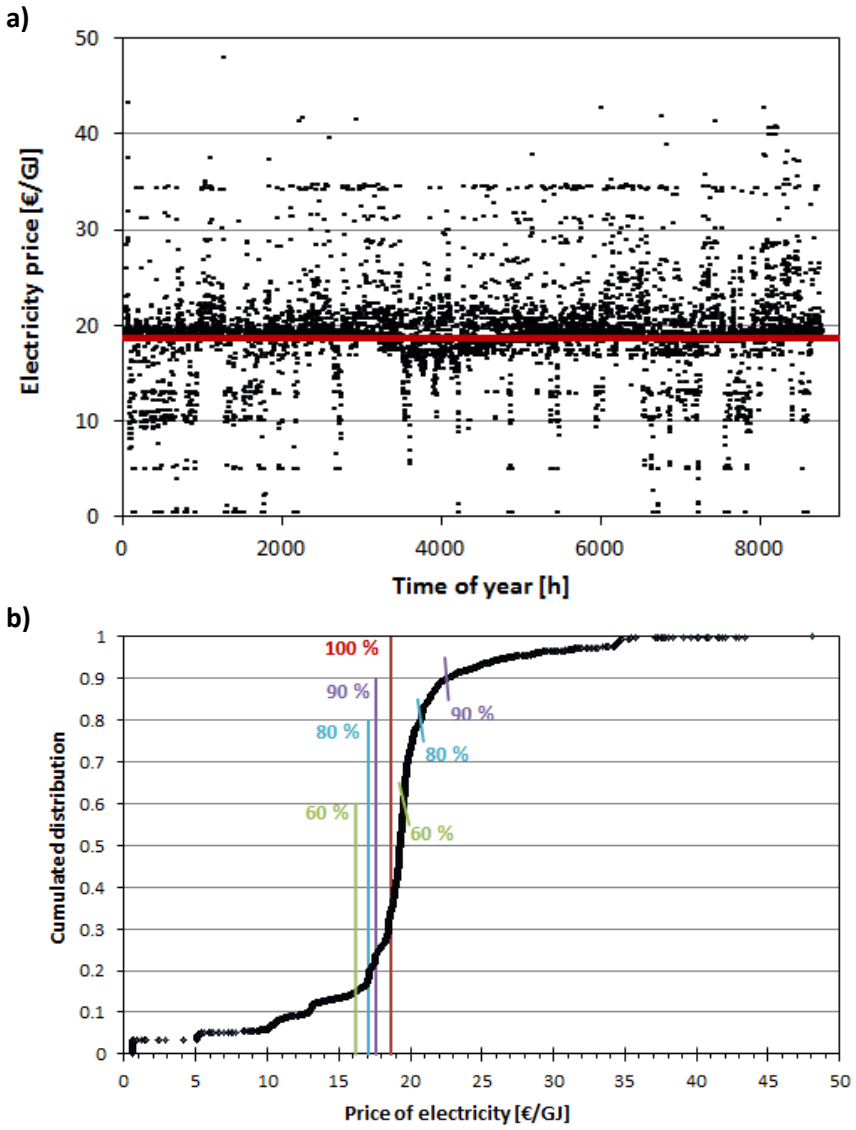

Figure 11-1. Projected hourly electricity prices in Denmark, 2035. a) Projected prices vs. time of year. The simple average (red line) is shown. b) Cumulated distribution of the prices. The average price is shown (red) along with the average prices calculated for the lower 90 % (purple), 80 % (teal) and 60 % (green) of the dataset. The upper limits of the ranges are marked on the curve. Data from [1, 129]

Figure 11-1 b shows the cumulated distribution of the data, with the average electricity price marked by the red line. The other vertical lines in the figure mark the average values calculated for the lower 90 %, 80 % and 60 % ranges of the data representing situations where the plant

might be shot down during times with very high electricity prices. The upper limits of these ranges are marked on the curve by short line segments.

11.1.2 Price of district heating

The price of district heating was projected by Energinet.dk in the Energikoncept 2035 report along with the electricity prices [1, 129]. The district heating prices are given as a 48h running average on an hourly basis and presented in Figure 11-2. The yearly average price was calculated to 6.39 €/GJ (red line in the figure), and this value is used for the economic analysis.

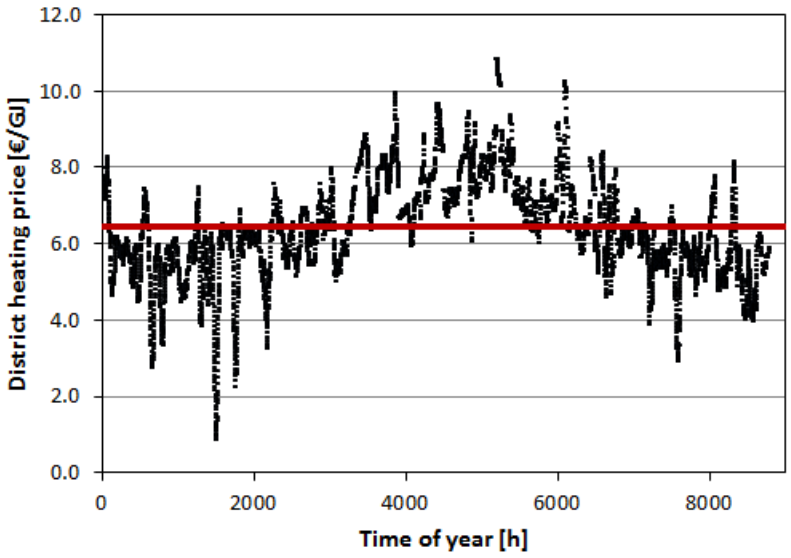

Figure 11-2. Projected hourly prices of district heating utilities for one year in Denmark, 2035 given as 48 hour averages. The simple average over the year of 6.39 €/GJ is marked by the red line.

11.1.3 Price of high temperature heat

Determining the prices of high temperature heat is difficult, as heat is not as easily transportable as electricity. For this reason, Energinet.dk expects heat-intense industries, and especially those producing and consuming high temperature heat, to be clustered geographically to minimize heat losses from transportation [128]. These clusters are assumed to be connected by the electrical grid, and to be connected to a larger centralized district heating grid, as Energinet.dk expect a larger geographical interconnection of the district heating system. Such a scenario makes it difficult to project the prices, as the usual market mechanisms are not in play on a national scale. For this reason, the local price at which heat can be traded between industries will be highly dependent on the local supply and demand structure of the specific industry cluster [128]. Based on this setup, two extreme situations of local supply and demand are considered. It is important to remember, that in the 2035 scenario, no fossil fuels can be consumed to produce the required heating on site.

In the first situation, a cluster of industries with a large production of high temperature process heat, and no consumers of this heat is considered. Energynet.dk expect a high degree

of geographical integration in terms of the district heating grid, and thus, if no local demand for high temperature heat exists, the marginal price of district heating will be the price at which the heat supplying industries can sell their excess heat. With these assumptions, the district heating prices as described above, will serve as a lower bound on the price for high temperature process heat even though, in all probability, this will be a gross underestimate.

In the second case, the opposite scenario is considered. In an industrial cluster with a large demand for high temperature heating services, and no excess high temperature process heat exists, the price of generating this heat with electricity will be the marginal price of high temperature heat. Thus, upgrading district heating to the required temperatures is used as the upper bound on the price of hot utilities.

The upper bound on the price based on the situation described above, is determined as the price of buying district heat and upgrading it to the wanted temperature (300 °C in this case) using high temperature heat pumps and an electric boiler.

The Energikoncept 2035 report [1] estimated the price of heat production at 120 °C with a high temperature heat pump using district heating as the input heat source. The estimate is repeated in Table 11-1 along with a case calculated for the 8,400 operating hours assumed in this work. The last case uses the prices for electricity and district heating estimated above, whereas the first case is a recalculation of the one presented by Energinet.dk.

Table 11-1. Estimated prices of heat production using a high temperature heat pump and district heating as input heat source in Denmark, 2035. The first row represents Energinet.dks projections. The last row uses the electricity and district heating prices estimated above. [1]

T_{low} [°C]	T_{high} [°C]	COP	Investment cost [€/MW]	lifetime [y]	Operating hours/year h/y	CAPEX [€/GJ]	Electricity price [€/GJ]	Input heat price [€/GJ]	Output heat price [€/GJ]
70	120	5.2	653,333	15	3,000	5.47	23.07	5.33	15.24
70	**120**	**5.2**	**653,333**	**15**	**8,400**	**1.95**	**18.60**	**6.39**	**11.92**

From 120 °C to the outlet temperature of 300 °C, an electric boiler is used. The initial enthalpy flow in the inlet district heating stream was calculated using PRO/II, calibrating the flow rate to produce an output enthalpy flow of 1 GJ/h.

The price of the boiler was estimated based on the Technology Data for Individual Heating Plants data sheet published by the Danish Energy Agency. The calculation is summarized in Table 11-2.

Table 11-2. Estimated prices of upgrading heat from 120 °C to 250 °C using an electric boiler, in Denmark in 2035 [117].

Efficiency [%]	Investment cost [€/MW]	lifetime [y]	Operating hours/year h/y	Lifetime O&M [€/MW]	CAPEX [€/GJ]	Electricity price [€/GJ]	Output heat price [€/GJ]
99	130000	20	8400	106000	0.39	18.60	18.99

The flow rate of the inlet district heating stream was 0.366 Nm^3/h with an enthalpy rate of 0.185 GJ/h at 2.22 €/h. The additional heating of 0.815 GJ/h at the price given in Table 11-2 results in a total prices of heat at 300 °C of 17.7 €/GJ. The higher and lower bounds calculated with the lowest and highest price estimates for district heating and electricity were 7.4 and 116.4 €/GJ.

11.1.4 Cooling

The plant needs cooling at several temperatures, the lowest of which is at 15 °C. No prices for cold utilities are found in the 2035 scenario or the assumptions, it is based on. Thus, a price for cooling water at 10 °C of 0.11 €/GJ is obtained from Peters et al. [99]

11.1.5 Utility prices summary

The prices resulting from the above considerations are summarized in Table 11-3. In this study, the utility prices calculated from the average district heat and electricity prices are used.

The hot utilities are named U1 for the upgraded district heating stream at 120 °C and U2 for the high temperature stream at 300 °C. The cold utility is named U3. The naming is shown in the table along with the utility temperatures, and chosen limits on the acceptable return temperatures. For the hot utilities, the acceptable return temperatures were chosen as typical values from the district heating system [127]. The limit for the cold utility was set, somewhat arbitrarily, to the maximum hot utility temperature.

Table 11-3. Estimated prices of utilities to be used in this project. Hot utility @ 120 °C is calculated as raising the temperature of district heat to 120 °C with a high temperature heat pump. The hot utility @ 300 degrees is calculated as further increasing the temperature to 300 °C with an electric boiler.

Utility	Temperature [°C]	Acceptable return temperature	Average price [€/GJ]
Electricity, grid mix			18.6
Heating			
District heating (lower bound)	70	-	6.4
Hot utility (U1)	120	30	11.9
Hot utility (U2) (upper bound)	300	30	19.8
Cooling			
Cold utility (U3)	10	300	0.11

As was discussed in Chapter 8 on the heat integration study, hot utilities were needed at two different temperatures for the low temperature plant design case 2 (T_{stack} = 600 °C). One at app. 110 °C and one at 300 °C. In the design of the plant, the upper bound price on high temperature heat was used as the price for hot utilities, and the price for upgraded district heat (at 120 °C) was used for the intermediate temperature hot utility stream. The average prices for electricity and district heating were used. As such, the plant was designed using the upper bound estimates which are probably significantly higher than in reality. This is discussed further in section 12.4 of the economic analysis chapter.

11.1.6 Revenue streams

As has been mentioned in Chapter 9 on the plant integration, two minor revenue streams are produced in addition to the main SNG product stream. These include the large production of pressurized oxygen and the minor production of district heating produced from part of the cold utility consumption. The small stream of water produced was assumed to be consumed on site.

The price of the oxygen stream has been hard to find reliable numbers for, but a price of 0.14 €/kg is assumed, based on [130].

For the district heat production, the price was estimated above. The energy content of the streams was calculated in PRO/II based on a return temperature of 30 °C and calculated flowrates.

The production price of the SNG is calculated from the overall economic analysis of the plant.

11.2 Economic Prerequisites

As was described in the introduction of this thesis, the plant is analyzed within the framework of the Energikoncept 2035 report from the Danish grid operator, Energinet.dk [1]. The main reason for this choice is that it represents a coherent scenario for an energy system with no fossil fuels in the electricity or heat mixes. This is important, as the main goal of the technology discussed in this report is to produce carbon neutral fuels from air captured CO_2. This also means that a long range of the basic economic parameters are settled either as parts of the Energikoncept 2035 scenario or in the standards which were used for the development of it. This will be clear in the following sections.

11.2.1 Exchange rates

It is assumed that currency exchange rates are constant throughout the projection period. This is a practical assumption as economic projections do not factor in changing exchange rates, and as such, the exchange rates are in effect constant in the projections even though this is not the case in reality.

The following exchange rated are used between Danish kroner (DKK / kr.), US dollars (USD / $) and euro (EUR / €): 750 DKK = 100 EUR = 139 USD. This is based on the DKK-EUR fixed rate policy of the Danish government and the DKK/USD exchange rates assumed by the Danish Energy Agency [131] for the years after 2018.

11.2.2 Inflation and index prices

The 2035 scenario presents all economic data using 2011 prices, as do the technology catalogs from the Danish Energy Authority used in this study[117]. Based on this, *all prices in this work are given as 2011 prices*, unless otherwise noted. Estimates for inflation in the period from 2011 to 2035 exist[131], but in order to ensure comparability with other available prices and the scenario forming the basis of the analysis, inflation in this period is ignore.

Price estimates for equipment and utilities are found in the literature given for various index years. In order to ensure comparability between the individual estimates, all prices of equipment and utilities are adjusted to 2011 prices using the annual chemical engineering plant cost index (CEPCI) [132].

11.2.3 Interest rates

According to the Danish Energy Agency's Instructions for Socio Economic Analyses of the Energy Sector [133, 134], a yearly interest rate of 4 % (not counting inflation) is used in this study for projects with lifetimes up to 35 years. This value is also used as the opportunity cost or the minimum risk free rate of return, which is the rate of return which could have been obtained on a given amount of capital if it was not invested in the plant in consideration in this study for example.

The minimum acceptable rate of return (MARR) is the minimum rate of return, which an investor is willing to accept on a specific investment [85]. Usually this should account for the minimum risk free rate of return in addition to the risks involved in the project. In this work, the bare minimum value is used, in the form of the minimum risk free rate of return which is set equal to the interest rate of 4 % per year.

11.2.4 Lifetime

The plant is expected to have an overall technical lifetime of 20 years, based on the expected lifetime of SOEC systems [117] and the air capture system. This include more frequent replacements of the sorbent material, filter material, SOEC stacks and methanation catalysts. The individual lifetime estimates for these parts of the plant were included in the costs calculated in the equipment tables at the end of Chapter 9. The replacement costs are included in the initial capital investment for simplicity.

11.2.5 Depreciation

In this project, straight-line depreciation over the entire lifetime of the plant was used as this resembles the actual decline of the plants value over time most closely. This disadvantages the project from a tax-optimization point of view, but represents the most intuitive and a generally applicable way of depreciating assets [135, 136].

11.2.6 Salvage and scrap value

The salvage value represents the value of an asset which has not yet been depreciated. If parts of an asset is still valuable as it is at the end of life of the plant, and has not yet been depreciated, its value needs to be subtracted from the total capital investment for calculation of depreciation. The scrap value is the price which can be obtained from selling parts of a plant for material recovery. This is usually treated as a capital income and is not included in calculations of depreciation.

At the end of the plant lifetime in this project, most of the equipment is expected to be sold as scrap-metal and active components such as catalysts, SOEC cells, sorbent material etc. are expected to be sold for material reclaim, or disposed of. This means the salvage value is

expected to be zero at the end of the project life, and the scrap value is treated as a capital income. For simplicity, it is assumed, that the scrap value will pay for the disposal of the remaining parts of the plant, and the scrap value is in effect zero [135]. The reclaim value represents the amount of capital which can be reclaimed from a project at the end of its lifetime, and is set equal to the land cost plus the operating capital investment.

The operating capital investment is estimated to be equal to 2 % of the fixed capital investment [135] (see next section).

11.3 Method for economic analysis

11.3.1 Cost estimation, components and uncertainties.

In addition to the costs of the equipment of the plant, the capital expenditures (CAPEX) include delivery of purchased equipment, installation of delivered equipment, instrumentation and controls, piping, electrical systems, buildings, land improvement and service facilities. Also included in the CAPEX are engineering and supervision, construction expenses, legal expenses, contractor's fees and contingency. All of the above are also called the fixed-capital investment.

The cost of land cannot be depreciated and is not included in the fixed-capital investment for calculations of depreciation. It is however, considered part of the overall CAPEX category of expenses. The land costs were calculated as 7 % of the purchased equipment costs in design case 1, resulting in a cost of 36,000 €. The same value was used for design case 2.

The operating expenditures (OPEX) consist of the annual prices for utilities, and the costs of the air capture sorbent material, the impurity filtering material and the methanation catalysts. The latter three are replaced at regular intervals over the lifetime of the plant. In this analysis, the annualized costs these components are calculated simply by dividing their total costs for the full life of the plant with the plant lifetime in years (20 years).

In addition to the above, labor and supervision, maintenance and repairs, operating supplies, laboratory charges and royalties are included in the OPEX. Also included are property taxes, cost of financing and plant overhead.

Except for the equipment, utilities, sorbent, filter material and catalyst, all of the additional cost components of both CAPEX and OPEX are estimated as percentages of the delivered equipment costs or the fixed capital investment. This simplified method is generally accepted and the factors for each category of costs are obtained from [135].

Table 11-4 summarizes the chosen factors used in the cost estimation.

Estimating the costs of a plant is not a simple task as incomplete information is available. The method used in this works is based on sizing and costing of the used equipment and utilities, and estimating the costs of all other cost components based on these calculations. If the initial costing calculations are based on firm values, this method usually obtains results better than

order of magnitude estimates, and based on [135], the uncertainties of the economic calculations in this project are assumed to be approximately ± 25 % - 35 %.

Table 11-4. Cost component factors used for estimating the total capital investment and the total operating expenditures, in addition to selected economic parameters used in the profitability analysis. For the cost components, the cost factor is given in % along with the calculation basis.

Parameter	Value	Unit	Reference
Fixed capital investment			
- Delivery of purchased equipment	10	% of Purchased equipment	[43, 135]
- Installation of purchased equipment	47	% of Delivered equipment	[43, 135]
- Instrumentation and control	36	% of Delivered equipment	[135]
- Piping	68	% of Delivered equipment	[43, 135]
- Electrical systems	11	% of Delivered equipment	[43]
- Buildings	18	% of Delivered equipment	[135]
- Yard improvement	10	% of Delivered equipment	[43, 135]
- Engineering and supervision	33	% of Delivered equipment	[43, 135]
- Construction expenses	41	% of Delivered equipment	[43, 135]
- Legal expenses	4	% of Delivered equipment	[43]
- Contractor fee	22	% of Delivered equipment	[43, 135]
- Contingency	44	% of Delivered equipment	[43, 135]
Also included in CAPEX			
- Land cost	7	% of Purchased equipment	[135][d]
Operating expenditures			
- Operating labor	2	% of Fixed capital investment	[43]
- Operating supervision	15	% of Operating labour	[43, 135]
- Maintenance and repairs	6	% of Fixed capital investment	[43, 135]
- Operating supplies	15	% of Maintenance and repairs	[43, 135]
- Laboratory charges	15	% of Operating labour	[43, 135]
- Plant overhead	60	% of Labor + Supervision + Maintenance	[43, 135]
- Property taxes	2	% of Fixed capital investment	[43]
- Financing interest	4	% of Fixed capital investment	[133, 134]
- Insurance	1	% of Fixed capital investment	[43, 135]
Economic parameters			
- Working capital investment	2	% of Fixed capital investment	[43]
- Start-up costs	10	% of Fixed capital investment	[43]
- Minimum acceptable rate of return	4	% per year	
- Depreciation type	Linear		
- Year of depreciation	20		
- Income tax	24.5	%	
- Project life time	20	years	

[d]: Not included in Fixed Capital Investment for depreciation calculations.

The costs of the air capture plant (500.000 – 1.000.000 $) is assumed to be given as the installed costs including piping, instrumentation and electrical system (see above). For this reason, parts of the costs are subtracted from the given price before it is added to the total list of equipment. The effects of this operation can be seen in Table 9-7 in the plant integration chapter.

11.3.2 Profitability

The profitability of the plant is analyzed as the discounted cash flow return on investment (DCFROI). The return on investment is calculated as the percentage of all costs of the process

(CAPEX and OPEX over the plant lifetime) made up by the total net profit obtained by sales of the SNG product and all byproducts over the full lifetime, in addition to the salvage value.

In order to calculate this, the yearly cash flows are calculated discretely at the end of each year, and interests are compounded discretely at the end of each year. The cash flows are discounted to year zero which is the last year before the production starts, using the discounting factor for annual, end of year cash flows and discrete, annual, end of year interest compounding. Finally, the cash flows are cumulated over the plant lifetime, and the return on investment can be calculated. It is beyond the scope of this work to introduce the economic theory behind these calculations, and the reader is referred to the literature. Especially Peters et al. [85, 135, 136] has been useful in this work.

Chapter 12 Economic analysis

In this chapter an economic analysis of the installation and cost operation of the designed plant is performed. The main goal is to analyze the plant as it was designed over the preceding chapters, with regards to the production price of substitute natural gas in both design cases (Case 1: T_{stack} = 850 °C and case 2: T_{stack} = 600 °C).

In the first section, and overview of the plant economics is given, and the results of the analysis are presented along with the main cost drivers of the plant.

Following this, the sensitivity of the SNG price to the estimated prices related to the main cost drivers is studied. This is done by looking at the basic assumptions behind the estimated prices.

12.1 Economic overview

The economics of the plant operation consist of three main components: The capital expenditures, the operating expenditures and the revenue. These are defined below, and the values are presented in Table 12-1 for the two design cases (case 1: T_{stack} = 850 °C and case 2: T_{stack} = 600 °C).

The total capital expenditures (CAPEX), herein defined as all expenditures paid during the construction, commissioning and start-up of the plant, were calculated from the purchased equipment costs which were calculated in Chapter 9 and the additional component cost factors outlined in Table 11-4.

Similarly, the operating expenditures (OPEX) were calculated based on the utility consumption presented in Chapter 10; the utility prices estimated in the previous chapter, and additional cost components from Table 11-4.

Finally, the revenues from the district heating and oxygen streams (secondary revenue) were calculated with the prices estimated in 0. The revenue from sales of SNG is a variable in the calculations of the SNG prices below. An overview is presented in Table 12-1 for both design cases.

Table 12-1. Summary of the plant economics for the two design cases. The table is split into Capital Expenditures (CAPEX), Operating Expenditures (OPEX) and secondary revenue streams. The OPEX and Secondary revenue are calculated per year.

	Case 1 T_{stack} = 850 °C	Case 2 T_{stack} = 600 °C
CAPEX	**[k€]**	**[k€]**
- Equipment	513	930
- Other cost components	1,937	3511
- Land	36	36
- Working capital investment	49	89
- Startup costs	245	444
OPEX	**[k€/y]**	**[k€/y]**
- Utilities	508	496
- Sorbent, filter material, catalyst	21	21
- Other cost components	547	975
Secondary revenue	**[k€/y]**	**[k€/y]**
- O_2	219	219
- District heat	1	1
CAPEX, total [k€]	**2,781**	**5010**
OPEX per year [k€/y]	**1,076**	**1491**
Secondary revenue per year [k€/y]	**220**	**220**

The table shows that the revenue from the O_2 and district heating streams is small, and only make up app. 13 % and 7 % of the OPEX each year for case 1 and 2 respectively. Thus, a large fraction is left for the primary revenue, the sales of SNG, to cover. Especially when counting the CAPEX as well.

12.2 Production price of substitute natural gas

In order to calculate the SNG price in the two cases, the plant was required to be profitable at a minimum acceptable rate of return (MARR) equal to 4 %. With all other economic parameters known, the SNG price was then found numerically. As mentioned in the previous chapter (section 11.3.2), the discounted cash flow return on investment (DCFROI) was used as the profitability measure. This means, that the cash flow was discounted to year zero of the plant lifetime, and the return on investment (ROI) was calculated based on the discounted cash flow. Year zero is defined as the last year before the plant operation begins. The cash flow is discounted in order to adjust for the time value of money, which accounts for the standard rate of return on a safe investment. The interest rate obtained from [133, 134] (4 %) was used for the discounting (see section 11.2.3).

With MARR = 4 %, the net profit (that is the profit after taxes and depreciation) of the entire plant lifetime needs to be at least 4 % of the CAPEX. With this constraint, the SNG production prices were found to be 1.88 €/Nm^3 and 2.94 €/Nm^3 for case 1 and 2 respectively, i.e. these SNG prices are necessary in order to pay back the CAPEX over 20 years bearing an interest rate of 4 %, and resulting in a discounted rate of return of 4 %.

Figure 12-1 shows the cumulated discounted cash flows for both cases. Interests are compounded and cash flows calculated discretely at one-year intervals at the end of each year. In accordance with ECON [43], the construction period is assumed to be three years with the expenditures for land and 35 % of the capital investment paid in the first year. In the second year, 50 % of the capital investment is paid and 15 % is paid in the third year (year -1 – 0). In year one (0 – 1) the operating capital investment and the start-up expenses are paid, resulting in a cash flow close to zero. In the remaining years, a net profit after taxes and depreciation is made of app. 90,000 €/y and 170,000 €/y in the two cases. At the end of life of the plant (shown in the insert), the land costs and operating capital investment are reclaimed, resulting in the short vertical part of the curves. The curves are calculated with the above mentioned SNG product prices in order to achieve a DCFROI = MARR = 4 % (see section 11.3.2).

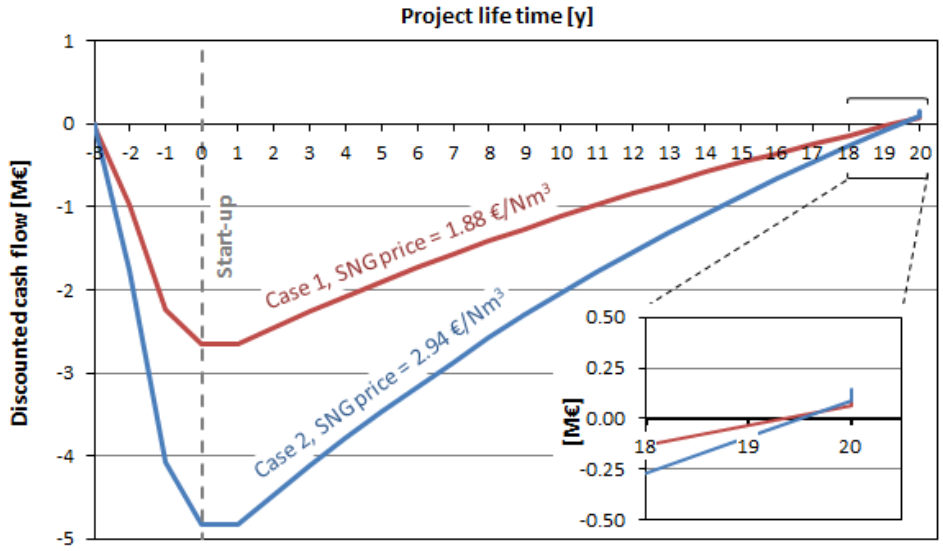

Figure 12-1. Discounted cash flow over the plant lifetime for design cases 1 and 2 (T_{stack} = 850 °C and 600 °C respectively) , when the CAPEX has to be paid back over 20 years bearing an interest rate of 4 % and resulting in a DCFROI of 4 %. Net present values are calculated for year 0 which corresponds to 2035. The insert shows the last part of the graph magnified.

The slopes of the curves represent the sum of the net profit per year and the yearly depreciation. The large difference between the two cases is caused by the large difference in capital investment and operating expenditures, as the plant is required to be profitable in these calculations.

Several observations about the results presented above are immediately important: The calculated SNG production prices reflect the bare minimum costs of producing SNG in the two cases, with the economic prerequisites and assumptions mentioned in the previous chapter. The constraint is that the plant needs to be profitable at the lowest viable level, MARR = 4.0 %, which means that an investment of the same magnitude in government bonds will give the same return on investment over 20 years. This means that the calculated prices are bare minimum prices.

The large difference between the prices of the two cases is driven by the large difference in CAPEX between the cases. This is seen from the magnitude of the minimum of the cash flow curves in Figure 12-1 and can be read from the numbers in Table 12-1. In order to get a better idea of the cost structure, the cost drivers of the plants was analyzed. This is presented below.

12.3 Cost drivers

In this section, the breakdown of the capital and operating expenditures (CAPEX and OPEX) into their various contributions is presented. There are several ways to split the expenses, which is done in a series of pie-charts.

12.3.1 CAPEX breakdown

The capital expenditures, not counting the operating capital investment and the start-up expenses, were calculated based on the purchased costs of the equipment in the plant. This was explained in 11.3.1 in the *Part V - Analysis*

Economic prerequisites, assumption and method chapter. The breakdown of the expenses into the different cost components are shown in Figure 12-2, which also shows the equipment costs distributed on the various equipment in the two cases of the plant. The sizes of the circles in the diagrams are not to scale. The percentages given for the equipment relate to the percentages of the total equipment costs, not the total capital expenditures. Only equipment making up more than 1.5 % of the total equipment costs is marked in the diagrams.

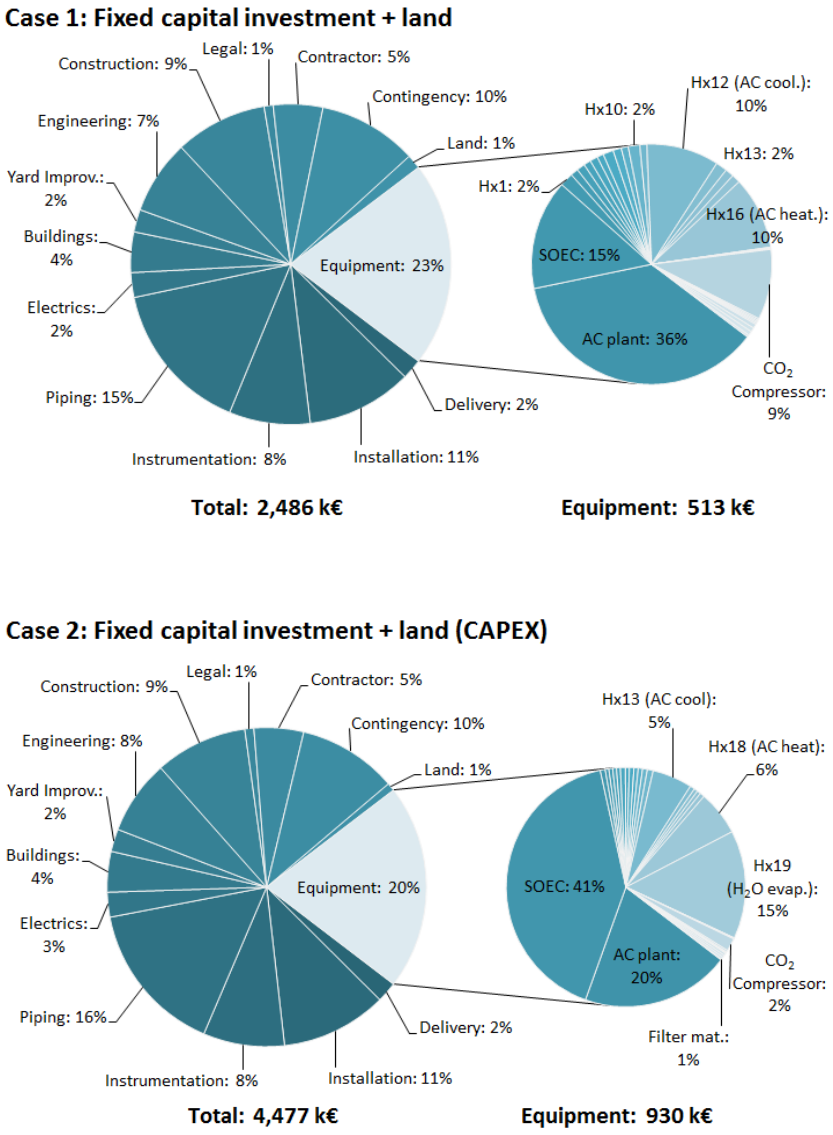

Figure 12-2. Breakdown of the capital expenditures for the two design cases, not counting operating capital investment and start-up costs. The circles on the left represent the total expenses. The circles on the right represent the purchased equipment costs. The percentages for the equipment represent the percentages of the equipment costs, not the total capital costs. The circles are not to scale. For the equipment costs, equipment taking up less than 1.5 % is not marked. The equipment was specified in Table 9-4 through Table 9-11 in section 9.4 . Hx# refers to heat exchangers. "AC cool" refers to the cooling of the vacuum pump in the air capture plant. "AC heat" refers to the heating of the sorbent material in the air capture plant, and "H2O evap," refers to heat exchangers involved in evaporation of the H_2 inlet stream.

Since the cost components of the plant are calculated as factors multiplied by the purchased and installed equipment costs, they are close to identical for the two cases. The total capital investment and the total purchased equipment costs are given in the figure, showing the large discrepancy between the cases.

In case 1, the largest contributor to the equipment costs is the air capture plant (AC plant), followed by the SOEC subsystem and the heat exchanger Hx19 used in the air capture plant for

heating the sorbent, and finally the CO_2 compressor in that order. Combined, these make up 70 % of the equipment costs with the SOEC and air capture plant alone taking up 51 %. In case 2, the SOEC sub-system is the largest contributor to the equipment costs by 41 % alone followed by the AC plant and the heat exchanger Hx 19 used for steam generation. In total, these three make up 76 % of the total equipment costs in case 2, with the SOEC and AC plant taking up 61 % alone.

The contributions of individual heat exchangers is difficult to compare between the cases because the heat exchanger networks are different (see Chapter 8 on the heat integration study). In both cases, the total costs of the heat exchanger networks (summed costs of all heat exchangers) is 36 % of the purchased equipment costs. This means that the network is significantly more expensive in case 2, which overall have higher equipment costs. This will be discussed further in Chapter 13.

The large difference on the SOEC costs is caused by the significantly larger ASR assumed for the low temperature cells (case 2) than for the standard cells (0.5 $\Omega \cdot cm^2$ vs. 0.24 $\Omega \cdot cm^2$), which in turn requires a significantly larger cell area.

12.3.2 OPEX breakdown

The annual operating expenditures (OPEX) are calculated using cost component factors, as explained in 11.3.1 of the chapter on *Economic prerequisites, assumption and method*, based on the fixed capital investment which is the total capital costs, without land costs, operating capital investment and start-up costs. In addition to this, the annual expenses for utilities, air capture sorbent, impurity filter material and methanation catalyst are included in the operating costs as well.

The breakdown of the total operating costs is given in Figure 12-3 along with the distribution of the utility costs on the different processes in the plants. In the figure, the percentages of the cost components in the left hand circle are percentages of the total costs, whereas for the utilities, the percentages of the total utility costs are given. All contributions to the utility costs are accounted for, but only utility contributions taking up more than 0.5 % of the utility costs are specified.

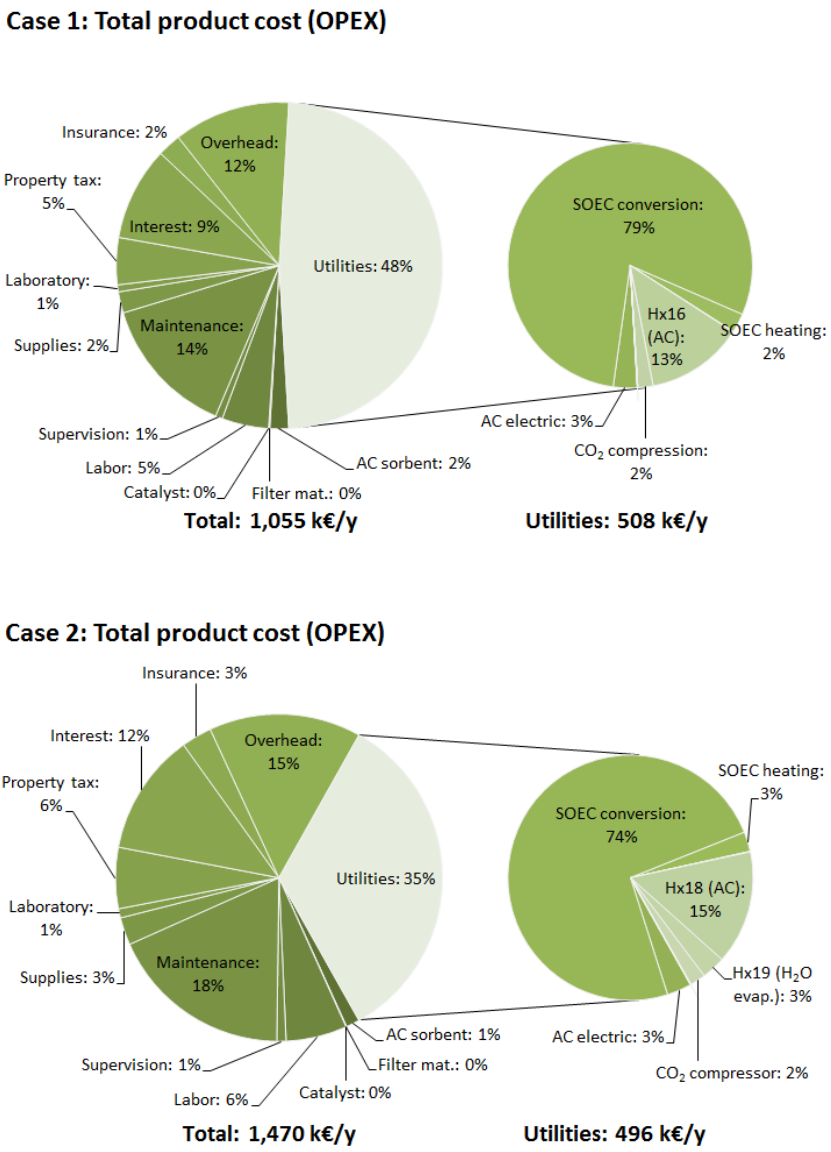

Figure 12-3. Breakdown of the operating expenditures (OPEX) for the two design cases. The circles on the left represent the total operating expenditures (see Table 11-4 in the previous chapter for details). The circles on the right represent the annual utility costs (see Table 10-6 in the plant integration results chapter for details). Circle sizes are not to scale. In the utility costs, consumption below 0.5 % are not specified in the figure but were included in the calculations. This includes all pressure change operations except for the inlet CO_2 compression.

The utility costs of the two cases are of comparable sizes, but they take up a different fraction of the total operating costs as the remaining components are calculated based on the fixed capital investment costs as explained above. The main difference between the cases apart from the absolute values is that a larger part of the utility costs are taken up by the hot utilities (Hx18 for heating the air capture sorbent and Hx19 for H_2O evaporation) in case 2. Also, a smaller fraction is taken up by electricity compared to case 1 as was already discussed in Chapter 10. In both cases however, the electricity used for the electrochemical conversion

takes up the vast majority of the utility costs which was expected, as it takes up comparable percentages of the plant energy consumption. The expenses for cold utilities and pressure changes (except for the CO_2 compression) vanish in the diagrams as their combined costs make up less than 0.2 % of the total utility expenses in both cases. The CO_2 compression is visible, but makes up a very small part, as was expected already in the discussion on alternative compression strategies in Chapter 5.

12.3.3 Cost drivers summary

In the above sections, the breakdowns of the CAPEX and OPEX were laid out. While cost components other than equipment and utility costs take up fractions of the total capital and operating expenditures comparable to those of individual pieces of equipment or utilities, these are not investigated in this project. The reason is, that those cost components are calculated as factors from standard tables (see references in Table 11-4), and optimizing these components has little technological meaning and is outside the scope of this work. Taking a critical look at the assumptions on the equipment and utility prices in the context of the plant economics, however, points out the hotspots in the price structure and places where technological improvements could be beneficial and viable, as is discussed over the following sections.

The main cost drivers were identified as the following: SOEC sub-system, air capture plant, heat exchanger network, electricity consumption and hot utility consumption. For the CAPEX components, the order in which they appear after size varies between the two cases, as the change from high to low temperatures have a large effect on the SOEC price, which becomes the dominant cost component in case 2. The remaining equipment take up comparatively tiny fractions of the total equipment price compared to the three mentioned above, and for the utilities, the cold utility completely vanishes in the costs of heat and electricity.

12.4 Sensitivity of SNG price to cost drivers price estimates

In the following sections, each of the cost drivers are examined with regards to the initial assumptions behind their price estimates and the effects on the SNG price are calculated. This is done by calculating the production price of SNG from the discounted cash flow, with the requirement that the plant has to be profitable with a Minimum Acceptable Rate of Return (MARR) of 4 %. This is the same strategy which was used above in section 12.2 above.

12.4.1 Price of SOEC sub-system

As one of the main cost drivers, the SOEC sub-system takes up 15 % and 41 % of the purchased equipment costs in design case 1 and 2 respectively. The large difference is that the area specific resistance (ASR) is strongly dependent on temperature. Therefore, in the low temperature design case (case 2, T_{stack} = 600 °C), ASR is significantly higher (0.5 $\Omega \cdot cm^2$ versus 0.239 $\Omega \cdot cm^2$) than in the high temperature case (case 1, T_{stack} = 850 °C).

The price of cell area was determined from the Technology Data for Energy Plants by the Danish Energy Agency [117] as described in section 9.3.6 in the process integration chapter. The cells considered in the reference is of the same type as the ones considered for case 1 in

this works, and very similar to those considered for case 2. The cells were assumed to be operated at power densities of 0.5 W/cm^2 in the reference. In this work, however, the cells are operated at power densities of 2.24 in case 1 and 0.41 in case 2. In case two, the power densities are close, and this is not assumed to have any influence on the economics. In case 1, however, the discrepancy is larger. The assumed power density of 0.5 for the cells mentioned in the reference is not used in any calculations in the modelling in this work. But as increased power densities might lead to larger degradation of SOEC stacks, the increased power density in this work compared to the reference, could mean that the lifetime of the cells is overestimated. If this is true, the purchased cost of the SOEC subsystem in case 1 is too low. This depends strongly on the technological development of SOEC technology over the coming years, and was not studied in detail.

It should be emphasized here, that the model in both design cases is operated with the power density calculated by the model from the ASR, conversion current and cell voltage, as described in section 5.4 . The assumed 0.5 W/cm^2 are only used to adjust the units of the price in the reference.

The referenced prices listed in Table 9-3 in section 9.3.6 range from 0.072 Ω·cm^2 to 0.380 Ω·cm^2. This corresponds roughly to the estimated price of 0.23 Ω·cm^2 ±66 %. This range was used for analyzing the sensitivity of the SNG production costs to the purchased SOEC cost for both design cases.

In addition to the design cases 1 and 2, two alternative cases were also calculated. In the diagrams, these are named “Case 1*” and “Case 2*”. For Case 1*, the calculations were performed using the ASR values from the experimental cell which is also used in Case 2 (See section 5.4.2 in the syngas plant model chapter for details). The ASR of this cell has been found experimentally to be 0.101 Ω·cm^2 at 850 °C. In case 1, this corresponds to a reduced total cell area of 8.6 m^2 compared to 33.0 m^2. This alternative case is plotted as “Case 1*” in the figures.

For case 2, the alternative case uses a different type of experimental cell, currently under development by Barnett et al. [137]. This cell type is at an even earlier state of development, but the calculations serve as an illustration of the effects of cells with very low ASR. At 600 °C. The ASR of this cell has been measured to 0.24 Ω·cm^2. Note that this is the same level as the standard cell in case 1 at 850 °C. The cells operate at very different voltages, however, and the total cell area in Case 2* is 80 m^2 compared to 166 m^2 in Case 2. This alternative case is named “Case 2*” in the figures.

The SOEC costs and SNG prices were calculated for the two design cases and two alternative cases outlined above, and the results are presented in Figure 12-4.

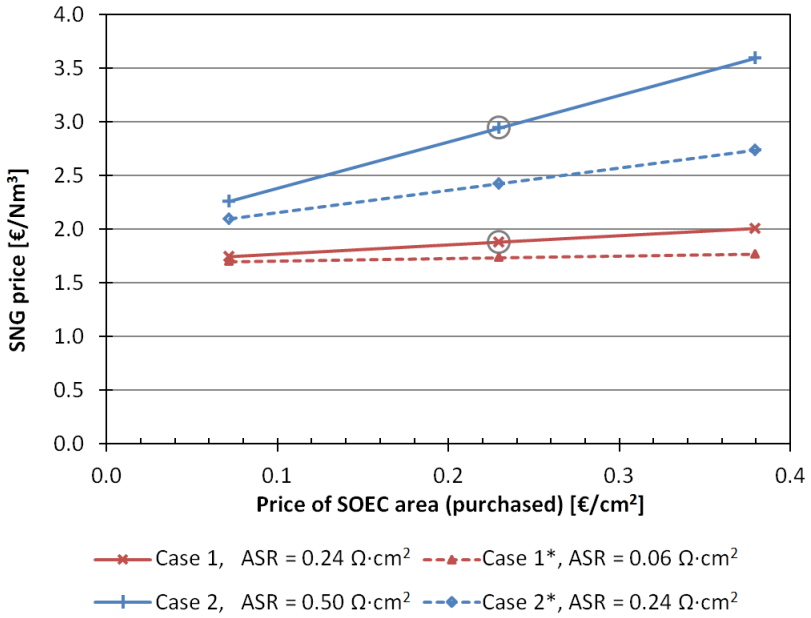

Figure 12-4. Production price of SNG in the two design cases (full lines) and two alternative cases (dashed lines) vs. the cost of SOEC area. The prices used in the model are circles for the two design cases. The alternative to case 1 (case 1*) uses the same cells as case 2. For the alternative to case 2 (Case 2*) the ASR of experimental cells is used. See text.

The figure shows that the dependence of the SNG production price on the price of cell area (the slope of the lines) changes with ASR (comparing each curve). This is not surprising as ASR sets the needed cell area for a given set of operating conditions. Comparing each design case with its alternative case shows the effect of lowering ASR when keeping the voltage and currents constant (these are fixed by the SOEC model). The lower ASR results in lower cell areas resulting in lower SNG production costs.

For design case 1, only little is to be gained on the SNG price, both in terms of lowering ASR (selecting the experimental cell in place of the standard cell) and in terms of the price on cell area. The reason for this low sensitivity to the price of cell area is that the SOEC subsystem takes up a relatively small amount of CAPEX (see Figure 12-2). At the higher ASR and significantly larger required cell areas (see paragraphs above the figure) in Case 2 and Case 2*, the dependence on the price of cell area becomes significantly larger. The reasons for this are, that at higher ASR and lower cell voltages, larger cell areas are needed, and that the SOEC subsystem takes up a larger price of the CAPEX (see Figure 12-2).

12.4.2 Price of air capture plant

In design case 1, the air capture plant accounted for more than a third of the equipment costs (36 %), and thus determines 36 % of the fixed capital costs. In design case 2, the fraction is 20 %. As the air capture system is still under development by Climeworks Ltd., the cost is bound to be an estimate, and as described in section 3.2.1 in the chapter on air capture technology, the costs have not been projected to 2035. The range of the purchased cost was 125 k€ - 250 k€, and the average (187,000) was used as the price estimate in the analysis. As such, the price is accompanied by a large uncertainty. The effect of the price estimate on the production price

of SNG in the two cases was investigated by calculating the SNG price for the average upper and lower bound prices of the air capture plant. The resulting SNG prices are shown in Figure 12-5 where the original cost estimates are marked by circles.

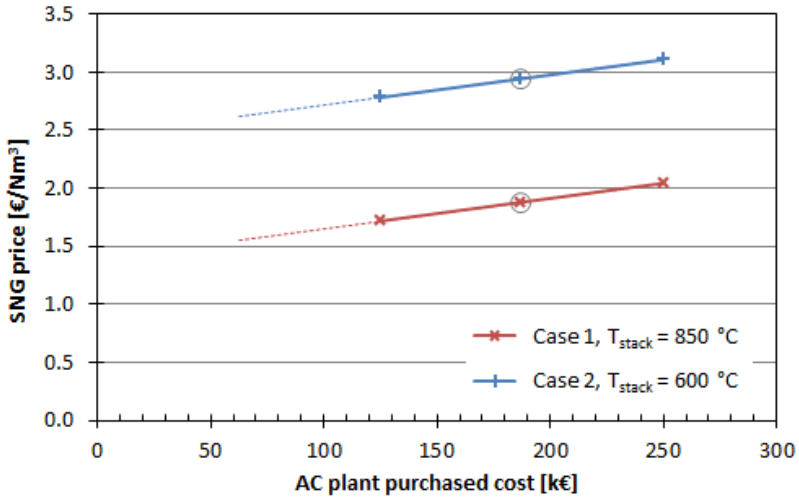

Figure 12-5. Production price of SNG in the two design cases vs. the cost estimates for the air capture plant (dashed line) sorbent (solid line) and combined (dotted line). The average values of the ranges were used in the model, and the resulting SNG prices are marked by circles in the curves. The trend lines are extended to purchased costs 33 % lower than the lower end of the range. See text.

The upper and lower bounds corresponds to the average value ± 33 %. For the high temperature case 1, the impact on the SNG production price of replacing the average price by the upper or lower bound prices is roughly ±9 %. In case 2, the corresponding number is roughly ±5 %. The difference is not surprising as the AC plant takes up a larger plant of the equipment costs in case 1.Thus, even though the air capture plant is one of the main cost drivers, the impact of changes in the price within the range estimated by Climeworks ltd. is minor.

12.4.3 Electricity price

The electricity consumption takes up a large fraction of the total utility consumption of the plant. As seen in **Error! Reference source not found.** above, this represents 82 % and 86 % of the total utility costs is case 1 and case 2 respectively. The main difference between the cases is the amount of electricity consumed by the SOEC. This is lower in case 2 as the extra heat generated directly in the cell by the methanation reaction lowers the thermoneutral potential, and thus the cell voltage.

The electricity price estimate was based on data from Energinet.dk related to the 2035 scenario [1, 129], where the average price over one year was used. This was calculated to 18.6 €/GJ. In Figure 12-6, the resulting SNG prices are presented as a function of the electricity price. The price variations were based on the average value (the one used in the model) as well as the upper bound and lower bounds on the price. The secondary horizontal axis (on top)

shows the increase or decrease in price compared to the average value used. Thus, the lower and upper bounds can be read on the lower horizontal axis to be 1.7 and 35.6 €/GJ which corresponds to the average price ±91 % as read on the upper horizontal axis.

The average electricity prices were calculated without highest 10 % or 40 % of the data. This results in the average prices for the lowest 90 % and 60 %. This was presented in Figure 11-1 b in the previous chapter on economic assumptions (section 11.1.1). The average prices and resulting SNG prices are marked on the curves in Figure 12-6. Please note that the SNG prices have been calculated for full operating capacity of the plant as set in the mode even for these reduced prices.

The electricity price also has an impact on the costs of hot utilities. The prices of the two hot utilities were calculated based on the electricity prices in section 11.1.3 on the *Price of high temperature heat*. This dependency was accounted for in the calculations, by replacing the average electricity price with the higher and lower estimates in the calculations of the utility prices.

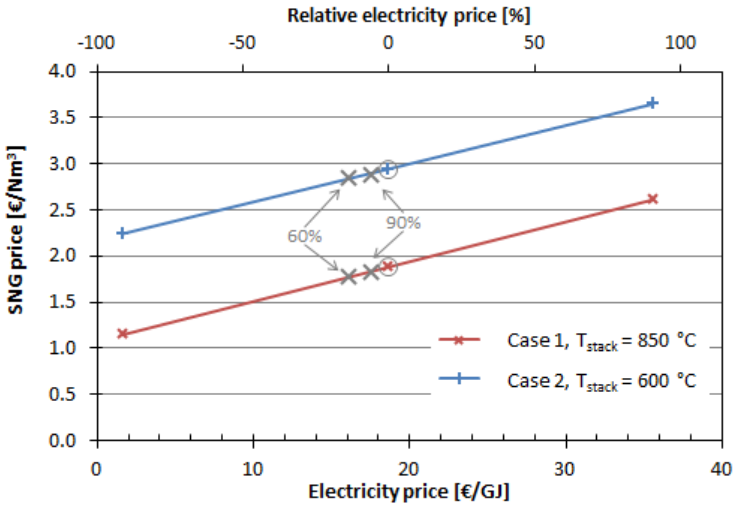

Figure 12-6. SNG prices calculated for the two cases vs. various electricity price estimates. The dependency of the heat price on the electricity price was accounted for in the calculations. The SNG prices calculated for the electricity price values used in the model are circled on the diagram.

The figure shows the sensitivity of the production price of SNG to the electricity price, including the effect on the hot utility prices. It is worth noting, that the extreme cases of the upper and lower bounds, resulting in electricity prices of 1.7 and 35.6 €/GJ are highly unlikely for steady state operation.

A reduction or increase in electricity prices by for example 33 % results in a corresponding change of the SNG production price of around 13 % in case 1, and 8 % in case 2.

The electricity prices calculated for the prices obtained for the lower 90 %, 80 % and 60 % of the price-time distribution were plotted in the figure. Note that the operating time was kept

constant in the SNG price calculations. The reductions in price by not using the most expensive GJ over the year are small, and reduce the operating time in favor of lower electricity prices is not expected to be viable.

12.4.4 Hot utility price

The hot utility price estimates were based on discussions with Energinet.dk and the 2035 scenario [1, 128, 129]. The plant was imagined to be placed in an industrial cluster connected to the electricity and district heating grids, and two extreme scenarios for the supply and demand structure of high temperature process heat were considered: In the first scenario, the cluster had a large excess of high temperature process heat, and the incremental price on this heat was assumed to be set by the price of district heating services, regardless of the temperature. In the second scenario, the cluster was assumed to have little or no high temperature process heat available, but a large demand. In this case, the prices were calculated, assuming that district heat is upgraded to the needed temperatures. This led to the two hot utilities where U1 was defined as district heating upgraded to 120 °C by a high temperature heat pump, and U2, as the first utility further upgraded to 300 °C, using an electric boiler. The latter scenario was used as the upper bound on the heat price, and these prices were used in the heat integration analysis (Chapter 8) and in the initial calculations of the SNG price (section 12.2).

The sensitivity of the production price of SNG towards these assumptions was investigated by calculating the SNG prices for each of the price estimates. Figure 12-7 presents the SNG prices calculated for the two design cases (T_{stack} = 850 °C and 600 °C) using the upper bound prices (U1: 11.9 €/GJ and U2: 17.7 €/GJ), lower bound prices (both U1 and U2: 6.4 €/GJ) and the average price estimated for the two utilities (U1: 9.2 €/GJ and U2: 12.1 €/GJ). Also the extreme case of free process heat was considered.

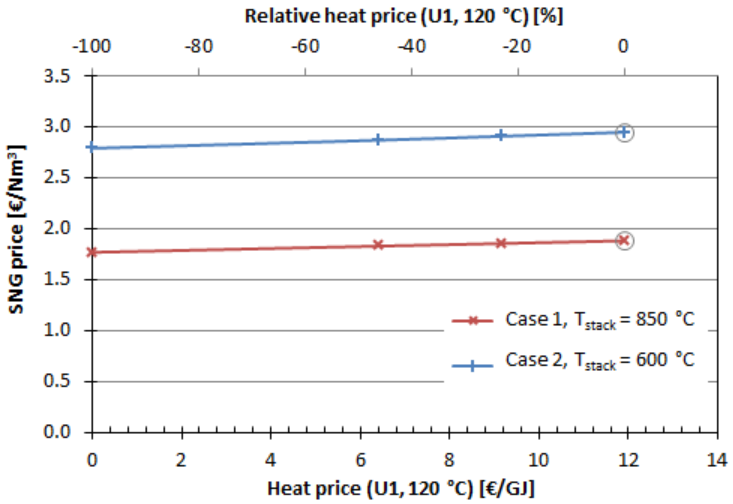

Figure 12-7. Production price of SNG vs. the price estimates for the hot utilities, here exemplified by the one at 120 °C (U1). The high temperature hot utility (U2) depends on U1, and is not shown. The top horizontal axis shows the decrease in heat price compared to the upper bound value used in the model. This value is circled on the curves.

The diagram shows, somewhat surprisingly, that the dependence of the SNG price on the price estimates for heating is minimal. The reason is that even though 13 % and 18 % of the utility costs are taken up by the hot utilities in case 1 and case 2 respectively, this represent only 6 % of the operating expenditures in the two cases. This is emphasized by the inclusion of the theoretical, extreme case of free process heat, showing how only around 5% of the SNG price is made up by the hot utilities. This was calculated from the difference between the highest and lowest SNG price in each case.

It should be mentioned in this connection, that the heat integration study was not performed for each set of utility prices. Doing so would have resulted in slightly lowered capital expenditures, as the need for large heat exchange areas in the network would have been lowered, as larger parts of the heating demands could have been economically covered by the cheaper utilities. This effect was not included in the above calculations. The purchased costs of the heat exchanger networks represented around 36 % of the total equipment costs in both design cases.

Further, the possibility of supplying a larger part of the SOEC energy requirements as heat has not been studied but will be treated in the discussion.

12.5 Influence of CAPEX on SNG price

As was presented at the beginning of this chapter, the consumption of utilities (primarily electricity and heat) takes up only a fraction (48 % and 35 %) of the operating costs in the two cases (see Figure 12-3). The reason is that the remaining operating costs are calculated from the CAPEX and thus, the large discrepancy between the cases is caused by the large difference between the capital costs, primarily stemming from the ASR of the SOEC stack in the low temperature case (case 2).

This means that due to the large prices of the air capture and SOEC sub-systems, the utility consumption does not have a large impact on the calculated SNG price as was seen in Figure 12-6 and Figure 12-7.

In order to more thoroughly investigate dependence of the SNG price on price of electricity, a scenario was constructed, where lower price estimates for the purchased costs of the SOEC sub-system and the air capture plant were used to construct the CAPEX for case 1 and case 2. For the air capture plant the lower end of the price range was used (Table 9-7 and Table 9-11). For the SOEC in both cases, the alternative cells with lower ASR were used. Thus, in case 1, the experimental cell type normally used in case 2 was used. In case 2, the experimental values from [137] for the experimental low temperature cell were used, recognizing that operating temperatures as low as 600 °C will lead to prohibitively high costs, until technological development is able to produce stable cells of significantly lower ASR at these low temperatures. In both cases the price of cell area estimated in this study to 0.23 €/cm^2 was used. The resulting fixed capital costs including land were 1.9 M€ and 3.2 M€ in case 1 and 2 respectively, compared to 2.5 M€ and 4.5 M€ with the model values (see Figure 12-2).

The operating expenditures were recalculated with lower CAPEX, and with varying electricity prices, taking into account the effect on the heating price estimates as explained in the previous section (Figure 12-6). The results are shown in Figure 12-8.

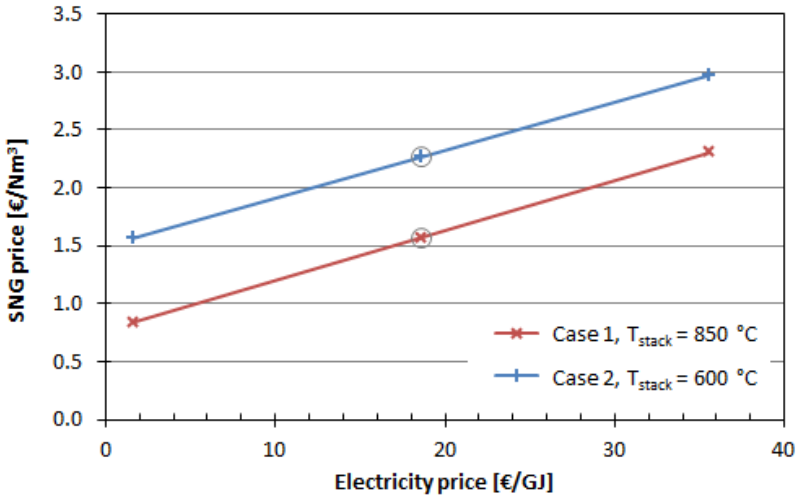

Figure 12-8. Sensitivity of the SNG price to variations in the electricity price in the reduced CAPEX scenario. The lower ends of the price rages were used for the air capture plant, and the SOEC prices were calculated with the experimental cells in both cases. In case one, the cell normally used in case 2 was used, and in case 2, the experimental cell from [137] was used. The price on cell area was the one estimated in this work (0.23 €/cm2) The yearly average electricity prices are circled, and the minimum and maximum values chosen from the dataset, not counting the most extreme outliers.

The table shows how large reductions in CAPEX for the dominant equipment (SOEC and air capture plant) lower the production costs of SNG. This is visible by comparing to Figure 12-6 above and the reduction obtained by lowering the costs of the air capture oplant ans selecting cells with lower ASR is 16 % and 23 %. At the lowered capital investment, the electricity price becomes a more important parameter in the SNG production price, and changes of 30 % lead to increases or reductions in SNG prices of 15 % and 11 % in case 1 and 2 respectively.

The lowered CAPEX influences the relatively large difference between Figure 12-7 and Figure 12-8 in two ways. The total capital investment costs are calculated based on the equipment cost. Lowering the price of the SOEC and air capture systems, thus results in lowered capital investment. In addition to this, the operating expenditures are calculated based on the utility costs and a percentage of the capital investment.

The overall price reduction by selecting the lower end of the price range for the air capture plant, selecting cells with lower ASR and reducing the electricity costs by 30 % (including the effect on the hot utility costs) is 30 % in both cases, yielding prices of 1.3 €/Nm^3 a and 2.0 €/Nm^3.

Based on the above considerations, significantly lower SNG prices can be obtained primarily through lowering the capital investment. Once this is achieved, the electricity price appears as

an important cost driver. At the high capital costs of the basic assumptions in this work, however, the energy prices have only a minor impact on the production prices of SNG.

12.6 Summary

In this chapter, the SNG price was calculated for a minimum acceptable rate of the return equal to the minimum risk free rate of return which was assumed to be 4 %. The calculated production costs with the values assumed in the model were found to be 3.59 €/Nm^3 and 6.98 €/Nm^3 for case 1 and 2 respectively.

The different contributions to the CAPEX and OPEX where identified in terms of the cost components as well as the purchased equipment costs and utility costs according to the chosen method [135]. This showed that both CAPEX and OPEX depended strongly on the total equipment costs.

The main cost drivers where identified to be the purchased costs of the SOEC sub-system, and the air capture plant and sorbent. In design case 1, the air capture plant and sorbent dominated the equipment costs, accounting for 50 %, whereas in case 2, the SOEC costs alone took up 61 % of the purchased equipment due to the increased area specific resistance (ASR).

The consumption of utilities (electricity and thermal energy) turned out to have only a minor influence, and almost negligible in the case of heating, as the OPEX was dominated by other operation costs, calculated from the CAPEX. Thus the dependence on the heat cost was almost negligible whereas a larger dependence was observed for the electricity costs.

In a scenario of lowered capital investment related to the SOEC and air capture sub-systems, SNG prices of 2.38 €/Nm3 and 3,59 €/Nm3 were achieved for case 1 and case 2, calculated with the yearly average electricity prices. In this scenario, a strong dependence of the SNG production costs on the electricity price was observed.

The revenue obtainable from the displacement of CO_2 emissions is debatable, with regards to the assumptions in the scenario and to the pricing. Calculating the value of the CO_2 displacements of the produced SNG from projected prices however, showed that only a very small fraction of the total SNG production price can be off-set by CO_2 credits. The obtained credit was calculated to be 0.06 €/Nm^3.

Chapter 13 Discussion

The overarching goal of this work was to investigate the integration of technologies for capture of CO_2 from the atmosphere, solid oxide electrolyzer cells and catalytic methanation technology for synthetic fuel production. The aim of the technology is to produce sustainable, carbon neutral fuels in a future energy system, where fossil fuels are being phased out.

The goal of the project was to design the plant and model it in a way which allowed analysis of central concepts such as selection of operating parameters, internal heat recovery and energy balancing. Especially the interfaces between the main technologies were of interest, and this led to the careful study of impurities in the CO_2 stream (Chapter 4) as this is a main concern for any gas to be fed into solid oxide electrolyzer cells (SOEC). In Chapter 5, the thermodynamic steady state model of the syngas plant, including the SOEC model was designed. The model was used to analyze the initial heat balance and to look into alternative ways of pressurizing CO_2 via cryogenic routes. This proved to be inefficient. In Chapter 6 the space of operating parameters of the SOEC syngas plant model was investigated with regards to syngas product composition and risk of forming solid carbon in the electrolyzer cells.

In Chapter 7, the methanation plant was investigated by various modelling studies and the plant design was settled on two design cases: Case one with an electrolyzer temperature of 850 °C and case 2 with a temperature of 600 °C. In Chapter 8, the possibilities for internal recovery of heat were studied and the network of heat exchangers needed to integrate heating and cooling demands was synthesized. In Chapter 9, the final flow sheets of the plant were presented and the dimensions and costs of all equipment in the plant were calculated. In Chapter 10 the plant model was put to work, to see how the plant would perform. The resulting production and quality of the SNG products were reported, and results were presented for the mass balance, water balance, heat balance and overall energy balance.

In 0 and Chapter 12, the economics of the plant were analyzed with respect to profitability, cost drivers and sensitivity of the SNG production cost.

The results and discussions presented along the way showed that from a technological point of view, the designed plant is feasible. There are various areas of continued interest for research and development, but generally, the plant is capable of producing 575 Nm^3 of substitute

natural gas with sufficiently high quality to be injected into the natural gas grid. From a mass balance point of view, the plant can operate without raw material inputs except for ambient air. The conversion of CO_2 to methane was 100 % and the energy efficiency of the plant was 65 % (HHV) and 58 % (LHV).

In this chapter, the findings of the work are discussed within the framework of the economic analysis, and the point of reference are the mass, heat, energy and economic balances.

13.1 2035 scenario, energy market and sustainability

The scenario by Energinet.dk, *Energikoncept 2035*, posits that the Danish electricity and heat sectors are entirely fossil-free in 2035. The transportation sector, however, is not projected to be free of fossil fuels until 2050 [1]. The report uses the term sustainable energy gasses (Danish: VE-gas) to cover biogas, upgraded bio gas, and various types of electrolysis derived gasses such as hydrogen, syngas or SNG. These gasses are imagined to be utilized primarily for production of high temperature process heat for industry, and for electricity production in peak-load, gas turbine based power plants. Secondarily, sustainable energy gasses are imagined to be part of the gradual displacement of fossil fuels from the heavy transport sector not easily electrified; especially aviation.

Within this framework, the main competitor to the technology considered in this work would be upgraded biogas (bio natural nas, BioNG), as the two products share a range of qualities: Both fuels are considered close to carbon neutral, they have sufficiently high Wobbe indices (See Chapter 7) to be stored, transported and utilized in the existing natural gas (NG) infrastructure, and they may be produced under consumption of large quantities of electricity. The price of BioNG is thus a relevant benchmark for the production price of SNG in this work.

13.1.1 Price of biogas and comparison

The prices of biogas and BioNG were investigated by The Danish Energy Authority in [138] based on experience from the Danish biogas industry, and the production costs were 19 €/GJ for biogas and 22 €/GJ for BioNG. The latter corresponds to around 0.81 €/Nm^3. For comparison, the production cost of SNG in this project was calculated to 53€/GJ and 80 €/GJ in case 1 and case 2 respectively corresponding to 1.9 €/Nm^3 and 2.9 €/Nm^3. Obviously, the SNG is not readily competitive, but in a study with inherent uncertainties in the economic assumptions like this, a factor of 2.3 (BioNG compared to SNG in case 1) is encouraging as it appears highly possible that further decreasing the capital investment is technologically feasible and will influence the SNG price positively.

In this connection, it should be mentioned, that the NG prices are projected to be even lower. The Danish Energy Agency projects the NG price to be 9.1 €/GJ in 2035 [131]. This means that competition with NG is not immediately viable.

13.1.2 Carbon shortage in 2035?

In the *Energikoncept 2035* [1], Energinet.dk presumes a total potential for biofuel production of 150-300 PJ. Following their argument, extensive electrification of the transport sector or expansion of the synfuel production capacity is needed, as the need for transportation fuels is expected to increase from around 420 PJ today. Counting the need for carbon based fuel or feedstock for industrial furnaces and peek-load electric production capacity, the Danish energy system might face a carbon shortage. Based on this, synthetic fuel produced from alternative carbon sources such as the atmosphere might not have to compete on price with biofuels, as biomass is considered a limited resource in this timeframe. Thus synfuels might be the marginal fuel compared to biofuels, capable of obtaining a higher spot price.

The above notion rests on the restrictions in the scenario that no biomass may be imported for energy production in 2035, which is ultimately going to be a political decision. From a global sustainability and equality point of view, importing biomass from third world countries to Europe and North America for production of fuels does not constitute viable options, especially in the long term. Whether this will impact the actual situation is questionable. In a scenario with abundant, relatively cheap, imported biomass for fuel production, the economic optimization of synfuel processes like the one discussed in this work will become increasingly challenging.

13.1.3 Sustainability considerations and carbon footprint

The above benchmarking of the technology against BioNG rests on the assumption that the produced SNG is equally sustainable and first of all, carbon neutral. At a glance, the entire carbon content of the SNG originates from CO_2 in the atmosphere, and technologies like these are usually regarded to be close to carbon neutral.

A central issue related to implementation of sustainable technologies, especially in the energy sector, is *burden shifting*. Burden shifting is the concept of alleviating one type of environmental impact by introducing or aggravating another. Examples are abundant in for example biofuel production from energy crops, and include deforestation, threats to biodiversity, etc.

In order to fully claim that the SNG production treated in this work can be classified as carbon neutral, a parallel study is being conducted, evaluating the life cycle environmental impacts of the technology. A paper is currently being drafted, but the full analysis was not concluded at the time of writing this thesis. A set of preliminary results are included below [139].

The life cycle impact assessment (LCIA) study was based on the plant design case 1 developed in this work. The functional unit was defined as the plant including all equipment, and the assessment covers the production of equipment, from original raw materials, construction of the plant, operation and decommissioning. For these preliminary data, combustion of SNG for peak load electricity production was compared to electricity production from other energy services. Due to confidentiality issues, the construction and decommissioning of the air capture plant and sorbent has not yet been included in the assessment. This is expected to

have negligible effects on the environmental impacts, as this was found to be the case for the SOEC and methanation plants. This will be further investigated.

The input data for the modelling was based on existing models in the published literature and the unit sizing tables from section 9.4 in the process integration chapter. Grid mixes for electricity and heat in Denmark from 2013 and projected for the fossil free 2035 scenario were obtained from Energinet.dk [129]. The difference between the 2013 and 2035 cases for SNG and NG combustion are primarily the change in grid mixes. Secondarily, a slightly higher efficiency of electricity production was assumed in 2035 based on [117].

Figure 13-1 shows the life cycle impacts in four selected impact categories of 1 GJ of electricity production in a combined heat and power plant compared to various other means of electricity production. The impact scores in each category are normalized to the yearly impacts of an average EU citizen, allowing for comparison across categories. The unit is milli-person equivalents per GJ electricity produced (mPE/GJ). It should be mentioned that comparing impacts across categories is only valid if they are weighed equally. This should be taken into account in the detailed analysis.

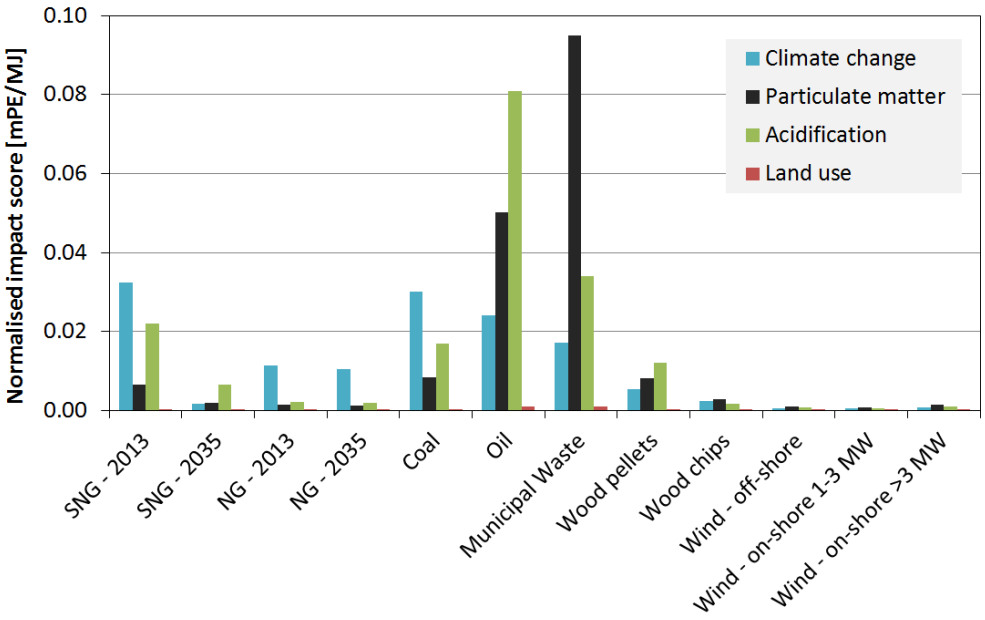

Figure 13-1. Life cycle impacts in four selected impact categories for 1 MJ of centralized electricity production for various energy services. Impact scores are normalized to the yearly impacts one EU citizen (person equivalent, PE).

The figure shows that depending on the composition of the electricity and district heating grid mixes, electricity production from the produced SNG has either a carbon footprint larger than coal power (SNG – 2013) or below that of wood chips and close to large scale on-shore wind power (SNG – 2035). The underlying reason for this immense difference in climate gas emissions is that above 95 % of all environmental impacts from combustion of the SNG comes

from the electricity and heat consumed in the SNG production phase. The results are more or less as expected, but it is interesting to note how small the carbon footprint is in 2035. It is also interesting to note, that the climate change impact of the technology is already very close to coal. When operating on energy from the grids, this technology will always perform worse than the grid, as the energy efficiency is bound to be below 100%. It will be very close to the grid, however, and at some point in time, the impacts of some technologies in the grid will become larger than the ones from SNG, at least as long as fossil fuels are still employed.

Other impact categories such as particulate emissions and acidification are seen to depend strongly on the energy mixes as well, and the normalized impacts drop from 2015 to 2035. Comparing to natural gas (NG) in 2035, the climate change impact is significantly lowered for SNG combustion, and the emission of particulate matter is similar or slightly higher. Some degree of burden shifting is observed however, as the lowered climate change impact comes at a trade-off with higher acidification impacts.

At the time of writing, it is not yet clear what causes the increase in acidification or whether burden shifting takes place in other categories as well. This is an important part of the assessment of replacement technologies for future energy systems.

13.1.4 CO_2 displacement

Until this point, only the production costs of SNG has been considered based on the equipment, total CAPEX, utilities consumption, yearly OPEX and secondary revenue streams (oxygen and district heating). Based on the preliminary results of the life cycle impact assessment presented above, the carbon footprint of SNG utilization is very close to zero in the framework of the 2035 energy scenario.

According to the guidelines on socioeconomic analyses set up by the Danish Energy Agency [133], the CO_2 reduction resulting from any initiative should be calculated as the actual reduction at the site of consumption. This means that the CO_2 reductions should be counted as the difference between the SNG and the natural gas or other fuel which is replaced by the SNG. The guidelines also state, the calculations should be based on the price on CO_2 quota whether or not the application is part of the quota covered sector.

The Danish Energy Agency has projected prices on CO_2 quota towards 2035, and arrive at 45 $ per ton of CO_2 [131]. For comparison, Royal Dutch Shell is working with a carbon tax of 40 $ per ton of CO_2 when evaluating the economic viability of long term investments, requiring that they are profitable even if this tax is implemented in the relevant sector.

The price of 40 $/ton of CO_2 equals 32 €/ton or 0.06 € per Nm^3 of SNG. With this value, the CO_2 quota price is roughly 3 % of the SNG price. This means that even a doubling of the price on CO_2 will have only a minor impact on the SNG price, and thus on the long-term profitability of the plant. It should also be noted, that the benchmark price of BioNG of 0.81 €/Nm^3 will be able to obtain the same revenue from zero carbon emissions.

13.2 Heat integration study

A main point in process integration studies like the one performed in this work is studying the possibilities for heat recovery internally in the system. Hansen et al. [103] studied the modelling of a co-electrolysis based plant for methane production similar to the one considered in this work. They found that for sufficiently high conversion in the SOEC, the downstream methanation plant was capable of supplying the heat needed for H_2O evaporation and CO_2 preheating.

In the present work, analysis of composite curves of the heat duties in the full plant showed, that even though the heating and cooling duties could be integrated in a way where the heat available at high temperatures could cover the high temperature heating duties, substantial amounts of hot utilities were needed to balance the heating demands. While evaporation and pre-heating made up a large portion of the heating needs in the plant, the heating of the air capture sorbent during the release of CO_2 accounted for the single largest single heating duty in the plant, and the hot utilities needed to cover this accounted for most of the hot utility consumption (see 8.1 on *heat balance and composite curves*).

This is an important result, as both SOEC and air capture studies tend to rely on available heat from downstream fuel synthesis processes to supply low cost process heat to increase the electrical efficiencies of the systems. In this case, already a portion of the SOEC feed pre-heating takes place directly in the electrolyzer at the cost of 2 % of the total utility costs. The heat exchanger network synthesis showed, that even allowing very close temperature approached in the low temperature heat exchangers (at the cost of large equipment costs), the hot utility requirements amounted to more than 60 % of the internally recovered energy (Table 10-5 in the chapter on *process integration, results and discussion*). This is a clear sign that even though significant amounts of heat is available in the methanation plant, it will not be able to supply heat for both electrolysis and CO_2 capture systems at the same time.

The temperature vacuum swing system has the great advantage over some comparable air capture technologies, that the heat is required at relatively low temperatures. In this study, this resulted in all hot utility consumption taking place at 120 °C in design case 1 (high temperature operation). In design case 2 (low temperature SOEC operation), around 15 % of the hot utility consumption had to be supplied at 300 °C, for pressurized steam generation.

In this connection, alternative technologies for capture of CO_2 not relying on large amounts of heat to regenerate the sorbent are of significant interest. The humidity swing system studied in Chapter 3 constitute such a process, as it enables the supply of energy for CO_2 desorption and sorbent regeneration in the form of the heat of evaporation of water at ambient temperatures. Provided, the technological issues around water management and especially production of a pure CO_2 stream can be solved without adding significant energy consumption either in the form of heating or electricity, this technology seems a promising candidate for integration with co-electrolysis and downstream methane production.

13.2.1 Economics of heat integration and utility consumption

In the high temperature case (case 1) the hot utilities consumed by the plant operation constituted app. 13 % of the total utility consumption, translating into 6 % of the total operating costs. In case 2 (low temperature), 18 % of the utilities were heat corresponding to app. 6 % as well. The relatively low price on the intermediate temperature hot utility (U1) compared to the high temperature hot utility (U2) of which significantly less was used, meant that the utility costs were dwarfed by the cost of electricity consumption in both cases. Thus the impact of the hot utility price on the production cost of SNG was minute. In this light, the large consumption of hot utilities in the air capture system is not a problem economically, compared to the total costs of electricity and other components of the operating costs.

The combined capital costs of the heat exchanger network on the other hand constitute app. 35 % of the purchased equipment costs in both design cases. With the given price estimates for the hot utilities (11.9 €/GJ and 17.7 €/GJ for U1 and U2 respectively). The capital and operating costs of the network and utilities are weighed against each other, during the network synthesis calculations in HEXTRAN. This is done in order to find the lowest annual costs of the network. There are two issues with these calculations however.

First of all, the networks were synthesized using the price of the heigh temperature hot utility (U2), after which it was replaced by U1. This ensured the correct price estimates in the heat exchanger sizing and economic calculations, but the network was optimized for a different price and set of heat transfer coefficients. Optimizing for too high prices and too low heat transfer coefficients result in an overestimation of the capital component of the heat exchanger network (compared to the utility costs). It is unclear how large this error is, but since the heat exchangers were sized with the correct utility streams, it is expected to be of minor importance.

Further, a similar problem arises when the heat prices are varied in the sensitivity analysis. With lower prices of hot utilities, the balance between capital and utility costs related to the heat exchanger network should shift towards larger utility consumption and smaller, cheaper heat exchangers (and *vice versa* for increasing heat prices). Thoroughly investigating this requires the network synthesis to be re-calculated for each new price of heat, which was not possible due to time constraints in this project. This probably caused an overestimation of the capital costs of the heat exchangers in the sensitivity analysis, resulting in a lowered sensitivity of the SNG price to variations in prices of heat. This is especially clear in the extreme calculation case of free process heat: In such a case, the temperature approaches of the heat exchangers would decrease significantly and the utility consumption would increase correspondingly resulting in significant cost reductions in the equipment costs of the plant.

Based on the above consideration, if a source of cheap, abundant process heat could be found, this might have a significant impact on the production costs. However, such a situation is expected to be highly unlikely within the framework of the 2035 scenario where integration of

process heat in industrial clusters is expected to be wide-spread, and heat will consequently be traded on (localized) market terms.

In a case where very high temperature (> 800 °C) process heat could be obtained well under the price of electricity, parts of the energy requirements of the SOEC could be supplied by heating, replacing parts of the electricity consumption. The maximum theoretical value of heat which might be supplied is $T\Delta S$ of the electrolysis reactions. It was briefly mentioned in the section on SOEC thermodynamics in Chapter 2, that a part of $T\Delta S$ has to be supplied as Joule heating, as the cell needs to be operated at a certain overvoltage (η_{cell}) above the reversible voltage (E_{rev}) in order to draw a current. It is unclear how much electrical energy can be exchanged for heating of the stack in this way. In the present work, the last part of the preheating of the feed gas from the operating temperature of the filter to the stack temperature is supplied as Joule heating, taking up 2 % of the entire energy input of the plant. At least this fraction could be replaced by high temperature process heat in the probably rare case, where this is cheaply available.

13.3 Design case 1 2, high or low temperature operation

Two design cases of the full plant were treated in this work. The main fundamental difference being the operating temperature of the SOEC sub-system (T_{stack} = 850 °C in case 1 and T_{stack} = 600 °C in case 2). 850 °C is within the range of temperatures normally considered for SOEC operation for fuel production, whereas 600 °C is usually considered for reversible operation for energy storage services. The advantage of low-temperature operation at elevated pressure (80 atm in both design cases) is that the methanation reaction equilibrium is shifted towards methane. This results in production of relatively large amounts of methane directly in the fuel electrode of the electrolyzer cells. The above is well known and was also seen in this work. See for example **Error! Reference source not found.** in Chapter 6 on results from syngas plant model.

In the full plant model, lowering the temperature from 850 °C to 600 °C resulted in CH_4 concentrations in the syngas streams (after H_2O recovery, S18) of 16 % in case 1 and 52 % in case 2. This dramatic change had two main impacts on the plant integration and operation, which are treated below.

13.3.1 Effect on capital investment

Increasing the methane production in the SOEC increases the H_2O content in the SOEC effluent stream (before H_2O recovery, S16) from 40 % (case 1) to 59 % (case 2) in addition to increasing the CH_4 content. This H_2O is removed by condensation before the syngas is led to the methanation plant. As the methanation reaction reduces the amount of molecules in the gas stream, and due to the removal of water, the flowrate of the syngas stream in case 2 is only 55 % compared to the syngas stream in case 1. This should result in smaller in the methanation plant units (reactors, intercooling heat exchangers, blowers, and recycle pump) and a lower catalyst volume, accompanied by lower equipment costs. The costs of the methanation plant

in each case was calculated from the equipment tables at the end of Chapter 9, resulting in a total purchased equipment cost plus catalyst of 39 k€ and 36 k€ in case 1 and case 2 respectively. The catalyst took up 6 and 3 k€ in the two cases. The reason for the fairly small difference is that many units in the plant are on the lower limits of the size ranges in which the costing equations apply. This means that the base costs of linear costing calculations become dominating. This is the case for both pumps and blowers in the methanation plant; units where costs would usually scale more quickly with their size. The reason for this is that the plant treated in this work is fairly small compared to electrolysis plants otherwise under consideration (app 700 kW compared to 5 MW [117]), and even extremely small compared to methanation plants (1,640 Nm^3/h compared to ~5,000,000 Nm^3/day [102]).

With the above considerations, the difference between the two plants is expected to decrease if the plant is scaled up, which would lower the SNG price in case 2, everything else being equal. As these considerations apply mainly to the small units such as blowers and pumps, and the SOEC and air capture units are expected to scale in the same way for the two cases, the result of this effect will be minor. Apart from this effect, however, upscaling the plant is expected to significantly improve the economic viability of the plant.

13.3.2 Heat integration

The second impact from the lowered operating temperature of the design case 2 and the increased CH_4 content in the syngas is related to heat integration between the methanation and SOEC sub-systems:

When half of the methane production takes place in the SOEC instead of in the methanation plant, less heat is generated in the methanation plant, and more heat is generated in the SOEC stack. This shifts energy from the methanation train into the SOEC where thermal energy replaces electrical energy. This is seen as a lowered thermoneutral voltage (E_{tn}) (see Table 10-7 In Chapter 10). This is usually preferable as electricity is usually more expensive than heat.

A side-effect of this change is, that the heat removed from the methanation plant is lacking in the heat integration. Except for the high temperature heat generated in the first methanation reactor, only the after-cooling of SOEC effluent and O_2 byproduct streams can supply high temperature heat for the steam generation and SOEC preheating, and these duties do not match, as might be seen from Table 8-1 and Table 8-2 in the chapter on heat integration. This is the reason why the high temperature design case (1) works with hot utility input at 120 °C whereas the low temperature case (2) requires hot utility input at 300 °C as well.

As a consequence of the lack of available heat in the process at ~300 °C, the heat exchanger network in design case 2 becomes app. 75 % more expensive in terms of capital investment compared to case 1. This effect is caused by the balancing of capital investment cost versus operating costs at the introduction of significantly more expensive high temperature hot utility. This was calculated in the heat integration study in Chapter 8. See Table 8-4.

Based on the above considerations, lowering the temperature of operation seems to be a more viable option when the heat prices are significantly lower than the electricity prices. This may not be the case in 2035 if no process heat is available at high temperatures, where heat pumps cannot supply the needed heat.

13.4 Case 1 vs. case 2

Above, the main benefits of lowering the operating temperature of the SOEC plant were discussed. On the other hand, the area specific resistance (ASR) was estimated to double from case 1 to case 2, with Ni/YSZ based cells produced at DTU Energy (0.24 $\Omega \cdot cm^2$ versus 0.5 $\Omega \cdot cm^2$). This results in a dramatic increase of capital costs of the SOEC sub-system, as was seen in the CAPEX breakdown (Figure 12-2) in the chapter on the economic analysis (Chapter 12). The dependence of the SNG price on the ASR of the electrolyzer cells is further discussed in section 13.7.3 below.

13.5 Electricity consumption and economy of operation

The economic analysis (Chapter 12) showed that the total production costs of SNG with the given assumptions were 51 €/GJ and 80 €/GJ in the high temperature and low temperature cases respectively. The main cost drivers were identified as the capital costs of the SOEC and air capture subsystems as well as the electricity price. The impact of the electricity price is most clearly seen in the case of lowered capital costs of the two main cost drivers (Figure 12-8). On the surface, this does not agree well with earlier findings such as Jensen et al. [140], clearly identifying the electricity price as the main cost driver, taking up 66 % of the production price of H_2.

Jensen et al. used an electricity price as low as 2.59 €/GJ compared to 18.6 €/GJ in this study, and assumed a cost of cell area of 0.15 €/cm^2 compared to 0.23 €/cm^2 in this work. Their resulting production cost of H_2 was 4.1 €/GJ. Extrapolating their results for the production cost of H_2 to the electricity price used in this study, yields a production cost of H_2 of 11.1 €/GJ compared to 51 €/GJ in this study. They did not include an air capture plant as hydrogen was the end product. Also, they only took the electrolyzer stack into account, and not the whole plant. It should be mentioned, however, that a plant for electrolysis of steam is significantly simpler than the one analyzed in this study.

Even though H_2 and SNG production are strictly not comparable, this shows how accounting for all the extra components of the production cost of synthetic fuels will have a major impact on the obtained price. At least, based on this study which shows how electricity prices and electrolyzer capital costs are main cost drivers, but still constitute only a fraction of the total production costs of SNG. This comparison also serves as an example of the need for techno-economic optimization of the plant in this study.

The capital cost drivers are discussed below in section 13.7.1 and section 13.7.3. The impact of the electricity consumption and price is discussed in the following.

In Chapter 12, the breakdown of the total energy inputs per Nm^3 of SNG were presented in Figure 12-3. 72 % was made up by electricity and 66 % were spent on conversion in the SOEC in case 1 (T_{stack} = 850 °C). In case 2 (T_{stack} = 600 °C), the corresponding numbers for electricity and SOEC conversion were 67 % and 60 % respectively. Short of replacing electrical energy in the SOEC and the last 100 °C of pre-heating of the feed, as has been discussed above, preciously little can be done to bring down the consumption of electrical energy consumption of the plant. As was mentioned above, it is not clear how large a part of the entropy of the electrolysis reaction could be delivered by external heat sources, and the preheating only accounted for 2 % of the total energy consumption of the plant. Also, the CO_2 compression accounted for 2 % of the energy consumption in both design cases.

This means, that the only real influence on the total cost of electricity consumption is the price of electricity. In the previous chapter, the dependence of the SNG production price on the electricity price was investigated (see 12.4.3). This showed that a reduction in price of 33 % led to a reduction in the SNG price of app. 13 % in case 1. In case 2, the SNG price reduction was app. 8 %. This shows that the electricity price is important for the SNG price, but nowhere near the steep slope obtained by other authors, for example Jensen et al. The reason is that the electricity consumption makes up a significantly smaller fraction of the total costs than in other studies. This is in part caused by the additional cost components included in the economic analysis in this work, which should give the benefit of approaching a more “real” implementation of the technology. Also, the more detailed analysis of the system in terms of equipment and auxiliary energy consumption contribute to this effect. Finally, the air capture plant takes up around a third of the energy consumption and 36 % and 20 % of the equipment costs in the two cases. This is often not accounted for in other studies.

One possibility, which is often mentioned for alleviating the high costs imposed by electricity prices is to operate intermittently, following the time profile of the electricity prices. This is treated in the next section.

13.6 Mode of operation

A system like the one studied in this work could be integrated in the wider energy system in several ways. A detailed study of this was not part of this work, but two main concepts are discussed in the following, shedding some light on such integration.

Long term energy storage of electricity as chemical energy is not discussed explicitly in the 2035 scenario by Energynet.dk. It is, however, a possibility which has attracted a fair amount of attention recently [77, 141]. In such setups, reversible solid oxide cells may be used in either electrolysis mode, producing syngas or H_2 in periods of low electricity prices, or in fuel cell mode producing electricity and heat under conversion of hydrogen or syngas to H_2O and/or CO_2 in periods with high electricity prices. Such applications are favorable at low temperature and high pressure, due to the promotion of the methanation reaction. Apart from lowering the demand for electricity, methanation also reduced the amount of gas molecules, thus increasing the energy density of the stored gas.

An air capture plant does not necessarily fit well into such a concept, as the gasses are assumed to reside in a closed system, working in essence like a flow battery. Thus there is no need capturing more CO_2. One could imagine a setup, however, where the plant (including air capture) ran for fuel production when the electricity prices were low. At times with high electricity costs, the SOEC part of the plant could operate in fuel cell mode. In such a setup, the air capture plant would probably be scaled down compared to the SOEC system and operate continuously feeding off the heat produced by the SOC stack in fuel cell mode. Such hybrid systems need further study closely considering the variations in energy prices in order to analyze the viability.

he attractiveness of low temperature and high pressure operation in such systems inspired the choice of investigating a similar design case in this study (case 2). The evaluation of the attractiveness of low temperature operation was discussed in section 13.3 above, and it was concluded, that with current ASR values, the additional capital investment tied in the SOEC area overwhelms other positive effects such as increased methane production in the SOEC stack. Also, the heat from the methanation reaction is needed for pressurized steam generation, which might otherwise be expensive to cover with external utilities.

Following the time profile of the electricity prices could still be interesting however. In the previous chapter, a superficial peek into load following operation was presented. The average electricity prices were calculated for reduced datasets where the 10 % and 40 % of hours over the year with the highest prices had been removed. This corresponds to operating only when the electricity price is in the lower 60^{th} and 90^{th} percentiles. Without correcting for the reduction in on-stream hours of the plant, the resulting SNG prices were calculated, and price reductions between 2 % and 5 % were obtained. A 5 % reduction in SNG price in case 1 would then require the plant to be shut down for 40 % of the year. Following these superficial results, it was concluded that the effect of such a strategy on the profitability of the plant would not be attractive.

It should be mentioned in this regard, that this does not invalidate load following reversible SOCs for energy storage. But the large capital investment of this plant including the air capture plant, heat exchanger network and minor contribution from the methanation plant, does not warrant this level of reduction in stream time.

Thus a plant like this is firmly in the business of fuel production, and should be thought of as a means of producing valuable hydrocarbon fuels for the parts of the energy system, not easily electrified rather than as an adaptable energy storage application, as was discussed in the first sections of this chapter.

13.7 Areas of interest for technological development

Part of the objectives of this study was to use the simulation and economic analysis to identify the main cost drivers and areas of interest for technological development.

The main cost drivers of the plant serves as a clear reminder of areas where technological development might contribute to enhancing the economic viability of the studied technology.

13.7.1 Air Capture

The economic analysis showed that the CO_2 air capture plant was the main cost driver in case 1 and second to the SOEC sub-system in case 2. The plant price was based on estimates from Climeworks Ltd.[24] (see also 3.2.1 in the air capture chapter), where the average value was adopted as the price estimate in this study. The price estimate from Climeworks assumes plants early on the learning curve, and no economics of mass production of the repeating units of which the plant consist of 12 – 14. With the price reduction of 33 % corresponding to the lower end of the estimated price range, the SNG production price drops by 9 % in case 1 and 5 % in case 2. It is assumed to be possible to realize substantial reductions in the capital costs of Climeworks Ltd. air capture plants as soon as the number of produced units can be increased.

Apart from the capital costs, the air capture plant has a large utility consumption, and the heating associated with the desorption part of the CO_2 capture cycle is the largest single heating duty in the full plant. As mentioned in section 13.2 the advantage of the TVS system is that the heat is to be supplied at relatively low temperatures just above 105 °C. Thus, 230 kJ/mole is supplied for desorption, and the cost is 50 k€/year, corresponding to 13 % of the utility consumption in case 1 and 15 % in case 2. Out of the total operating expenditures, however, this is only 6 % and 5 % respectively. Thus, even though the air capture plant has a large utility consumption, this only has a moderate influence on the SNG price.

Another way of viewing this is to calculate the production costs of CO_2 as was done in 3.2.1 in the chapter on air capture. With the numbers from Climeworks, the utility prices from 0, etc. and after taxes and depreciation, the CO_2 costs in the stand-alone air capture plant were calculated to 83 €/ton – 121 €/ton (3.2.1). Repeating those calculations, but adjusting for the integrated parts of the energy consumption, yielded CO_2 smaller prices by around 4 %. This shows that only a small amount is saved by the heat integration, as most of the CO_2 plant duties are covered by external utilities.

There are three main points of interest related to the air capture system in this study:

- First, the capital costs should be decreased as this could contribute to the plant economy by lowering the SNG price by 5 % - 10 % for the lower end of the estimated price range. Further decreasing the cost through economy of mass production of the single repeating units is assumed to be viable.
- The air capture plant has relatively large energy consumptions, especially the heating duty for desorbing CO_2. There is close to no heat available in the other parts of the plant, and internal heat integration in case 1 only lowers the CO_2 production cost by app. 4 %.
- Still, the hot utilities contribute only moderately to the SNG price, even at the upper bound for heat prices, and while optimization of the sorbent affinity to CO_2 could be a relevant area of optimization for lowering the energy consumption in the desorption step, only minor decreases in the SNG price should be expected.

13.7.2 Impurities and filtering

The content of impurities in the CO_2 streams from the Temperature Vacuum Swing and Humidity Swing systems were analyzed in Chapter 4. The analysis showed that a series of impurities, known to be detrimental to solid oxide electrolyzer cell operation were present in the streams in concentrations from sub-ppb levels up to around 20 ppb. The study confirmed, that development efforts on the part of Climeworks Ltd. managed to decrease the concentration of several detrimental impurities in the gas stream, and even though some aggregation of impurities in the system or gradual separation of impurities from the system over the time period of 10 months was observed, the concentrations of detrimental impurities such as sulfurous compounds decreased; also over time. Still, even in the prototype plant of the temperature vacuum swing system, trace impurities were left, and a filtering strategy had to be implemented. The filter used for the investigation was originally developed [53] and attempted patented [54, 55] for cleaning the inlet gasses of solid oxide cells, and it was used in this project as well.

In the sizing calculations regarding the filter (See section 9.3.10 in the chapter on process integration), a regeneration strategy capable of regenerating the filter on a monthly basis was assumed to be technologically possible. It was mentioned in the chapter, that work is under way to develop such strategies at DTU energy.

In the absence of a regeneration concept, it was assumed that the costs could be covered by using a regeneration frequency of once per year instead of once per month which was used to calculate the amount of material in each loading. This makes some sense because the needed amount of filtering material is inversely proportional with the regeneration frequency. Also, it was assumed that with monthly regenerations, each filter loading would have a lifetime similar to that of the electrolyzer stack, which is assumed to be 5 years [117].

With the above assumptions, the filter material over the lifetime of the plant was calculated to be 17600 €. If no regeneration strategy could be found, and the filter was replaced as soon as it is saturated, the total cost over the plant lifetime would be app. 1,000 k€, which is around twice the purchased cost of all equipment in the plant. On the other hand, one could require that the filtering and regeneration subsystem should not be allowed to be more expensive than the SOEC subsystem. With the assumption of monthly regeneration and replacements at five-year intervals, this would yield a maximum cost of the regeneration process of around 58 k€. This was calculated as the purchased costs of the SOEC system (76 k€) minus the purchased costs of the filter material (17.6 k€). This figure could be used as a guiding principle in the design of a regeneration system.

Also, it was assumed that more fine-grained filtering material than what is currently in use could be employed in a real system. This is a good assumption, since Ni-YSZ electrodes for SOCs are routinely produced with even finer structures. Possible degradation of the structures was not taken into account however, and very fine grained Ni microstructures are known to be vulnerable to agglomeration and sintering of Ni particles. Especially at high partial pressures of

H_2O as is the case in the electrolyzer feed gas. Agglomeration of Ni particles would decrease the surface area and extent of the triple phase boundary which is detrimental to the capacity of the filter. Different strategies exist for counteracting such structural degradation, and this issue should be carefully considered in connection with the further development of regeneration strategies and of the filter material itself.

13.7.3 Area specific resistance

The sizing parameter of the SOEC stack is the cell area, which was calculated to 33 m^2 and 166 m^2 in cases 1 and 2 respectively. The parameter tying the area to the operation of the stack is the ASR which depends on the specific cell type, temperature and pressure as was discussed in section 5.4.2 in the syngas plant model chapter.

The cost driver analysis showed that the SOEC sub-system made up 15 % and 41 % of the purchased equipment costs in case 1 and 2 respectively. With the total purchased equipment costs being 513 k€ and 930 k€, the difference is even larger. The production price of SNG was observed to have a very weak dependence on the price of purchased cell area in case 1, and even a lowering of ASR by a factor of 4, by adopting the experimental Ni/YSZ based cell [98], only had a minor influence. The reason is, that the area is already quite low at the relatively high voltage (U_{cell} = 1.22 V) and that the SOEC subsystem only takes up a small fraction of the total CAPEX. Case 2 had a significantly larger influence on the production price of SNG, which is not surprising as large cell areas were needed at the low operating voltage (U_{cell} = 1.11 V).

The calculations rest on the assumptions that all three cells will eventually have the same price per area. Under mass production, this might me more or less true, but the experimental cell assumed in case 2 [98] is significantly more complicated with two extra layers (CGO barrier layer between electrolyte and oxygen electrode, and oxygen electrode current collector layer). This is assumed to add to the price. The ultimate parameter of importance in this regard is the longevity of the cells. SOECs are known to degrade faster at increased current densities and here, case 1 with I_A = -1.84 A/cm^2. This is a quite large value compared to stability tests performed for this type of cells [142].

Based on the above considerations, three main conclusions for the economics of the SOEC subsystem can be drawn:

- Firstly, the ASR does not urgently need to be lowered significantly from the value of 0.23 Ω·cm^2 which was extrapolated for high pressure operation, as this will have only minute effects on the overall economics of the plant. It does need to be lowered for the low temperature case, if low temperature operation is to become viable for either synthetic fuel production or energy storage operation based on reversible SOCs.
- Secondly, the lifetime of this type of cells needs further study and development in order to ensure, firm numbers for the long-term stability of SOECs under technologically relevant operating conditions. Also, development of stable cells with long life at high current densities relevant to synthetic fuel production should be a high priority goal.

- Thirdly, a better understanding of the prices of SOEC area, both the numbers and the drivers is relevant for further studies of various implementations and operating strategies of SOECs. A high level of transparency is of special interest, enabling adjustment of the prices to fit the specific application in question.

Chapter 14 Conclusion

The topic of this thesis was integration of CO_2 air capture technology with solid oxide electrolyzer cells for co-electrolysis with H_2O followed by catalytic methane production. The main task was to design a plant consisting of the mentioned technologies and to develop a thermodynamic model enabling analyses of operating parameters, internal heat recovery, mass and energy balances etc. In addition to the modelling, experimental work was conducted on an example of a CO_2 air capture system, and on analysis of impurities in CO_2 streams to provide input for the system design. Finally, an economic analysis of the plant was conducted, and a life cycle impact assessment of the technology is underway.

Based on this work, the following conclusions are drawn:

- A small experimental study was conducted, in which a model scale test reactor for CO_2 air capture was constructed, using the humidity swing (HS) technology The setup was used to probe the water uptake and CO_2 release properties of the anion exchange resin used:
  - Supplying H_2O to the dry resin in the vapor phase in saturated N_2 led to extremely slow H_2O uptake and CO_2 desorption. It is unclear whether this should be attributed to slow transport in the reactor and support material or uptake kinetics at the resin surface.
  - Supplying H_2O as liquid water led to an extremely fast initial release of CO_2 from the resin, after which, the release slowed down over a few hours.
  - In both cases, the time to desorb ~70 % of the CO_2 loading was above 40 h, suggesting further work on uptake and release kinetics should be prioritized.
- A strategy and setup was developed for elemental analysis of sub-ppm level impurities in the CO_2 streams of two different CO_2 air capture technologies. The temperature vacuum Swing (TVS) system and the HS system were analyzed.
  - The strategy included adsorption of gas phase impurities on filters consisting of Ni-yttria stabilized zirconia fuel electrode material at SOEC operating temperatures followed by elemental analysis through glow discharge mass spectrometry.

  - The method had sub-ppm detection limit and validation showed that it is a good assumption that all impurities prone to be detrimental to SOEC operation are sampled.
  - Across all tested systems, a range of impurities known to be detrimental so solid oxide cell (SOC) operation were detected in the range from sub-ppm levels to 20 ppm.
  - Cleaning of the inlet gasses of electrolyzer cells will be part of technological implementations. The size and cost of such a filter for treating 1000 tons of CO_2 per year in addition to H_2O was calculated to app. 19 k€ over 20 years.

- A 0-dimensional model of a SOEC plant for production of synthesis gas was developed in PRO/II from the thermodynamic model by Sun et al. [2].
  - The model included two control loops for 1: Fixing the syngas composition to relevant ratios for methane production. 2: Maintaining a recycle stream from the SOEC effluent keeping the Ni-phases of the filter and fuel electrode in the reduced state.
  - Especially the first loop had important influences on the syngas composition.
  - The model was used for mapping the syngas composition with regards to operating parameters, and the behavior was used as a qualitative validation of the model

- From the syngas plant model, a full plant for production of substitute natural gas (SNG) was designed and modelled.
  - The model included data for the TVS system provided by Climeworks Ltd. but the air capture system was not modeled in detail due to confidentiality issues.
  - Two design cases were studied, with SOEC operating temperatures of 850 °C (case 1) and 600 °C (case 2). The operating pressure was 80 atm and conversion in the electrolyzer cell was 70 %.
  - During the modelling process, the model was used to study the following design questions, among others:
    - Two alternative compression strategies using cryogenic routes where studied.
    - The dependence of methane production on the so-called feed module (FM) was studied, and it was found that the FM had to be 3.000 ±0.010 to satisfy the need for high CH_4 production
    - The omission of a recycle loop normally present in methanation plants to prevent large temperature increases in the first reactor was studied. It was found that at SOEC temperatures of 850 °C the minimum pressure at which the recycle loop could be omitted was well above 200 atm. for SOEC temperatures of 600 °C the minimum pressure without recycle loop was 9 atm.

  - The risks of carbon formation in the SOEC and methanation reactors were studied thermodynamically. In the SOEC, pressurized operation at 80 atm is safe until close to 100 % conversion. Due to risk of local variations in composition, 70 % conversion was chosen. In the methanation reactors, the composition was in the region of thermodynamically stable carbon formation. The MCR catalysts by Haldor Topsøe A/S are known to be resistant to carbon formation, and carbon formation was expected not to be problematic in the methanation reactors.

- The potential for internal heat recovery was analyzed by studying composite curves and the heat exchanger network was synthesized:
  - The theoretical potential for process-process recovery of heat was found from the composite curve analyses was 1.1 GJ/h in case 1 and 0.66 GJ/h in case 2.
  - The heat exchanger network enabled process-process recovery of 1.04 GJ/h and 0.63 GJ/h in cases 1 and 2, at a minimum exchanger approach temperature of 5 K.
  - The SOEC and methanation sub-systems integrated well in terms of heating and cooling demands.
  - With the top 100 °C of SOEC preheating taking place in the stack, the available high temperature heat covered the heating requirements down to app. 120 °C. in case 1.
  - Case 2 was favored by increased heat production in the SOEC stack, resulting in a lack of available heat around 300 °C. This had to be covered by expensive utilities.
  - The majority of the heating and cooling demands of the air capture system could not be covered by internal recovery, and had to be supplied as external utilities.
- Important results from the mass and energy balances of the model include:
  - The plant produced 575,000 Nm^3/y of SNG with a CH_4 content above 98.5 %.
  - The Wobbe index of the SNG was 49 MJ/Nm^3, which is equal to the lower limit for the natural gas grid.
  - The SOEC stack power was around 700 kW, and the operating voltages were 1.22 V and 1.11 V in the two cases.
  - The electricity consumption accounted for around 70 % of the total energy consumption, and the energy efficiency was 64 % (HHV) and 58 % (LHV).
- A lifecycle impact assessment is being conducted. The analysis has not been finished at the time of writing, but preliminary results for four selected impact categories were discussed:

  - Electricity production from the SNG is close to CO_2 neutral in absolute terms and in comparison with natural gas. The climate change impact score is comparable with that of electricity production from wood pellets or on-shore wind power.
  - Some burden shifting to acidification is observed compared to electricity production from natural gas.

- Cost calculations for the plant equipment were based on literature values and other estimates. Additional cost factors were accounted for by standard methods from chemical process engineering.
- The economic viability of the plant was analyzed using as profitability measure a discounted cash flow return on investment of 4 % over the plant lifetime of 20 years.
  - Accounting for interests, taxes, depreciation, etc. the production price of SNG was calculated to 1.88 €/Nm^3 and 2.94 €/Nm^3 in cases 1 and 2 respectively.
  - The main cost drivers in the equipment costs were identified as the purchased cost of the SOEC sub-system (15%/41%) (case1/case2), the air capture plant (36%/20%) and the heat exchanger network (36%/36%).
  - In the operating costs, the cost driver was the electricity cost (41%/29%). The heat price had a minor influence only.
- Based on the lifecycle assessment, electricity production from SNG is CO_2 neutral.
  - The obtainable CO_2 credits amounts to only 0.06 €/Nm^3 of SNG and will not have a significant impact on the SNG price.
- The potential for increasing the economic viability of the plant lies in technological development, more than operating strategies:
  - The low temperature case is not viable before lower ASR values have been obtained, and it is severely compromised by the lower cell voltage and resulting power density.
  - Intermittent operation with the time profile of electricity prices used is not viable due to the large capital investment in the plant.
- The considered plant is comparable in size to a pilot plant when it comes to the methanation and SOEC subsystems. This means that upscaling is expected to result in lower SNG prices at the same profitability measure.

14.1 Outlook/future work

Part of the goal of this study was to identify the main areas of interest for future technology development, in order to drive the studied technology towards commercialization. These are presented in the following.

- Capture of CO_2 from the atmosphere
  - Regarding the humidity swing system, the following concepts should be studies experimentally:
    - The uptake kinetics of water should be studied in order to develop technological solutions for the supply of water to the resin.
    - The desorption kinetics of CO_2 should be studied to form a basis for optimization of the sorbent and reactor geometries
    - Other resin materials, carrier materials and geometries should be experimentally investigated to enhance the kinetics of water uptake and CO_2 desorption.
  - Regarding the temperature vacuum swing system, the techno economic analysis pointed out two main research areas:
    - Further optimization of the sorbent chemistry should be pursued with the goal of lowering the desorption temperature and/or decreasing the energy requirement.
    - Decreasing the investment through economy of mass production is underway, and reductions on the order of 30 % and seem highly viable and will have a large impact on the profitability of the plant.
- Impurities and purification
  - Further studies on the effects of various impurities on the operation of solid oxide electrolyzer cells are needed as most studies were carried out in fuel cell operating mode, which have significantly different operating conditions.
  - Cheap and efficient non-specific filtering strategies should be developed.
  - Strategies for regeneration of Ni/YSZ based filters should be developed. This may have a very large impact on the cost of filtering, and thus on plant operation.
- Solid Oxide Electrolysis
  - For high temperature operation, the resistance of the cell is not a problem from an economic point of view. For low temperature applications, however, significantly lower resistances are needed fo cells of equal price and lifetime.
  - The lifetime of cells and stacks under industrially relevant testing conditions, such as high conversion, high current density, high steam content and low H_2 content should be characterized during long-term tests.
  - Pressurized operation of SOECs should be tested and analyzed in detail, providing firm measurements of resistances under high pressures, as well as analyzing degradation behavior, poisoning and product compositions at intermediate and high pressures.
  - Experimental determination of the amount of energy which may be supplied by external heat sources to replace electrical energy in the operation of SOECs should be investigated.

Bibliography

1. *Energikoncept 2035,* Energinet.dk (2014).

2. X. Sun, M. Chen, S. H. Jensen, S. D. Ebbesen, C. Graves and M. Mogensen, *Thermodynamic analysis of synthetic hydrocarbon fuel production in pressurized solid oxide electrolysis cells, Int J Hydrogen Energy.,* **37**, 22 (2012).

3. *Energi 2050 - Udvilingsspor for energisystemet,* **41538/10,** Energinet.dk (2010).

4. *Energi 2050 - Vindspor,* **Dok.6357/11,** Energinet.dk (2011).

5. *Energiscenarier frem mod 2020, 2035 og 2050,* Danish Energy Agency (2014).

6. C. Harte, E. Baker and H. Purcell, *Absorption of carbon dioxide in sodium carbonate-bicarbonate solutions I Equilibrium in system carbon dioxide-sodium carbonate-sodium bicarbonate-water, Industrial and Engineering Chemistry.,* **25** (1933).

7. S. Satyapal, T. Filburn, J. Trela and J. Strange, *Performance and properties of a solid amine sorbent for carbon dioxide removal in space life support applications, Energy Fuels.,* **15**, 2 (2001).

8. B. Metz, O. Davidson, H. d. Coninck, M. Loos and M. Meyer, *IPCC Special Report on Carbon Dioxide Capture and Storage,* Cambridge University Press (2005).

9. A. Goeppert, M. Czaun, G. K. S. Prakash and G. A. Olah, *Air as the renewable carbon source of the future: an overview of CO2 capture from the atmosphere, Energy & Environmental Science.,* **5**, 7 (2012).

10. K. S. G. Lackner P. and H. Ziock, *Carbon Dioxide Extraction from Air: Is it an Option? Proceedings of the 24th Annual Technical Conference on Coal Utilization and Fuel Systems.,* (1999).

11. K. Lackner, *A guide to CO2 sequestration, Science.,* **300**, 5626 (2003).

12. K. Z. House, A. C. Baclig, M. Ranjan, E. A. van Nierop, J. Wilcox and H. J. Herzog, *Economic and energetic analysis of capturing CO2 from ambient air, Proc Natl Acad Sci USA.,* **108**, 51 (2011).

13. K. S. Lackner, *The thermodynamics of direct air capture of carbon dioxide, Energy.,* **50** (2013).

14. K. S. Lackner, *Capture of carbon dioxide from ambient air, Eur. Phys. J. Special Topics.,* **176** (2009).

15. Q. Wang, J. Luo, Z. Zhong and A. Borgna, *CO2 capture by solid adsorbents and their applications: current status and new trends, Energy & Environmental Science.,* **4**, 1 (2011).

16. C. W. Jones, *CO2 Capture from Dilute Gases as a Component of Modern Global Carbon Management, Annual Review of Chemical and Biomolecular Engineering, Vol 2.,* **2** (2011).

17. R. Baciocchi, G. Storti and M. Mazzotti, *Process design and energy requirements for the capture of carbon dioxide from air, Chem Eng Process.,* **45**, 12 (2006).

18. D. W. Keith, M. Ha-Duong and J. K. Stolaroff, *Climate strategy with CO2 capture from the air, Clim Change.,* **74**, 1-3 (2006).

19. F. Zeman, *Energy and material balance of CO2 capture from ambient air, Environ Sci Technol.,* **41**, 21 (2007).

20. J. A. Wurzbacher, C. Gebald and A. Steinfeld, *Separation of CO2 from air by temperature-vacuum swing adsorption using diamine-functionalized silica gel, Energy Environ. Sci.,* **4**, 9 (2011).

21. C. Gebald, J. A. Wurzbacher, P. Tingaut, T. Zimmermann and A. Steinfeld, *Amine-Based Nanofibrillated Cellulose As Adsorbent for CO2 Capture from Air, Environ Sci Technol.,* **45**, 20 (2011).

22. J. A. Wurzbacher, C. Gebald, N. Piatkowski and A. Steinfeld, *Concurrent Separation of CO2 and H2O from Air by a Temperature-Vacuum Swing Adsorption/Desorption Cycle, Environ Sci Technol.,* **46**, 16 (2012).

23. C. Gebald, J. A. Wurzbacher, P. Tingaut and A. Steinfeld, *Stability of Amine-Functionalized Cellulose during Temperature-Vacuum-Swing Cycling for CO2 Capture from Air, Environ Sci Technol.,* **47**, 17 (2013).

24. J. A. Wurzbacher, **Personal communication** (2013).

25. T. Wang, K. S. Lackner and A. Wright, *Moisture Swing Sorbent for Carbon Dioxide Capture from Ambient Air, Environ Sci Technol.,* **45**, 15 (2011).

26. T. Wang, K. S. Lackner and A. Wright, *Moisture-swing sorption for carbon dioxide capture from ambient air: a thermodynamic analysis, Physical Chemistry Chemical Physics.,* **15**, 2 (2013).

27. K. S. Lackner and A. Wright, **Personal communication** (2013).

28. S. Brandani, *Carbon Dioxide Capture from Air: a Simple Analysis, Energy Environ.,* **23**, 2-3 (2012).

29. S. D. Ebbesen, C. Graves and M. Mogensen, *Production of Synthetic Fuels by Co-Electrolysis of Steam and Carbon Dioxide, Int J Green Energy.,* **6**, 6 (2009).

30. K. Sasaki and Y. Teraoka, *Equilibria in fuel cell gases - I. Equilibrium compositions and reforming conditions, J Electrochem Soc.,* **150**, 7 (2003).

31. K. Sasaki and Y. Teraoka, *Equilibria in fuel cell gases - II. The C-H-O ternary diagrams, J Electrochem Soc.,* **150**, 7 (2003).

32. C. M. Stoots, J. E. O'Brien, J. S. Herring and J. J. Hartvigsen, *Syngas Production via High-Temperature Coelectrolysis of Steam and Carbon Dioxide, Journal of Fuel Cell Science and Technology.,* **6**, 1 (2009).

33. S. D. Ebbesen, R. Knibbe and M. Mogensen, *Co-Electrolysis of Steam and Carbon Dioxide in Solid Oxide Cells, J Electrochem Soc.,* **159**, 8 (2012).

34. Haldor Topsø A/S, *From solid fuels to substitute natural gas (SNG) using TREMP™, Product datasheet.,* (2009).

35. J. H. Jensen, J. M. Poulsen and N. U. Andersen, *From Coal to Clean Energy, Nitrogen+Syngas.,* **310** (2011).

36. T. Umeda, J. Itoh and K. Shiroko, *Heat-Exchange System Synthesis, Chem Eng Prog.,* **74**, 7 (1978).

37. J. Itoh, K. Shiroko and T. Umeda, *Extensive applications of the T-G diagram to heat integrated system synthesis, Computen and Chemical Engineering.,* **10**, 1 (1986).

38. M. S. Peters, K. D. Timmerhaus and R. E. West, in *Heat-Transfer Equipment - Design and Costs in:* Plant design and economics for chemical engineers, 5th ed., B. Halevi, Editor, p. 642, McGraw-Hill, New York (2004).

39. L. T. Biegler, I. E. Grossmann and A. W. Westerberg, in *Synthesis of heat exchanger networks in:* Systematic methods of chemical process design, Anonymous , p. 527, Prentice Hall Inc., NJ, USA (1997).

40. Wikipedia contributors, *Heat exchanger, Wikipedia, The Free Encyclopedia.,* **2015**, January (2015).

41. T. B. Challand, R. W. Colbert and C. K. Venkatesh, *Computerized Heat-Exchanger Networks, Chem Eng Prog.,* **77**, 7 (1981).

42. Invensys Systems Inc., *HEXTRAN,* **9.2** (2008).

43. P. Saengwirun, *ECON Economic Analysis Tools,* (2011).

44. P. Saengwirun, *Cost Calculations and Economic Analysis*, The Petroleum and Petrochemical College, Chulalongkorn University, Bangkok, Thailand (2011).

45. S. Kalakul, P. Malakul, K. Siemanond and R. Gani, *Integration of life cycle assessment software with tools for economic and sustainability analyses and process simulation for sustainable process design, J Clean Prod.,* **71**, 0 (2014).

46. T. Wang, J. Liu, M. Fang and Z. Luo, *A Moisture Swing Sorbent for Direct Air Capture of Carbon Dioxide: Thermodynamic and kinetic analysis, Ghgt-11.,* **37** (2013).

47. Climeworks Ltd., *Personal Communication,* (2014).

48. S. D. Ebbesen and M. Mogensen, *Electrolysis of carbon dioxide in Solid Oxide Electrolysis Cells, J.Power Sources.,* **193**, 1 (2009).

49. J. J. Helble, W. Mojtahedi, J. Lyyränen, J. Jokiniemi and E. Kauppinen, *Trace element partitioning during coal gasification, Fuel.,* **75**, 8 (1996).

50. D. D. Papadias, S. Ahmed and R. Kumar, *Fuel quality issues with biogas energy - An economic analysis for a stationary fuel cell system, Energy.,* **44**, 1 (2012).

51. J. Van herle, A. Schuler, L. Dammann, M. Bosco, T. Truong, E. De Boni, F. Hajbolouri, F. Vogel and G. G. Scherer, *Fuels for fuel cells: Requirements and fuel processing, Chimia.,* **58**, 12 (2004).

52. S. D. Ebbesen, C. Graves, A. Hauch, S. H. Jensen and M. Mogensen, *Poisoning of Solid Oxide Electrolysis Cells by Impurities, J Electrochem Soc.,* **157**, 10 (2010).

53. S. D. Ebbesen and M. Mogensen, *Exceptional Durability of Solid Oxide Cells, Electrochem. Solid State Lett.,* **13**, 9 (2010).

54. S. D. Ebbesen and M. B. Mogensen, *Method and system for purification of gas streams for solid oxide cells,* **10001715.1**, EP2362475 (2011).

55. S. D. Ebbesen and M. B. Mogensen, *Method and system for purification of gas streams for solid oxide cells,* **11704416.4**, EP2537203 (2011).

56. T. Ramos, K. Thyden and M. Mogensen, *
Electrochemical Characterization of Ni/(Sc)YSZ Electrodes, ECS Trans.,* **28**, 11 (2010).

57. A. Hauch, C. Birkl, K. Brodersen and P. S. Jørgensen, *Multilayer tape cast SOFC - Effect of anode sintering temperature, Proceedings of 10th European SOFC Forum.,* (2012).

58. C. W. Bale, P. Chartrand, S. A. Decterov, G. Eriksen, K. Hack, R. Mahfoud, A. D. Pelton, W. T. Thompson, I. Jung, J. Melancon and S. Petersen, *FactSage thermochemical software and databases, Calphad.,* **6.2** (2002).

59. K. Sasaki, K. Haga, T. Yoshizumi, D. Minematsu, E. Yuki, R. Liu, C. Uryu, T. Oshima, T. Ogura, Y. Shiratori, K. Ito, M. Koyama and K. Yokomoto, *Chemical durability of Solid Oxide Fuel Cells: Influence of impurities on long-term performance, J. Power Sources.,* **196**, 22 (2011).

60. R. Kiebach, K. Norrman, C. Chatzichristodoulou, M. Chen, X. Sun, S. D. Ebbesen, M. B. Mogensen and P. V. Hendriksen, *TOF-SIMS characterization of impurity enrichment and redistribution in solid oxide electrolysis cells during operation, Dalton Trans.,* **43**, 40 (2014).

61. K. V. Jensen, S. Primdahl, I. Chorkendorff and M. Mogensen, *Microstructural and chemical changes at the Ni/YSZ interface, Solid State Ionics.,* **144**, 3-4 (2001).

62. Y. Matsuzaki and I. Yasuda, *The poisoning effect of sulfur-containing impurity gas on a SOFC anode: Part I. Dependence on temperature, time, and impurity concentration, Solid State Ionics.,* **132**, 3-4 (2000).

63. I. Alstrup, J. R. Rostrup-Nielsen and S. Røen, *High-Temperature Hydrogen-Sulfide Chemisorption on Nickel-Catalysts, Applied Catalysis.,* **1**, 5 (1981).

64. J. B. Hansen, *Correlating sulfur poisoning of SOFC nickel anodes by a Temkin isotherm, Electrochem. Solid State Lett.,* **11**, 10 (2008).

65. C. H. Bartholomew, *Mechanisms of catalyst deactivation, Applied Catalysis A-General.,* **212**, 1-2 (2001).

66. S. D. Ebbesen, J. B. Hansen and M. B. Mogensen, *Biogas Upgrading Using SOEC with a Ni-ScYSZ Electrode, Solid Oxide Fuel Cells 13 (Sofc-Xiii).,* **57**, 1 (2013).

67. R. Knibbe, A. Hauch, J. Hjelm, S. D. Ebbesen and M. Mogensen, *Durability of Solid Oxide Cells, Green.,* **1**, 2 (2011).

68. H. Yokokawa, K. Yamaji, M. E. Brito, H. Kishimoto and T. Horita, *General considerations on degradation of Solid Oxide Fuel Cell anodes and cathodes due to impurities in gases, J Power Sources.,* **196**, 17 (2011).

69. A. Hauch, S. H. Jensen, J. B. Bilde-Sorensen and M. Mogensen, *Silica segregation in the Ni/YSZ electrode, J Electrochem Soc.,* **154**, 7 (2007).

70. M. Gong, X. Liu, J. Trembly and C. Johnson, *Sulfur-tolerant anode materials for solid oxide fuel cell application, J Power Sources.,* **168**, 2 (2007).

71. O. A. Marina, L. R. Pederson, E. C. Thomsen, C. A. Coyle and K. J. Yoon, *Reversible poisoning of nickel/zirconia solid oxide fuel cell anodes by hydrogen chloride in coal gas, J Power Sources.,* **195**, 20 (2010).

72. J. Bao, G. N. Krishnan, P. Jayaweera, J. Perez-Mariano and A. Sanjurjo, *Effect of various coal contaminants on the performance of solid oxide fuel cells: Part I. Accelerated testing, J Power Sources.,* **193**, 2 (2009).

73. O. A. Marina, L. R. Pederson, C. A. Coyle, E. C. Thomsen and D. J. Edwards, *Polarization-Induced Interfacial Reactions Between Nickel and Selenium in Ni/Zirconia SOFC Anodes and Comparison with Sulfur Poisoning, J Electrochem Soc.,* **158**, 1 (2011).

74. K. V. Jensen, R. Wallenberg, I. Chorkendorff and M. Mogensen, *Effect of impurities on structural and electrochemical properties of the Ni-YSZ interface RID C-7282-2008 RID B-1852-2010, Solid State Ionics.,* **160**, 1-2 (2003).

75. M. Zhi, X. Chen, H. Finklea, I. Celik and N. Q. Wu, *Electrochemical and microstructural analysis of nickel-yttria-stabilized zirconia electrode operated in phosphorus-containing syngas, J Power Sources.,* **183**, 2 (2008).

76. Y. Tao, S. D. Ebbesen and M. B. Mogensen, *Carbon Deposition in Solid Oxide Cells during Co-Electrolysis of H2O and CO2, J Electrochem Soc.,* **161**, 3 (2014).

77. D. M. Bierschenk, J. R. Wilson and S. A. Barnett, *High efficiency electrical energy storage using a methane-oxygen solid oxide cell, Energy & Environmental Science.,* **4**, 3 (2011).

78. K. Huang and J. B. Goodenough, *Solid oxide fuel cell technology*, Woodhead Publishing Ltd., Cambridge, UK (2009).

79. K. V. Hansen, S. Primdahl and M. B. Mogensen, *Studies of the Ni/YSZ interface in solid oxide fuel cell anodes, CIMTEC Conference on Mass and Charge Transport in Inorganic Materials.,* (2000).

80. P. S. Jørgensen, S. L. Ebbehøj and A. Hauch, *Triple Phase Boundary Specific Pathway Analysis for Quantitative Characterization of Solid Oxide Cell Electrode Microstructure, J Power Sources.,* **279** (2015).

81. J. M. Douglas, *Conceptual design of chemical processes*, McGraw-Hill, New York (1988).

82. L. T. Biegler, I. E. Grossmann and A. W. Westerberg, in *Equipment Sizing and Costing in:* Systematic methods of chemical process design, Anonymous , p. 110, Prentice Hall Inc., NJ, USA (1997).

83. Invensys Systems Inc., *PRO/II,* **9.3** (2014).

84. D. Peng and D. B. Robinson, *A New Two-Constant Equation of State, Ind Eng Chem Fund.,* **15**, 1 (1976).

85. M. S. Peters, K. D. Timmerhaus and R. E. West, in *Profitability, Alternative Investments, and Replacaments in:* Plant Design and Economics for Chemical Engineers, 5th ed., B. Halevi, Editor, p. 319, McGraw-Hill, New York (2004).

86. F. Salvati, A. S. Pedersen, P. Leone and M. B. Mogensen, *Synthesis of dimethyl ether (DME) and methanol via high-temperature co-electrolysis of steam and carbon dioxide: process design and plant energy performance, Transactions of the 11th European SOFC & SOEC Forum 2014.,* (2014).

87. J. E. O'Brien, X. Zhang, G. K. Housley, K. DeWall, L. Moore-McAteer and G. Tao, *High Temperature Electrolysis Pressurized Experiment Design, Operation, and Results, Report for U.S. Department of Energy Office of Nuclear Energy Under DOE Idaho Operations Office Contract DE-AC07-05ID14517.,* (2012).

88. L. A. Chick, O. A. Marina, C. A. Coyle and E. C. Thomsen, *Effects of temperature and pressure on the performance of a solid oxide fuel cell running on steam reformate of kerosene, J Power Sources.,* **236** (2013).

89. C. Willich, C. Westner, M. Henke, F. Leucht, J. Kallo and K. A. Friedrich, *Pressurized Solid Oxide Fuel Cells with Reformate as Fuel, J Electrochem Soc.,* **159**, 11 (2012).

90. P. C. Wu, H. S. Jheng and S. S. Shy, *Pressurized Solid Oxide Fuel Cells: Measurements of Impedance Spectra and Anodic Concentration Polarization, Solid Oxide Fuel Cells 13 (Sofc-Xiii).,* **57**, 1 (2013).

91. A. Momma, K. Takano, Y. Tanaka, T. Kato and A. Yamamoto, *Experimental Investigation of the Effect of Operating Pressure on the Performance of SOFC and SOEC, Solid Oxide Fuel Cells 13 (Sofc-Xiii).,* **57**, 1 (2013).

92. A. A. Burke, L. G. Carreiro and J. R. Izzo Jr., *Pressurized testing of a planar solid oxide fuel cell stack, Int J Hydrogen Energy.,* **38**, 31 (2013).

93. S. Primdahl and M. Mogensen, *Gas conversion impedance: A test geometry effect in characterization of solid oxide fuel cell anodes, J Electrochem Soc.,* **145**, 7 (1998).

94. S. Primdahl and M. Mogensen, *Gas diffusion impedance in characterization of solid oxide fuel cell anodes RID B-1852-2010, J Electrochem Soc.,* **146**, 8 (1999).

95. E. C. Thomsen, G. W. Coffey, L. R. Pederson and O. A. Marina, *Performance of lanthanum strontium manganite electrodes at high pressure, J Power Sources.,* **191**, 2 (2009).

96. M. B. Mogensen, J. V. T. Høgh, K. V. Hansen and T. Jacobsen, *A Critical Review of Models of the H_2/H_2O/Ni/SZ Electrode Kinetics, E C S Transactions.,* **7**, 1 (2007).

97. J. Høgh, *Influence of impurities on the H2/H2O/Ni/YSZ electrode*, Risø National Laboratory, Roskilde, Denmark (2005).

98. J. Njodzefon, C. R. Graves, J. Hjelm, M. B. Mogensen, A. Weber, J. Njodzefon, C. R. Graves, J. Hjelm, M. B. Mogensen and A. Weber, *Kinetic Studies on State of the Art Solid Oxide Cells, Meeting Abstracts of the Electrochemical Society 226th Meeting.,* **MA2014-02** (2014).

99. M. S. Peters, K. D. Timmerhaus and R. E. West, *Plant design and economics for chemical engineers*, McGraww-Hill, NY, USA (2004).

100. D. M. Bierschenk, J. R. Wilson, E. Miller, E. Dutton and S. A. Barnett, *A Proposed Method for High Efficiency Electrical Energy Storage Using Solid Oxide Cells, Solid Oxide Fuel Cells 12 (Sofc Xii).,* **35**, 1 (2011).

101. A. H. Pedersen, *Injection of Hydrogen into Natural Gas Systems,* DONG Energy A/S (2014).

102. T. Nguyen and F. Joensen, *Overview of Topsoe synthesis technologies for BTL and bio-SNG, Presentation; not published.,* (2012).

103. J. B. Hansen, N. Christiansen and J. U. Nielsen, *Production of Sustainable Fuels by Means of Solid Oxide Electrolysis, Solid Oxide Fuel Cells 12 (Sofc Xii).,* **35**, 1 (2011).

104. H. S. Bengaard, J. K. Norskov, J. Sehested, B. S. Clausen, L. P. Nielsen, A. M. Molenbroek and J. R. Rostrup-Nielsen, *Steam reforming and graphite formation on Ni catalysts, Journal of Catalysis.,* **209**, 2 (2002).

105. J. R. Rostrup-Nielsen and J. Sehested, *Whisker Carbon Revisited, Studies in Surface Science and Catalysis.,* **139**, 0 (2001).

106. W. D. Seider, J. D. Seader, D. R. Lewin and S. Widagdo, *Product and Process Design Principles: Synthesis, Analysis and Design*, p. 728, John Wiley and Sons Ltd. (2010).

107. J. Park, Y. Kim and J. Bae, *A numerical study on the heat and mass transfer characteristics of metal-supported solid oxide fuel cells, Int J Hydrogen Energy.,* **36**, 4 (2011).

108. W. Bi, D. Chen and Z. Lin, *A key geometric parameter for the flow uniformity in planar solid oxide fuel cell stacks, Int J Hydrogen Energy.,* **34**, 9 (2009).

109. S. Assabumrungrat, N. Ruangrassamee, S. Vivanpatarakij, N. Laosiripojana and A. Arpornwichanop, *Influence of stack arrangement on performance of multiple-stack solid oxide fuel cells with non-uniform potential operation, J.Power Sources.,* **187**, 1 (2009).

110. B. Cooper, B. Donnis and B. Moyse, *Hydroprocessing conditions affect catalyst shape selection, Oil Gas J.;(United States).,* **84**, 49 (1986).

111. H. Topsøe, B. S. Clausen and F. E. Massoth, *Hydrotreating catalysis, Science and technology*, Springer-Verlag, Berlin (1996).

112. H. Cho and M. Takemoto, *Hydrogen related brittle cracking of metastable type-304 stainless steel, J Acoustic Emission.,* **25** (2007).

113. C. San Marchi and B. P. Somerday, *Technical Reference on Hydrogen Compatibility of Materials,* Sandia National Laboratories (2005).

114. M. S. Peters, K. D. Timmerhaus and R. E. West, in *Materials Handling Equipment - Design and Cost in:* Plant design and economics for chemical engineers, 5th ed., B. Halevi, Editor, p. 485, McGraw-Hill, New York (2004).

115. J. R. Rostrup-Nielsen, K. Pedersen and J. Sehested, *High temperature methanation Sintering and structure sensitivity, Applied Catalysis A-General.,* **330** (2007).

116. M. Sudiro, A. Bertucco, G. Groppi and E. Tronconi, *Simulation of a structured catalytic reactor for exothermic methanation reactions producing synthetic natural gas, 20th European Symposium on Computer Aided Process Engineering.,* **28** (2010).

117. *Technology Data for Energy Plants, Danish Energy Agency and Energinet.dk.,* (2014).

118. B. D. James, A. B. Spisak and W. G. Colella, *Manufacturing Cost Analysis of Stationary Fuel Cell Systems,* Strategic Analysis Inc. / National Renewable Energy Laboratory (2012).

119. R. Newby and D. Kearins, *Analysis of Natural Gas Fuel Cell Plant Configurations,* **DOE/NETL – 2011/1486,** National Energy Technology Laboratory, DOE (2011).

120. R. Newby and D. Kearins, *Analysis of Integrated Gasification Fuel Cell Plant Configurations,* **DOE/NETL – 2011-1482,** National Energy Technology Laboratory, DOE (2011).

121. N. Christiansen, *Development of next generation metal based SOFC stack technology,* **METSOFC - 211940,** (2011).

122. Pingxiang Baisheng Chemical Packing Co., Ltd, *http://www.ec21.com/product-details/Methanation-Catalyst--7559630.html,* **2015**, January (2015).

123. Legumex Impex Private Ltd., *https://www.zauba.com/export-METHANATION+CATALYST+CRG+S2SR-hs-code.html,* **2015**, January (2015).

124. Inframat Advanced Materials, *8mol% Yttria Stabilized Zirconia (YSZ) Powder Superfine Grade, http://www.inframat.com/products/4039OR-8601.htm.,* **2015**, January (2015).

125. Inframat Advanced Materials, *Nickel (III) Oxide (20nm), http://www.advancedmaterials.us/28N-0801.htm.,* **2015**, January (2015).

126. Z. Zhan, D. M. Bierschenk, J. S. Cronin and S. A. Barnett, *A reduced temperature solid oxide fuel cell with nanostructured anodes, Energy Environ Sci.,* **4**, 10 (2011).

127. Danish Energy Agency, *Håndbog for energikonsulenter*, p. 127, Copenhagen (2012).

128. A. B. Hansen and L. Algren, **Personal communication** (2014-2015).

129. A. B. Hansen and L. Algren, *Unpublished data.,* (2014).

130. Anonymous *Oxygen, Chemicool Periodic Table.,* **2014**, November (2012).

131. Danish Energy Agency, *Forudsætninger for samfundsøkonomiske analyser på energiområdet,* (2014).

132. Anonymous *Economic Indicators, Chemical Engineering - 2014.,* **121**, 10 (2014).

133. Danish Energy Agency, *Vejledning i samfundsøkonomiske analyser på energiområdet,* (2007).

134. Danish Energy Agency, *Opdateret tillægsblad om kalkulationsrente, levetid og reference til Vejledning i samfundsøkonomiske analyser på energiområdet,* (2013).

135. M. S. Peters, K. D. Timmerhaus and R. E. West, in *Analysis of Cost Estimation in:* Plant Design and Economics for Chemical Engineers, 5th ed., B. Halevi, Editor, p. 226, McGraw-Hill, New York (2004).

136. M. S. Peters, K. D. Timmerhaus and R. E. West, in *Interest, Time Values of Money, Taxes, and Fixed Charges in:* Plant Design and Economics for Chemical Engineers, 5th ed., B. Halevi, Editor, p. 279, McGraw-Hill, New York (2004).

137. Z. Zhan, D. Han, T. Wu, X. Ye, S. Wang, T. Wen, S. Cho and S. A. Barnett, *A solid oxide cell yielding high power density below 600 degrees C, RSC Adv.,* **2**, 10 (2012).

138. *Biogas i Danmark - status, barrierer og perspektiver,* Danish Energy Agency (2014).

139. S. L. Ebbehøj and A. Laurent, *Unpublished results: Life cycle impact assessment of substitute natural gas,* (2015).

140. S. H. Jensen, P. H. Larsen and M. Mogensen, *Hydrogen and synthetic fuel production from renewable energy sources, Int J Hydrogen Energy.,* **32**, 15 (2007).

141. D. M. Bierschenk, J. R. Wilson, E. Miller, E. Dutton and S. A. Barnett, *A Proposed Method for High Efficiency Electrical Energy Storage Using Solid Oxide Cells, Solid Oxide Fuel Cells 12 (Sofc Xii).,* **35**, 1 (2011).

142. Y. Tao, S. D. Ebbesen and M. Mogensen, *Degradation of Solid Oxide Cells during Co-Electrolysis of H2O and CO2: Carbon Deposition under High Current Densities, Renewable Fuels from Sunlight and Electricity.,* **50**, 49 (2013).

Appendices

Appendix A PRO/II input file: Base case syngas plant

```
$ Generated by PRO/II Keyword Generation System <version 9.3>
$ Generated on: Thu Feb 26 17:31:37 2015
TITLE
  PRINT SPTPRINT=ON, STREAM=ALL, RATE=M, TBP
  TOLERANCE   STREAM   =0.01,-0.555556,0.01,0.01,   TEMPERATURE=-
0.0555556, &
         PRESSURE=0.005,     DUTY=0.001,     MISCELLANEOUS=0.003,
FLASH=3E-6
  DIMENSION SI, TEMP=K, PRES=ATM, WT=KG, TIME=HR, LENGTH=M, &
         FLENGTH=MM, LIQVOL=M3, VAPVOL=M3, LDENSITY=KG/M3, &
         VDENSITY=KG/M3, XDENSITY=DENS, SPVOL=M3/KG-MOL, &
         SPVVOL=M3/KG-MOL, ENERGY=KJ, WORK=KW, DUTY=KJ/HR, &
         CONDUCT=W/MK,  HTCOEF=KW/MK,  FOUL=MK/KW,  VISCOSITY=PAS,
&
         KVIS=CST,          SURFACE=N/M,          STDTEMP=293.15,
STDPRES(KPA)=101.325, &
         PBASIS(KPA)=101.325
  SEQUENCE PROCESS
  CALCULATION TRIALS=20, RECYCLE=ALL, TVPBASIS=310.928, &
         RVPBASIS=APIN,      COMPCHECK=CALC,      MAXOPS=1000000,
CDATA=FIX, &
         FLASH=DEFAULT, DVARIABLE=ON
COMPONENT DATA
  LIBID                    1,H2O/2,H2/3,CO2/4,CO/5,N2/6,CH4/7,O2,
BANK=SIMSCI,PROCESS
  ASSAY       FIT=ALTERNATE,       CHARACTERIZE=TWU,       MW=TWU,
CONVERSION=API94, &
         GRAVITY=WATSONK, TBPIP=1, TBPEP=98, NBP=LV, &
         CURVEFIT=CURRENT, KVRECONCILE=TAILS, FORMATION=VER91
THERMODYNAMIC DATA
  METHOD SYSTEM=PR, SET=PR01, DEFAULT
    WATER PROPERTY=IF97, TRANSPORT=IF97
STREAM DATA
  PROPERTY  STREAM=S1,  TEMPERATURE=293.15,  PRESSURE=1,  PHASE=M,
&
        RATE(GV)=60.484,
COMPOSITION(M)=1,0.011713/3,99.3/5,0.51/ &
        7,0.19, NORMALIZE, SET=PR01
  PROPERTY  STREAM=S2,  TEMPERATURE=293.15,  PRESSURE=1,  PHASE=M,
&
        RATE(M)=7.2686, COMPOSITION(M)=1,1, NORMALIZE
  NAME S18,SYNGAS/S19,O2
  OUTPUT FORMAT=PERSONAL, STREAMS=S18,S19, SPTPRINT=ON
```

```
  OUTPUT FORMAT=PERSONAL, SPTPRINT=ON
  OUTPUT FORMAT=Molar comp. 8 digits, STREAMS=S9,S15,S18, &
         SPTPRINT=ON
  OUTPUT FORMAT=Molar comp. 8 digits, STREAMS=S9,S15,S18, &
         SPTPRINT=ON
  FORMAT
IDNO=PERSONAL,SID,NAME,DOUBLINE,PHASE,LINE,TEMP,PRESSURE, &
        LINE,RATE(M),LINE,CFRAC(M),LINE,RATE(WT),CFRAC(WT),LINE,
&
        HTOTAL,BTAP,VAPOR,ARATE(GV),LIQUID,ARATE(LV)
  FORMAT IDNO=Molar comp. 8 digits,SID,NAME,PHASE,DOUBLINE,TEMP,
&

PRESSURE,HTOTAL,MW,VFRAC,LFRAC,RATE(M),TEXT,CFRAC(M),TEXT, &
        VFRAC,LFRAC,SFRAC
RXDATA
  RXSET ID=SHIFT+METH
    REACTION ID=SHIFT_R
      STOICHIOMETRY 1,-1/2,1/3,1/4,-1
    REACTION ID=METH_R
      STOICHIOMETRY 1,1/2,-3/4,-1/6,1
  RXSET ID=ELECTROLYSIS
    REACTION ID=CO2_ELECTROL
      STOICHIOMETRY 3,-2/4,2/7,1
    REACTION ID=H2O_ELECTROL
      STOICHIOMETRY 1,-2/2,2/7,1
  RXSET ID=SHIFT+BURN
    REACTION ID=SHIFT_R
      STOICHIOMETRY 1,1/2,-1/3,-1/4,1
    REACTION ID=METH_R
      STOICHIOMETRY 1,1/2,-3/4,-1/6,1
    REACTION ID=BURN_R
      STOICHIOMETRY 1,2/2,-2/7,-1
UNIT OPERATIONS
  COMPRESSOR UID=C1
      FEED S1
      PRODUCT  V=S3
      OPERATION CALCULATION=ASME, COPT=SING, PRES=50, EFF=75
  PUMP UID=P1
      FEED S2
      PRODUCT  M=S4
      OPERATION EFF=80
      DEFINE PRES(ATM) AS  COMPRESSOR=C1, PRES(ATM)
  GIBBS UID=FILT
      FEED S9
      PRODUCT M=S10
```

```
    OPERATION PHASE=M, TEMPERATURE=1023.2, ADIABATIC
    ELEMENTS REACTANTS= 1/2/3/4/6/7
    RXSTOIC RXSET=SHIFT+BURN
    REACTION SHIFT_R
    REACTION METH_R
    REACTION BURN_R
HX   UID=OHMIC_HEAT, NAME=Ohmic heating of the cell
    COLD FEED=S10, M=S11
    DEFINE CTEM(K) AS  STREAM=S9, TEMPERATURE(K), PLUS,100
GIBBS UID=SHIFT1, NAME=Cathode inlet shift and methanation
    FEED S11
    PRODUCT M=S12
    OPERATION PHASE=M, ISOTHERMAL
    ELEMENTS REACTANTS= 1/2/3/4/6
    RXSTOIC RXSET=SHIFT+METH
    REACTION SHIFT_R
    REACTION METH_R
    DEFINE TEMP(K) AS  STREAM=S11, TEMPERATURE(K)
CONREACTOR UID=ECHEM, NAME=Electrolysis reactions
    FEED S12
    PRODUCT  M=S13
    OPERATION ISOTHERMAL
    RXCALCULATION MODEL=STOIC
    RXSTOIC RXSET=ELECTROLYSIS
    REACTION CO2_ELECTROL
    BASE COMPONENT=3
    CONVERSION 1
    REACTION H2O_ELECTROL
    BASE COMPONENT=1
    CONVERSION 1
STCALCULATOR UID=SEPARATOR, NAME=Electrolyte
    FEED S13,1
    OVHD M=S14
    BTMS M=S15
    FOVHD(M) 7,7,1
    FBTMS(M) 1,6,1
    OPERATION STOP=ZERO
GIBBS UID=SHIFT2, NAME=Cathode outlet shift and methanation
    FEED S15
    PRODUCT M=S16
    OPERATION PHASE=M, ISOTHERMAL
    ELEMENTS REACTANTS= 1/2/3/4/6
    RXSTOIC RXSET=SHIFT+METH
    REACTION SHIFT_R
    REACTION METH_R
    DEFINE TEMP(K) AS  STREAM=S11, TEMPERATURE(K)
```

```
  SPLITTER UID=SP1
      FEED S16
      PRODUCT  M=S21, M=S17
      OPERATION OPTION=FILL
      SPEC STREAM=S21, RATE(KGM/H), COMP=2,WET, VALUE=0.25
  HX   UID=E4
      HOT  FEED=S17, M=S23
      OPER HTEMP=417
  FLASH UID=CONDENSER
      FEED S23
      PRODUCT  V=S18, L=S20
      TPSPEC TESTIMATE=450
      SPEC STREAM=S18,FRACTION, COMP=1,WET, VALUE=0.05
  MIXER UID=M3
      FEED S4,S20
      PRODUCT  M=S22
  HX   UID=E1
      HOT  FEED=S22, M=S6
      OPER HLFRAC=0
  MIXER UID=M1
      FEED S6,S3,S21
      PRODUCT  M=S7
  HX   UID=E2
      COLD FEED=S7, M=S9
      OPER CTEMP=1023.2
  CALCULATOR UID=CA2, NAME=Design value: 3.00
      DIMENSION  C(1), P(3), R(1), V(1), IX(1), IS(1)
      SEQUENCE  STREAM=S18
      RESULT 1,Feed_Module
      DEFINE P(1) AS  STREAM=S18,FRACTION, COMP=2,WET
      DEFINE P(2) AS  STREAM=S18,FRACTION, COMP=4,WET
      DEFINE P(3) AS  STREAM=S18,FRACTION, COMP=3,WET
      PROCEDURE
R(1) = (P(1) - P(3)) / (P(2) + P(3))
RETURN
  MVC  UID=MV1
      SPEC    ID=MVCSPEC30,    STREAM=S7,FRACTION,    COMP=2,WET,
VALUE=0.01
      SPEC    ID=MVCSPEC32,    CALCULATOR=CA2,    R(1),    VALUE=3,
ATOLER=0.01
      SPEC ID=MVC1SPEC1, FLASH=CONDENSER, DUTY(KJ/HR), VALUE=0
      VARY SPLITTER=SP1, SPEC(1)
      VARY STREAM=S2, RATE(KGM/H)
      VARY HX=E4, HTEM(K)
      MVCPARAMETERS CYCL=100, SOLVE
  HX   UID=E3
```

```
      COLD FEED=S14, M=S19
      OPER CTEMP=293.15
  CALCULATOR UID=CA1
      RESULT 1,U_cell/2,E_tn/3,RU_H2O/4,RU_CO2
      DEFINE P(1) AS  HX=OHMIC_HEAT, DUTY(KJ/HR)
      DEFINE P(2) AS  GIBBS=SHIFT1, DUTY(KJ/HR)
      DEFINE P(3) AS  CONREACTOR=ECHEM, DUTY(KJ/HR)
      DEFINE P(4) AS  GIBBS=SHIFT2, DUTY(KJ/HR)
      DEFINE P(5) AS  STREAM=S12, RATE(KGM/H), COMP=1,WET
      DEFINE P(6) AS  STREAM=S12, RATE(KGM/H), COMP=3,WET
      DEFINE P(7) AS  STREAM=S13, RATE(KGM/H), COMP=1,WET
      DEFINE P(8) AS  STREAM=S13, RATE(KGM/H), COMP=3,WET
      PROCEDURE
R(1)=P(1)+P(2)+P(3)+P(4)
R(2)=P(2)+P(3)+P(4)
R(3)=P(7)-P(5)
R(4)=P(8)-P(6)
RETURN
END
```

Appendix B PRO/II input file: Full plant design case 1

```
$ Generated by PRO/II Keyword Generation System <version 9.3>
$ Generated on: Thu Feb 26 17:23:47 2015
TITLE
  PRINT SPTPRINT=ON, STREAM=ALL, RATE=M, TBP
  TOLERANCE   STREAM   =0.01,-0.555556,0.01,0.01,   TEMPERATURE=-
0.0555556, &
         PRESSURE=0.005,     DUTY=0.001,     MISCELLANEOUS=0.003,
FLASH=3E-6
  DIMENSION SI, TEMP=K, PRES=ATM, WT=KG, TIME=HR, LENGTH=M, &
         FLENGTH=MM, LIQVOL=M3, VAPVOL=M3, LDENSITY=KG/M3, &
         VDENSITY=KG/M3, XDENSITY=DENS, SPVOL=M3/KG-MOL, &
         SPVVOL=M3/KG-MOL, ENERGY=KJ, WORK=KW, DUTY=KJ/HR, &
         CONDUCT=W/MK,  HTCOEF=KW/MK,  FOUL=MK/KW,  VISCOSITY=PAS,
&
         KVIS=CST,          SURFACE=N/M,          STDTEMP=293.15,
STDPRES(KPA)=101.325, &
         PBASIS(KPA)=101.325
  SEQUENCE SIMSCI
  CALCULATION TRIALS=20, RECYCLE=ALL, TVPBASIS=310.928, &
         RVPBASIS=APIN,      COMPCHECK=CALC,      MAXOPS=1000000,
CDATA=FIX, &
         FLASH=DEFAULT, DVARIABLE=ON
COMPONENT DATA
  LIBID                    1,H2O/2,H2/3,CO2/4,CO/5,N2/6,CH4/7,O2,
BANK=SIMSCI,PROCESS
  ASSAY       FIT=ALTERNATE,       CHARACTERIZE=TWU,       MW=TWU,
CONVERSION=API94, &
         GRAVITY=WATSONK, TBPIP=1, TBPEP=98, NBP=LV, &
         CURVEFIT=CURRENT, KVRECONCILE=TAILS, FORMATION=VER91
THERMODYNAMIC DATA
  METHOD SYSTEM=PR, SET=PR01, DEFAULT
    WATER PROPERTY=IF97, TRANSPORT=IF97
STREAM DATA
  PROPERTY  STREAM=S1,  TEMPERATURE=293.15,  PRESSURE=1,  PHASE=M,
&
        RATE(M)=2.8803, COMPOSITION(M)=1,1.1713/3,98.14/5,0.5/ &
        7,0.19, NORMALIZE, SET=PR01
  PROPERTY  STREAM=S2,  TEMPERATURE=293.15,  PRESSURE=1,  PHASE=M,
&
        RATE(M)=7.2686, COMPOSITION(M)=1,1, NORMALIZE
  PROPERTY  STREAM=S5,  TEMPERATURE=293.15,  PRESSURE=80,  PHASE=M,
&
        RATE(M)=2.585, COMPOSITION(M)=1,1, NORMALIZE
```

```
  PROPERTY    STREAM=S29,    TEMPERATURE=493,    PRESSURE=79.441,
PHASE=M, &
         RATE(M)=8.38143, COMPOSITION(M)=1,0.05/2,0.611042/ &
        3,0.0864449/4,0.088653/5,0.00171816/6,0.162142
  NAME S18,SYNGAS/S19,O2/S42,WATER
  OUTPUT      FORMAT=PERSONAL,      STREAMS=S17,S22,S18,S42,S19,
SPTPRINT=ON
  OUTPUT FORMAT=PERSONAL, STREAMS=S18,S19,S29,S30,S31,S32,S33, &
         SPTPRINT=ON
  OUTPUT      FORMAT=PERSONAL,      STREAMS=S31,S35,S37,S41,S42,
SPTPRINT=ON
  OUTPUT FORMAT=PROPLIST, STREAMS=S5,S42,S2, SPTPRINT=ON
  OUTPUT                                          FORMAT=PERSONAL,
STREAMS=S1,S10,S11,S12,S13,S14,S15,S16,S17, &

S18,S19,S2,S20,S21,S22,S23,S29,S3,S30,S31,S32,S33,S34,S35, &

S36,S37,S4,S40,S41,S42,S5,S6,S7,S8,S9,S24,S25,S26,S27,S28, &
        S38,S39,S44,S46, SPTPRINT=ON
  OUTPUT FORMAT=GAS, STREAMS=S26,S46, SPTPRINT=ON
  OUTPUT FORMAT=PROPLIST, STREAMS=S39,S30,S31,S32,S33,S45, &
         SPTPRINT=ON
  OUTPUT FORMAT=Molar comp. 8 digits, STREAMS=S46, SPTPRINT=ON
  FORMAT
IDNO=PERSONAL,SID,NAME,DOUBLINE,PHASE,LINE,TEMP,PRESSURE, &
        LINE,RATE(M),LINE,CFRAC(M),LINE,RATE(WT),CFRAC(WT),LINE,
&
        HTOTAL,BTAP,VAPOR,ARATE(GV),LIQUID,ARATE(LV)
  FORMAT IDNO=Molar comp. 8 digits,SID,NAME,PHASE,DOUBLINE,TEMP,
&

PRESSURE,HTOTAL,MW,VFRAC,LFRAC,RATE(M),TEXT,CFRAC(M),TEXT, &
        VFRAC,LFRAC,SFRAC
RXDATA
  RXSET ID=SHIFT+METH
    REACTION ID=SHIFT_R
      STOICHIOMETRY 1,-1/2,1/3,1/4,-1
    REACTION ID=METH_R
      STOICHIOMETRY 1,1/2,-3/4,-1/6,1
  RXSET ID=ELECTROLYSIS
    REACTION ID=CO2_ELECTROL
      STOICHIOMETRY 3,-2/4,2/7,1
    REACTION ID=H2O_ELECTROL
      STOICHIOMETRY 1,-2/2,2/7,1
  RXSET ID=SHIFT+BURN
    REACTION ID=SHIFT_R
```

```
      STOICHIOMETRY 1,1/2,-1/3,-1/4,1
    REACTION ID=METH_R
      STOICHIOMETRY 1,1/2,-3/4,-1/6,1
    REACTION ID=BURN_R
      STOICHIOMETRY 1,2/2,-2/7,-1
UNIT OPERATIONS
  PUMP UID=P3
      FEED S5
      PRODUCT  M=S38
      OPERATION EFF=80, PRESSURE=80.845
  PUMP UID=P1
      FEED S2
      PRODUCT  M=S4
      OPERATION EFF=80, PRESSURE=81.845
  COMPRESSOR UID=C1
      FEED S1
      PRODUCT  V=S3
      OPERATION CALCULATION=ASME, COPT=SING, PRES=80.504, EFF=75
  GIBBS UID=FILT
      FEED S9
      PRODUCT M=S10
      OPERATION PHASE=M, DP=0.3, TEMPERATURE=1023.2, ADIABATIC
      ELEMENTS REACTANTS= 1/2/3/4/6/7
      RXSTOIC RXSET=SHIFT+BURN
      REACTION SHIFT_R
      REACTION METH_R
      REACTION BURN_R
  HX   UID=OHMIC_HEAT, NAME=Ohmic heating of the cell
      HOT  FEED=S10, M=S11
      OPER HTEMP=1123.2
  GIBBS UID=SHIFT1, NAME=Cathode inlet shift and methanation
      FEED S11
      PRODUCT M=S12
      OPERATION PHASE=M, ISOTHERMAL
      ELEMENTS REACTANTS= 1/2/3/4/6
      RXSTOIC RXSET=SHIFT+METH
      REACTION SHIFT_R
      REACTION METH_R
      DEFINE TEMP(K) AS  STREAM=S11, TEMPERATURE(K)
  CONREACTOR UID=ECHEM, NAME=Electrolysis reactions
      FEED S12
      PRODUCT  M=S13
      OPERATION ISOTHERMAL, DP=0.05
      RXCALCULATION MODEL=STOIC
      RXSTOIC RXSET=ELECTROLYSIS
      REACTION CO2_ELECTROL
```

```
    BASE COMPONENT=3
    CONVERSION 0.7
    REACTION H2O_ELECTROL
    BASE COMPONENT=1
    CONVERSION 0.7
STCALCULATOR UID=SEPARATOR, NAME=Electrolyte
    FEED S13,1
    OVHD M=S14
    BTMS M=S15
    FOVHD(M) 7,7,1
    FBTMS(M) 1,6,1
    OPERATION STOP=ZERO
GIBBS UID=SHIFT2, NAME=Cathode outlet shift and methanation
    FEED S15
    PRODUCT M=S16
    OPERATION PHASE=M, ISOTHERMAL
    ELEMENTS REACTANTS= 1/2/3/4/6
    RXSTOIC RXSET=SHIFT+METH
    REACTION SHIFT_R
    REACTION METH_R
    DEFINE TEMP(K) AS  STREAM=S11, TEMPERATURE(K)
SPLITTER UID=SP1
    FEED S16
    PRODUCT  M=S21, M=S17
    OPERATION OPTION=FILL
    SPEC STREAM=S21, RATE(KGM/H), COMP=2,WET, VALUE=0.25
HX   UID=E4
    HOT  FEED=S17, M=S23, DP=0.2033
    OPER HTEMP=417
FLASH UID=FLASH1
    FEED S23
    PRODUCT  V=S18, L=S20
    TPSPEC TESTIMATE=450
    SPEC STREAM=S18,FRACTION, COMP=1,WET, VALUE=0.05
PUMP UID=P2
    FEED S20
    PRODUCT  M=S28
    OPERATION EFF=80, PRESSURE=80.845
MIXER UID=M3
    FEED S4,S28,S38
    PRODUCT  M=S22
HX   UID=E1
    COLD FEED=S22, M=S6, DP=0.3405
    OPER CLFRAC=0
MIXER UID=M1
    FEED S6,S3
```

```
    PRODUCT  M=S7
HX   UID=E2
    COLD FEED=S7, M=S8, DP=0.2043
    OPER CTEMP=1003
COMPRESSOR UID=B1
    FEED S21
    PRODUCT  V=S27
    OPERATION CALCULATION=ASME, COPT=SING, PRES=80.3, EFF=75
MIXER UID=M2
    FEED S8,S27
    PRODUCT  M=S9
COMPRESSOR UID=B2
    FEED S18
    PRODUCT  V=S29
    OPERATION CALCULATION=ASME, COPT=SING, PRES=80.204, EFF=75
HX   UID=E5
    COLD FEED=S29, M=S39, DP=0.2043
    OPER CTEMP=493.15
MIXER UID=M4
    FEED S39,S45
    PRODUCT  M=S30
GIBBS UID=RX1
    FEED S30
    PRODUCT M=S31
    OPERATION PHASE=M, DP=0.1085, ADIABATIC
    ELEMENTS REACTANTS= 1/2/3/4/6
    RXSTOIC RXSET=SHIFT+METH
    REACTION SHIFT_R
    REACTION METH_R
HX   UID=E6
    HOT  FEED=S31, M=S32, DP=0.2033
    OPER HTEMP=493
SPLITTER UID=SP2
    FEED S32
    PRODUCT  M=S33, M=S34
    OPERATION OPTION=FILL
    SPEC STREAM=S33, RATE(KGM/H),TOTAL,WET, VALUE=3.325
COMPRESSOR UID=B3
    FEED S33
    PRODUCT  V=S45
    OPERATION CALCULATION=ASME, COPT=SING, PRES=80
GIBBS UID=RX2
    FEED S34
    PRODUCT M=S35
    OPERATION PHASE=M, DP=0.0879, ADIABATIC
    ELEMENTS REACTANTS= 1/2/3/4/6
```

```
        RXSTOIC RXSET=SHIFT+METH
        REACTION SHIFT_R
        REACTION METH_R
    HX   UID=E7
        HOT  FEED=S35, M=S36, DP=0.1017
        OPER HTEMP=493
    GIBBS UID=RX3
        FEED S36
        PRODUCT M=S37
        OPERATION PHASE=M, DP=0.0847, ADIABATIC
        ELEMENTS REACTANTS= 1/2/3/4/6
        RXSTOIC RXSET=SHIFT+METH
        REACTION SHIFT_R
        REACTION METH_R
    HX   UID=E8
        HOT  FEED=S37, M=S40, DP=0.2033
        OPER HTEMP=293.15
    FLASH UID=FLASH2
        FEED S40
        PRODUCT  V=S41, L=S42
        TPSPEC TESTIMATE=293.15
        SPEC STREAM=S41,FRACTION, COMP=1,WET, VALUE=0.005
    CONTROLLER UID=CN1
        SPEC FLASH=FLASH2, DUTY(KJ/HR), VALUE=0, ATOLER=0.0001
        VARY HX=E8, HTEM(K)
        CPARAMETER IPRINT, CONTINUE
    HX   UID=E9
        COLD FEED=S41, M=S24, DP=0.2043
        OPER CTEMP=493.15
    COMPRESSOR UID=B4
        FEED S24
        PRODUCT  V=S43
        OPERATION CALCULATION=ASME, COPT=SING, PRES=80.477, EFF=75
    CALCULATOR UID=CA1, NAME=Design value: 3.00
        DIMENSION  C(1), P(3), R(1), V(1), IX(1), IS(1)
        SEQUENCE  STREAM=S18
        RESULT 1,Feed_Module
        DEFINE P(1) AS  STREAM=S18,FRACTION, COMP=2,WET
        DEFINE P(2) AS  STREAM=S18,FRACTION, COMP=4,WET
        DEFINE P(3) AS  STREAM=S18,FRACTION, COMP=3,WET
        PROCEDURE
R(1) = (P(1) - P(3)) / (P(2) + P(3))
RETURN
    MVC  UID=MV1
        SPEC ID=MVCSPEC28, STREAM=S9, TEMPERATURE(K), VALUE=1023.2
```

```
      SPEC    ID=MVCSPEC30,    STREAM=S9,FRACTION,    COMP=2,WET,
VALUE=0.01
      SPEC    ID=MVCSPEC32,    CALCULATOR=CA1,    R(1),    VALUE=3,
ATOLER=0.01
      SPEC ID=MVC1SPEC1, FLASH=FLASH1, DUTY(KJ/HR), VALUE=0
      VARY HX=E2, CTEM(K)
      VARY SPLITTER=SP1, SPEC(1)
      VARY STREAM=S2, RATE(KGM/H)
      VARY HX=E4, HTEM(K)
      MVCPARAMETERS CONTINUE
  GIBBS UID=RX4
      FEED S43
      PRODUCT M=S25
      OPERATION PHASE=M, DP=0.0679, ISOTHERMAL
      ELEMENTS REACTANTS= 1/2/3/4/6
      RXSTOIC RXSET=SHIFT+METH
      REACTION SHIFT_R
      REACTION METH_R
  HX   UID=E3
      HOT  FEED=S14, M=S19, DP=0.8172
      OPER HTEMP=293.15
  HX   UID=E10
      HOT  FEED=S25, M=S26, DP=0.4086
      OPER HTEMP=293.15
  FLASH UID=F1
      FEED S26
      PRODUCT  L=S44, V=S46
      TPSPEC TESTIMATE=293.15
      SPEC STREAM=S46, LFRAC, VALUE=0
END
```

Appendix C PRO/II input file: Full plant design case 2

```
$ Generated by PRO/II Keyword Generation System <version 9.3>
$ Generated on: Thu Feb 26 17:28:11 2015
TITLE
  PRINT SPTPRINT=ON, STREAM=ALL, RATE=M, TBP
  TOLERANCE   STREAM   =0.01,-0.555556,0.01,0.01,   TEMPERATURE=-
0.0555556, &
         PRESSURE=0.005,     DUTY=0.001,     MISCELLANEOUS=0.003,
FLASH=3E-6
  DIMENSION SI, TEMP=K, PRES=ATM, WT=KG, TIME=HR, LENGTH=M, &
         FLENGTH=MM, LIQVOL=M3, VAPVOL=M3, LDENSITY=KG/M3, &
         VDENSITY=KG/M3, XDENSITY=DENS, SPVOL=M3/KG-MOL, &
         SPVVOL=M3/KG-MOL, ENERGY=KJ, WORK=KW, DUTY=KJ/HR, &
         CONDUCT=W/MK,  HTCOEF=KW/MK,  FOUL=MK/KW,  VISCOSITY=PAS,
&
         KVIS=CST,          SURFACE=N/M,          STDTEMP=293.15,
STDPRES(KPA)=101.325, &
         PBASIS(KPA)=101.325
  SEQUENCE SIMSCI
  CALCULATION TRIALS=20, RECYCLE=ALL, TVPBASIS=310.928, &
         RVPBASIS=APIN,      COMPCHECK=CALC,      MAXOPS=1000000,
CDATA=FIX, &
         FLASH=DEFAULT, DVARIABLE=ON
COMPONENT DATA
  LIBID                    1,H2O/2,H2/3,CO2/4,CO/5,N2/6,CH4/7,O2,
BANK=SIMSCI,PROCESS
  ASSAY       FIT=ALTERNATE,       CHARACTERIZE=TWU,       MW=TWU,
CONVERSION=API94, &
         GRAVITY=WATSONK, TBPIP=1, TBPEP=98, NBP=LV, &
         CURVEFIT=CURRENT, KVRECONCILE=TAILS, FORMATION=VER91
THERMODYNAMIC DATA
  METHOD SYSTEM=PR, SET=PR01, DEFAULT
    WATER PROPERTY=IF97, TRANSPORT=IF97
STREAM DATA
  PROPERTY  STREAM=S1,  TEMPERATURE=293.15,  PRESSURE=1,  PHASE=M,
&
        RATE(M)=2.8803, COMPOSITION(M)=1,1.1713/3,98.14/5,0.5/ &
        7,0.19, NORMALIZE, SET=PR01
  PROPERTY  STREAM=S2,  TEMPERATURE=293.15,  PRESSURE=1,  PHASE=M,
&
        RATE(M)=7.2686, COMPOSITION(M)=1,1, NORMALIZE
  PROPERTY  STREAM=S5,  TEMPERATURE=348.98,  PRESSURE=80,  PHASE=M,
&
        RATE(M)=0.974, COMPOSITION(M)=1,1, NORMALIZE
```

```
  PROPERTY    STREAM=S29,    TEMPERATURE=493,    PRESSURE=79.684,
PHASE=M, &
         RATE(M)=4.63149,  COMPOSITION(M)=1,0.0500011/2,0.336654/
&
        3,0.0786368/4,0.00727335/5,0.00310901/6,0.524326
  PROPERTY   STREAM=S13,   TEMPERATURE=873.15,   PRESSURE=80.194,
PHASE=M, &
         RATE(M)=22.7483,   COMPOSITION(M)=1,0.174115/2,0.438803/
&

3,0.039118/4,0.0940887/5,0.000701082/6,0.00440161/7,0.248772
  NAME S18,SYNGAS/S19,O2/S42,WATER
  OUTPUT      FORMAT=PERSONAL,      STREAMS=S17,S22,S18,S42,S19,
SPTPRINT=ON
  OUTPUT      FORMAT=PERSONAL,      STREAMS=S18,S19,S29,S31,S32,
SPTPRINT=ON
  OUTPUT      FORMAT=PERSONAL,      STREAMS=S31,S35,S37,S41,S42,
SPTPRINT=ON
  OUTPUT FORMAT=PROPLIST, STREAMS=S5,S42,S2,S20, SPTPRINT=ON
  OUTPUT                                          FORMAT=PERSONAL,
STREAMS=S1,S10,S11,S12,S13,S14,S15,S16,S17, &

S18,S19,S2,S20,S21,S22,S23,S29,S3,S31,S32,S35,S36,S37,S4,S40, &
        S41,S42,S5,S6,S7,S8,S9,S24,S25,S26, SPTPRINT=ON
  OUTPUT FORMAT=GAS, STREAMS=S26,S39, SPTPRINT=ON
  OUTPUT FORMAT=PERSONAL, STREAMS=S26,S39, SPTPRINT=ON
  FORMAT
IDNO=PERSONAL,SID,NAME,DOUBLINE,PHASE,LINE,TEMP,PRESSURE, &
        LINE,RATE(M),LINE,CFRAC(M),LINE,RATE(WT),CFRAC(WT),LINE,
&
        HTOTAL,BTAP,VAPOR,ARATE(GV),LIQUID,ARATE(LV)
RXDATA
  RXSET ID=SHIFT+METH
    REACTION ID=SHIFT_R
      STOICHIOMETRY 1,-1/2,1/3,1/4,-1
    REACTION ID=METH_R
      STOICHIOMETRY 1,1/2,-3/4,-1/6,1
  RXSET ID=ELECTROLYSIS
    REACTION ID=CO2_ELECTROL
      STOICHIOMETRY 3,-2/4,2/7,1
    REACTION ID=H2O_ELECTROL
      STOICHIOMETRY 1,-2/2,2/7,1
  RXSET ID=SHIFT+BURN
    REACTION ID=SHIFT_R
      STOICHIOMETRY 1,1/2,-1/3,-1/4,1
    REACTION ID=METH_R
```

```
      STOICHIOMETRY 1,1/2,-3/4,-1/6,1
    REACTION ID=BURN_R
      STOICHIOMETRY 1,2/2,-2/7,-1
UNIT OPERATIONS
  PUMP UID=P3
      FEED S5
      PRODUCT  M=S30
      OPERATION EFF=800, PRESSURE=81.117
  PUMP UID=P1
      FEED S2
      PRODUCT  M=S4
      OPERATION EFF=80, PRESSURE=81.117
  COMPRESSOR UID=C1
      FEED S1
      PRODUCT  V=S3
      OPERATION CALCULATION=ASME, COPT=SING, PRES=80.504, EFF=75
  GIBBS UID=FILT
      FEED S9
      PRODUCT M=S10
      OPERATION PHASE=M, DP=0.3, TEMPERATURE=1023.2, ADIABATIC
      ELEMENTS REACTANTS= 1/2/3/4/6/7
      RXSTOIC RXSET=SHIFT+BURN
      REACTION SHIFT_R
      REACTION METH_R
      REACTION BURN_R
  HX   UID=OHMIC_HEAT, NAME=Ohmic heating of the cell
      HOT  FEED=S10, M=S11
      OPER HTEMP=873.15
  GIBBS UID=SHIFT1, NAME=Cathode inlet shift and methanation
      FEED S11
      PRODUCT M=S12
      OPERATION PHASE=M, ISOTHERMAL
      ELEMENTS REACTANTS= 1/2/3/4/6
      RXSTOIC RXSET=SHIFT+METH
      REACTION SHIFT_R
      REACTION METH_R
      DEFINE TEMP(K) AS  STREAM=S11, TEMPERATURE(K)
  CONREACTOR UID=ECHEM, NAME=Electrolysis reactions
      FEED S12
      PRODUCT  M=S13
      OPERATION ISOTHERMAL, DP=0.05
      RXCALCULATION MODEL=STOIC
      RXSTOIC RXSET=ELECTROLYSIS
      REACTION CO2_ELECTROL
      BASE COMPONENT=3
      CONVERSION 0.7
```

```
    REACTION H2O_ELECTROL
    BASE COMPONENT=1
    CONVERSION 0.7
STCALCULATOR UID=SEPARATOR, NAME=Electrolyte
    FEED S13,1
    OVHD M=S14
    BTMS M=S15
    FOVHD(M) 7,7,1
    FBTMS(M) 1,6,1
    OPERATION STOP=ZERO
GIBBS UID=SHIFT2, NAME=Cathode outlet shift and methanation
    FEED S15
    PRODUCT M=S16
    OPERATION PHASE=M, ISOTHERMAL
    ELEMENTS REACTANTS= 1/2/3/4/6
    RXSTOIC RXSET=SHIFT+METH
    REACTION SHIFT_R
    REACTION METH_R
    DEFINE TEMP(K) AS  STREAM=S11, TEMPERATURE(K)
SPLITTER UID=SP1
    FEED S16
    PRODUCT  M=S21, M=S17
    OPERATION OPTION=FILL
    SPEC STREAM=S21, RATE(KGM/H), COMP=2,WET, VALUE=0.25
HX   UID=E4
    HOT  FEED=S17, M=S23, DP=0.3062
    OPER HTEMP=417
FLASH UID=FLASH1
    FEED S23
    PRODUCT  V=S18, L=S20
    TPSPEC TESTIMATE=450
    SPEC STREAM=S18,FRACTION, COMP=1,WET, VALUE=0.05
PUMP UID=P2
    FEED S20
    PRODUCT  M=S28
    OPERATION PRESSURE=81.117
MIXER UID=M3
    FEED S4,S28,S30
    PRODUCT  M=S22
HX   UID=E1
    HOT  FEED=S22, M=S6, DP=0.6124
    OPER HLFRAC=0
MIXER UID=M1
    FEED S6,S3
    PRODUCT  M=S7
HX   UID=E2
```

```
    COLD FEED=S7, M=S8, DP=0.2041
    OPER CTEMP=773
COMPRESSOR UID=B1
    FEED S21
    PRODUCT  V=S27
    OPERATION CALCULATION=ASME, COPT=SING, PRES=80.3, EFF=75
MIXER UID=M2
    FEED S8,S27
    PRODUCT  M=S9
COMPRESSOR UID=B2
    FEED S18
    PRODUCT  V=S29
    OPERATION CALCULATION=ASME, COPT=SING, PRES=80.204, EFF=75
HX   UID=E5
    COLD FEED=S29, M=S33, DP=0.2041
    OPER CTEMP=493
GIBBS UID=RX1
    FEED S33
    PRODUCT M=S31
    OPERATION PHASE=M, DP=0.0797, ADIABATIC
    ELEMENTS REACTANTS= 1/2/3/4/6
    RXSTOIC RXSET=SHIFT+METH
    REACTION SHIFT_R
    REACTION METH_R
HX   UID=E6
    HOT  FEED=S31, M=S32, DP=0.4083
    OPER HTEMP=493
GIBBS UID=RX2
    FEED S32
    PRODUCT M=S35
    OPERATION PHASE=M, DP=0.07571, ADIABATIC
    ELEMENTS REACTANTS= 1/2/3/4/6
    RXSTOIC RXSET=SHIFT+METH
    REACTION SHIFT_R
    REACTION METH_R
HX   UID=E7
    HOT  FEED=S35, M=S36, DP=0.2041
    OPER HTEMP=493
GIBBS UID=RX3
    FEED S36
    PRODUCT M=S37
    OPERATION PHASE=M, DP=0.0679, ADIABATIC
    ELEMENTS REACTANTS= 1/2/3/4/6
    RXSTOIC RXSET=SHIFT+METH
    REACTION SHIFT_R
    REACTION METH_R
```

```
  HX   UID=E8
       HOT  FEED=S37, M=S40, DP=0.3062
       OPER HTEMP=293.15
  FLASH UID=FLASH2
       FEED S40
       PRODUCT  V=S41, L=S42
       TPSPEC TESTIMATE=293.15
       SPEC STREAM=S41,FRACTION, COMP=1,WET, VALUE=0.005
  CONTROLLER UID=CN1
       SPEC FLASH=FLASH2, DUTY(KJ/HR), VALUE=0, ATOLER=0.0001
       VARY HX=E8, HTEM(K)
       CPARAMETER IPRINT, CONTINUE
  HX   UID=E9
       COLD FEED=S41, M=S24, DP=0.4083
       OPER CTEMP=493.15
  COMPRESSOR UID=B4
       FEED S24
       PRODUCT  V=S34
       OPERATION CALCULATION=ASME, COPT=SING, PRES=80.476, EFF=75
  GIBBS UID=RX4
       FEED S34
       PRODUCT M=S25
       OPERATION PHASE=M, DP=0.0679, ISOTHERMAL
       ELEMENTS REACTANTS= 1/2/3/4/6
       RXSTOIC RXSET=SHIFT+METH
       REACTION SHIFT_R
       REACTION METH_R
  CALCULATOR UID=CA2, NAME=Design value: 3.00
       DIMENSION  C(1), P(3), R(1), V(1), IX(1), IS(1)
       SEQUENCE  STREAM=S18
       RESULT 1,Feed_Module
       DEFINE P(1) AS  STREAM=S18,FRACTION, COMP=2,WET
       DEFINE P(2) AS  STREAM=S18,FRACTION, COMP=4,WET
       DEFINE P(3) AS  STREAM=S18,FRACTION, COMP=3,WET
       PROCEDURE
R(1) = (P(1) - P(3)) / (P(2) + P(3))
RETURN
  MVC  UID=MV1
       SPEC ID=MVCSPEC28, STREAM=S9, TEMPERATURE(K), VALUE=773.15
       SPEC    ID=MVCSPEC30,    STREAM=S9,FRACTION,    COMP=2,WET,
VALUE=0.01
       SPEC    ID=MVCSPEC32,    CALCULATOR=CA2,    R(1),    VALUE=3,
ATOLER=0.01
       SPEC ID=MVC1SPEC1, FLASH=FLASH1, DUTY(KJ/HR), VALUE=0
       VARY HX=E2, CTEM(K)
       VARY SPLITTER=SP1, SPEC(1)
```

```
        VARY STREAM=S2, RATE(KGM/H)
        VARY HX=E4, HTEM(K)
        MVCPARAMETERS CONTINUE
    HX   UID=E3
        COLD FEED=S14, M=S19, DP=0.8166
        OPER CTEMP=293.15
    HX   UID=E10
        HOT  FEED=S25, M=S26, DP=0.4083
        OPER HTEMP=293.15
    FLASH UID=F1
        FEED S26
        PRODUCT  L=S38, V=S39
        ADIABATIC
    CONTROLLER UID=CN6
        CPARAMETER IPRINT, SOLVE, ITER=50
END
```

Appendix D Process flow diagram: full plant design case 1

Reference sheet. The reader is encouraged to cut out this page for easy reference while reading.

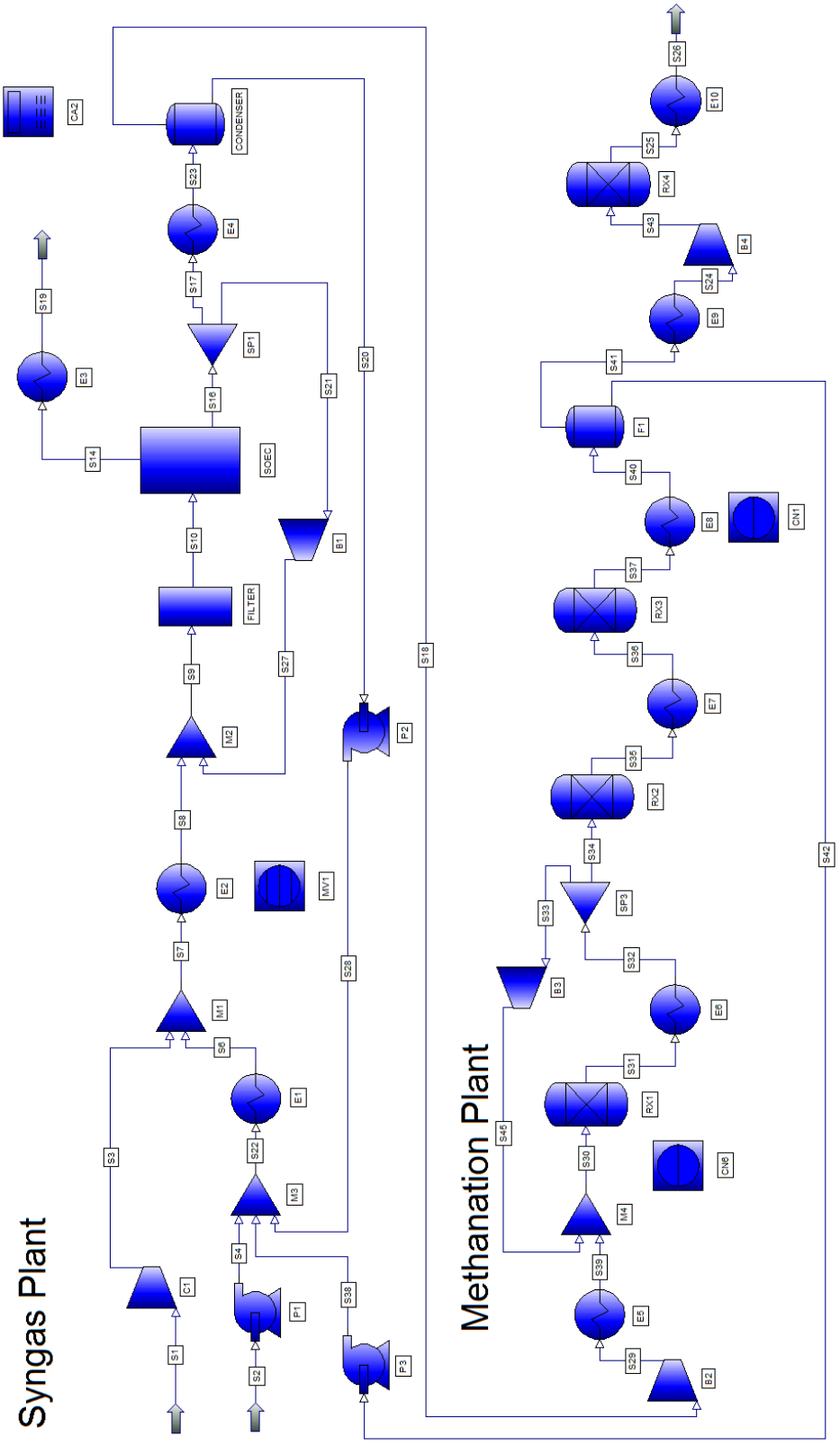

Syngas Plant

- **S1:** CO_2 inlet stream.
- **C1:** CO_2 inlet compressor ($\eta_{adiabatic}$=75 %).
- **S2:** H_2O inlet stream.
- **P1:** H_2O inlet pump ($\eta_{adiabatic}$=80 %).
- **M3: M**ixes the H_2O inlet and recycle streams.
- **E1:** H_2O evaporator.
- **M1**: Mixes the CO_2 and H_2O streams.
- **E2:** SOEC pre-heater.
- **M2:** Mixes the SOEC input stream with the SOEC recycle stream.
- **FILTER:** removing impurities and O_2 (adiabatic Gibbs reactor).
- **SOEC:** Models SOEC stack. See section SOEC model: SOEC model
- **E3:** O_2 byproduct heat recovery.
- **SP1:** Splits off SOEC recycle stream (app. 3 %) to keep filter and SOEC-cathode reduced.
- **B1:** Blower for re-pressurization of the SOEC recycle stream ($\eta_{adiabatic}$=75 %).
- **E4:** Condenser cooling.
- **CONDENSER:** Flash drum, separating the liquid water from the vapor phase. Recovery: 5%
- **P2:** Pump for re-pressurization of the H_2O recycle ($\eta_{adiabatic}$=80 %).
- **S18:** syngas product stream.

Methanation plant

- **B2:** Blower for re-pressurization of the syngas stream ($\eta_{adiabatic}$=75 %).
- **E6:** Methanation preheater, increasing the temperature of the syngas stream (S18) to the required inlet temperature of the first methanation reactor (Rx 1) which is 220 °C.
- **M4:** mixer adding the Rx 1 recycle stream to the feed stream. This is only included in case 1.
- **Rx1: Fi**rst methanation reactor. Adiabatic Gibbs reactor with the methanation and WGS reactions.
- **E6:** First intercooler heat exchanger which cools the effluent stream of Rx 1 to 220 °C.
- **SP3:** Splitter which removes a part of the stream S32 and sends it back to M4 upstream of Rx 1.
- **B3:** Blower for re-pressurization of the Rx1 recycle stream ($\eta_{adiabatic}$=75 %).
- **Rx2:** Second methanation reactor with the same settings as Rx 1.
- **E7:** Second intercooler heat exchanger which cools the effluent stream of Rx 2 to 220 °C.
- **Rx3:** Third methanation reactor with the same settings as Rx 1 and Rx 2.
- **E8:** Condenser, cooling the effluent stream from Rx 3 to 76 °C in order to recover the H_2O fraction.
- **F1:** Flash drum, separating the water from the SNG product. Recovery: 5%
- **P3:** Pump for re-pressurization of the H_2O recycle ($\eta_{adiabatic}$=80 %).
- **E9:** Heat exchanger heating the inlet stream of Rx 4 to 220 °C.
- **B3:** Blower for re-pressurization of the inlet stream for Rx4 ($\eta_{adiabatic}$=75 %).
- **Rx4:** Fourth and last methanation reactor. It has the same settings as Rx 1, Rx 2 and Rx 3.
- **E10**: Heat exchanger for recovery of heat from the SNG stream.
- **S41:** Product exit stream, leading the SNG product to the NG grid at at 20 °C and 80 atm.

Control loops

- **Feed module and water input flow rate:** FM of syngas stream (S18) adjusted by flowrate of S2.
- **Redox potential of the filter inlet stream:** Adjusted by the split fraction of the SP1 splitter.
- **Temperature of filter inlet stream:** Adjusted to 750 °C by the E2 heat exchanger.
- **Water recovery:** Adjusted by the condenser operating temperature.
- **Rx 1 temperature control.** Controls split fraction of SP3 to keep Rx1 temperature below 700 °C.

Appendix E Process flow diagram: full plant design case 2

Reference sheet. The reader is encouraged to cut out this page for easy reference while reading.

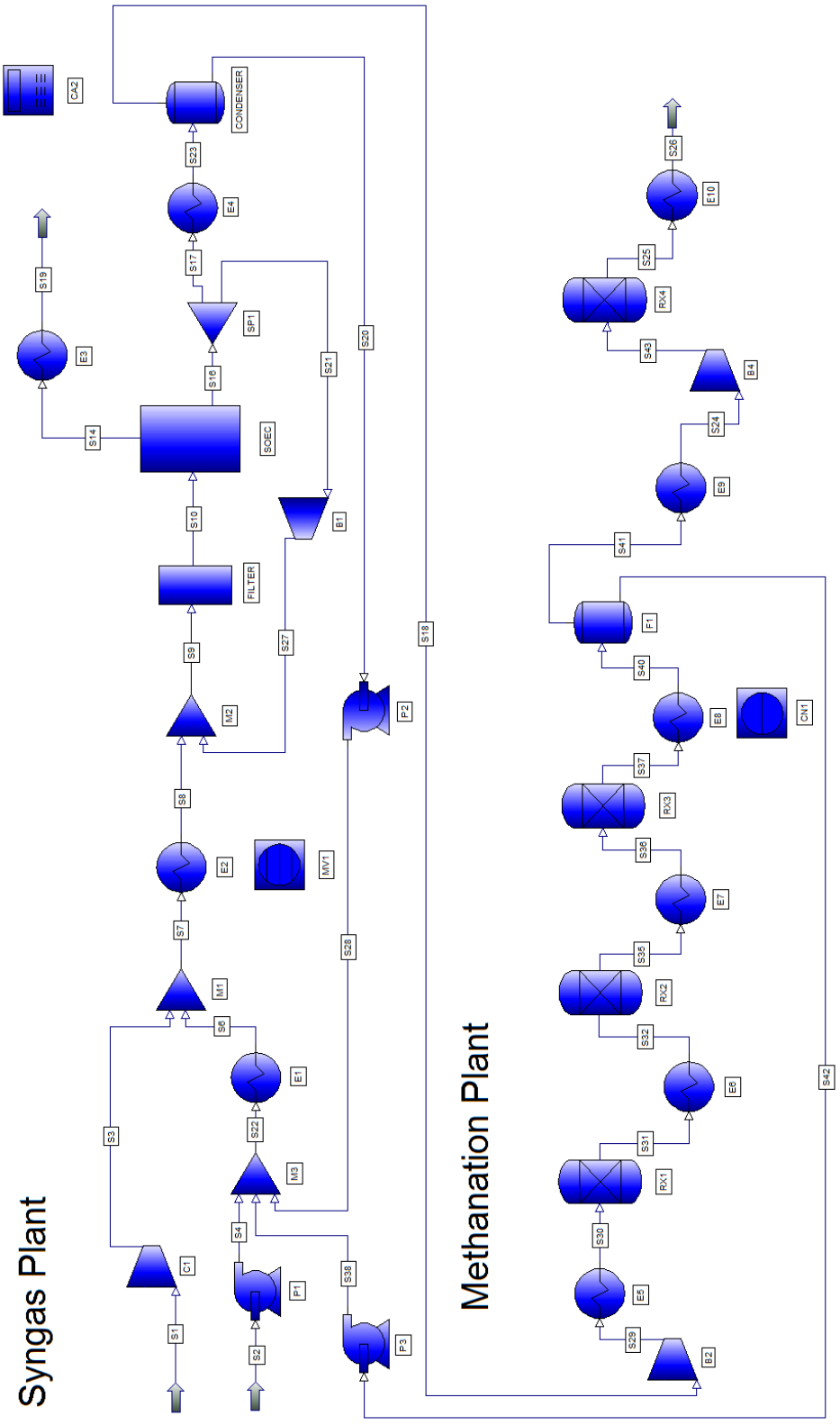

Syngas Plant

- **S1:** CO_2 inlet stream.
- **C1:** CO_2 inlet compressor ($\eta_{adiabatic}$=75 %).
- **S2:** H_2O inlet stream.
- **P1:** H_2O inlet pump ($\eta_{adiabatic}$=80 %).
- **M3: M**ixes the H_2O inlet and recycle streams.
- **E1:** H_2O evaporator.
- **M1**: Mixes the CO_2 and H_2O streams.
- **E2:** SOEC pre-heater.
- **M2:** Mixes the SOEC input stream with the SOEC recycle stream.
- **FILTER:** removing impurities and O_2 (adiabatic Gibbs reactor).
- **SOEC:** Models SOEC stack. See section SOEC model: SOEC model
- **E3:** O_2 byproduct heat recovery.
- **SP1:** Splits off SOEC recycle stream (app. 3 %) to keep filter and SOEC-cathode reduced.
- **B1:** Blower for re-pressurization of the SOEC recycle stream ($\eta_{adiabatic}$=75 %).
- **E4:** Condenser cooling.
- **CONDENSER:** Flash drum, separating the liquid water from the vapor phase. Recovery: 5%
- **P2:** Pump for re-pressurization of the H_2O recycle ($\eta_{adiabatic}$=80 %).
- **S18:** syngas product stream.

Methanation plant

- **B2:** Blower for re-pressurization of the syngas stream ($\eta_{adiabatic}$=75 %).
- **E6:** Methanation preheater, increasing the temperature of the syngas stream (S18) to the required inlet temperature of the first methanation reactor (Rx 1) which is 220 °C.
- **Rx1: Fi**rst methanation reactor. Adiabatic Gibbs reactor with the methanation and WGS reactions.
- **E6:** First intercooler heat exchanger which cools the effluent stream of Rx 1 to 220 °C.
- **Rx2:** Second methanation reactor with the same settings as Rx 1.
- **E7:** Second intercooler heat exchanger which cools the effluent stream of Rx 2 to 220 °C.
- **Rx3:** Third methanation reactor with the same settings as Rx 1 and Rx 2.
- **E8:** Condenser, cooling the effluent stream from Rx 3 to 76 °C in order to recover the H_2O fraction.
- **F1:** Flash drum, separating the water from the SNG product. Recovery: 5%
- **P3:** Pump for re-pressurization of the H_2O recycle ($\eta_{adiabatic}$=80 %).
- **E9:** Heat exchanger heating the inlet stream of Rx 4 to 220 °C.
- **B3:** Blower for re-pressurization of the inlet stream for Rx4 ($\eta_{adiabatic}$=75 %).
- **Rx4:** Fourth and last methanation reactor. It has the same settings as Rx 1, Rx 2 and Rx 3.
- **E10**: Heat exchanger for recovery of heat from the SNG stream.
- **S41:** Product exit stream, leading the SNG product to the NG grid at at 20 °C and 80 atm.

Control loops

- **Feed module and water input flow rate:** FM of syngas stream (S18) adjusted by flowrate of S2.
- **Redox potential of the filter inlet stream:** Adjusted by the split fraction of the SP1 splitter.
- **Temperature of filter inlet stream:** Adjusted to 750 °C by the E2 heat exchanger.
- **Water recovery:** Adjusted by the condenser operating temperature.

Appendix F HEXTRAN input: Case 1 heat exchanger network synthesis

```
$ GENERATED FROM HEXTRAN KEYWORD EXPORTER
$
$     General Data Section
$
TITLE PROJECT=PROBLEM, PROBLEM=SITE, SITE=
$
DIME  SI, AREA=M2, CONDUCTIVITY=WMK, DENSITY=KG/M3, *
      ENERGY=KJ, FILM=WMK, LIQVOLUME=M3, POWER=KW, *
      PRESSURE=KPA, SURFACE=NM, TIME=HR, TEMPERATURE=K, *
      UVALUE=WMK, VAPVOLUME=M3, VISCOSITY=PAS, WT=KG, *
      XDENSITY=DENS, STDVAPOR=22.414
$
PRINT ALL, *
      RATE=M, *
      FRACTION=M
$
CALC  PGEN=New, WATER=Saturated
$
$     Component Data Section
$
COMPONENT DATA
$
 LIBID    1, H2O /*
          2, H2 /*
          3, CO2 /*
          4, CO /*
          5, N2 /*
          6, CH4 /*
          7, O2
$

$
$     Thermodynamic Data Section
$
THERMODYNAMIC DATA
$
 METHODS  SET=PRO,  KVALUE=PRP,  ENTHALPY(L)=PRP,  ENTHALPY(V)=PRP,
*
               ENTROPY(L)=PRP,   ENTROPY(V)=PRP,   DENSITY(L)=PRP,
*
               DENSITY(V)=PRP,                 VISCOS(L)=LIBRARY,
VISCOS(V)=LIBRARY,  *
```

```
                CONDUCT(L)=LIBRARY,            CONDUCT(V)=LIBRARY,
SURFACE=LIBRARY
$
 WATER DECANT=ON, SOLUBILITY = Simsci, PROP = Saturated

$
$Stream Data Section
$
STREAM DATA

$
 PROP STRM=S1, NAME=S1, TEMP=373.15, PRES=101.325, *
      TOUT=378.15, RATE(M)=2.8803, *
   COMP(M)=  1, 0.033737 / 3, 2.82669 / *
        5, 0.014401 /   7, 0.005472, NORMALIZE, *
         Duty(AVG)=0.743414
$
 PROP STRM=S1_1, NAME=S1_1, TEMP=293.15, PRES=101.325, *
      TOUT=288.15, RATE(M)=2.8803, *
   COMP(M)=  1, 0.033737 / 3, 2.82669 / *
        5, 0.014401 /   7, 0.005472, NORMALIZE, *
         Duty(AVG)=0.340358
$
 PROP STRM=S1_2, NAME=S1_2, TEMP=313.15, PRES=101.325, *
      TOUT=308.15, RATE(M)=2.8803, *
   COMP(M)=  1, 0.033737 / 3, 2.82669 / *
        5, 0.014401 /   7, 0.005472, NORMALIZE, *
         Duty(AVG)=0.058219
$
 PROP STRM=S17, NAME=S17, TEMP=1123.15, PRES=8106, *
      TOUT=417.27, RATE(M)=13.2980, *
   COMP(M)=  1, 5.3345 / *
        2, 5.1223 /   3, 0.7243 /   4, 0.7424 / *
        5, 0.0144 /  6, 1.3601, NORMALIZE, *
         Duty(AVG)=0.5446
$
 PROP STRM=S22, NAME=S22, TEMP=340.18, PRES=8106, *
      TOUT=569.08, RATE(M)=13.1446, *
   COMP(M)=  1, 13.1446, *
         NORMALIZE, Duty(AVG)=0.583952
$
 PROP STRM=S7, NAME=S7, TEMP=581.45, PRES=8106, *
      TOUT=1020.81, RATE(M)=13.1783, *
   COMP(M)=  1, 13.1783 / *
        3, 2.8267 /   5, 0.0144 /   7, 0.005472, *
         NORMALIZE, Duty(AVG)=0.328589
```

```
$
 PROP STRM=S14, NAME=S14, TEMP=1123.31, PRES=8106, *
      TOUT=293.15, RATE(M)=5.6579, *
   COMP(M)=  7, 5.6579, *
         NORMALIZE, Duty(AVG)=0.1583
$
 PROP STRM=s18, NAME=s18, TEMP=417.2378, PRES=8106, *
      TOUT=493.00, RATE(M)=8.3826, *
   COMP(M)=  1, 0.4191 / *
        2, 5.1223 / 3, 0.7243 / 4, 0.7424 / 5, 0.0144 / 6,
1.3601, *
         NORMALIZE, Duty(AVG)=0.02167
$
 PROP STRM=s31, NAME=s31, TEMP=972.68, PRES=8106, *
      TOUT=493, RATE(M)=9.5425, *
   COMP(M)=  1, 3.0013 / *
        2, 2.1811   / 3, 0.4121 / 4, 0.1807 / 5, 0.0221 / 6,
3.7452, *
         NORMALIZE, Duty(AVG)=0.2254
$
 PROP STRM=s35, NAME=s35, TEMP=699.61, PRES=8106, *
      TOUT=493, RATE(M)=5.5662, *
   COMP(M)=  1, 2.4931 / *
        2, 0.2310 / 3, 0.0589 / 4, 0.0006 / 5, 0.0144 / 6,
2.7682, *
         NORMALIZE, Duty(AVG)=0.009649
$
 PROP STRM=s37, NAME=s37, TEMP=504.05, PRES=8106, *
      TOUT=349.32, RATE(M)=5.4582, *
   COMP(M)=  1, 2.6004 / *
        2, 0.0157 / 3, 0.0055 / 4, 0.000000295 / 5, 0.0144 / *
            6, 2.8222, NORMALIZE, Duty(AVG)=0.10162
$
 PROP STRM=s41, NAME=s41, TEMP=349.322, PRES=8106, *
      TOUT=493.15, RATE(M)=2.8721, *
   COMP(M)=  1, 0.0144 / *
        2, 0.0157 / 3, 0.0055 / 4, 0.000000295 / 5, 0.0144 / *
            6, 2.8222, NORMALIZE, Duty(AVG)=0.10162
$
 PROP STRM=s25, NAME=s25, TEMP=493.15, PRES=8106, *
      TOUT=293.15, RATE(M)=2.8650, *
   COMP(M)=  1, 0.0215 / *
        2, 0.0105 / 3, 0.0019 / 4, 0.000000295 / 5, 0.0144 / *
            6, 2.8257, NORMALIZE, Duty(AVG)=0.0268
$
 UTILITY STREAM=U2, TEMP=573.15, TOUT=283.15, *
```

```
       FILM=10, COST=17.7
$
 UTILITY STREAM=U3, TEMP=283.15, TOUT=573.15, *
       FILM=1000, COST=0.11
$
$ Calculation Type Section
$
SYNTHESIS
$
 SPEC   HRAT=15, 20, 25, *
       EMAT=5, 5, 5,
$
 PARAMETER FILM=100.00,
$
 PRINT  SPLIT=NONE, UNSPLIT=LAST
$
 PLOT HOT, ALL, COLD
$
HXCOST     BSIZE=0, BCOST=0, LINEAR=119.3, *
        EXPONENT=0.00, CONSTANT=3043.15
$
ECONOMICS     DAYS=350,     CURRENCY=EURO,     EXCHANGERATE=0.779,
RATE=0.04, LIFE=20
$
 LIMITS MAXP=10,  MAXS=10,  MAXAREA=557.418000,  *
          MINFT=0.800000
$

$ End of keyword file...
```

Appendix G HEXTRAN input: Case 1 heat exchanger network synthesis

```
$ GENERATED FROM HEXTRAN KEYWORD EXPORTER
$
$     General Data Section
$
TITLE PROJECT=PROBLEM, PROBLEM=SITE, SITE=
$
DIME  SI, AREA=M2, CONDUCTIVITY=WMK, DENSITY=KG/M3, *
      ENERGY=KJ, FILM=WMK, LIQVOLUME=M3, POWER=KW, *
      PRESSURE=KPA, SURFACE=NM, TIME=HR, TEMPERATURE=K, *
      UVALUE=WMK, VAPVOLUME=M3, VISCOSITY=PAS, WT=KG, *
      XDENSITY=DENS, STDVAPOR=22.414
$
PRINT ALL, *
      RATE=M, *
      FRACTION=M
$
CALC  PGEN=New, WATER=Saturated
$
$     Component Data Section
$
COMPONENT DATA
$
 LIBID    1, H2O /*
          2, H2 /*
          3, CO2 /*
          4, CO /*
          5, N2 /*
          6, CH4 /*
          7, O2
$

$
$     Thermodynamic Data Section
$
THERMODYNAMIC DATA
$
 METHODS  SET=PRO,  KVALUE=PRP,  ENTHALPY(L)=PRP,  ENTHALPY(V)=PRP,
*
               ENTROPY(L)=PRP,   ENTROPY(V)=PRP,   DENSITY(L)=PRP,
*
               DENSITY(V)=PRP,                 VISCOS(L)=LIBRARY,
VISCOS(V)=LIBRARY,  *
```

```
                CONDUCT(L)=LIBRARY,            CONDUCT(V)=LIBRARY,
SURFACE=LIBRARY
$
 WATER DECANT=ON, SOLUBILITY = Simsci, PROP = Saturated

$
$Stream Data Section
$
STREAM DATA

$
 PROP STRM=S1, NAME=S1, TEMP=373.15, PRES=101.325, *
      TOUT=378.15, RATE(M)=2.8803, *
   COMP(M)=  1, 0.033737 / 3, 2.82669 / *
        5, 0.014401 /   7, 0.005472, NORMALIZE, *
         Duty(AVG)=0.743414
$
 PROP STRM=S1_1, NAME=S1_1, TEMP=293.15, PRES=101.325, *
      TOUT=288.15, RATE(M)=2.8803, *
   COMP(M)=  1, 0.033737 / 3, 2.82669 / *
        5, 0.014401 /   7, 0.005472, NORMALIZE, *
         Duty(AVG)=0.340358
$
 PROP STRM=S1_2, NAME=S1_2, TEMP=313.15, PRES=101.325, *
      TOUT=308.15, RATE(M)=2.8803, *
   COMP(M)=  1, 0.033737 / 3, 2.82669 / *
        5, 0.014401 /   7, 0.005472, NORMALIZE, *
         Duty(AVG)=0.058219
$
 PROP STRM=S17, NAME=S17, TEMP=873.15, PRES=8106, *
      TOUT=417.20, RATE(M)=10.7515, *
   COMP(M)=  1, 6.3510 / *
        2, 1.5598 /   3, 0.3651 /   4, 0.03379 / *
        5, 0.0144 /  6, 2.4275, NORMALIZE, *
         Duty(AVG)=0.3823
$
 PROP STRM=S22, NAME=S22, TEMP=353.30, PRES=8106, *
      TOUT=569.08, RATE(M)=12.7294, *
   COMP(M)=  1, 12.7294, *
         NORMALIZE, Duty(AVG)=0.4905
$
 PROP STRM=S7, NAME=S7, TEMP=581.35, PRES=8106, *
      TOUT=765.74, RATE(M)=15.6097, *
   COMP(M)=  1, 12.7631 / *
        3, 2.8267 /   5, 0.014401 /   7, 0.005472, *
         NORMALIZE, Duty(AVG)=0.1260
```

```
$
 PROP STRM=S14, NAME=S14, TEMP=873.54, PRES=8106, *
      TOUT=293.15, RATE(M)=5.6576, *
   COMP(M)=  7, 5.6576, *
         NORMALIZE, Duty(AVG)=0.1583
$
 PROP STRM=s18, NAME=s18, TEMP=417.2378, PRES=8106, *
      TOUT=493.00, RATE(M)=4.6322, *
   COMP(M)=  1, 0.2316 / *
        2, 1.5598 / 3, 0.3651 / 4, 0.03379 / 5, 0.0144 / 6,
2.4275, *
         NORMALIZE, Duty(AVG)=0.0124
$
 PROP STRM=s31, NAME=s31, TEMP=787.90, PRES=8106, *
      TOUT=493, RATE(M)=3.9779, *
   COMP(M)=  1, 0.8567 / *
        2, 0.2804   / 3, 0.067122 / 4, 0.004655 / 5, 0.0144 / 6,
2.7546, *
         NORMALIZE, Duty(AVG)=0.0523
$
 PROP STRM=s35, NAME=s35, TEMP=556.32, PRES=8106, *
      TOUT=493, RATE(M)=3.8492, *
   COMP(M)=  1, 0.9808 / *
        2, 0.02759 / 3, 0.007399 / 4, 0.0000408 / 5, 0.0144 / 6,
2.8190, *
         NORMALIZE, Duty(AVG)=0.0105
$
 PROP STRM=s37, NAME=s37, TEMP=497.07, PRES=8106, *
      TOUT=349.31, RATE(M)=3.8407, *
   COMP(M)=  1, 0.9893 / *
        2, 0.01067 / 3, 0.003172 / 4, 0.00000025 / 5, 0.0144 / *
            6, 2.8232, NORMALIZE, Duty(AVG)=0.0561
$
 PROP STRM=s41, NAME=s41, TEMP=349.32, PRES=8106, *
      TOUT=493.15, RATE(M)=2.8658, *
   COMP(M)=  1, 0.0143 / *
        2, 0.01067 / 3, 0.003172 / 4, 0.00000025 / 5, 0.0144 / *
            6, 2.8232, NORMALIZE, Duty(AVG)=0.0165
$
 PROP STRM=s25, NAME=s25, TEMP=493.15, PRES=8106, *
      TOUT=293.15, RATE(M)=2.8613, *
   COMP(M)=  1, 0.0188 / *
        2, 0.001702 / 3, 0.000931 / 4, 0.00000051 / 5, 0.0144 /
*
            6, 2.8255, NORMALIZE, Duty(AVG)=0.0236
$
```

```
 UTILITY STREAM=U2, TEMP=573.15, TOUT=283.15, *
       FILM=10, COST=17.7
$
 UTILITY STREAM=U3, TEMP=283.15, TOUT=573.15, *
       FILM=1000, COST=0.11
$
$ Calculation Type Section
$
SYNTHESIS
$
 SPEC   HRAT=10, 15, 20,  *
       EMAT=5, 5, 5
$
 PARAMETER FILM=100.00,
$
 PRINT  SPLIT=NONE, UNSPLIT=LAST
$
 PLOT HOT, ALL, COLD
$
HXCOST     BSIZE=0, BCOST=0, LINEAR=119.3, *
        EXPONENT=0.00, CONSTANT=3043.15
$
ECONOMICS DAYS=350, CURRENCY=EURO, EXCHANGERATE=0.779, RATE=4.0,
LIFE=30
$
 LIMITS MAXP=10,  MAXS=10,  MAXAREA=557.418000,  *
          MINFT=0.800000
$

$ End of keyword file...
```